DOE/ER--0046/17
DE84 016957

Damage Analysis and Fundamental Studies

Quarterly Progress Report
January-March 1984

May 1984

U.S. Department of Energy
Office of Energy Research
Office of Fusion Energy
Washington, DC 20545

DISCLAIMER

FOREWORD

This report is the twenty-fifth in a series of Quarterly Technical Progress Reports on *Damage Analysis and Fundamental Studies* (DAFS), which is one element of the Fusion Reactor Materials Program, conducted in support of the Magnetic Fusion Energy Program of the U.S. Department of Energy (DOE). The first eight reports in this series were numbered DOE/ET-0065/1 through 8. Other elements of the Fusion Materials Program are:

- Alloy Development for Irradiation Performance (ADIP)
- Plasma-Materials Interaction (PMI)
- Special Purpose Materials (SPM).

The DAFS program element is a national effort composed of contributions from a number of National Laboratories and other government laboratories, universities, and industrial laboratories. It was organized by the Materials and Radiation Effects Branch, DOE/Office of Fusion Energy, and a Task Group on *Damage Analysis and Fundamental Studies,* which operates under the auspices of that branch. The purpose of this series of reports is to provide a working technical record of that effort for the use of the program participants, the fusion energy program in general, and the DOE.

This report is organized along topical lines in parallel to a Program Plan of the same title so that activities and accomplishments may be followed readily, relative to that Program Plan. Thus, the work of a given laboratory may appear throughout the report. Note that a new chapter has been added on Reduced Activation Materials to accommodate work on a topic not included in the early program plan. The Contents is annotated for the convenience of the reader.

This report has been compiled and edited under the guidance of the Chairman of the Task Group on *Damage Analysis and Fundamental Studies,* D. G. Doran, Hanford Engineering Development Laboratory (HEDL). His efforts, those of the supporting staff of HEDL, and the many persons who made technical contributions are gratefully acknowledged. T. C. Reuther, Materials and Radiation Effects Branch, is the DOE counterpart to the Task Group Chairman and has responsibility for the DAFS program within DOE.

G. M. Haas, Chief
Reactor Technologies Branch
Office of Fusion Energy

CONTENTS

	Page
Foreword	iii
CHAPTER 1: IRRADIATION TEST FACILITIES	1
1. RTNS-II Irradiations and Operations (LLNL)	2

Irradiations were performed for 13 different experimenters during this quarter. An investigation is underway into the implosion of two 50-cm targets. An isotransformer and a target water system malfunctioned but are back in service. The HEDL furnace shut down due to vacuum leak. The fourth U.S.-Japan Steering Committee meeting was held February 27-28 at RTNS-II.

CHAPTER 2: DOSIMETRY AND DAMAGE PARAMETERS	4
1. Hafnium Core Piece Test in ORR-MFE4 (ANL)	5

Test results show a thermal shielding of 40%, an epithermal effect of 56%, and a fast neutron reduction of about 7%. Flux gradients are reported with and without the hafnium liner.

2. Measurement of $^{54}Fe(n,2n)^{53}Fe$ Cross Section Near Threshold (ANL)	11

The threshold for this reaction, a producer of long-lived radioactivity from ^{53}Mn, falls quite close to the centroid of the neutron energy distribution emitted by a D-T plasma. This makes the reaction rate quite sensitive to the ion temperature of the plasma; hence these measurements will be used in a new method for measuring D-T plasma ion temperatures.

3. Helium Generation Measurements for EBR-II and ORR (RI-ESG)	14

Helium generation measurements for Fe, Cu, and Ti samples show significant differences from helium concentrations calculated using ENDF/B-V cross-section evaluations.

Page

CHAPTER 3: REDUCED ACTIVATION MATERIALS 17

1. Swelling Behavior of Manganese-Bearing Steel AISI 216 (HEDL) 18

The inclusion of 8.5 wt% manganese in AISI 216 (Fe-6.7Ni-8.5Mn-20Cr-2.7Mo-0.32Si) does not appear to alter the swelling behavior from that found to be typical of austenitic alloys with comparable levels of austenitite-stabilizing elements.

CHAPTER 4: FUNDAMENTAL MECHANICAL BEHAVIOR 23

1. Correlation of AISI 316 Stainless Steel Yield Strength with Irradiation-Induced Microstructure (HEDL) 24

Improvements in the correlation of change in yield strength in AISI 316 stainless steel with microstructure were effected by re-examining the role of short-range obstacles. It is concluded that large changes in yield strength may be produced in high swelling materials.

2. A Rate-Theory Model for the Evolution of Network Dislocations in Irradiated Metals (U. of Wisconsin) 38

The growth of dislocation loops and the climb of edge dislocations can result both in an increase of dislocation line length as well as in the annihilation of dislocation dipoles. These two competing processes form the basis of an evolution model for the dislocation network, which was fitted to experimental data for the dislocation density in irradiated type 316 stainless steels. Predictions are made for the dislocation evolution in ferritic steels.

3. Relations Among Tensile Test Temperature and Strain Rate in the Fracture of Helium-Irradiated Type 316 Stainless Steel (U. of Virginia) 51

Conducting one tensile test at two temperatures has shown that a given crack propagates intergranularly at 700°C and immediately changes to transgranular propagation when the temperature is lowered to 550°C. It is shown that this temperature effect is strain rate sensitive and that helium embrittlement is a dynamic phenomenon likely dependent on submicroscopic helium clusters rather than helium bubbles.

Page

4. Effective Thermophysical and Elastic Properties of Materials with Voids (HEDL) 58

Appropriate equations are given to describe the influence of voidage on thermal and electrical conductivity and on shear, bulk and Young's moduli and Poisson's ratio.

CHAPTER 5: CORRELATION METHODOLOGY 70

1. Constitutive Design Equations for Thermal Creep Deformation of HT-9 (UCLA) 71

Design equations are given for HT-9 for rupture time and rupture strain as a function of stress and temperature, and creep strain as a function of time, stress, and temperature.

2. OWR/RTNS-II Low-Exposure Spectral Effects Experiment (HEDL) 76

Irradiation of miniature flat tensile specimens has begun at RTNS-II on Fe, Cu, 316 SS and A302B pressure vessel steel. Comparison irradiations will be performed at OWR at the same temperatures, 90 and 290°C.

3. Image Interaction Between a Prismatic Dislocation Loop and a Bubble (U. of Wisconsin) 80

The elastic interaction between a spherical cavity and a prismatic dislocation loop has been derived. In spite of the complexity of the elasticity solution, the image interaction can be written in a relatively simple form and be evaluated readily.

4. Stability of Helium-Vacancy Clusters During Irradiation (UCLA) 87

The stability of helium-vacancy clusters, determined by a continuum approach, was used to define regimes of temperature and He/dpa for spontaneous and delayed nucleation. Applications are made to HFIR, EBR-II, and ion irradiations.

5. Fundamental Alloy Studies (HEDL) 93

A series of four alloy groups has been produced to investigate the origin of swelling and creep resistance in the Invar regime of the Fe-Ni-Cr austenitic system and to explore the possible existence of high swelling resistance in the corresponding Fe-Cr-Mn austenitic system.

Page

6. Swelling Behavior of Titanium-Modified AISI 316 Alloys (HEDL) 102

It appears that titanium additions to stainless steels covering a wide compositional range around the specifications of AISI 316 result only in an increased delay period before neutron-induced void swelling proceeds. Once swelling is initiated, the post-transient behavior of both annealed and cold-worked steels is quite consistent with that of AISI 316.

CHAPTER 6: FUNDAMENTAL STUDIES OF SPECIAL PURPOSE MATERIALS 109

1. Mechanical Properties and Microstructures of High-Strength Copper Alloys Following Thermal Annealing (U. of Wisconsin) 110

Vickers microhardness measurements on as-received AMZIRC and AMAX-MZC copper alloys as a function of annealing time and temperature indicate that both alloys have an unirradiated recrystallization temperature of about 475°C.

2. Comparison of Thermal and Irradiated Behavior of High-Strength, High-Conductivity Copper Alloys (U. of Wisconsin) 117

Ion irradiation results imply that MZC and AMZIRC copper alloys may undergo a serious degradation in mechanical properties when exposed to irradiation at temperatures around 400°C.

3. Irradiation of Copper Alloys in FFTF (HEDL) 133

Miniature tensile specimens and TEM disks of nine copper-base alloys in thirteen material conditions are being irradiated in FFTF at 450°C.

4. Comparison of Neutron- and Gamma-Irradiation Damage in Organic Insulators (LANL) 135

Flexural mechanical properties were measured at 75 K of one polyimide and two exopy-based materials irradiated at 4 K at IPNS-II. Some differences were found when compared with the effects of gamma irradiation.

CHAPTER 1

IRRADIATION TEST FACILITIES

RTNS-II IRRADIATIONS AND OPERATIONS

C. M. Logan and D. W. Heikkinen (Lawrence Livermore National Laboratory)

1.0 Objective

The objectives of this work are operation of RTNS-II (a 14-MeV neutron source facility), machine development, and support of the experimental program that utilizes this facility. Experimenter services include dosimetry, handling, scheduling, coordination, and reporting. RTNS-II is supported jointly by the U.S. and Japan and is dedicated to materials research for the fusion power program. Its primary use is to aid in the development of models of high-energy neutron effects. Such models are needed in interpreting and projecting to the fusion environment, engineering data obtained in other spectra.

2.0 Summary

Irradiations were performed for 13 different experimenters during this quarter. Two fifty-centimeter targets imploded. Ion source development continues. Haefely's iso-transformer had arcing between output terminals. Target water system malfunctioned due to temperature controller. HEDL furnace shut down due to vacuum leak. The fourth U.S.-Japan Steering Committee meeting was held February 27-28 at RTNS-II.

3.0 Program

Title: RTNS-II Operations (WZJ-16)
Principal Investigator: C. M. Logan
Affiliation: Lawrence Livermore National Laboratory

4.0 Relevant DAFS Program Plan Task/Subtask

TASK II.A.2,3,4.
TASK II.B.3,4
TASK II.C.1,2,6,11,18.

5.0 Irradiation - C. M. Logan, D. W. Heikkinen and M. W. Guinan

During this quarter, irradiations (both dedicated and add-on) were done for the following people.

Experimenter	P or A*	Sample Irradiated
R. Smither (ANL)	A	Al - the $^{27}Al(n,2n)^{26}Al$ cross section near threshold
K. Saneyoshi (TIT)	A	LiF - determine the feasibility of TLD self irradiation as a tritium production monitor
D. Heikkinen (LLNL)	A	Nb - dosimetry calibration
K. Abe (Tohoku) H. Matsui (Tohoku) H. Kayano (Tohoku) M. Kiritani (Hokkaido) H. Takahashi (Hokkaido) K. Shinohara (Kyushu)	P	Metals - mechanical properties room temperature

E. Kuramoto (Kyushu) N. Yoshida (Kyushu) T. Kinoshita (Kyushu) N. Igata (Tokyo) A. Kohyama (Tokyo) K. Mihayara (Tokyo) H. Kawanishi (Tokyo) K. Kamada (Nagoya) M. Iseki (Nagoya) K. Sata (Nagoya)		
Y. Shimomura (Hiroshima) M. Kiritani (Hokkaido) N. Yoshida (Kyushu) M. Doyama (Tokyo) H. Yoshida (Kyoto) S. Ishino (Tokyo) N. Igata (Tokyo) H. Takahashi (Hokkaido) E. Kuramoto (Kyushu)	P	Metals - low temperature experiment - cascade and microstructural damages
H. Heinisch (HEDL) N. Yoshida (Kyushu) M. Kiritani (Hokkaido) H. Takahashi (Hokkaido) S. Ishino (Tokyo) Y. Shimomura (Hiroshima) E. Kuramoto (Kyushu)	P	Metals-displacement damage & mechanical at 90 and 290°C
K. Sumita (Osaka)	A	Insulators - electrical and mechanical properties
Y. Tabata (Tokyo)	A	Polymers - tensile strength
Y. Yamaoka (Kyoto)	A	Polymers - tensile strength
P. Hahn (Vienna)	A	Nb-Ti - measure fluxoid pinning strength
K. Kawamura (TIT)	A	$Pd_{80}Si_{20}$ - Property Change
K. Okamura (Tohoku)	A	Silicon carbide fibers - mechanical
M. Moran (LLNL)	A	Neutron detectors - calibration

*P - primary, A = Add-on

5.1 RTNS-II Status - C. M. Logan and D. W. Heikkinen

The ion source system development continues on the right machine.

Both the left and right machines had a target implode; an investigation is in progress as to the reason why.

The Haefely iso-transformer on the right machine was breaking down between terminals, due to improper grounding. It was repaired and has had no further malfunction.

The target water chiller for the left machine failed due to a temperature controller. A new controller was installed.

The HEDL furnace failed due to a vacuum leak during irradiation on the left machine.

6.0 Future Work

Irradiations will be continued for K. Abe (Tohoku) et al., Y. Shimomura (Hiroshima) et al., K. Sumita (Osaka), K. Saneyoshi (TIT) H. Heinisch (HEDL) et al., D. Heikkinen (LLNL) and R. Smither (ANL). Also during this period, irradiations for J. Fowler (LANL) will be initiated.

CHAPTER 2

DOSIMETRY AND DAMAGE PARAMETERS

HAFNIUM CORE PIECE TEST IN ORR-MFE4

L. R. Greenwood and R. K. Smither (Argonne National Laboratory)

1.0 Objective

To test the neutronics design of a hafnium core piece to be used in the MFE4 spectral-tailoring experiment in ORR.

2.0 Summary

Dosimetry measurements were conducted in the ORR during February 1984 to test the performance of a hafnium core piece for the MFE4 spectral-tailoring experiment. Flux gradients were measured in position C3, both with and without the hafnium liner. The results agree rather well with expectations. The status of all other experiments is summarized in Table I.

TABLE I

STATUS OF DOSIMETRY EXPERIMENTS

	Facility/Experiment	Status/Comments
ORR	- MFE 1	Completed 12/79
	- MFE 2	Completed 06/81
	- MFE 4A1	Completed 12/81
	- MFE 4A2	Completed 11/82
	- MFE 4B	Analysis in Progress
	- MFE 4C	Irradiation in Progress
	- TBC 07	Completed 07/80
	- TRIO-Test	Completed 07/82
	- TRIO-1	Completed 12/83
	- Hf Test	Completed 03/84
HFIR	- CTR 32	Completed 04/82
	- CTR 31, 34, 35	Completed 04/83
	- CTR 30	Irradiation in Progress
	- T2, RB1	Completed 09/83
	- T1, CTR 39	Completed 01/84
	- RB2, RB3, T3	Irradiations in Progress
	- CTR 40-52	Irradiations in Progress
	- JP 1-8	Irradiations in Progress
Omega West	- Spectral Analysis	Completed 10/80
	- HEDL1	Completed 05/81
	- HEDL2	Samples Sent 05/83
EBR II	- X287	Completed 09/81
IPNS	- Spectral Analysis	Completed 01/82
	- LANL1 (Hurley)	Completed 06/82
	- Hurley	Completed 02/83
	- Coltman	Completed 08/83

3.0 Program

Title: Dosimetry and Damage Analysis
Principal Investigator: L. R. Greenwood
Affiliation: Argonne National Laboratory

4.0 Relevant DAFS Program Plan Task/Subtask

Task II.A.1 Fission Reactor Dosimetry

5.0 Accomplishments and Status

Dosimetry measurements have been completed for a test of the hafnium core piece designed for the MFE4 spectral-tailoring experiment in the Oak Ridge Research Reactor (ORR). The purpose of the Hf liner is to reduce the thermal flux, thereby reducing helium production from the two-step thermal capture on ^{58}Ni. A recent description of the experiment has been published by R. A. Lillie (Neutronics Calculations in Support of the ORR-MFE-4A and 4B Spectral-Tailoring Experiments, Alloy Development for Irradiation Performance, Semiannual Progress Report, pp. 38-39, DOE/ER/-0045/11, September 1983). The present tests were conducted in core position C3 of the ORR on February 25-26, 1984, both with and without the Hf liner. Both irradiations lasted four hours at a reduced power level of 330 kW.

Dosimetry tubes were placed at four locations inside the core piece, labelled North, South, East, and West. Each aluminum dosimetry tube measured 18" in length and contained Fe, Ni, Ti, and Co-Al dosimetry wires. Following the irradiations, the tubes were shipped to Argonne for analysis. Each wire was cut into 17 pieces, 16 one-inch pieces, and one 1/2" piece. The wires were then weighed and mounted for Ge(Li) gamma spectroscopy. The Co and Ni wires were completely analyzed on the North side. In all other cases only every third section of each wire was analyzed.

The measured radioactivities are listed in Tables II-VI and plotted in Figures 1-2. The values have an estimated accuracy of ±1.5% in all cases. As can be seen, the bare wires indicate that the flux peak occurs at about 5" below midplane. The uncovered thermal flux also rises at about 4" above midplane corresponding to the top of the inner aluminum core piece which also clearly attenuates the thermal flux by about 40-50%.

TABLE II

$^{59}Co(n,\gamma)^{60}Co$ ACTIVITIES MEASURED IN ORR-Hf TEST
(Average power = 330 kW; core position C3)
Activation Rate, x 10^{-11} atom/atom-s

	Bare				Hf Shield			
Average Height, in.	N	E	S	W	N	E	S	W
-9.84	7.22	6.71	6.71	6.85	4.53	4.55	4.36	4.46
-8.84	7.48				3.91			
-7.84	7.87				3.90			
-6.84	8.23	7.99	7.73	7.69	3.94	3.82	3.67	3.60
-5.84	8.28				3.87			
-4.84	8.33				3.91			
-3.84	8.34	7.95	7.74	7.93	3.83	3.83	3.62	3.60
-2.84	7.90				3.69			
-1.84	7.51				3.50			
-0.84	6.78	6.56	6.66	6.54	3.33	3.28	3.23	3.13
0.16	6.06				3.09			
1.16	5.58				2.99			
2.16	5.26	5.18	5.14	5.07	3.41	3.47	3.65	3.44
3.16	4.84				4.11			
4.16	5.34	5.79	5.81	5.62	5.25	5.13	5.71	5.51
5.16	7.12				6.73			
5.41							6.93	6.83
5.91	7.09	7.31	7.35	6.93	6.87	7.16		

TABLE III

$^{58}Ni(n,p)^{58}Co$ ACTIVITIES MEASURED IN ORR-Hf TEST
Activation Rate, x 10^{-13} atom/atom-s

	Bare				Hf Shield			
Average Height, in.	N	E	S	W	N	E	S	W
-9.84	1.78	1.72	1.64	1.65	1.59	1.55	1.45	1.50
-8.84	1.90				1.71			
-7.84	1.97				1.78			
-6.84	2.04	2.02	1.94	1.99	1.83	1.85	1.70	1.73
-5.84	2.03				1.83			
-4.84	2.01				1.82			
-3.84	1.92	1.98	1.93	1.91	1.80	1.79	1.71	1.72
-2.84	1.81				1.69			
-1.84	1.70				1.65			
-0.84	1.55	1.73	1.68	1.62	1.48	1.53	1.52	1.51
0.16	1.47				1.40			
1.16	1.34				1.28			
2.16	1.25	1.37	1.38	1.31	1.22	1.27	1.25	1.23
3.16	1.17				1.12			
4.16	1.04	1.12	1.17	1.06	1.01	1.10	1.09	1.08
5.16	0.945				0.927			
5.41				0.955			0.777	0.930
5.91	0.883	0.934	0.982		0.871	0.959		

TABLE IV

$^{54}Fe(n,p)^{54}Mn$ ACTIVITIES MEASURED IN ORR-Hf TEST
Activation Rate, x 10^{-13} atom/atom-s

	Bare				Hf Shield			
Average Height, in.	N	E	S	W	N	E	S	W
-9.84	1.23	1.25	1.18	1.22	1.22	1.12	1.05	1.10
-6.84	1.48	1.47	1.41	1.42	1.39	1.30	1.23	1.30
-3.84	1.43	1.45	1.45	1.40	1.33	1.28	1.22	1.25
-0.84	1.18	1.26	1.24	1.20	1.09	1.15	1.08	1.06
2.16	0.936	0.996	0.985	0.954	0.893	0.928	0.909	0.852
4.16	0.809	0.834	0.862	0.813	0.740	0.814	0.816	0.762
5.41			0.759	0.702			0.751	0.709
5.91	0.650	0.680			0.645	0.693		

TABLE V

$^{58}Fe(n,\gamma)^{59}Fe$ ACTIVITIES MEASURED IN ORR-Hf TEST
Activation Rate, x 10^{-12} atom/atom-s

	Bare				Hf Shield			
Average Height, in.	N	E	S	W	N	E	S	W
-9.84	2.20	2.12	2.07	2.06	1.32	1.29	1.27	1.31
-6.84	2.47	2.38	2.31	2.36	1.04	1.01	0.957	0.947
-3.84	2.46	2.45	2.31	2.36	1.03	1.01	0.956	1.00
-0.84	2.02	2.03	1.96	1.95	0.862	0.901	0.842	0.834
2.16	1.49	1.58	1.54	1.50	0.976	1.01	1.05	1.04
4.16	1.73	1.63	2.02	1.74	1.70	1.59	1.85	1.79
5.41			2.42	2.11			2.13	2.21
5.91	2.28	2.39			2.09	2.19		

TABLE VI

$^{46}Ti(n,p)^{46}Sc$ ACTIVITIES MEASURED IN ORR-Hf TEST
Activation Rate, x 10^{-14} atom/atom-s

	Bare				Hf Shield			
Average Height, in.	N	E	S	W	N	E	S	W
-9.84	1.60	1.62	1.62	1.57	1.53	1.50	1.42	1.47
-6.84	1.96	1.92	1.83	1.89	1.75	1.71	1.63	1.64
-3.84	1.87	1.93	1.88	1.82	1.73	1.69	1.64	1.64
-0.84	1.56	1.59	1.63	1.58	1.46	1.50	1.42	1.42
2.16	1.28	1.43	1.34	1.25	1.16	1.23	1.21	1.16
4.16	1.06	1.11	1.15	1.07	1.00	1.14	1.08	1.02
5.41			1.01	0.964			0.969	0.926
5.91	0.920	0.961			0.885	0.956		

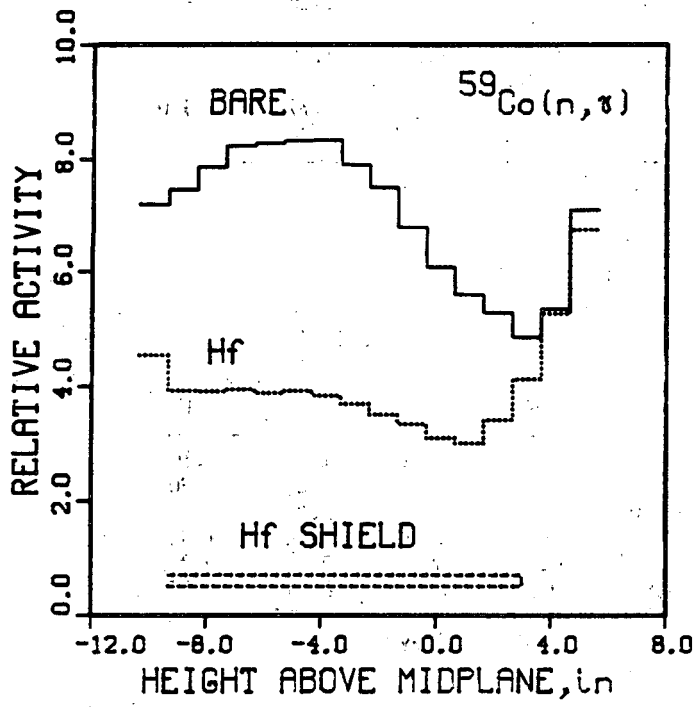

FIGURE 1. Measured $^{59}Co(n,\gamma)^{60}Co$ Activities for the Hf Test in ORR. The position of the Hf shield is indicated.

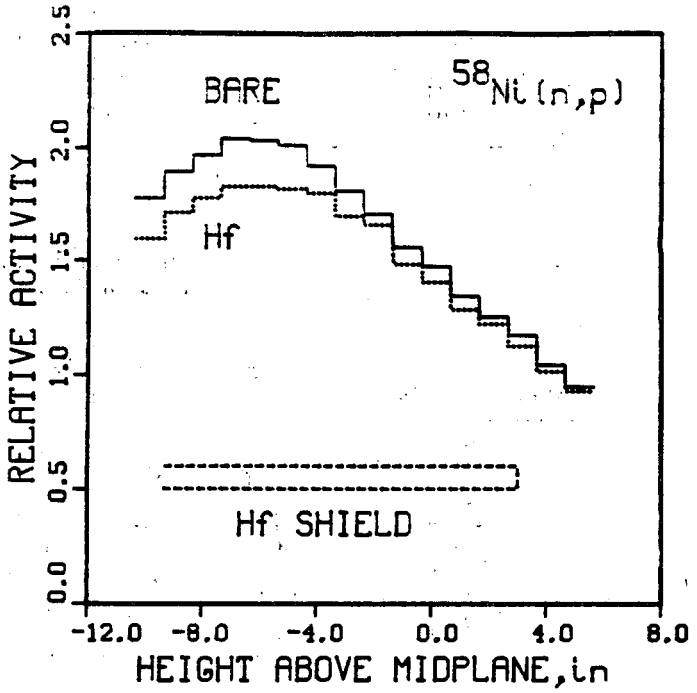

FIGURE 2. Measured $^{58}Ni(n,p)^{58}Co$ Activities for the Hf Test in Orr. The position of the Hf shield is indicated.

The hafnium covered wires clearly show a large reduction in the thermal flux. Near the bottom the flux falls as we go up the core piece, then flattens out, and finally rises near the top. The seemingly strange behavior on the ends is clearly due to "end effects", since our dosimetry wires are longer than the hafnium shield. The Hf piece measured 12-1/4" in length and the position relative to our wires is indicated on Figures 1 and 2.

The radial gradients between the four different tubes at a given height are certainly rather small, <10% in all cases. The North and East positions are typically 5-10% higher than the South and West positions, presumably due to the fact that the center of the ORR core lies Northeast of the C3 position.

The shielding effect of the hafnium liner is about 50% for the ^{58}Fe and $^{59}Co(n,\gamma)$ reactions. The fast reactions also show an effect of about 10%, probably due to the unusually large scattering cross section of Hf of about 7b in the 1-3 MeV energy range.

The maximum bare and shielded activities were used to adjust the neutron flux spectrum used previously in the ORR-MFE4 experiments.[1] Table VII lists our adjusted fluxes for each case. A simple analytical approximation[2] was used to calculate the Hf shielding due to the 40 mil thick liner. This treatment should be a good approximation in the present case due to the small thickness of the liner. However, scattering effects are not treated properly. The shielded spectrum is compared to the bare spectrum in Figure 3. As can be seen, the epithermal shielding is greater than the thermal since the resonance integral is 1900b compared to a thermal cross section of 104b.

TABLE VII

ADJUSTED FLUX VALUES-ORR-Hf TEST
Average Power 330 kW: Core C3

Energy Range	Neutron Flux, x 10^{12} n/cm^2-s		Ratio
	Bare	Hf Shield	Shield/Bare
Total	7.22	4.75	0.66
Thermal*	2.36	1.41	0.60
0.5eV-0.11MeV	2.40	1.05	0.44
>0.11MeV	2.46	2.29	0.93

*Total flux <0.5eV assuming an average temperature of 95°C. The 2200 m/s flux is equal to 0.79 times the above value.

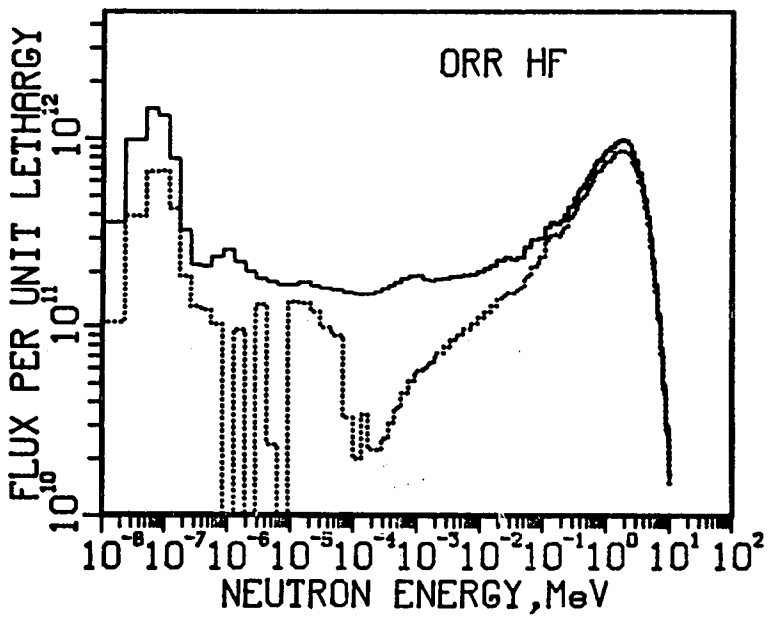

FIGURE 3. Comparison of the unshielded and Hf shielded neutron spectra derived by spectral adjustment with the STAYSL computer code.

The net effect of the Hf liner is to reduce the thermal flux by 40%, the epithermal flux by 56%, and the fast flux by about 7%. These results will be compared to a more exact neutronics calculation by R. A. Lillie (ORNL).

6.0 References

1. L. R. Greenwood, Dosimetry and Damage Analysis for the MFE4A Spectral Tailoring Experiment in ORR, Damage Analysis and Fundamental Studies Quarterly Progress Report, DOE/ER-0046/12, pp. 14-23, 1983.

2. Neutron Fluence Measurements, IAEA Technical Reports Series 107, IAEA, Vienna, 1970.

7.0 Future Work

We will continue to monitor the progress of the MFE4 spectral-tailoring experiment in ORR. Samples are now being analyzed from the MFE4B experiment. Samples were also prepared for further experiments in HFIR.

8.0 Publications

Two papers have been submitted for publication in the Proceedings of the 12th International Symposium on the Effects of Radiation on Materials, Williamsburg, VA, 18-20 June 1984.

1. Measured Radiation Environment at the LAMPF Irradiation Facility, D. R. Davidson, R. C. Reedy, W. F. Sommer, and L. R. Greenwood.

2. The Calculation of Radiation Damage Parameters for the LAMPF Irradiation Facility, D. R. Davidson, W. F. Sommer, M. S. Wechsler, and L. R. Greenwood.

MEASUREMENT OF $^{54}Fe(n,2n)^{53}Fe$ CROSS SECTION NEAR THRESHOLD

R. K. Smither and L. R. Greenwood (Argonne National Laboratory)

1.0 Objective

To develop new cross sections and techniques for dosimetry and damage calculations.

2.0 Summary

A series of experiments were performed at the Princeton Plasma Physics Laboratory to measure the cross section of the $^{54}Fe(n,2n)^{53}Fe$ reaction near threshold. Measurements were made at 6 different neutron energies and cover the 1 MeV energy range from threshold (13.64 MeV) to 14.64 MeV. The $^{54}Fe(n,2n)$ cross section was measured relative to the $^{27}Al(n,p)^{27}Mg$ cross section to an accuracy of a few percent. These accurate cross-section measurements will be useful in calculating damage caused by 14 MeV D-T plasma neutrons in Fe and calculating the production of the long-lived ^{53}Mn nuclei that account for much of the buildup of long-lived radioactivity in steel structures and other ferrous materials used in the construction of fusion reactors. They will also play an important part in a new method for measuring the plasma ion temperature of a D-T plasma.

3.0 Program

Title: Dosimetry and Damage Analysis
Principal Investigator: L. R. Greenwood
Affiliation: Argonne National Laboratory

4.0 Relevant DAFS Program Plan Task/Subtask

Task II.A.5 Technique Development for Dosimetry Applications
Task II.B.1.2 Acquisition of Nuclear Data for the Calculation of Defect Production Cross Sections

5.0 Accomplishments and Status

5.1 Introduction

The threshold for the $^{54}Fe(n,2n)^{53}Fe$ reaction (13.64 MeV, lab) is quite close to the center of the energy distribution of the 14 MeV neutrons generated by a D-T plasma (14.06-14.10 MeV for 1-9 keV ion temperatures). This means that the (n,2n) cross section is varying rapidly in this energy region and is quite sensitive to both the centroid and the width of the neutron energy distribution. It is this sensitivity to the width of the neutron energy distribution that makes the $^{54}Fe(n,2n)^{53}Fe$ very special and allows one to use it to measure the plasma ion temperature in D-T plasmas by comparing the yield of this reaction to the yield of a reaction like $^{27}Al(n,p)^{27}Mg$ that does not vary rapidly with neutron energy.

5.2 Experimental Method

The small D-T neutron generator at the Princeton Plasma Physics Laboratory (PPPL) was used as the neutron source to irradiate samples of iron that were enriched to 97% in the ^{54}Fe isotope. Most of the rest of the iron sample was ^{56}Fe at 2.57% abundance. The neutron generator was operated at 180 keV and accelerated a molecular beam of deuterium with an average beam current of 3 ma. The range of neutron energies seen by

the ^{54}Fe samples was controlled by varying the angular position of the sample relative to the direction of the deuteron beam in the generator. In this manner the mean neutron energy as seen by the sample was varied from 13.95 to 14.64 MeV, corresponding to an angular variation of 100° to 0°, respectively. An important part of the PPPL irradiation facility is their fast rabbit that allows one to measure short lived radioactivity with a Ge gamma detector system. The Fe samples were sandwiched between two disks of pure Al. The actual experiment consisted of irradiating the Fe-Al sandwich with 14 MeV neutrons for 20 minutes, then transporting the sample back to the counting system and counting and comparing the radioactivity from the $^{54}Fe(n,2n)$ reaction (a 378 keV gamma with a half-life of 8.53 min.) with the radioactivity from the $^{27}Al(n,p)$ reaction (a 844 keV gamma with a half-life of 9.54 min.).

5.3 Experimental Results

A plot of the $^{54}Fe(n,2n)^{53}Fe$ cross section data as a function of neutron energy is shown in Fig. 1. The squares are the early data taken in July 1983, while the circles are the more recent and more accurate data taken in February 1984. These cross sections were measured relative to the cross section for the $^{27}Al(n,p)^{27}Mg$ reaction (Ref. 1) and the errors shown correspond to these relative values. Some of the data points show no error bars. The errors in these points are equal to or less than the size of the points. These errors do not include the absolute error in the cross section for the $^{27}Al(n,p)$ reaction. A solid line is fit through the more accurate data of February 1984. The two sets of data agree to within a few

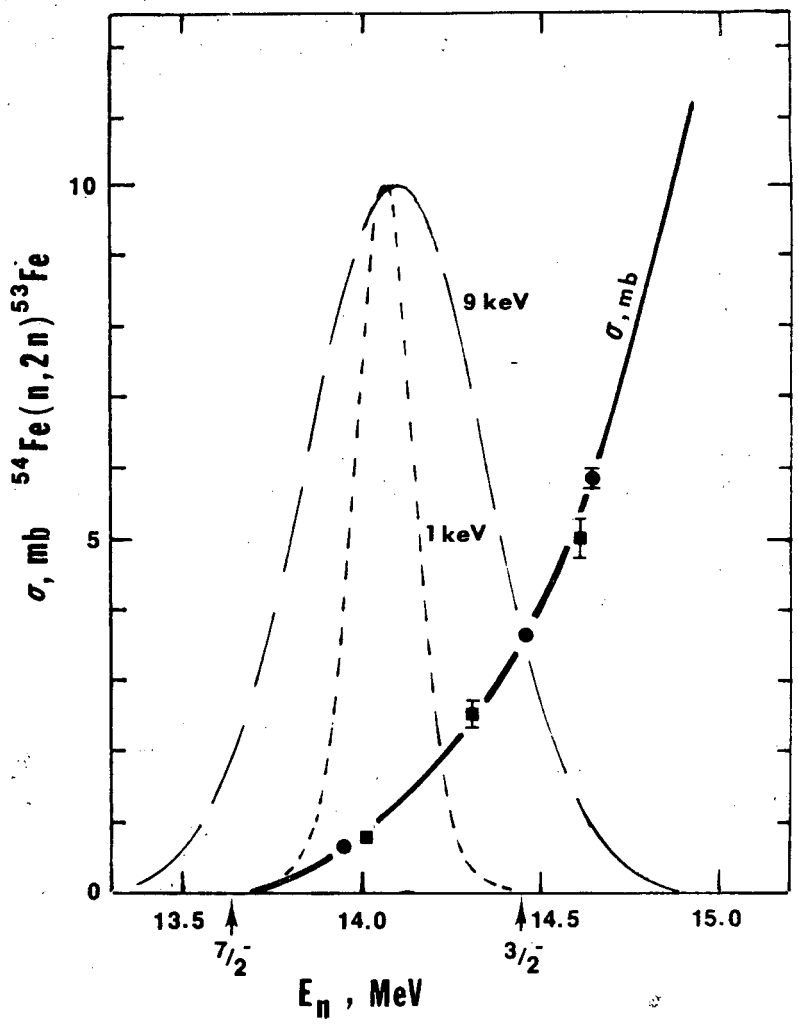

FIGURE 1. A plot of the $^{54}Fe(n,2n)^{53}Fe$ cross section as a function of neutron energy. The squares are the data taken in February 1984. Superimposed on the cross section data are two neutron energy distributions for D-T plasmas with ion temperatures of 1 keV (short dashed line) and 9 keV (long dashed line) in arbitrary units of neutron flux versus neutron energy.

percent. The upper part of the curve is fit through previously published data (Ref. 2) for neutron energies in the 16.5 to 18.0 MeV range. The previously published data on the $^{54}Fe(n,2n)$ reaction for neutron energies in the 14.0 to 14.6 MeV range[3] is not shown because their uncertainties are quite large, 50% to 100%, and in most cases they are 3 to 10 times higher which puts them off scale. The arrow on the horizontal axis labeled "7/2-", indicates the threshold for the $^{54}Fe(n,2n)$ reaction. The arrow labeled "3/2-" indicates the threshold for the production of the 3/2- first excited state in ^{53}Fe. This second threshold is high enough in neutron energy so that one can safely assume that most of the observed cross section observed in these experiments is associated with the direct production of the 7/2- ground state in ^{53}Fe.

5.4 Ion Temperature

Superimposed on the cross section data in Fig. 1 are plots of the distribution of neutron energies produced by a D-T plasma with a 1 keV ion temperature (short dashed line) and with a 9 keV ion temperature (long dashed line). These two distributions cover the expected operating range of the new fusion reactor TFTR when it operates with a D-T plasma. The relative yield of the $^{54}Fe(n,2n)$ reaction to the $^{27}Al(n,p)$ reaction increases by 34% as the ion temperature increases from 1 keV to 9 keV (assuming a thermal equilibrium distribution of velocities) and should be quite easy to monitor with these two reactions.[1] The accuracy of this method of measuring ion temperatures depends only on the errors related to the values of the relative cross sections so it is not necessary to know the value of the absolute cross sections with any precision to use this approach.

5.5 Production of ^{53}Mn

^{53}Fe decays to the long-lived nucleus ^{53}Mn which has a 3.8×10^6 yr half-life. This production of ^{53}Mn will be one of the major sources of long lived radioactivity in steel and other ferrous materials used in the construction of fusion reactors. The accurate cross sections measured in this experiment allow one to make accurate calculations of this long-lived activity from ^{53}Mn that will be present in fusion reactor structures. As can be seen in Fig. 1 the production of ^{53}Fe and thus ^{53}Mn is a sensitive function of the ion temperature of the plasma. The new cross-section values are appreciably lower than most of the previously published values (2 to 10 times lower depending on which old results are used) so the calculated amount of long-lived ^{53}Mn activity will be appreciably lower as well.

5.6 Acknowledgments

The authors wish to thank Hans Hendel and Keith Chase for their assistance in performing these measurements and the Princeton Plasma Physics Laboratory for allowing us to use their neutron generator.

6.0 References

1. "Measurement of the $^{27}Al(n,2n)^{26}Al$ Reaction Cross Section for Fusion Reactor Applications," R. K. Smither and L. R. Greenwood, to be published in the Journal of Nuclear Materials.

2. ENDF/B-V, Dosimetry File, National Neutron Cross Section Center, Brookhaven National Laboratory, 1979.

3. Neutron Cross Sections, BNL-325, Third Edition, Volume II, D. I. Garber and R. R. Kinsey, National Neutron Cross Section Center, Brookhaven National Laboratory, 1976.

7.0 Publications

A paper is being prepared describing these experiments for publication in The Physical Review.

8.0 Future Plans

These highly accurate relative cross sections for the $^{54}Mn(n,2n)^{53}Fe$ reaction will be combined with similar measurements made on the $^{27}Al(n,2n)^{26}Al$ reaction to develop a new method to measure D-T plasma ion temperatures with dosimetry foils.

HELIUM GENERATION MEASUREMENTS FOR EBR-II AND ORR

B. M. Oliver, D. W. Kneff, and R. P. Skowronski (Rockwell International, Energy Systems Group)

1.0 Objective

The objectives of this work are to apply helium accumulation neutron dosimetry to the measurement of neutron fluences and energy spectra in mixed-spectrum fission reactors utilized for fusion materials testing, and to measure helium generation rates of materials in these irradiation environments.

2.0 Summary

Helium generation measurements have been performed for Fe, Cu, and Ti samples irradiated in the Experimental Breeder Reactor-II (EBR-II) experiment X287 and for iron samples irradiated in the Oak Ridge Research Reactor (ORR) experiment MFE4A2. These measurements are part of a program to measure total helium production rates over the range of fission reactor spectra and fluences used for fusion materials testing, and to use the results for integral cross section testing. The present results are significantly different from the ENDF/B-V cross section evaluations for all three materials, with the largest difference being for titanium (~270%). The Ti and Cu samples from EBR-II also contained significant quantities of ^{3}He, presumably accumulated by the absorption and subsequent decay of tritium from the reactor environment.

3.0 Program

Title: Helium Generation in Fusion Reactor Materials
Principal Investigators: D. W. Kneff and H. Farrar IV
Affiliation: Rockwell International, Energy Systems Group

4.0 Relevant DAFS Program Plan Task/Subtask

Task II.A.1	Fission Reactor Dosimetry
Task II.A.4	Gas Generation Rates
Subtask II.A.5.1	Helium Accumulation Monitor Development

5.0 Accomplishments and Status

Helium generation measurements have been performed for Fe, Cu, and Ti samples irradiated in EBR-II and for iron samples irradiated in ORR. These measurements are part of a joint Rockwell-Argonne National Laboratory (ANL) program to measure total helium production rates over the range of fission reactor spectra and fluences used for fusion materials testing, and to use the results to integrally test helium production cross section evaluations used in damage calculations. Measurements and integral testing have been performed previously for nickel samples irradiated in nine different materials irradiations in three fission reactors.[1] The present results are part of a series of analyses to extend this work to several additional materials.

The Fe, Cu, and Ti samples from EBR-II were radiometric dosimetry wires from experiment X287 that were recently supplied by ANL.[2] These samples were etched, to remove all possible surface effects of helium recoil, and then segmented and analyzed by high-sensitivity gas mass spectrometry[3] for their irradiation-generated helium concentrations. Multiple specimens were analyzed for each sample location, with good reproducibility. The absolute uncertainty in each analysis was ±1-2%. The averaged ^{4}He

measurement results are presented in Column 4 of Table 1. The complete retention of generated helium in these materials at the elevated irradiation temperatures has been verified for Fe and Cu from a separate EBR-II experiment, but has not yet been done for titanium. Further verification tests will be performed for Ti, Fe, and Cu using encapsulated samples that have been irradiated in EBR-II and ORR.

TABLE 1

HELIUM PRODUCTION MEASUREMENTS FOR EBR-II EXPERIMENT X287

Material	Irradiation Location		^{4}He Concentration		
	z[a] (cm)	Radius (cm)	Measured (appm)[b]	Calculated[c] (appm)[b]	Calculated[c] / Measured
Fe	-0.4	30.0	4.37	3.03	0.69
	-11.4	34.0	2.14	1.54	0.72
	-17.1	33.6	1.52	1.10	0.72
Cu	+16.2	33.6	2.03	1.22	0.60
	-0.4	30.0	4.37	2.49	0.57
	-11.4	34.0	2.09	1.26	0.60
	-17.1	33.6	1.45	0.90	0.62
Ti	+16.2	33.6	1.86	4.80	2.58
	-0.4	30.0	3.56	9.02	2.53
	-11.4	34.0	1.93	5.55	2.88
	-17.1	33.6	1.41	3.95	2.79

(a) Distance above core midplane
(b) Atomic parts per million (10^{-6} atom fraction)
(c) Calculated by L. R. Greenwood using ENDF/B-V (Ref. 2)

Table 1 also includes the helium concentrations predicted in these materials by L. R. Greenwood of ANL.[2] These predictions are based on radiometric dosimetry analyses plus helium production cross sections from the ENDF/B-V General Purpose File. Comparisons between the measured and calculated helium concentrations (Table 1, Column 6) show significant differences. The predicted Fe and Cu helium concentrations are about 30% and 40% low, respectively, while the helium predictions for titanium are about 270% high. These differences suggest a need for adjustments in the ENDF/B-V files. Further comparisons will be made when the helium predictions are recalculated using the ENDF/B-V Gas Production File. This may raise the predictions slightly by including some previously omitted helium-producing reaction channels.

Selected samples from the EBR-II experiment were also analyzed for their ^{3}He content. The ^{3}He concentrations were presumably produced by the accumulation of reactor tritium in the samples, and its subsequent decay to ^{3}He. Much of the ^{3}He appears to have been produced subsequent to the 1977-78 irradiation, based on the relatively long tritium half-life (12.33 years). The titanium samples contained the greatest concentrations of ^{3}He, which would be expected because titanium is a good hydrogen getter. The measured ^{3}He concentrations in titanium ranged from 0.04 appm (4×10^{-8} atom fraction) at the irradiation location 16.2 cm above core midplane, to 8 appm at the irradiation location closest to core midplane (-0.4 cm). These measurements demonstrate the presence of relatively large quantities of ^{3}H in the samples during irradiation.

The analyzed iron samples from ORR experiment MFE4A2 (MFE4A, over the irradiation period June 12, 1980-April 26, 1982) were incorporated in that experiment for both helium accumulation and radiometric dosimetry measurements. After radiometric counting at ANL, they were etched and segmented at Rockwell for helium analysis. Helium measurements were then made for multiple segments from each irradiation location. The analysis results are summarized in Table 2, Column 4.

Predicted helium concentrations in the MFE4A2 samples are given in Column 5 of Table 2. These predictions are also based on the ENDF/B-V General Purpose File. They use Greenwood's calculations for the maximum-exposure core-height location (-5.84 cm) for MFE4A2[4] as an estimate for the -6.27-cm irradiation position. Predictions for the other two locations were calculated from these maximum-exposure values using the ratios of the measured ^{54}Fe(n,p) reaction rates in the four samples.[4] The predictions are about 10% below the present helium measurements, as seen in Column 6 of Table 2.

TABLE 2

HELIUM PRODUCTION MEASUREMENTS FOR ORR-MFE4A2 IRON

Sample	Irradiation Location		^{4}He Concentration		Calculated[c] / Measured
	z[a] (cm)	Radius	Measured (appm)[b]	Calculated[c] (appm)[b]	
Fe-5B	-6.27	inner	1.62	1.50	0.93
Fe-8B	-6.27	outer	1.80	1.57	0.87
Fe-4B	-14.69	outer	1.58	1.47	0.93
Fe-1B	-14.84	inner	1.54	1.40	0.91

[a] Distance above core midplane
[b] Atomic parts per million (10^{-6} atom fraction)
[c] Based on calculations by L. R. Greenwood (Ref. 4; see text) using ENDF/B-V

Sample preparation and helium analysis work are continuing for several additional samples of Fe, Cu, and Ti incorporated in a number of different experiments in ORR and HFIR (High Flux Isotopes Reactor). More detailed integral testing of the ENDF/B-V Gas Production Files will follow, in a joint effort with ANL.

6.0 References

1. D. W. Kneff, R. P. Skowronski, B. M. Oliver, and L. R. Greenwood, "A Comparison of Measured and Calculated Helium Production in Nickel for Fission Reactor Irradiations," in Damage Analysis and Fundamental Studies, Quarterly Progress Report July-September 1983, DOE/ER/0046/15, U.S. Department of Energy, 12 (1983).

2. L. R. Greenwood, "Fission Reactor Dosimetry," in Damage Analysis and Fundamental Studies, Quarterly Progress Report July-September 1981, DOE/ER-0046/7, U.S. Department of Energy, 8 (1981).

3. H. Farrar IV, W. N. McElroy, and E. P. Lippincott, "Helium Production Cross Section of Boron for Fast-Reactor Neutron Spectra," Nucl. Technol., 25, 305 (1975).

4. L. R. Greenwood, "Dosimetry and Damage Analysis for the MFE4A Spectral Tailoring Experiment in ORR," in Damage Analysis and Fundamental Studies, Quarterly Progress Report October-December 1982, DOE/ER-0046/12, U.S. Department of Energy, 14 (1983).

7.0 Future Work

Helium measurements and integral cross section testing are in progress for Cu, Fe, and Ti, irradiated in several mixed-spectrum fission reactor environments. Other materials will follow, including the irradiation of new materials, such as Cr and Mo. The goals of this work are the accurate prediction of helium generation in materials irradiation experiments and the further development of helium accumulation fluence monitors for stable-product neutron dosimetry.

8.0 Publications

None.

CHAPTER 3

REDUCED ACTIVATION MATERIALS

SWELLING BEHAVIOR OF MANGANESE - BEARING STEEL AISI 216

D. S. Gelles and F. A. Garner (Hanford Engineering Development Laboratory)

1.0 Objective

The object of this effort is to provide an early indication of the radiation response of low activation austenitic alloys based on manganese substitution for nickel.

2.0 Summary

The inclusion of 8.5 wt% manganese in AISI 216 (Fe-6.7Ni-8.5Mn-20Cr-2.7Mo-0.32Si) does not appear to alter the swelling behavior from that found to be typical of austenitic alloys with comparable levels of austenite-stabilizing elements. The swelling in AISI 216 in EBR-II is quite insensitive to irradiation temperature in the range 400 - 650°C. Microscopy reveals that this may arise from the low level of precipitation that occurs in the alloy.

3.0 Program

Title: Irradiation Effects Analysis (AKJ)
Principal Investigator: D. G. Doran
Affiliation: Hanford Engineering Development Laboratory

4.0 Relevant DAFS Program Plan Task/Subtask

Subtask II.C.1 Effects of Material Parameters on Microstructure

5.0 Accomplishments and Status

5.1 Introduction

The development of low activation alloys has been accepted as one of the goals of the materials program of the U.S. Magnetic Fusion Energy Program. Toward this objective, irradiation of a series of such alloys has already commenced in FFTF, utilizing the MOTA-1B experiment.[1,2] One group of these alloys is based on the substitution of manganese for nickel as an alternate Path A development approach.

In order to provide an early forecast of the behavior of such alloys in a radiation environment, three steps have been taken. One involves the use of a diffusivity-based swelling model to predict the compositional dependence of swelling. The second involves the use of ion bombardment to provide a survey of the compositional dependence of swelling in the Fe-Cr-Mn system. The third effort centers on the examination of manganese-stabilized alloys that have already been subjected to irradiation.

Several charged particle irradiations of manganese-stabilized austenitics have been reported in the scientific literature and show that manganese substitution does not in general confer immunity from either swelling or phase instabilities.[3-5] Only one set of neutron-induced swelling data on a manganese-bearing alloy has been published, however.

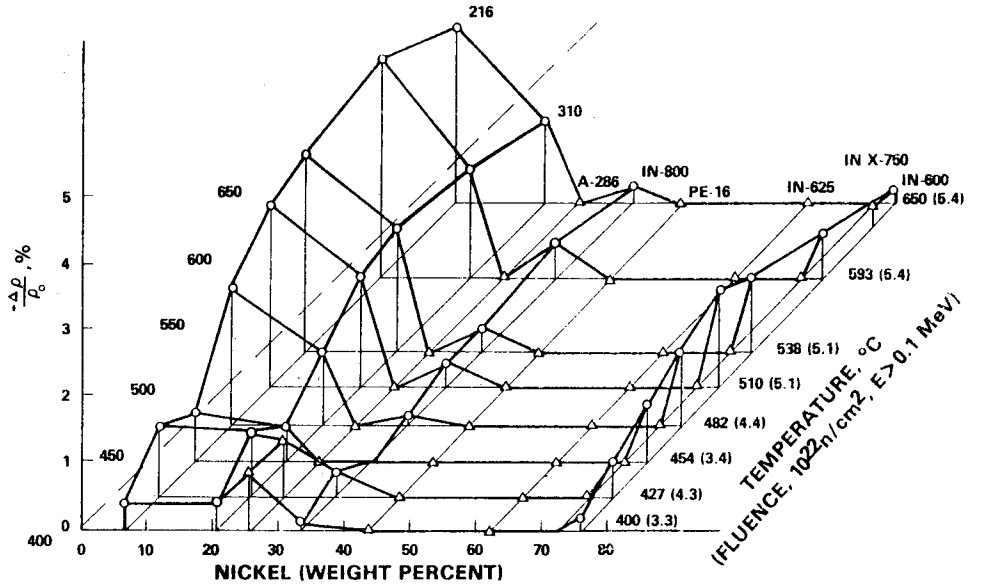

FIGURE 1. Swelling vs Nickel Content and Temperature for the Solution-Treated B109 Alloys.[6]

TABLE 1

DENSITY MEASUREMENT RESULTS FOR AISI 216
SPECIMENS CONTAINED IN THE B-109 EXPERIMENT.

Specimen Identification	Irradiation Temperature (°C)	Fluence 10^{22}n/cm^2 (E > 0.1 MeV)	(dpa)	Swelling (%)
NM	400	3.3	16.5	0.39
NL	427	4.3	21.5	1.04
NE	454	3.4	17	0.70
NF	482	4.4	22	2.08
NK	510	5.1	25.5	2.77
NG	538	5.1	25.5	3.01
NJ	593	5.4	27	3.35
NH	650	5.4	27	2.68

Bates and Powell reported swelling data for a large range of commercial alloys irradiated in the B109 and AA-I experiments conducted in EBR-II.[6] One of the commercial alloys was annealed AISI 216 which has a composition (wt%) of Fe-6.7Ni-8.5Mn-20Cr-2.7Mo-0.32Si-0.07C-0.16N. As shown in Figure 1 and Table 1, this alloy swelled more than the other alloys in the B109 experiment. Bates and Powell attributed this higher swelling primarily to the lower nickel content of the alloy.

The present report considers the response of AISI 216 from the B109 experiment in greater detail. Specimens irradiated at 427°C and at 593°C have been examined by transmission electron microscopy to assess the consequences on void swelling and microstructural evolution of manganese substitution for nickel.

5.2 Experimental Procedure

Specimens of AISI 216 irradiated in the B109 Test at 427°C to 4.3 x 10^{22} n/cm^2 (E > 0.1 MeV) and at 593°C to 5.4 x 10^{22} n/cm^2 (E > 0.1 MeV) were obtained from storage. The heat treatment given prior to irradiation was 1066°C for 1 hour, followed by a water quench. The specimens were in the form of 3.0 mm diameter x 0.3 mm thick disks which had been sliced from the irradiated 1.3 cm long rods. Specimen preparation for transmission electron microscopy and examination followed routine procedures.

5.3 Results

AISI 216 was found to have developed microstructures during irradiation similar to those of other austenitic stainless steels. Voids were found in both specimens examined; the 593°C condition contained higher void swelling as anticipated from the density measurements. Both Frank loops and perfect dislocation networks were found in the 427°C specimen but only perfect dislocation networks were observed at 593°C. Only a few precipitates were found in either of the specimens. In general, these few precipitates were associated with cavities.

Examples of these microstructures are provided in Figure 2. Figures 2a and 2b compare void structures in the vicinity of grain boundaries for specimens irradiated at 427 and 593°C. The grain boundaries tend to be denuded of voids and contain $M_{23}C_6$ particles. Away from the boundaries, the voids are uniformly distributed. The void structures are shown at higher magnification in Figure 2c and 2d. The voids are facetted and are in the shape of truncated octahedra, typical of austenitic steels. Several examples can be identified where precipitates are attached to voids. The dislocation structures are shown under dark field imaging conditions in Figures 2e and 2f. Two of the four sets of Frank loops are visible as fringed features in Figure 2e. In order to emphasize the reduced precipitation in this alloy, micrographs of AISI 316 (20% CW) which was irradiated under identical conditions are shown in Figures 2g and 2h. It is apparent that the swelling is not only lower in AISI 316 but that gamma prime (Ni_3Si) and G-phase precipitates are present at higher number densities.

5.4 Discussion

If the results of density measurements for AISI 216 specimens, as given in Table 1, are plotted as a function of neutron fluence, a new insight emerges. The swelling of annealed AISI 216 appears to exhibit essentially no dependence on irradiation temperature between 400 and 650°C. This is consistent with the temperature-independence of swelling often observed in austenitic alloys,[7] although it is surprising that the transient regime is insensitive over such a large regime of temperature. This insensitivity is likely due to the lack of precipitation in the alloy. The swelling curve for AISI 216 lies in the range between that usually inhabited by annealed AISI 304 and AISI 316 as might be expected from the total Ni + Mn level of the three steels. This is only a qualitative comparison since the transient duration is affected not only by the nickel and manganese content but also by other factors such as the annealing temperature and the silicon and carbon content.

It is encouraging, however, to note in a steel in which a substantial portion of the nickel has been replaced by manganese that the swelling behavior is quite typical of the class of austenitic stainless steels as we currently understand them.[7] The major questions remaining to be explored, therefore, involve the radiation-induced segregation and phase evolution as well as the effect of manganese content on swelling inhibition. If, however, the manganese and nickel are eventually removed from solution by precipitation in the same manner as is nickel in 300 series alloys, manganese-stabilized alloys may exhibit a loss of austenitic stability. It is hoped that much higher levels of manganese may provide swelling suppression similar to that observed in Fe-Cr-Ni ternary alloys with high nickel levels.

5.6 Conclusions

Microstructural examinations of AISI 216 specimens which had been neutron irradiated at 427 and 593°C show that manganese levels of 8.5% do not alter the swelling response of the alloy compared to the behavior of other austenitic stainless steels. Post-irradiation density measurements demonstrate that swelling of this alloy is independent of temperature, in good agreement with the observed behavior of other austenitic steels. Although a substantial fraction of the nickel content has been replaced by manganese, the swelling reponse remains typical of austenitic stainless steels.

6.0 References

1. F. A. Garner, H. R. Brager and D. S. Gelles, "Reduced Activation Activities," Damage Analysis and Fundamental Study Progress Report, DOE/ER-0046/16, p. 17, March 1984.

2. H. R. Brager and F. A. Garner, "Fundamental Alloy Studies," Damage Analysis and Fundamental Studies, Quarterly Progress Report DOE/ER-0046/17, p. 92, June 1984.

3. M. Snykers and E. Ruedl, J. Nucl. Mater. 103 & 104, p. 1075, 1981.

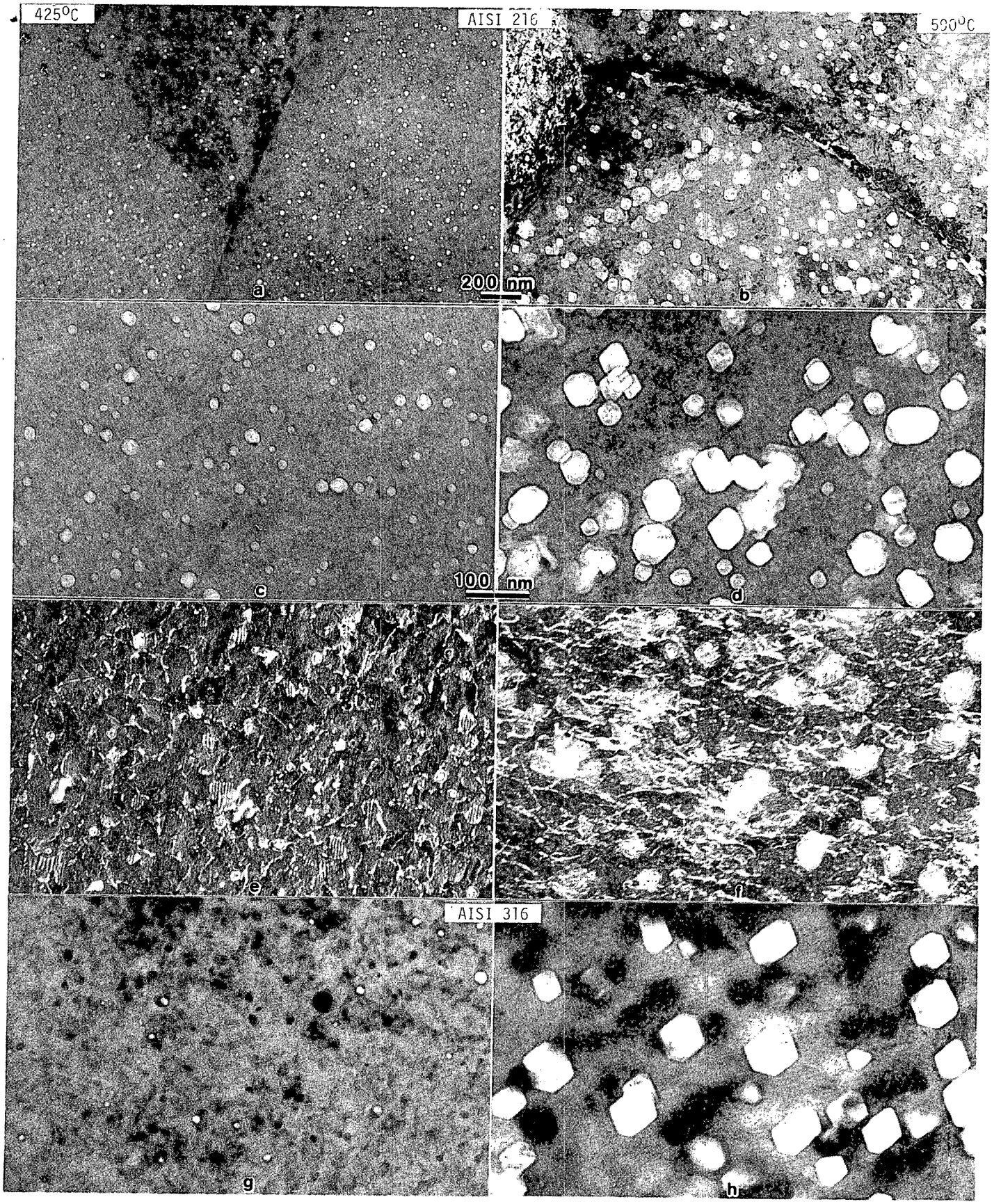

FIGURE 2. Examples of Microstructures Observed in AISI 216 Irradiated at 427 and 593°C. Figures 2g and 2h provide a comparison with 20% cold-worked AISI 316 specimens irradiated under identical conditions. The density changes of the AISI 316 specimens were -0.13% at 427°C and 1.34% at 593°C.

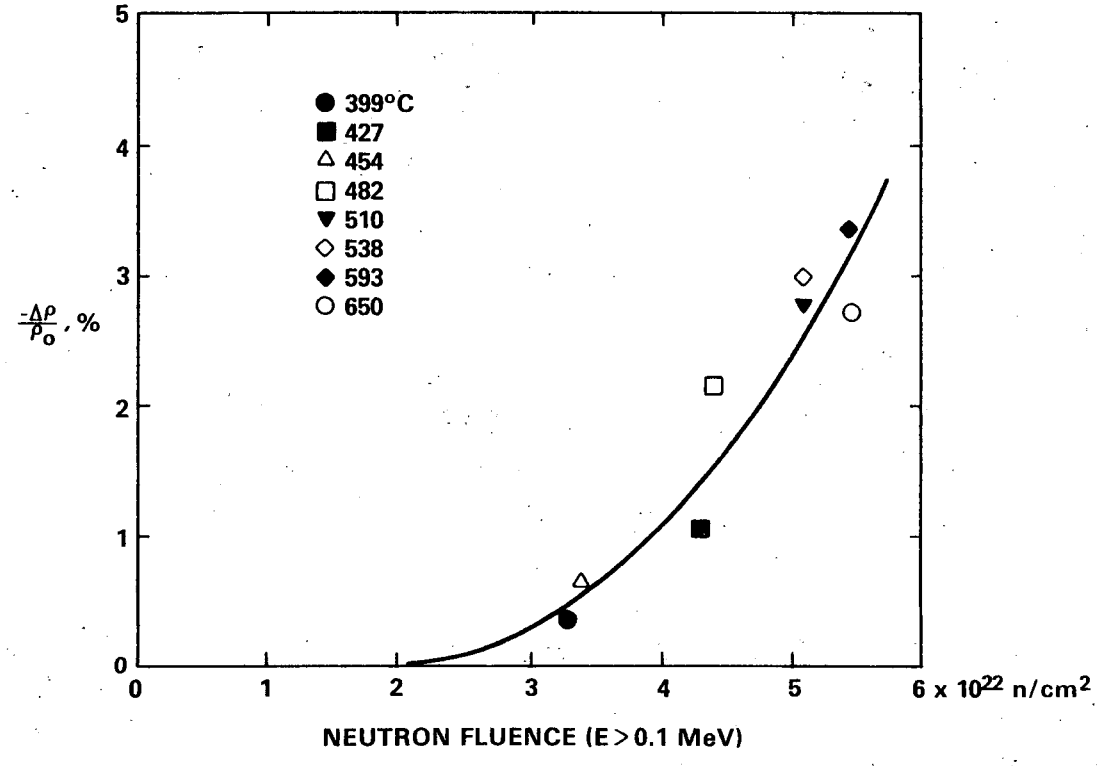

FIGURE 3. Swelling in AISI 216 Irradiated with the B109 Test Plotted as a Function of Fluence. No strong dependence on irradiation temperature is observed.

4. D. J. Mazey, J. A. Hudson and J. M. Titchmarsh, J. Nucl. Mater. 107, p. 2, 1982 .

5. R. M. Boothby, D. R. Harries and T. M. Williams, J. Nucl. Mater. 115, p. 16, 1983.

6. J. F. Bates and R. W. Powell, J. Nucl. Mater. 102, p. 200, 1981.

7. F. A. Garner, "Recent Insights on the Swelling and Creep of Irradiated Austenitic Alloys," in Ref. 1, p. 17, (to be published in J. Nucl. Mater.).

7.0 Future Work

This work is complete.

8.0 Publications

None.

CHAPTER 4

FUNDAMENTAL MECHANICAL BEHAVIOR

CORRELATION OF AISI 316 STAINLESS STEEL YIELD STRENGTH WITH IRRADIATION-INDUCED MICROSTRUCTURE

R. L. Simons (Hanford Engineering Development Laboratory) and L. A. Hulbert (Cornell University)

1.0 Objective

The objective of this effort is to model the change in yield strength due the various irradiation-induced microstructural components.

2.0 Summary

Improvements in the correlation of change in yield strength in AISI 316 stainless steel with microstructure were effected by re-examining the role of short-range obstacles. Effects due to the size of the obstacles relative to their spacing, shape of the obstacles, and the dislocation core radius were applied. In addition, the concept of shearing the precipitates instead of bowing around them was used to explain the effects of precipitate hardening. In this analysis it is concluded that large changes in yield strength may be produced in high swelling materials.

3.0 Program

Title: Irradiation Effects Analysis (AKJ)
Principle Investigator: D. G. Doran
Affiliation: Hanford Engineering Development Laboratory

4.0 Relevant DAFS Plan Task/Subtask

Subtask II.C.2 Effects of He on Microstructure
Subtask II.C.4 Effects of Solid Transmutants on Microstructure
Subtask II.C.14 Models of Flow and Fracture Under Irradiation

5.0 Accomplishments and Status

5.1 Introduction

The neutron service environment of a fusion device is more severe than is found in a fission reactor. The fusion environment can have higher dpa rate, total damage exposure, and differences in cascade morphology than found in fission reactors. The transmutation rate will be higher and will follow different paths, and subsequently, different end products will be formed. Transmutation products ultimately can affect the dimensional stability (void/bubbles) and mechanical integrity (voids/bubbles/ precipitates) of the material.

The strength of the metal is sensitive to the irradiation induced microstructure. The effect of differences in the irradiation induced microstructures caused by fission versus that caused by fusion neutrons are not easily studied. However there have been several attempts to partially simulate the effects expected in the fusion environment. Irradiation in the High Flux Isotope Reactor (HFIR) produces large concentrations of helium but the helium production rate is not linear in time and the major portion of the helium is produced in a damage exposure regime after nucleation has slowed.

Johnson et al.,[1] predicted the yield strength change from the microstructure of 316 SS. The general behavior of both solution annealed and 20% CW 316 stainless steel were successfully predicted. In their analysis they assumed Orowan forces impeded the motion of a dislocation. The dislocation obstacles were assumed to be small compared to their separation in the slip plane.

Garner et al.,[2] refined Johnson's analysis by treating faulted loops as another source of dislocation line length. They also determined that the increments of yield strength from short and long range forces were additive and the components of short range force were added in quadrature as were the components of long range forces.

Brager et al.,[3] compared measured yield strengths with predictions from the microstructures observed in the broken tensile grips of solution annealed 316 and 304 stainless steel specimens. He found fairly good agreement provided that the precipitate contribution to the yield strength used by Garner[1] was reduced by a factor of three. It is noted that Garners et al's precipitate contribution was based on the gamma prime (γ') precipitate only. Brager et al., observed both γ' (Ni_3Si) and a phosphorous rich rod precipitate (Fe_2 The rod precipitate decreased the mean distance between obstacles by a factor of three. This accounts for the success of the new β (1/3) factor used by Brager et al. This result illustrates a general problem that data on size and density of precipitate are frequently not quantitatively reported because of high variability within the material and at times within a grain.[4]

An Orowan obstacle impedes the movement of a dislocation by requiring it to bow around the obstacles. A loop should be left around the impeding obstacle. However, this is not generally observed. An alternate approach is to assume the obstacle is sheared by the dislocation. The force necessary to pass the dislocation by the obstacle is inversely proportional to the distance between the obstacles. In past analyses it was assumed that the diameter of the obstacle was much smaller than the distance between obstacles in the slip plane. For large obstacles their size can decrease the effective distance between them. These and other effects are addressed in this paper.

5.2 Analysis

Three microstructural components are considered in this analysis: 1) precipitates of various sizes and shapes, 2) voids or bubbles, and 3) dislocations, either as faulted loops or dislocation lines. The addition of stresses from the various obstacles is done in the same manner as Garner et al[2]. The dislocation barriers are classified as either long range (LR) or short range (SR). The long range interaction occurs due to the stress field around the obstacle and can affect the motion of the moving dislocation even if the obstacle and moving dislocation are not on the same slip plane. Short range interactions require contact between the dislocation and the obstacle on the same slip plane. In this analysis the conversion from shear stress to uniaxial tension stress is by the Von Mises factor ($\sqrt{3}$) which is incorporated in the calibration constants for each component of the barrier stresses.

The change in yield strength ($\Delta\sigma_{YS}$) is given by

$$\Delta\sigma_{YS} = \Delta\sigma_{LR} + \Delta\sigma_{SR} \tag{1}$$

The components of the LR and SR stresses are added in quadrature. That is

$$\Delta\sigma_{LR}^2 = \Delta\sigma_N^2 + \sum_i \Delta\sigma_{L_i}^2 \tag{2}$$

where $\Delta\sigma_{L_i}$ is the stress required to pass a stationary loop such as a Frank Loop. The stress $\Delta\sigma_N$ is due to the network dislocations. Differences between screw and edge dislocations are not considered in this analysis.

The components of the SR stresses are

$$\Delta\sigma_{SR}^2 = \Delta\sigma_V^2 + \sum_i \Delta\sigma_{P_i}^2 \tag{3}$$

where $\Delta\sigma_V$ is the contribution due to voids or bubbles and $\Delta\sigma_p$ is the contribution due to various precipitates.

5.3 Precipitates

There are two mechanisms by which a precipitate may harden a material[5,6]: 1) Orowan bowing around the precipitate, and 2) shearing of the precipitate. The shearing mechanism is expected in small coherent precipitates while the bowing mechanism is expected in large coherent or in incoherent precipitates. The applied stress necessary to force a dislocation through a coherent precipitate has four components: 1) the work to disorder the precipitate, 2) the work to create a jog in the dislocation when the slip planes do not match, 3) the work to create additional area within the precipitate during shearing, and 4) the work to overcome the misfit stress field around the precipitate. The first contribution is by far the dominant term. The applied tensile stress required to shear the coherent precipitate is given by

$$\Delta\sigma = \sqrt{3}\ \gamma_p\ \bar{d}\ /(b\ L) \tag{4}$$

where γ_p is the surface energy due to disordering the coherent precipitate, d is the geometry corrected average precipitate diameter (following Kelly[7] $d_S = \sqrt{2/3}d$ for spheres and $d_R = \sqrt{2}d$ for rods), b is the burgers vector, and L is the slip plane distance between precipitates. The value of L depends on the diameter as well as the density of the precipitates ($L = \sqrt{f/A} - d$), $\sqrt{f/A}$ is the center to center distance between precipitates, f is the fractional volume, and A is the projected area on the slip plane.

The only unknown is the surface energy γ_p. This was estimated by the method of Williams.[8] He assumed a critical ordering temperature (T_c) for dissolution of a precipitate. The critical temperature used in this analysis was 1035°C for $Ni_3Si(\gamma')$ and 1365°C for Fe_2P which are the dissolution temperatures in the binary system. The values of γ_p determined for Ni_3Si and Fe_2P were 102 and 44 ergs/cm^2, respectively. In both cases a long range ordering parameter of 1.0 was used. A shift in the critical temperature of ±100°C shifts γ_p by 10%. Since many of the precipitate contain silicon, the distribution of γ' is considered to be representative of precipitate behavior as a function of temperature. The γ' is not observed above ~550°C but is replaced by other precipitates. Each type of coherent precipitate should have a unique γ_p.

The resulting equation describing applied stress (MPa) to shear a spherical coherent γ' precipitate is

$$\Delta\sigma_{CS} = \frac{519\ d\ \sqrt{Nd}}{1 - 0.81\ d\ \sqrt{Nd}} \tag{5}$$

and for rod shaped Fe_2P precipitates is

$$\Delta\sigma_{CR} = \frac{304\ d\ \sqrt{N\ell}}{1 - d\ \sqrt{N\ell}} \tag{6}$$

where d is the diameter of the rod or sphere, ℓ is the length of the rod, and N is the precipitate density. These expressions account for effective diameters given by Kelly.[7] Rod shaped precipitates are more effective obstacles than spherical obstacles for the same volume fractions and surface energy.[7]

The dislocation bows around the precipitate when the precipitate becomes very large or is incoherent. In this case the form of the Orowan equation[7] relating spherical microstructural obstacles to change in yield strength is

$$\Delta\sigma_{IS} = \frac{0.28\ Gb\ \sqrt{Nd}}{1 - 0.81\ d\ \sqrt{Nd}}\ \mathrm{Log}_e\ (0.81\ d/2b) \tag{7}$$

and for rod shaped obstacles is

$$\Delta\sigma_{IR} = \frac{0.20\ Gb\ \sqrt{N\ell}}{1 - d\ \sqrt{N\ell}}\ \mathrm{Log}_e\ (\sqrt{2}d/2b) \qquad (8)$$

where N, ℓ, and d were defined above and G is the shear modulus. The constants 0.28 and 0.20 assumes a Poisson ratio of 0.3 and includes the $\sqrt{3}$ Von Mises factor and geometral corrections.

The operative hardening mechanism will be the one requiring the least applied stress to pass the obstacle in the slip plane. The transition occurs when the stress to shear and bow are equal. This will be shown graphically for a given precipitate distribution. Figure 1 shows Nd for a γ' precipitate in 20% CW 316 stainless steel irradiated in Dounreay Fast Reactor (DFR) to fluences of 29-39 dpa at temperatures from 400-520°C.[9] The γ' data on solution annealed 316 SS[3], and laves and η phase[10,11] data at higher temperature are also shown. All of the data generally follow the γ' distribution. Figure 2 shows the γ' diameter versus reciprocal temperature. The diameter of γ' increases with increasing irradiation temperature. The data for SA 316 SS fit the CW 316 data reasonably well even though the exposures is a factor of ten less. This suggests that the γ' reaches an equilibrium size early in the irradiation. The following empirical equations were fit to Nd_p and d_p for γ' as a function of temperature:

$$Nd_p = \frac{1}{2.98 \times 10^{-19} e^{+\,13800/T_k} + 3.81 \times 10^{-2} e^{-13800/T_k}}\ , \qquad (9)$$

and

$$d_p = 2.16 \times 10^{4} e^{-3676/T_k}\ , \qquad (10)$$

where T_k is the irradiation temperature in °k. The behavior of the shearing and bowing mechanisms were evaluated using these equations.

Figure 3 shows $\Delta\sigma$ versus temperature for spherical precipitates using each of the models. Also shown are comparable curves for Garner et al[2] and Brager et al's[3] normalization. The latter was made by multiplying the former by 1/3 at 400°C. However it is shown over a broader temperature range to show the implication of such a normalization. It is apparent that the shearing and bowing mechanisms have different temperature dependences. The transition between shearing and bowing occurs at ~600°C. This corresponds to a critical diameter of over 300Å.

5.4 Dislocations

Both network and Frank loop dislocations are treated the same as in previous analyses.[1,2] The average spacing is expressed in terms of the dislocation density and the prefactor term of 0.19 is multiplied by the Von Mises factor. This works reasonably well at temperatures >350°C. At lower temperatures the prefactor may be 30% higher. Correlation of unirradiated MFE heat 316 SS data indicate that the prefactor should be 0.25.[12] Furthermore, correlation of the HFIR irradiated data requires either a larger prefactor or nonobserved hardening mechanisms. One possiblity is microvoids with diameter less than the TEM resolution level (~20Å). However, at these low irradiation temperatures the helium atoms are not expected to be mobile enough to form bubbles including more than a few atoms. In this analysis the residual $\Delta\sigma$ not accounted for by Frank loops and network dislocations is attributed to the black spots. The black spots were reported to be loops[12]. However, the prefactor deduced from the data ($0.80\sqrt{3}$ = 1.39) is consistant with Orowan hardening obstacles.

5.5 Voids and Bubbles

In this analysis the equation for void hardening developed by Scattergood and Bacon[13] is used. The form of their equation for the case of a zero surface energy parameter is

$$\Delta\sigma_V = \frac{\alpha Gb\ \sqrt{Nd}}{(1 - 0.81\ d\ \sqrt{Nd})}\ \mathrm{Log}_e \left[\frac{0.81d}{nb} \quad (1-0.81\ d\ \sqrt{Nd}) \right] \qquad (11)$$

where G is the shear modulus, N is the density of voids or bubbles, d is the void or bubble diameter, and α and n are adjustable parameters. The parameters (α = 1.39 and n = 3.3) were determined by fitting the $\Delta\sigma_V$ equation to the residual $\Delta\sigma$ after subtracting the contributions due to the other hardening components in SA 316 SS data.[3]. This approach is fairly uncertain because $\Delta\sigma_V$ is determined from the difference between two large numbers. The correlation equation in Figure 4 extrapolates to zero at

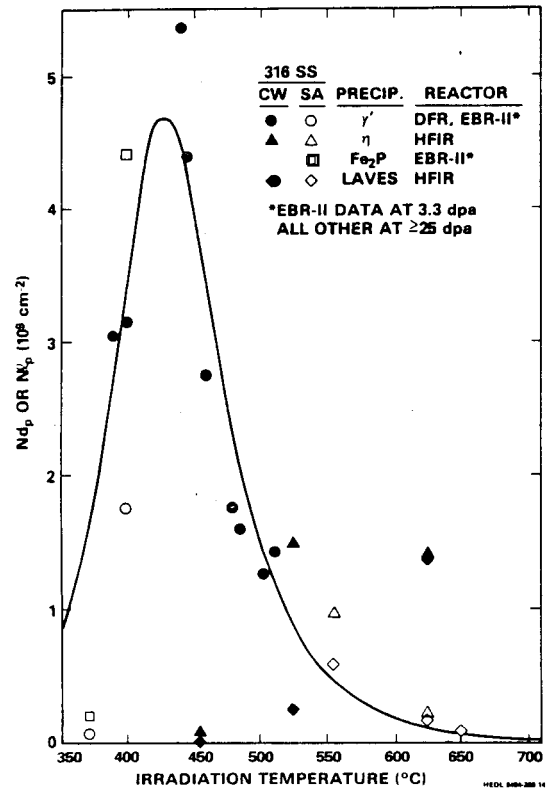

FIGURE 1. Nd_p Versus Irradiation Temperature for 316 SS.

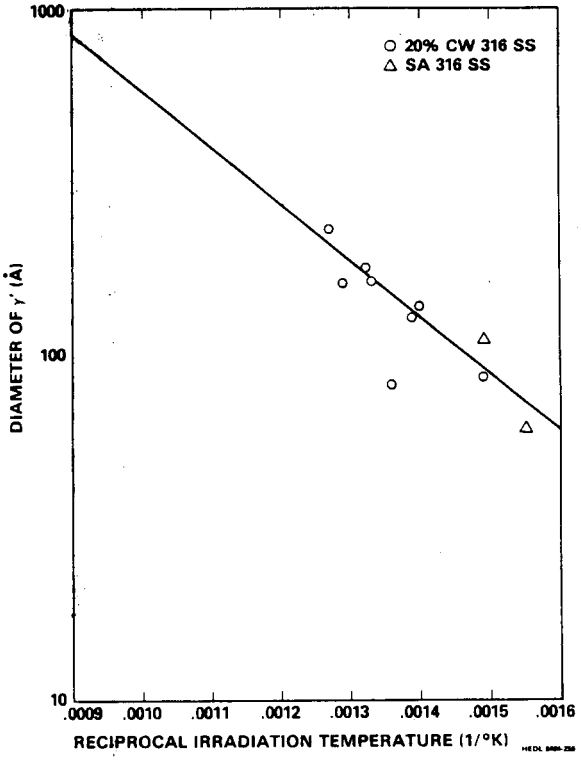

FIGURE 2. Diameter of γ' Precipitates Versus Reciprocal Irradiation Temperature.

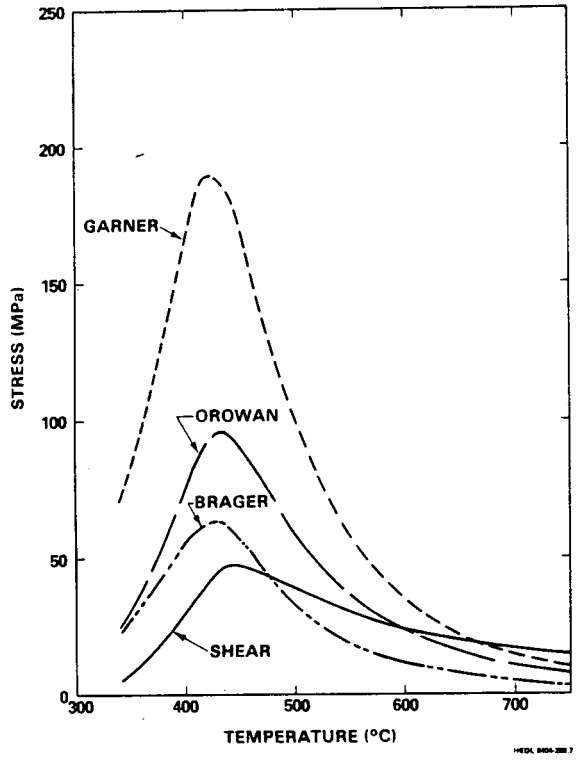

FIGURE 3. Precipitate Yield Stress Versus Temperature.

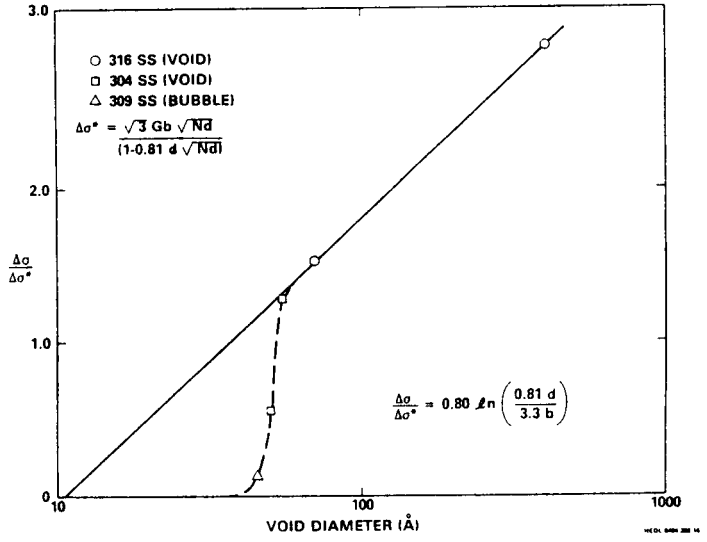

FIGURE 4. Normalized $\Delta\sigma_{ys}$ Versus Void/Bubble Diameter

~10Å. This is consistent with Brown and Hams[6] contention that voids or bubbles on the order of several burgers vectors in diameter should not contribute to hardening because they are too small to significantly lower the dislocation energy. Furthermore cross slip or climb could be a means of bypassing very small voids or bubbles during slow deformation processes. Equation (11) did not fit Thompson's[14] data on ^3He doped 309 SS which contained a high density of 45Å bubbles. In fact the 304SS and 309SS data suggest a void/bubble hardening threshold may exist at about 40Å.

5.6 Discussion

The discussion will involve application of the aforemention hardening models. Two areas will be discussed: 1) nominal saturation levels of yield strength when contributions other than voids have saturated (i.e., ~15 dpa) and 2) high fluence (i.e., high swelling conditions).

In order to calculate $\Delta\sigma_{YS}$ at specific damage exposures, the microstructural components Nd and d are needed. Figures 1, 2 and 5 through 8 show these microstructural parameters as a function of temperature for γ' precipitate, total dislocations, Frank loops and voids. The latter three microstructural parameters are based on Brager and Straalsund's data[15]. It will be assumed that SA and CW 316 precipitate γ' at the same rate and ultimate density, and γ' is representative of all precipitate in 316 SS. Figure 1 shows Nd for laves and η-phase precipitates in CW and SA stainless steels generally agrees with the correlation curve fit to the γ' data. These precipitates are all associated with Ni and Si which could be the reason for this trend. The total dislocation (Figure 5) and Frank loop (Figure 6) dislocation densities are assumed to be saturated levels for all exposures >15 dpa.

Figure 7 shows Nd_V for voids normalized by the helium content (appm) and irradiation temperature (°k). The normalization is based on the assumption that the void density is proportional to an equivalent distribution of equilibrium bubbles. The correlation between the equilibrium bubbles and the observed voids is an exponentially decreasing function of irradiation temperature. The correlation shown in Figure 7 appears to be equally good for cold worked and solution annealed 316 SS. Above 650°C the equation appears to be low. The temperature dependent function steepens with decreasing exposure below 15 dpa. Figure 8 shows the void diameter divided by the square root of dpa versus irradiation temperature. The normalize void diameter is independent of irradiation temperature between 400 and 700°C for exposures >10 dpa.

These microstructural correlations were used to calculate the $\Delta\sigma_{YS}$ in SA 316 SS at 15 dpa. The results are shown in Figure 9 along with Blackburn et al.[16] assessment of the maximum $\Delta\sigma_{YS}$ in SA 316 SS. The calculated values appear to be high by 50-100 MPa. However, it can be argued that the measured values are low. The $\Delta\sigma_{YS}$ is measured from the intrinsic yield strength of the material in a well annealed state which is not necessarily the unirradiated yield strenth. The initial yield strength of some of the material used by Blackburn et al., was possibly slightly cold worked. The dislocations in a cold-worked material will reach equilibrium with temperature and flux independent of the starting level of dislocation density. Thus, where small changes in yield strength are observed, substantial alteration in the microstructure can be present. The (+) symbols show that, when the data are normalized to the initial yield strength of a well annealed material, they agree with the calculated values.

Since Nd_V is related to the square root of helium concentration in Figure 7 and the helium production rate is low in a fast reactor, the $\Delta\sigma_{YS}$ will be increasing slowly in the apparent saturation exposure region (>15 dpa). This behavior was seen by Barnby,[17] and the variation is illustrated with the bars on his data points.

The partition of $\Delta\sigma_{YS}$ between the various microstructural components is of interest. Comparing short and long range obstacles, it was found at ~15 dpa that the short-ranged obstacles (voids and precipitates) contribute 63% to $\Delta\sigma_{YS}$ while the long-range obstacles (dislocation loops and network) contributes 37%. This is in contrast to Brager et al's.,[3] data at 3.3 dpa which showed the opposite distribution (i.e., 40-60 split). The difference between the distributions at 3.3 and 15 dpa is due to the fact that the dislocation structure enters early in the irradiation and the short range structure develops later in the irradiation and it contributes a larger increase in $\Delta\sigma_{YS}$ then the dislocation structure. Furthermore, the partition of $\Delta\sigma_{YS}$ between short and long-ranged obstacles is independent of irradiation temperature between 300 and 800°C at 15 dpa. This is possibly due to the similarity of the temperature dependences of the interstitial and vacancy sinks.

Also of interest is the partition of contributions to the long and short ranged obstacles. The contributors to the former are shown in Figure 10. Black spot damage dominates at low temperatures. Note, however, that gas-bubbles below TEM resolution may be included in the blackspot contribution due to the

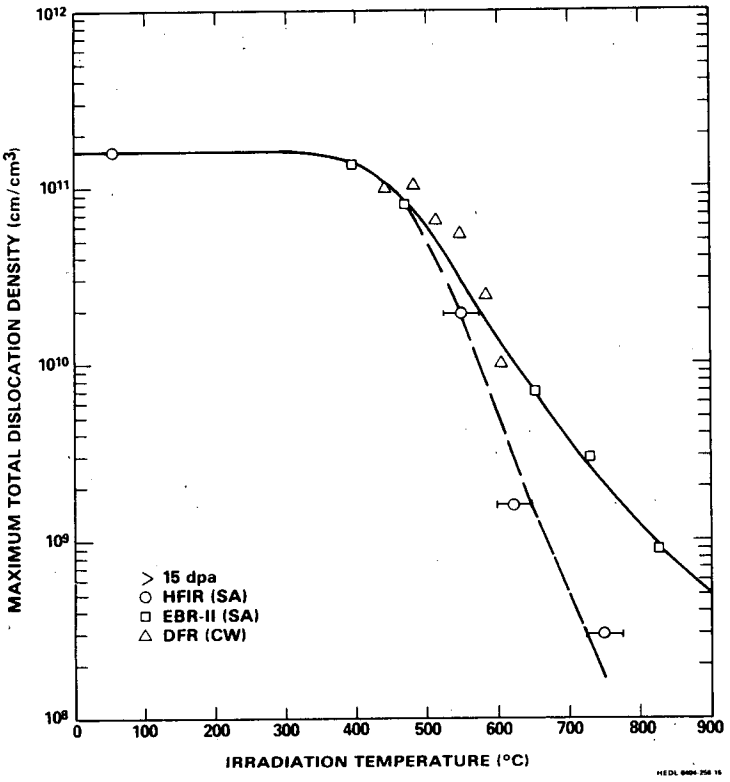

FIGURE 5. Total Dislocation Density (>15 dpa) Versus Irradiation Temperature.

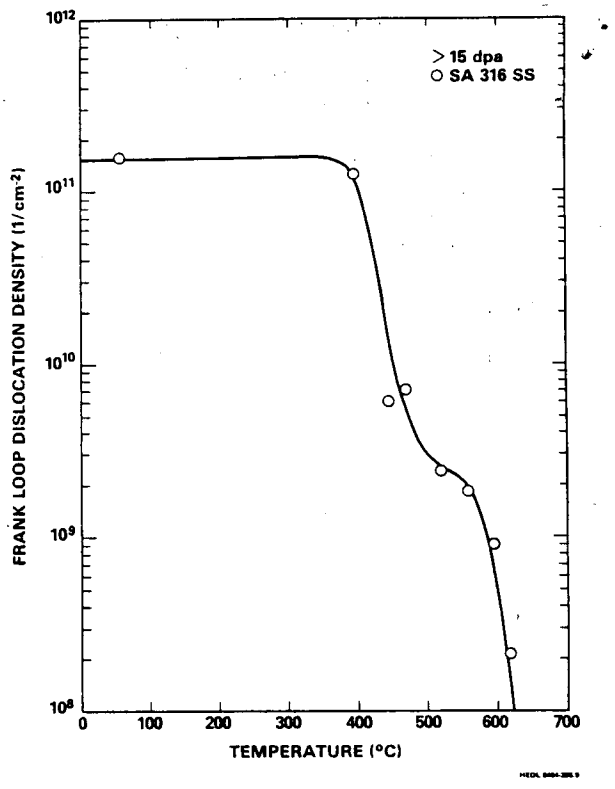

FIGURE 6. Frank Loop Dislocation Density Versus Irradiation Temperature.

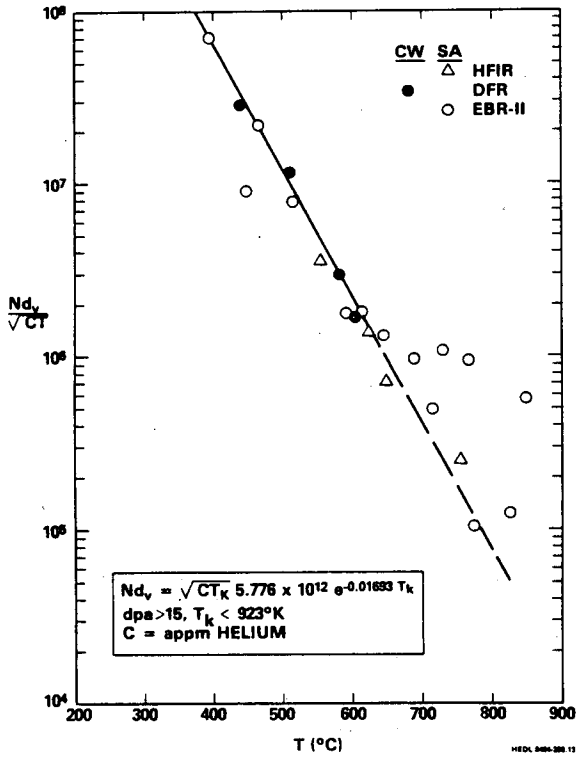

FIGURE 7. Nd_v Dependence on Temperature (T_k) and Helium Content (C).

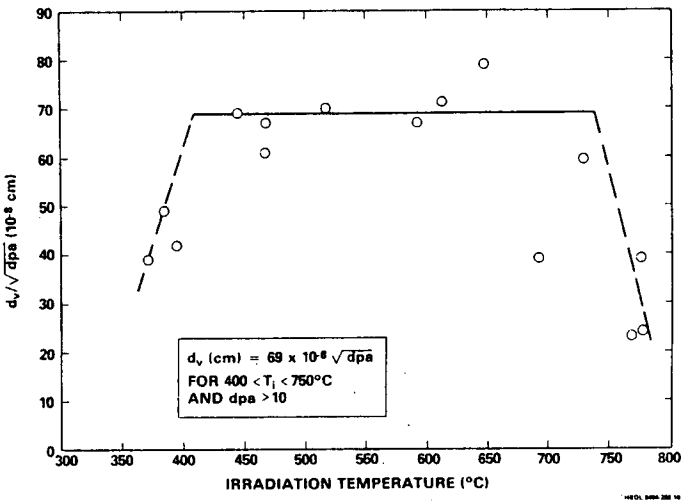

FIGURE 8. Normalized Void Diameter Versus Irradiation Temperature.

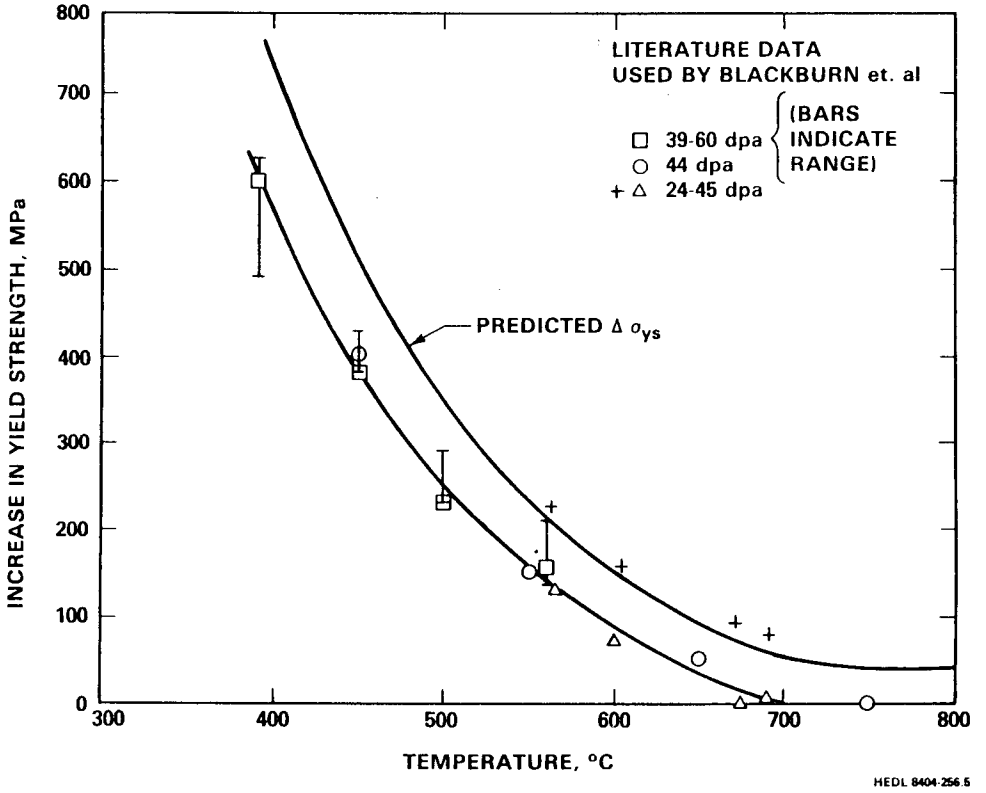

FIGURE 9. $\Delta\sigma_{YS}$ in SA Type 316 Stainless Steel.

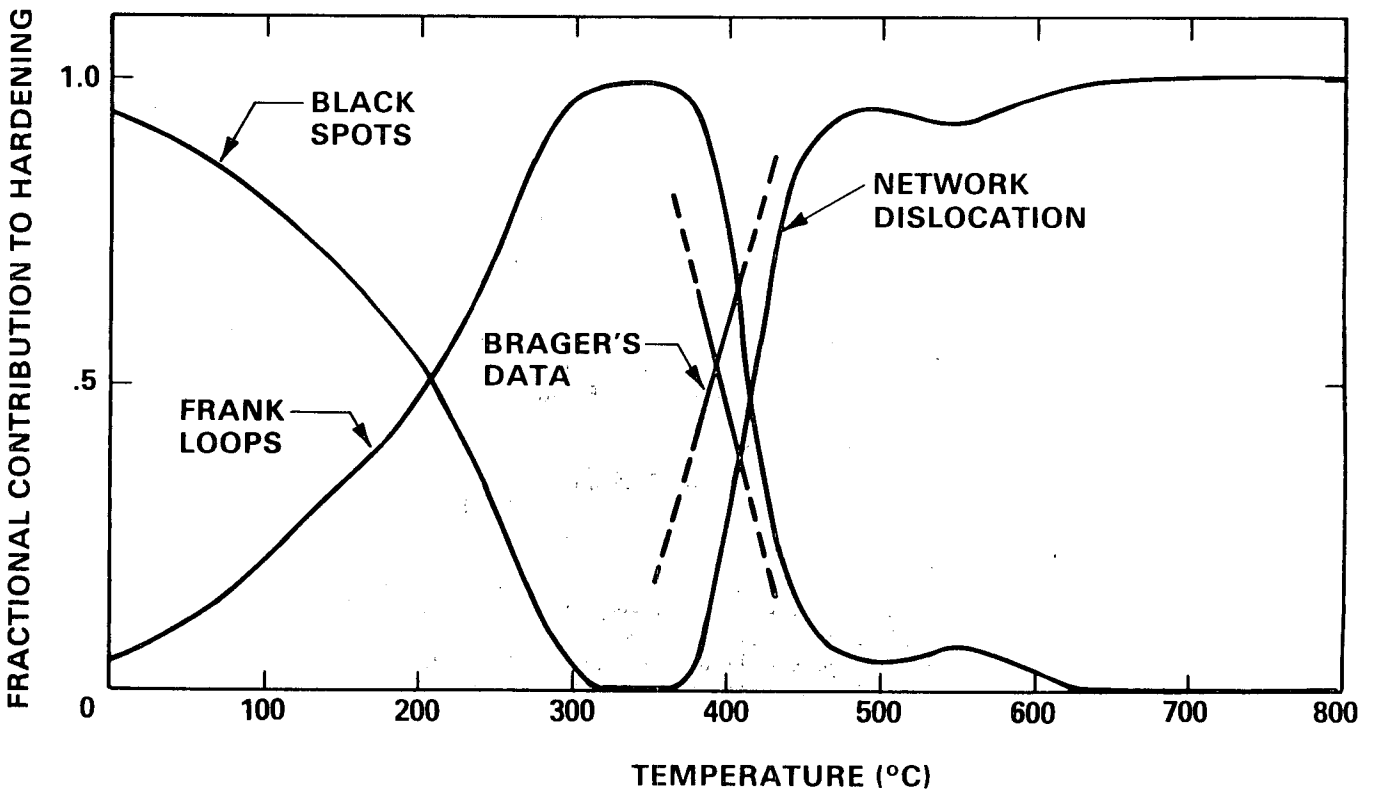

FIGURE 10. Components of Long Range Obstacle Hardening at >15 dpa.

normalization method used in this analysis. At intermediate temperatures the Frank loops are most important. Above ~500°C the network dislocations are the primary contributors. At 400°C and 3.3 dpa the data[3] shows the transition from Frank loop to network microstructure is shifted to low temperatures either due to the lower damage rate or damage exposure than the data at 15 dpa.

Short ranged contributions are shown in Figure 11. The voids totally dominate up to ~500°C. Above 500°C the precipitates contribute as much as 25%. Data[3] at 3.3 dpa show similar results at the low damage rate but show a 50-50 split at the high damage rate.

Apparently, microstructural evolution changes the hierarchy of hardening mechanisms as a function of time. The first hardening source is dislocations, followed by precipitates, and then voids. However, at high exposures, voids may become the dominant hardening mechanism at all temperatures. The dislocation structure saturates at levels nearly independent of temperature and is only weakly dependent on damage rate.[18] The precipitate contribution is limited by the amount of precipitate material available. Voids can increase the $\Delta\sigma_{YS}$ until the irradiation conditions terminate void nucleation and growth.

Since the void microstructure eventually dominate the hardening in stainless steel, it is of value to study this source further. Packan and Farrell[19] and Ayrault et al.,[20] looked at microstructure evolution in stainless steel irradiated with dual ions (Ni and Helium) at ~600°C. The helium to dpa ratio (hpa/dpa) used to simulated a fusion environment varied between 5:1 to 50:1.

In the former study, which reached 250 dpa, saturation of swelling at 25% was observed. Whether this is a real swelling phenonmenon or is caused by injected intertitial effects is open to debate.[21] In any case, $\Delta\sigma_{YS}$ was calculated from the observed microstructure. The results are shown in Figure 12. Whereas neutron irradiation results show "saturation" at ~100-150 MPa, these results indicate $\Delta\sigma_{YS}$ may reach 1600 MPa with >90% of the hardening due to voids. At high dpa some of the difference between calculated $\Delta\sigma_{YS}$ after irradiation with ions or neutrons may be due to differences in damage rate. Figure 13 shows Farrell and Packan's[22] data comparing neutron, dual ion, and single ion Nd_V data after ~10 dpa exposure when the hpa/dpa ratio is ~0.2. Above 600°C, the data are in substantial argreement even though the displacement rates differ by several orders of magnitude. The agreement implies that there is not a large rate effect in the transient evolution of the microstructural parameter Nd_V. On the other hand, Packan and Farrell's data with hpa/dpa = 10 shows much higher $\Delta\sigma_{YS}$ then Ayrault et al., data at the same dpa level. Thus, the dual ion data do not as yet resolve hpa/dpa and damage rate effects.

In the Ayrault et al's study, the helium to dpa ratio was varied by a factor of ten for damage exposures to ~30 dpa. Calculated $\Delta\sigma_{YS}$ based on their microstructural data are shown in Figure 14. It appears that the hpa/dpa ratio affects the rate of increase in $\Delta\sigma_{YS}$. Neutron irradiation data at the same temperatures but at a lower damage rate show a long incubation period prior to increase in $\Delta\sigma_{YS}$.[22] Plotting the same data versus hpa (Figure 15) shows that the neutron data are following the low hpa/dpa dual ion data very closely. This supports the premise that the neutron data show a very slow increase which follows the helium content. This is consistent with the correlation of Nd_V with helium concentration shown in Figure 7. It also appears that the Nd_V parameter is independent of hpa/dpa up to about 5.

Swelling is an important limiting property in a fusion environment. Equation 11 can be rewritten in terms of swelling and thus $\Delta\sigma_{YS}$ can be related to the swelling condition present in the stainless steel. The swelling fraction is approximately given by $S = Nd^3/(2-Nd^3)$. Equation 11 becomes

$$\Delta\sigma_V = \frac{1.39\ Gb\ \sqrt{2S/(1+S)}}{d\ [1-0.81\ \sqrt{2S/(1+S)}]}\ \mathrm{Log}_e\left\{\frac{0.81\ d}{3.3\ b}\ [1-0.81\ \sqrt{2S/(1+S)}]\right\} \qquad (12)$$

The swelling at 15 dpa is $\leq$1% for the results shown in Figure 9. In the design of reactor components, it is not reasonable to accommodate swelling in excess of 10-20%. Using data from Figure 8 for d_V, assuming an incubation swelling dose of 24.5 dpa, and a swelling rate of 1/2% per dpa from Brager and Garner's[22] evaluation of swelling in EBRII and HFIR, the swelling at 45 dpa would be 10%. Garner[23] indicates that the swelling is independent of temperature over a broad temperature range. The $\Delta\sigma_{YS}$ for high swelling material at 28, 45, and 65 dpa (corresponding to S = 1, 10, 20%) is shown in Figure 16. The yield stress contribution due to a dislocation density of $6 \times 10^{10}/cm^2$ is also shown for comparison. It is apparent that the materials which exhibit high swelling may potentially show high $\Delta\sigma_{YS}$. No correction for the effect of swelling on the shear modulus, G, was made.

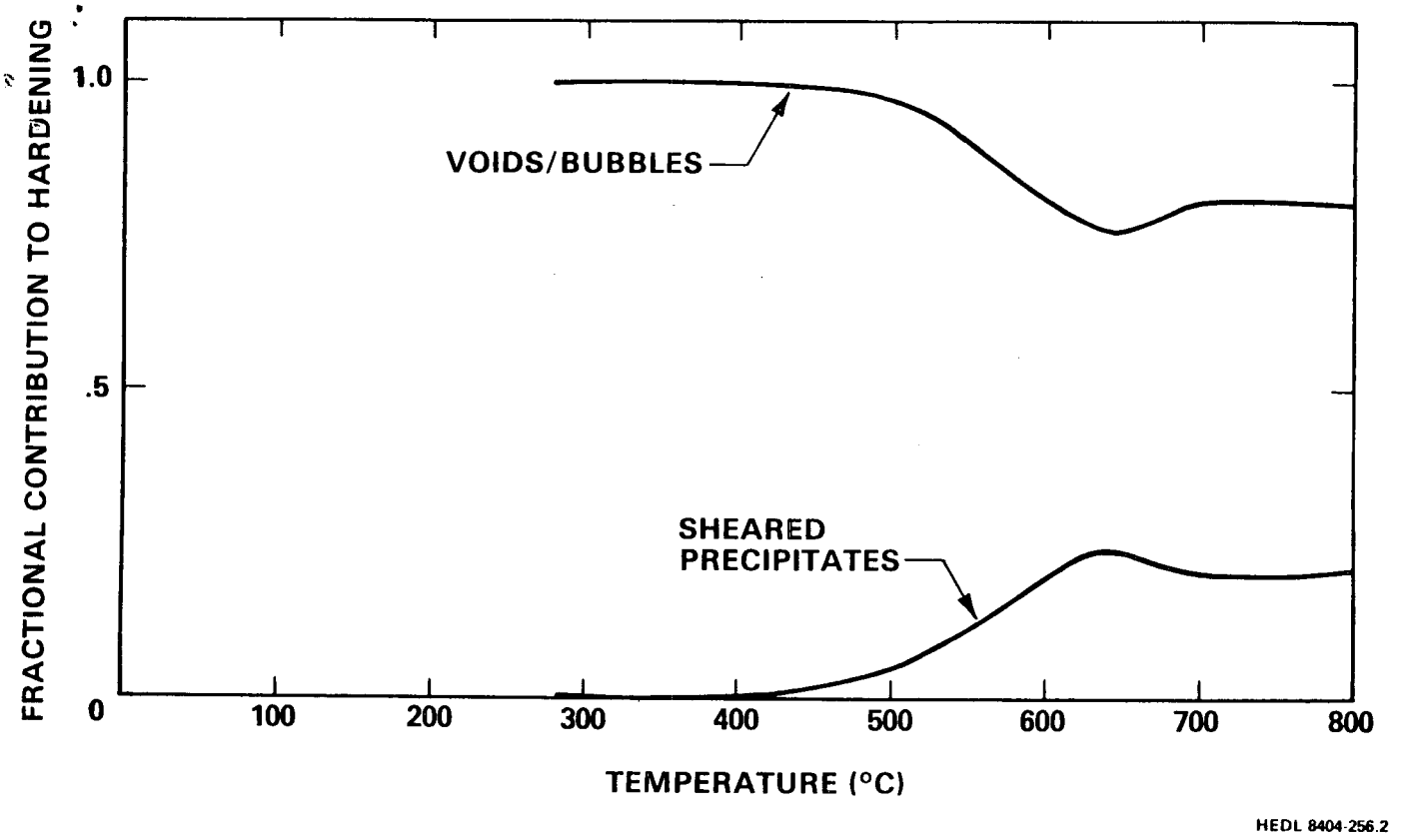

FIGURE 11. Components of Short-Ranged Obstacles Hardening >15 dpa.

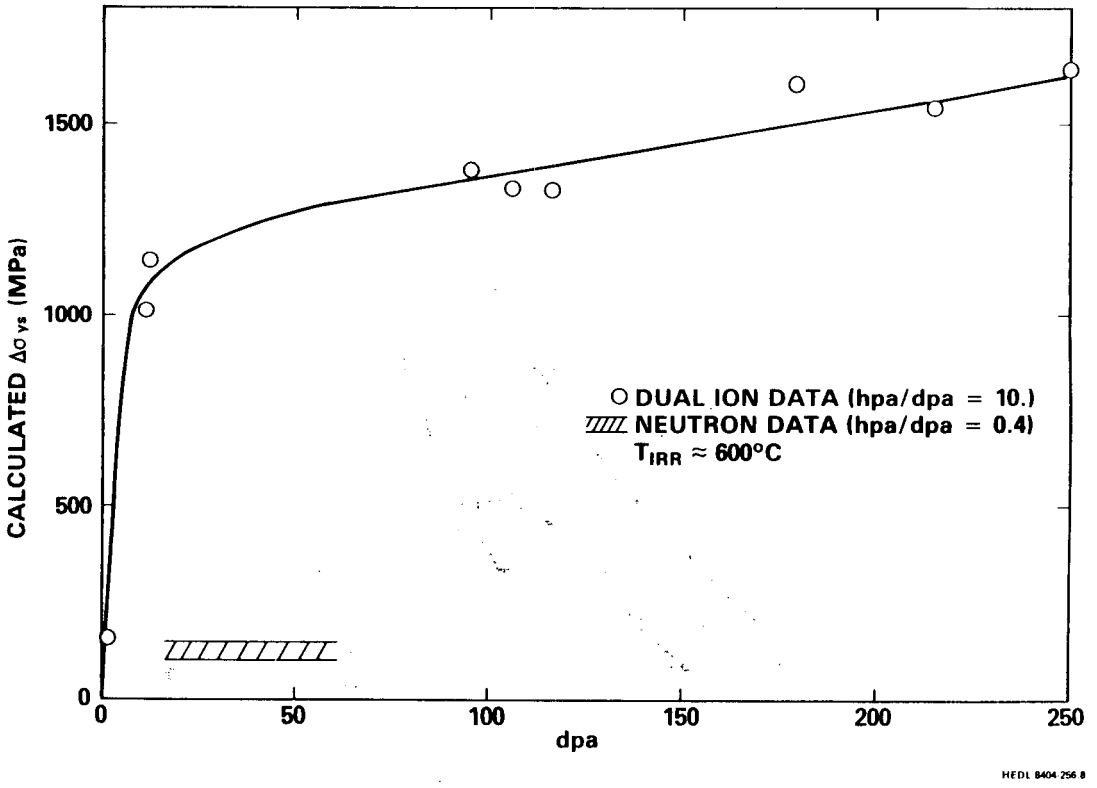

FIGURE 12. Comparison of Dual Ion and Neutron Irradiation $\Delta\sigma_{YS}$ Calculated from the Microstructure.

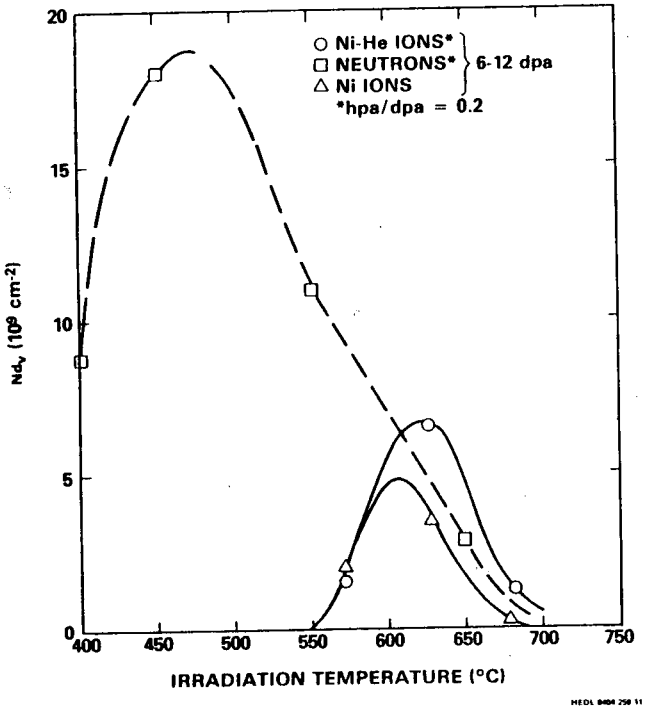

FIGURE 13. Farrell and Packan Nd_v Data from Three Irradiation Sources Versus Irradiation Temperatures When hpa/dpa = 0.2.

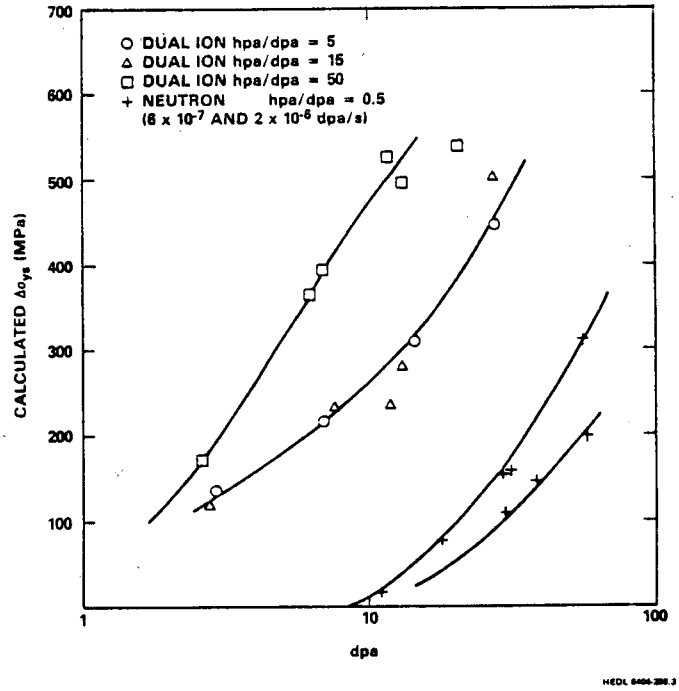

FIGURE 14. Calculated $\Delta\sigma_{YS}$ Versus dpa for Various hpa/dpa Ratios.

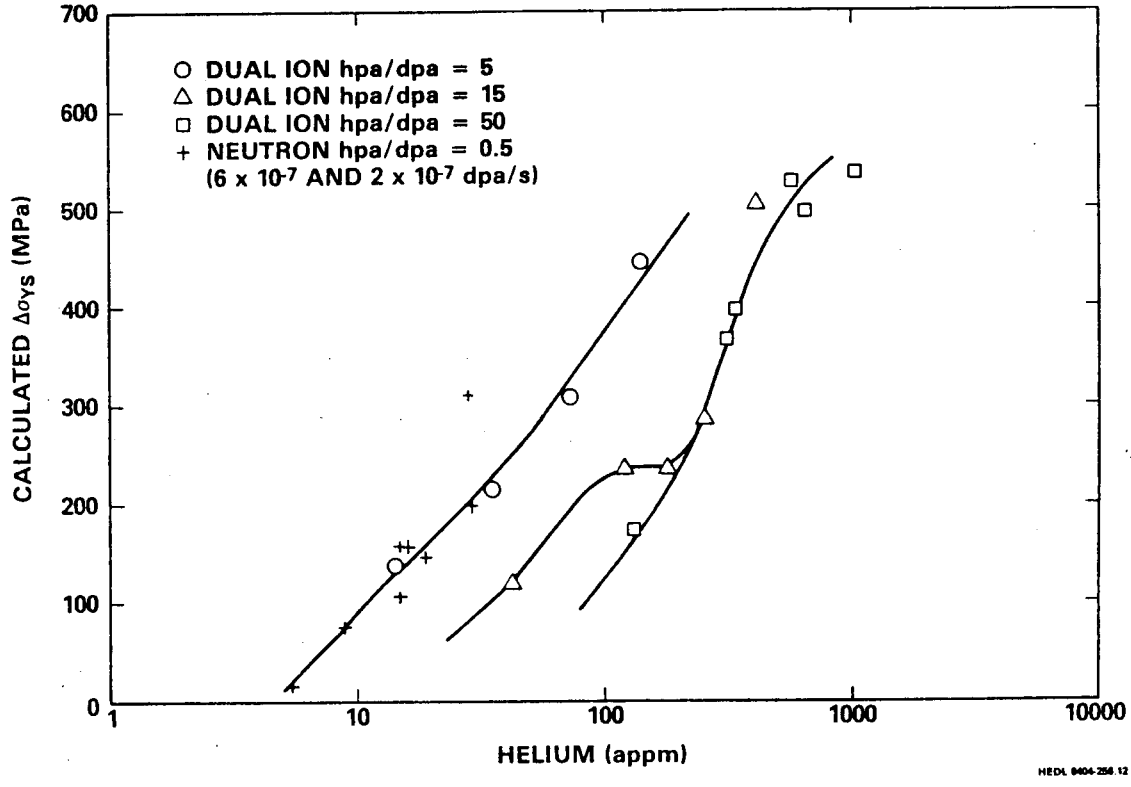

FIGURE 15. Calculated $\Delta\sigma_{YS}$ Versus dpa for Various hpa/dpa Ratios.

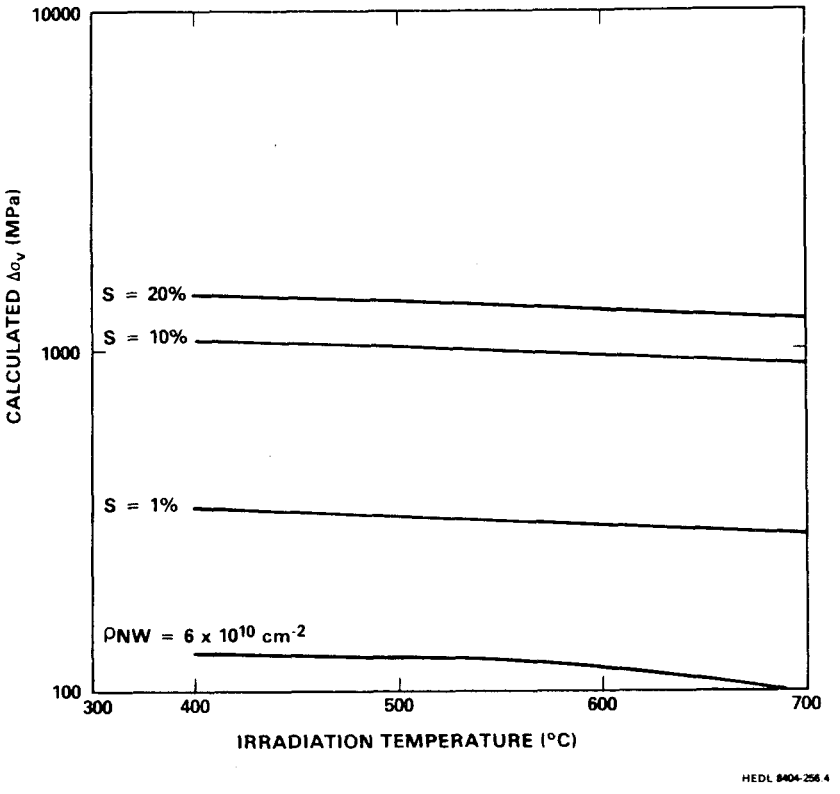

FIGURE 16. Hardening Due to Voids with Swelling Equal to 1, 10, and 20%.

Now let us examine Equation 12. The product of the prefactor (1.39) and the logarithmic term reaches a peak value on the order of four. The $[1-0.81\sqrt{2S/(1+S)}]$ term in the logarithmic term eventually drives the prefactor back to zero. The same factor in the denominator has the potential to drive $\Delta\sigma_{YS}$ to infinity. For a large swelling condition S and d are proportional to $\sqrt{dpa}$, consequently these two terms tend to cancel. The $[1-0.81\sqrt{2S/(1+S)}]$ factor is strongest inside the logarithmic term and it will eventually control the $\Delta\sigma_{YS}$ upper limit. The factor in the denominator comes from the size of the voids being large compared to their separation. The shear modulus decreases with increasing swelling but it is not expected to vary by more than 10%.[23] The question not yet answered is to what value of S can the relationship in Equation 12 be extended before it breaks down or another mechanism comes into play to limit $\Delta\sigma_{YS}$ increases.

It is also of interest to note that for a constant swelling condition the $\Delta\sigma_{YS}$ will depend on the size of the voids. Large, low density voids will cause a smaller $\Delta\sigma_{YS}$ than small, high density voids. Simulation work to date indicates that the void distribution in a fusion environment (i.e., high hpa/dpa) will contain a smaller size and higher density of voids than in a fission neutron environment. Thus, it is expected that a corresponding higher $\Delta\sigma_{YS}$ will be observed in a fusion environment compared to a fission environment. This may also explain some of the scatter in tensile data obtained from specimens irradiated at the same nominal temperature in HFIR but higher hpa/dpa than found in EBR-II.

In the event that precipitates reach a critical size, or they are incoherent, they will harden the steel by Orowan bowing around the obstacle. In this case the form of the Orowan equation should be similar to Equation 12 for swelling and the limitations discussed for swelling applies. However the volume fraction that can precipitate is limited by the available material. It has been noted earlier that the low swelling N lot stainless steel shows irradiation softening beyond ~25 dpa.[24] Examining Equation 12 shows that for a fixed precipitate volume fraction, coalesance of precipitates will lead to a decrease in $\Delta\sigma_{YS}$. This along with a decrease in the shear modulus with increasing swelling could explain the decrease observed in $\Delta\sigma_{YS}$ with increasing dpa exposure.

5.7 Conclusions

Improvements in the correlation of change in yield strength in AISI 316 stainless steel with microstructure were effected by re-examining the role of short-ranged obstacles. Effects due to the size of the obstacle

relative to their spacing, shape of the obstacles, and the dislocation core radius were applied. These corrections become increasingly important at high exposures where large increases in yield strength may be observed.

The shearing of precipitate rather than Orowan bowing around the precipitate was used as a hardening mechanism with the coherent γ' precipitate. This reduced the hardening contribution due to precipitate and alters the temperature dependents of precipitate hardening.

Voids were found to be a potentially dominating hardening mechanism in metals which exhibit high swelling. For ≥10% swelling in AISI 316 stainless steel, increases in yield strength may exceed 1000 MPa. The exact level of yield strength will depend on the size and density of voids.

6.0 References

1. G. D. Johnson, F. A. Garner, H. R. Brager and R. L. Fish, "A Microstructural Interpretation of the Fluence and Temperature Dependence of the Mechanical Properties of Irradiated AISI 316," Tenth Conference on Effects of Radiation on Materials, ASTM STP 725, pp. 393-412, 1981.

2. F. A. Garner, M. L. Hamilton, N. F. Panayotou and G. D. Johnson, "The Microstructural Origins of Yield Strength Changes in AISI 316 During Fission and Fusion Irradiation," J. Nucl. Mater. 103 & 104, pp. 803-808, 1981.

3. H. R. Brager, L. D. Blackburn and D. L. Greenslade, "The Dependence of Displacement Rate on the Radiation-Induced Changes in Microstructural and Tensile Properties of AISI 304 and 316," Proc. of the Third Topical Meeting on Fusion Reactor Materials, Albuquerque, NM, September 1983.

4. H. R. Brager and F. A. Garner, "Swelling as a Consequence of Gamma Prime (γ') and $M_{23}(C, Si)_6$ Formation in Neutron Irradiated 316 Stainless Steel," J. Nucl. Mater. 73, pp. 9-19, 1978.

5. A. Kelly and R. B. Nicholson, Precipitation Hardening, The MacMillian Company, 1963.

6. Strengthening Methods in Crystals, John Wiley and Son's, 1971.

7. P. M. Kelly, "The Effect of Particle Shape on Dispersion Hardening," Script. Met. 6, pp. 647-656, 1972.

8. R. O. Williams, Acta. Metall. 5, p. 1472, 1958.

9. J. I. Bramman et al., "Void Swelling and Microstructural Changes in Fuel Pin Cladding and Unstressed Specimens Irradiated in DFR," Radiation Effects on Breeder Reactor Structural Materials, M. L. Bleiberg and J. W. Bennett Eds., pp. 479-507, 1977.

10. P. J. Maziasz, F. W. Wiffen and E. E Bloom, "Swelling and Microstructural Changes in Type 316 Stainless Steel Irradiated Under Simulated CTR Conditions," Radiation Effects and Tritium Technology for Fusion Reactors, J. S. Watson and F. W. Wiffen Eds., CONF-750989, March 1976.

11. P. J. Maziasz, "Helium Trapping at Ti Rich MC Particles in Ti Modified Austentic Stainless Steel," AIME Symposium on Phase Stability During Irradiation, J. R. Holland, L.L. Mansur and D. L. Potter Eds., 1981.

12. F. W. Wiffin and P. J. Maziasz, "The Influence of Neutron Irradiation at 55°C on the Properties of Austenitic Stainless Steels," J. Nucl. Mater. 103&104, pp. 821-826, 1981.

13. R. O. Scattergood and D. J. Bacon, "The Strengthing Effect of Voids," Acta. Metall., 30, pp. 1665-1677, 1982.

14. A. W. Thompson, "Mechanical Behavior of Face-Centered Cubic Metals Containing Helium," Mat. Sci. & Eng. 21, pp. 41-48, 1975.

15. H. R. Brager and J. L. Straalsund, "Defect Development on Neutron Irradiated Type 316 Stainless Steel," J. Nucl. Mater. 46, pp. 134-158, 1973.

16. L. D. Blackburn, D. L. Greenslde, A. L. Ward, Mechanical Properties of Type 316 Stainless Steel Materials After Irradiation at 515°C and 585°C, HEDL-TME 81-4, Hanford Engineering Development Laboratory, Richland, WA, 1981.

17. J. Barnby et al., "The Post-Irradiation Mechanical Properties of AISI Type 316 Steel and Nimonic PE16 Alloy," Radiation Effects on Breeder Reactor Structural Materials, M. L. Bleiberg and J. W. Bennett Eds., pp. 479-507, 1977.

18. F. A. Garner and W. F. Wolfer, "A Model for the Evolution of Network Dislocation Density in Irradiated Metals," Eleventh Conference on Effects of Radiation on Materials, ASTM STP 782, pp. 1073-1087, 1982.

19. N. H. Packan and K. Farrell, "Ion Damage in 316 Stainless Steel Over a Broad Dose Range," Eleventh Conference on Effects of Radiation on Materials, ASTM STP 782, pp. 885-894, 1982.

20. G. Ayrault et al., "Influence of Helium Injection Rate on the Microstructure of Dual-Ion Irradiated Type 316 Stainless Steel," J. Nucl Mater. 103 & 104, pp. 1035-1040, 1981.

21. F. A. Garner, "Inpact of the Injected Interstitial on the Correlation of Changed Particule and Neutron - Induced Radiation Damage," J. Nucl. Mater. 117, pp. 177-197, 1983.

22. K. Farrell and N. H. Packan, "Comparison of Neutron and Heavy Ion Damage in a Single-Phase Austenitic," Eleventh Conference on Effects of Radiation on Materials, ASTM STP 782, pp. 953-962, 1982.

23. L. LeNaour, N. Vouillon and V. Levy, "Influence of Dose and Dose Rate on the Microstructure of Solution Annealed 316 Steel Irradiated Around 600°C," Eleventh Conference on Effects of Radiation on Materials, ASTM STP 782, pp. 885-894, 1982.

24. F. A. Garner, "Recent Insights on the Swelling and Creep of Irradiated Austentic Alloys," Proc. of the Third Topical Meeting on Fusion Reactor Materials, Albuquerque, NM, September 1983.

25. W. F. Wolfer and F. A. Garner "Effective Thermophysical and Elastic Properties of Materials with Voids," DAFS Quarterly Progress Report Jan-Mar 1984, DOE/ER-0046/17, May 1984.

26. R. L. Simons, "Tensile Property Correlations for 20% CW 316 Stainless Steel," J. Nucl. Mater. 103 & 104, pp. 815-820, 1981.

7.0 Future Work

Microstructural based modeling of work hardening in AISI 316 Stainless Steel is being developed.

8.0 Publications

This work is the basis for a paper to be presented at the Twelfth ASTM Symposium on the Effects of Radiation on Materials to be held June 18-20, 1984 in Williamsburg, VA.

A RATE-THEORY MODEL FOR THE EVOLUTION OF NETWORK DISLOCATIONS IN IRRADIATED METALS

W.G. Wolfer, B.B. Glasgow and Ji-Jung Kai (University of Wisconsin-Madison)

1.0 Objective

The evolution of the dislocation density during the early stages of irradiation influences the subsequent void nucleation as well as the length of the transient period preceding steady-state swelling. Furthermore, this evolution is also in part responsible for the change in mechanical properties such as yield and ultimate strength, ductility and fracture toughness. Accordingly, the purpose of this study is to develop a physical model based on rate theory, and to compare its predictions with experimental data. It is hoped that this will elucidate the major factors which determine in structural alloys both the stability of the unirradiated microstructure and the causes for its evolution during irradiation. In addition, the model forms an important component in predicting the performance of copper alloys and ferritic steels in future fusion reactors for which presently little experimental information is available.

2.0 Summary

The growth of dislocation loops and the climb of edge dislocations can result both in an increase of dislocation line length as well as in the annihilation of dislocation dipoles. These two competing processes from the basis of an evolution model for the dislocation network, and both processes are evaluated with rate theory. In order to provide a mechanism for dislocation climb in the absence of voids it is necessary to introduce the fact that the dislocation bias possesses a variance.

The annihilation of dislocation dipoles involves both climb and glide. As a result, the friction stress for dislocation glide enters as a parameter in the model. The increase in line length depends on the mesh length of the network, or on the average distance between pinning centers. This microstructural parameter is obviously related to the precipitate density and to mechanical properties such as the friction stress, the yield strength, etc. It appears in fact that the resolved shear stress for dislocation glide is determined by the mesh length. Hence, only this mesh length and the dislocation bias variance are treated as adjustable parameters.

These two adjustable parameters are determined by fitting the model predictions to experimental data for the dislocation density in irradiated type 316 stainless steels. Predictions are subsequently made for the dislocation evolution in ferritic steels.

3.0 Program

Title: Radiation Damage and Performance Analysis of Ferromagnetic Steels for Fusion Applications
(Supported by EPRI under contract RP1597-2 with the University of Wisconsin)
Principal Investigator: W.G. Wolfer
Affiliation: University of Wisconsin

4.0 Relevant DAFS Program Plan Task/Subtask

II.C.17 Microstructural Characterization
II.B.2.3, Subtask C: Correlation Methodology

5.0 Accomplishment and Status

5.1 Introduction

The displacement damage in metals at elevated temperature leads to a change of the dislocation structure and, in alloys, also to a change of the precipitate structure. Both changes profoundly affect the mechanical properties as well as the incubation time for swelling. For these reasons, it is important to understand the factors which determine the evolution of the dislocation density. In a previous paper Garner and Wolfer[1] have reviewed the data for the dislocation density in irradiated austenitic stainless steels and outlined a model which can in principle explain the following aspects of the experimental findings. First, the dose dependence of the network dislocation density can be rationalized by two competing processes: a generation rate which depends on the present dislocation density to a power between 1/2 and 1; and an annihilation term which depends on the dislocation density to a power between 3/2 and 2. Second, it was argued that both terms are furthermore proportional to the dislocation climb velocity. As a result, the steady state or saturation density reached after high doses becomes nearly independent of the irradiation temperature, as suggested by the experimental observations. The third aspect of the model is that the saturation density is independent of the initial dislocation density. The success of this model makes it worthwhile to develop it further and to put it on a firm rate-theory basis in order to integrate it with void nucleation and void growth models. The following sections describe the development and results of this model in detail.

5.2 The Basic Model

As mentioned above, the dislocation evolution is thought to be the result of two competing processes, the generation of dislocation line length by climb, and the annihilation or recovery of dislocation density by the recombination of edge dislocations with opposite Burgers vectors. These two processes will be analyzed in detail below, and it will become evident that they lead to the following evolution equation for the network dislocation density ρ:

$$\frac{d\rho}{dt} = B\rho - A\rho^2 \tag{1}$$

The rate coefficients A and B are proportional to the climb rate of edge dislocations and therefore weakly dependent on the dislocation density itself. As a result, Eq. (1) must be integrated numerically for accurate results. However, an approximate solution of Eq. (1) can be obtained by considering A and B to be constants. Then,

$$\rho(t) = \frac{\frac{B}{A}}{1 + \left(\frac{B}{A\rho_o} - 1\right) \exp(-Bt)} \tag{2}$$

where $\rho_o = \rho(0)$ is the starting dislocation density.

The saturation density is in this approximation simply given by $\rho_s = B/A$. Garner and Wolfer[1] have previously determined the "constants" B and A from the experimentally observed saturation density and from one measured density value $\rho(t)$ at a fluence in the transient regime. These "constants" are however proportional to the climb velocity of edge dislocations, and are therefore dependent on dose rate, temperature, and the sink strengths. In the following section, A and B will be evaluated and incorporated in a comprehensive rate theory.

5.3 The Recovery Process

It is assumed in the present model that the recovery mechanism under irradiation for the dislocation network is in principle the same as under thermal annealing. The major difference lies merely in the fact that irradiation enhances climb. A representative dislocation mechanism for recovery is the annihilation of a dislocation dipole, illustrated in Fig. 1. Upon the preferential absorption of interstitials (or vacancies), this "vacancy-type" (or interstitial-type) dipole will reduce its width h. If the mutual interaction between the two edge dislocations can overcome the critical resolved shear stress, the dipole configuration

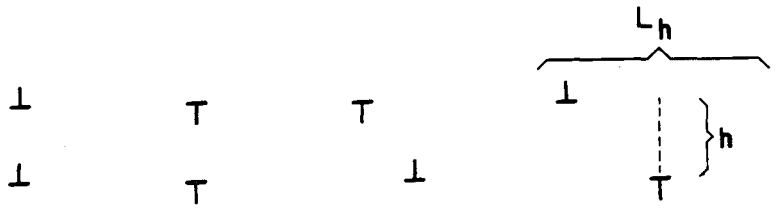

FIGURE 1. Possible Dipole Configurations of Two Edge Dislocations on Parallel Glide Planes with Separation Distance h.

will be maintained at about an angle of $\pi/4$, and the dislocations will inevitably annihilate.

If τ_o is the critical resolved shear stress for dislocation glide, a converging dipole will only be formed if the glide interaction force can overcome τ_o. This condition is expressed by the relationship

$$\frac{\mu b}{2\pi(1-\nu)h_{max}} = \tau_o \tag{3}$$

which defines the maximum dipole width h_{max}. Here, μ is the shear modulus, b the Burgers vector, and ν the Poisson's ratio. When the dislocation density is large, the distance between two parallel dislocation which may form a converging dipole is given by $8/\sqrt{\pi\rho/3}$. This value is obtained from the following considerations: The number of dislocations belonging to one of the 12 possible glide systems is $\rho_b = \rho/12$. Among the possible pairs of parallel edge dislocations only one pair out of four will form a converging dipole when interstitials are preferentially absorbed (see Fig. 1). To include then the case of a high dislocation density ρ which may control the maximum dipole distance h_{max} we select it such that

$$h_{max} = \text{Min}\ \{8/\sqrt{\pi\rho/3}\ ,\ \mu b/[2\pi(1-\nu)\tau_o]\} \tag{4}$$

The glide motion of dislocation is in many metals and alloys restricted by obstacles or pinning centers such as precipitate particles. In such cases, pinned sections of mesh length ℓ, where ℓ is the average distance between pinning centers, function as Frank-Read sources when a glide force acts upon them. The critical shear stress τ_o may therefore be approximated by the shear stress necessary to activate a Frank-Read source. Hence

$$\tau_o = \frac{\mu b}{2\pi(1-\nu)\ell} \ln\ (\ell/b)\ . \tag{5}$$

Combining this equation with Eq. (4) we find

$$h_{max} = \text{Min}\ [8/\sqrt{\pi\rho/3},\ \ell/\ln(\ell/b)]\ . \tag{6}$$

Next, it is necessary to evaluate the number of converging dipoles of a given width between h and h + dh at any given time. We imagine that if any two dislocations belonging to the same glide system encounter each other within a glide interval of length L_h (see Fig. 1) a stable dipole is formed. The number of such dipoles is then $\rho_b^2 L_h dh/4$. As long as $h < h_{max}$, L_h is on the order of 2h, and the total number of converging dipoles on all glide systems and with width between h and h + dh is then

$$12\ \frac{1}{4}\ \left(\frac{\rho}{12}\right)^2\ 2h\ dh = \frac{1}{24}\ \rho^2\ h\ dh\ .$$

The lifetime of these dipoles is now given by

$$\tau(h) = \int_b^h dh'/2V(h') \tag{7}$$

where V(h) is the climb velocity of one dislocation. Assuming, then, that the number of dipoles formed with initial width of h_{max} or less is equally probable, the rate of dislocation annihilation is finally given by

$$A\rho^2 = \frac{1}{24}\rho^2 \int_b^{h_{max}} h\, dh\, \tau^{-1}(h) . \tag{8}$$

Under irradiation, the climb velocity is due to two causes, the preferential absorption of interstitials and the climb force between the two dislocations. Kroupa[2] has shown that the climb force gives rise to a vacancy concentration in equilibrium with the dislocations of the dipole as given by

$$C_v^d(h) = C_v^{eq} \exp(Hb/h) \tag{9}$$

where

$$H = \mu\Omega/[2\pi(1 - \nu)kT] , \tag{10}$$

and Ω is the atomic volume, k the Boltzmann constant, and T the absolute temperature.

The total climb velocity is now given by

$$V = \frac{\Omega}{b}[Z_i^d D_i C_i - Z_v^d D_v C_v + Z_v^d D_v C_v^d(h)] \tag{11}$$

where Z_i^d and Z_v^d are the bias factors for interstitial and vacancy absorption, and D_i and D_v the interstitial and vacancy migration coefficients, respectively. The point defect concentrations, C_i and C_v, can be determined from rate theory, and V is found to be

$$V(h) = \frac{\Omega}{b}\left[\frac{Z_i^d}{Z_v^d} - \frac{\bar{Z}_i}{\bar{Z}_v}\right] D_v \Delta C_v + \frac{\Omega}{b} D_v Z_v^d C_v^{eq} \left[\exp\left(\frac{Hb}{h}\right) - 1\right] = V_R + V_T\left[\exp\left(\frac{Hb}{h}\right) - 1\right] . \tag{12}$$

The first term represents the radiation-induced climb rate, and it depends on the excess vacancy concentration ΔC_v and the net bias; the latter contains the sink-averaged bias factors $\bar{Z}_i$ and $\bar{Z}_v$. The second term represents the thermally induced climb rate as driven by the mutual interaction of the dislocations in the dipole. This term is present in the absence of irradiation when $\Delta C_v = 0$, and it is in part responsible for the thermal recovery of a cold-worked dislocation structure.

According to Eq. (12) we can now write for the dipole life-time

$$\tau = \frac{1}{2}\int_b^h \frac{dh'}{V_R + V_T[\exp(Hb/h') - 1]} . \tag{13}$$

When the exponential term is large, i.e. for small values of h', the integrand makes the least contribution to τ. Hence, we shall approximate the exponential by a linear Taylor expansion, i.e.

$$\tau(h) \cong \frac{1}{2}\int_b^h \frac{dh'}{V_R + V_T Hb/h'} \cong \frac{h}{2V_R}\left\{1 - \frac{V_T Hb}{V_R h} \ln\left(1 + \frac{V_R h}{V_T Hb}\right)\right\} . \tag{14}$$

The coefficient for dislocation annihilation is then given by

$$A = \frac{1}{12} V_T H b \int_{x_o}^{x_1} \frac{dx}{1 - \frac{1}{x} \ln (1 + x)} \tag{15}$$

where $x = V_R h / V_T H b$, $x_o = V_R / V_T H$, and $x_1 = V_R h_{max} / V_T H b$.

Since no closed-form solution apparently exists for the integral in Eq. (15), we consider first two limiting cases

a) If $V_R >> V_T$, then $1/x \ln x << 1$, and

$$A \cong \frac{1}{12} V_R h_{max} .$$

This approximation is valid at temperatures where self-diffusion is negligible.

b) At very high temperatures when $V_T >> V_R$ the variable $x << 1$. We may then expand $(1/x) \ln(1 + x) \cong 1 - x/2$, neglect V_R, and obtain

$$A \cong \frac{1}{6} V_T H b \ln (h_{max}/b) .$$

As a result of the strong temperature dependence of self-diffusion, and hence, of V_T, the range of temperatures where both V_R and V_T are of equal importance is rather narrow. Accordingly, we can simply add the results of the two limiting cases to obtain the approximation

$$A \cong \frac{1}{12} V_R h_{max} + \frac{1}{6} V_T H b \ln(h_{max}/b) , \tag{16}$$

suitable for all temperatures.

5.4 Dislocation Generation

The dislocation density may increase during irradiation as a result of two processes; by the formation and growth of interstitial-type loops, and by the climb of pinned edge dislocations. In the latter process, an initially straight edge dislocation segment may bow out by the preferrential absorption of interstitials. The resulting curved segment is similar to a section of a prismatic interstitial-type loop. Hence, by treating only the climb of pinned edge dislocations, interstitial loop growth is also covered in at least an approximate fashion.

Accordingly, consider a bowed-out segment of an edge dislocation pinned by two centers separated by a distance ℓ. With the notations and definitions shown in Fig. 2, the area covered by the climb of the segment is given by

$$F = \frac{1}{2} \left[LR - \ell \sqrt{R^2 - \ell^2/4} \right] . \tag{17}$$

The angle ϕ extended by the arc length L and the radius of curvature R are related by

$$L = \phi R \tag{18}$$

and

$$\ell = 2R \sin (\phi/2) . \tag{19}$$

If V is the climb velocity of the dislocation segment, then the area F increases at the rate

$$\frac{dF}{dt} = \frac{dF}{dL}\frac{dL}{dt} = LV \ ,$$

and the segment length at the rate

$$\frac{dL}{dt} = L\frac{dL}{dF}V \tag{20}$$

From the Eqs. (18) to (20) one finds

$$\frac{dF}{dL} = \frac{1}{2}\left[R + \frac{R - Lu}{1 - \phi u}\right] \tag{21}$$

where

$$u = \sqrt{R^2/\ell^2 - 1/4} \ . \tag{22}$$

The dislocation segment continues to climb, and L increases until a part of it encounters a dislocation with an opposite Burgers vector on a parallel glide plane and forms a converging dipole. This will eventually result in annihilation and the formation of a new segment pinned at two centers, namely at one from each of the previous dislocations which formed the dipole. The other fate of the expanding loop is that it encounters new pinning centers, and the loop is divided into shorter segments, each of which repeats the process of climb and extension by itself. On average, the loop expands then to a maximum arc length L_{max}, becomes subdivided into shorter segments of length ℓ, and each shorter segment repeats the process of its parent segment.

The average rate of increase in dislocation density is then obtained by averaging over one of these regeneration cycles, namely the expansion of a nearly straight segment of length ℓ to an arc of length L_{max}. If there exists on average N_ℓ segments per unit volume, then the rate of dislocation multiplication is given by

$$\frac{d\rho}{dt} = N_\ell \int \frac{dL}{dt} = N_\ell V \int_\ell^{L_{max}} \left(L\frac{dL}{dF}\right) dL = \rho V \frac{1}{L_{max}} \int_\ell^{L_{max}} dL \left(L\frac{dL}{dF}\right) = B\rho \tag{23}$$

where $\rho \cong N_\ell L_{max}$ is on average the dislocation density. Figure 3 shows the factor $\ell B/V$ as a function of L_{max}/ℓ.

If the spacing of the pinning centers is on the order of ℓ, the arc will on average extend to about a semicircle until it encounters new pinning centers. Hence $L_{max} \simeq \pi\ell/2$, and $\ell B/V \cong 1$ according to Fig. 3.

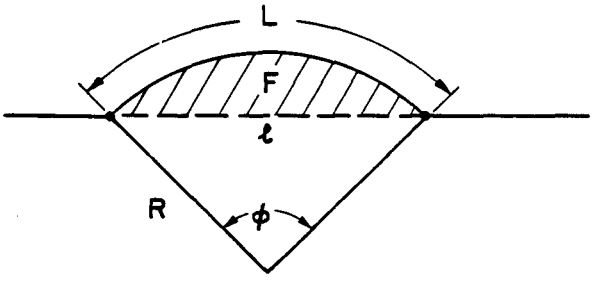

FIGURE 2. Bow-Out of an Edge Dislocation Segment of Initial Length ℓ due to Climb.

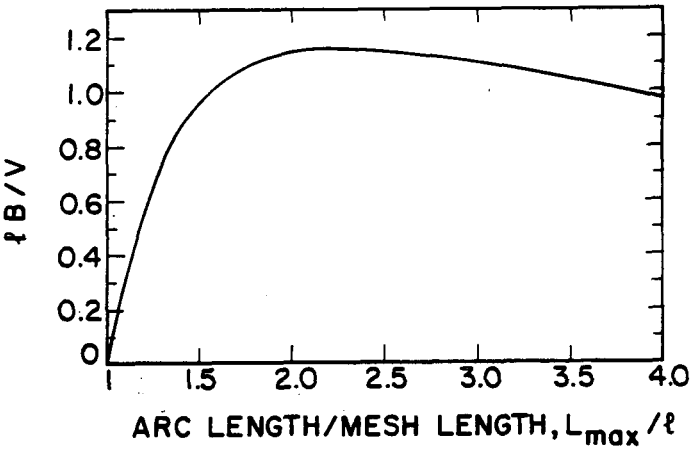

FIGURE 3. Variation of the Parameter $\ell B/V$ with Arc Length of the Climbing Edge Dislocation Segment.

In the above development it was assumed that the climb velocity of the bowed-out dislocation is independent of the radius of curvature R, and hence, independent of L. This assumption is only correct when $V_R \gg V_T$. At temperatures where self-diffusion becomes important V_T can no longer be neglected. As a result of the line tension of the dislocation, the vacancy concentration in thermodynamic equilibrium with the curved dislocation is given by[3]

$$C_v^b = C_v^{eq} \exp\left[-\frac{\mu\Omega}{2\pi(1-\nu)kT}\frac{b}{R}\ln\frac{R}{1.8b}\right] . \tag{24}$$

Figure 4 shows the ratio C_v^b/C_v^{eq} for nickel at various temperatures and as a function of (R/b). When the loop reaches the semi-circle, the minimum radius $R = \ell$ is obtained, and C_v^b also reaches its minimum value. Hence, the minimum climb velocity is

$$V_m = V_R + V_T\left\{\exp\left[-\frac{\mu\Omega}{2\pi(1-\nu)kT}\frac{b}{\ell}\ln\frac{\ell}{1.8b}\right] - 1\right\} . \tag{25}$$

When this velocity becomes zero, dislocation generation is no longer possible and B = 0. Accordingly, we may assume that

$$B \cong \begin{cases} V_m/\ell & \text{for } V_m > 0 \\ 0 & \text{for } V_m \leq 0 . \end{cases} \tag{26}$$

5.5 The Impact of Bias Variance

The radiation-induced climb velocity V_R is according to Eq. (12) proportional to the net bias $(Z_i^d/Z_v^d - \bar{Z}_i/\bar{Z}_v)$. For a microstructure containing only one sink type, for example only edge dislocations, the net bias would be zero. This is certainly correct for the mean climb velocity averaged over many different dislocations, but it is not true for any individual dislocation. The reason is to be found in the bias variance which originates from the partial cancellation of the long-range stress fields of groups of dislocations. Hence, the bias of an individual dislocation depends to some degree on the proximity of other dislocations. Wolfer et al.[4] have estimated this bias variance by considering dislocation multipoles. They found that the bias of an edge dislocation in a narrowly spaced dipole was only about half the value of the isolated dislocation. In a real microstructure with complex dislocation tangles, we may therefore assume that the individual dislocation net bias is given by

$$(1 + z)\frac{Z_i^d}{Z_v^d} - \frac{\bar{Z}_i}{\bar{Z}_v}$$

where z is a random variable. The probability of a dislocation having a bias deviation of z from the mean is assumed to be Gaussian. Hence, the average of the radiation-enhanced climb velocity V_R remains proportional to $(Z_i^d/Z_v^d - \bar{Z}_i/\bar{Z}_v)$, where Z_i^d and Z_v^d are average values for the dislocation bias factors. In the above average of V_R, both positive and negative climb directions are included.

The increase of dislocation line length is, however, independent of the climb directions, and depends only on the absolute value of the climb velocity. The average of the absolute climb velocity is now given by

$$\bar{V}_R = \frac{\Omega}{b} D_v \Delta C_v \int_{-\infty}^{+\infty} dz \left|\frac{Z_i^d}{Z_v^d}(1+z) - \frac{\bar{Z}_i}{\bar{Z}_v}\right| e^{-z^2/2\zeta^2} (\sqrt{2\pi}\,\zeta)^{-1} = \frac{\Omega}{b} D_v \Delta C_v \left|\frac{Z_i^d}{Z_v^d}\left(1 + \sqrt{2/\pi}\,\zeta\right) - \frac{\bar{Z}_i}{\bar{Z}_v}\right| \tag{27}$$

where ζ is the standard deviation of the dislocation bias.

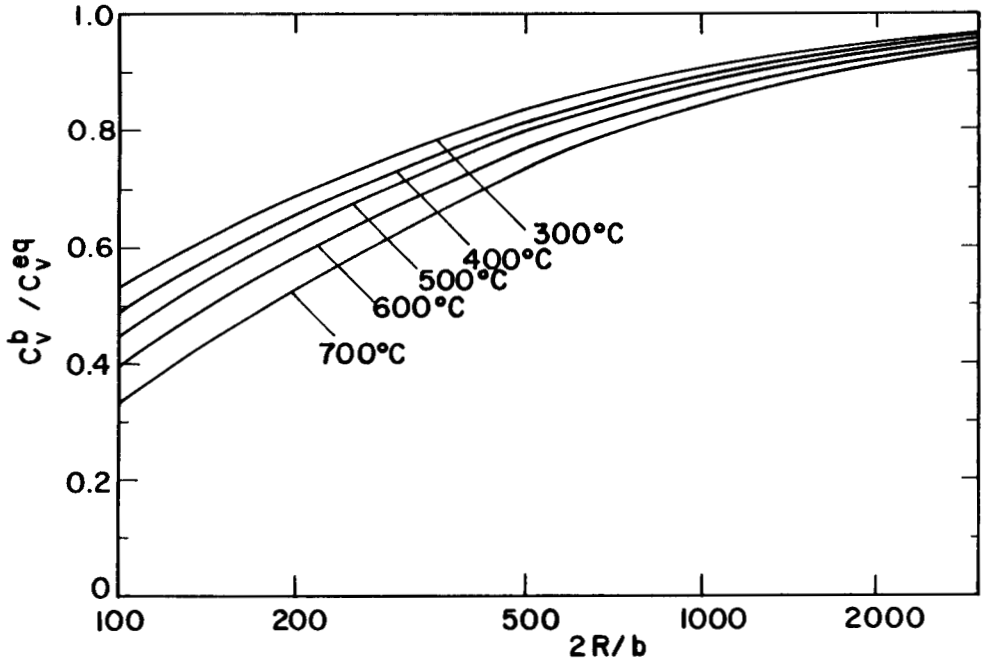

FIGURE 4. Variation of the Subsaturation of Vacancies in Thermodynamic Equilibrium with a Bardeen-Herring Source Climbing by Preferential Interstitial Absorption.

Since both the production and the annihilation of dislocations depend only on the absolute climb velocity, $\bar{V}_R$ is to be substituted for V_R in both Eq. (25) and Eq. (16). The importance of the inclusion of the bias variance is that dislocation evolution will proceed even in the absence of voids, i.e. when the net bias vanishes.

In a well-annealed material, we may assume that dislocations are isolated, and the bias variance is negligible. On the other hand, in a cold-worked material, dislocations are predominantly arranged in dense tangles. Assuming then that the bias of the tangled dislocations can differ by a factor of 0.5 from the bias of an isolated dislocation, the variance changes from about zero to 0.5 with increasing dislocation density. For a continuous variation we assume then that

$$\zeta = 0.5\ [1 - \exp(-\lambda\rho)] \tag{28}$$

where $\lambda \cong 10^{-15}\ m^2$. This selection of λ ensures that the bias variance becomes negligible when the dislocation density is smaller than $\rho \cong 10^{15}\ m^{-2}$.

5.6 Results

The following predictions for the evolution of the network dislocation density are carried out for two metals, namely nickel or austenitic stainless steel and α-Fe. At the present time we consider the properties of α-Fe to approximate those of the ferrite phase in ferritic and bainitic steels. The properties used in the calculations are listed in Table 1. The dislocation bias factors Z_i^d and Z_v^d are evaluated with the formulae given by Sniegowski and Wolfer[5] and using the relaxation volumes, shear polarizabilities and elastic properties given in Table 1. With the exception of the mesh length ℓ, all other parameters are based on actually measured values. The mesh length was selected such that the saturation dislocation density for type 316 stainless steels will be $6 \times 10^{14}\ m^{-2}$ for irradiation temperatures from 400°C to 500°C.

TABLE 1

MATERIALS PARAMETERS

Parameter	Ni or 316 SS	α-Fe
Displacement Rate, dpa/s	10^{-6}	10^{-6}
Cascade Efficiency	0.1	0.1
Lattice Parameter, a_o, nm	0.3639	0.2866
Burgers Vector, nm	0.2573	0.2482
Shear Modulus, GPa	82.95	80.65
Poisson's Ratio	0.264	0.254
Vacancy Migration Energy, J	1.92×10^{-19}	2.016×10^{-19}
Vacancy Formation Energy, J	2.88×10^{-19}	2.464×10^{-19}
Pre-exponential Factor D_v^o, m^2/s	1.29×10^{-6}	4.463×10^{-5}
Vacancy Relaxation Volume, Ω	-0.2	-0.5
Interstitial Relaxation Volume, Ω	1.5	0.85
Vacancy Shear Polarizability, J	-2.4×10^{-18}	-2.4×10^{-18}
Interstitial Shear Polarizability, J	-2.535×10^{-17}	-2.535×10^{-17}
Dislocation Densities, m^{-2}		
for Annealed	4×10^{12}	4×10^{12}
for Cold-Worked	7×10^{15}	7×10^{15}
Mesh Length ℓ, μm	0.4	0.4

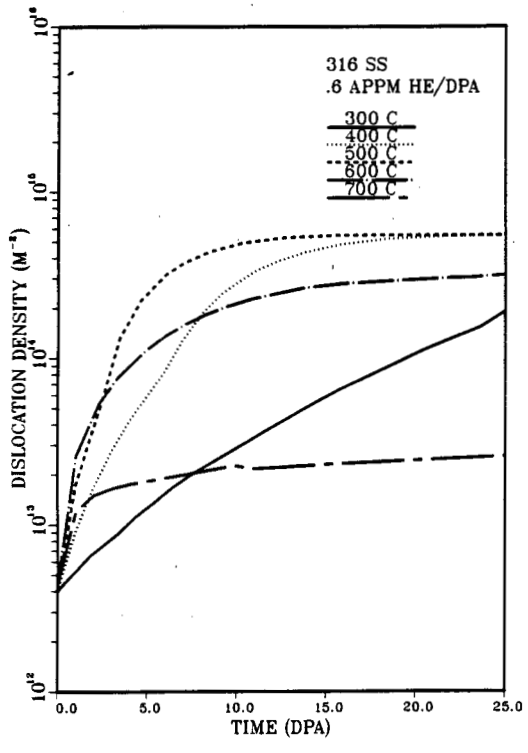

FIGURE 5. Dislocation Density Versus Dose for Solution-Annealed Type 316 Stainless Steel Irradiated in a Breeder Neutron Spectrum.

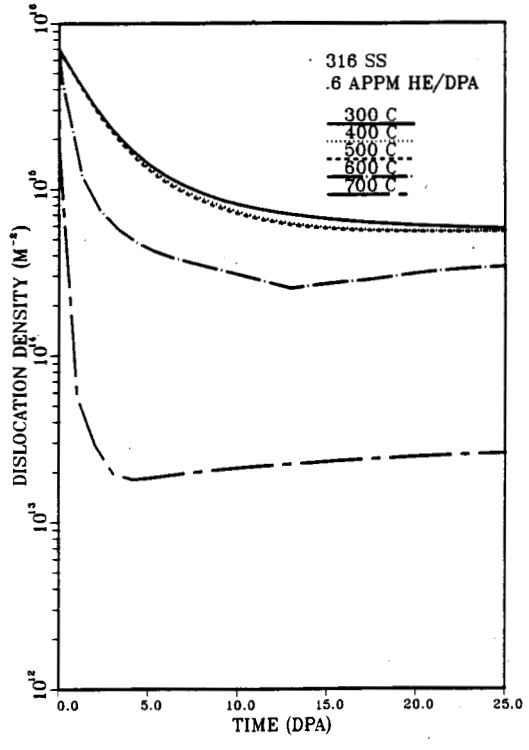

FIGURE 6. Same as in Fig. 5 but for a 20% CW 316 Stainless Steel.

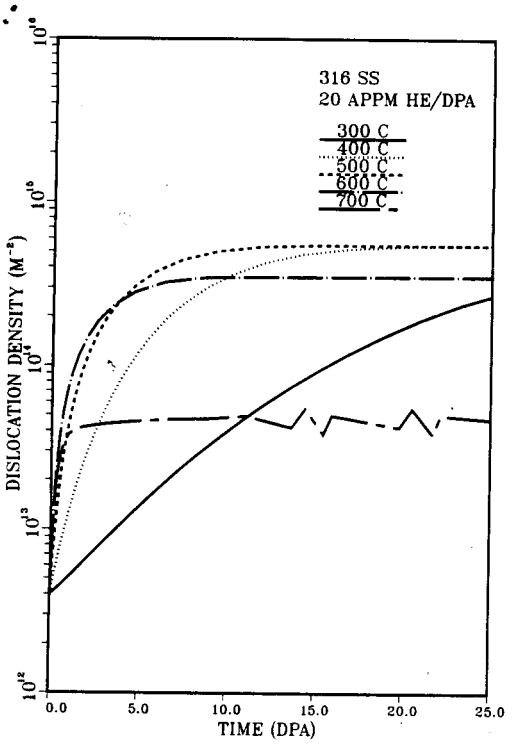

FIGURE 7. Dislocation Density Versus Dose for Solution-Annealed Type 316 Stainless Steel Irradiated in a Fusion Neutron Spectrum.

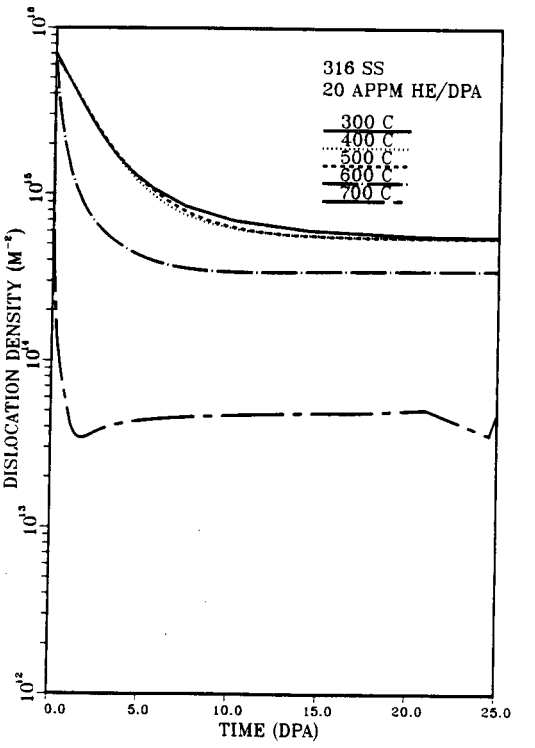

FIGURE 8. Same as in Fig. 7 but for a 20% CW 316 Stainless Steel.

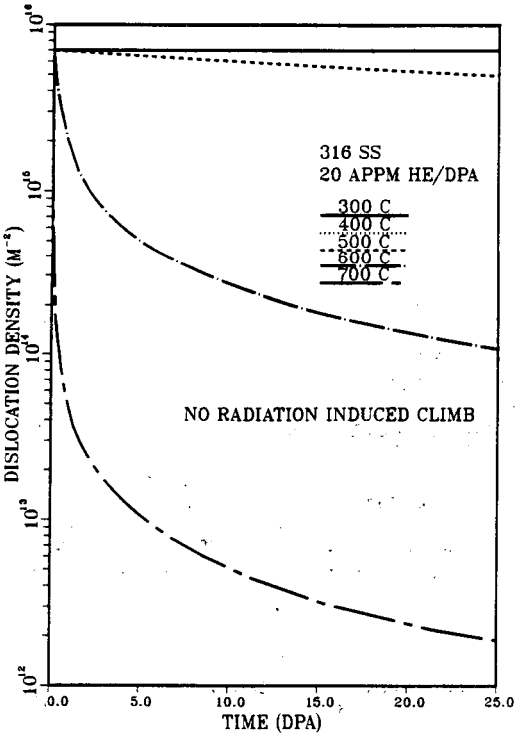

FIGURE 9. Recovery of Dislocation Density in Unirradiated 20% CW 316 SS Versus Time (unit of time expressed in dpa, 1 dpa = 10^6 seconds).

This value corresponds to the experimentally observed one in type 316 SS[1] irradiated in EBR-II. The chosen mesh length parameter ℓ implies a density of pinning centers of about 10^{19} m^{-3}.

The average point defect concentrations produced during the irradiations are evaluated with rate theory. A density of void embryos is assumed to exist from the beginning, i.e. after an irradiation dose of less than one dpa. The density of subcritical voids depends on the irradiation temperature, and its value is assumed to be equal to the terminal void number density reached at high fluences.[6] The stabilization and the early growth of these void embryos to their eventual critical size is controlled by the He/dpa ratio. Changing this ratio from 0.6 appm He/dpa, typical of breeder reactors, to 20 appm He/dpa, typical of fusion reactors, has however little effect on the dislocation evolution. This can be seen from the results shown in Figs. 5 through 8. The major difference between the two cases is that the saturation dislocation density at 700°C is higher for irradiations with 20 appm He/dpa than with 0.6 appm He/dpa. This is due to the fact that the climb rate of dislocations is somewhat higher when gas-driven swelling occurs.

The saturation dislocation density is found to be independent of temperature between 300°C and 500°C, but it begins to decrease with increasing temperature above about 550°C. The reason for this is the increasing contribution of thermally-induced climb as self-diffusion becomes important. The thermally-induced climb is of course also responsible for the high-temperature recovery of cold-worked materials. This can also be described by the present model by simply turning off the point defect production rate. Figure 9 gives the results for the thermal recovery of the dislocation structure in cold-worked 316 SS. For purposes of comparison with the previous figures, the time units of dpa have been retained; 1 dpa corresponds to 11.57 days of thermal annealing. It is seen that the dislocation density recovers to a value of 5×10^{13} m^{-2}, typical of solution-annealed material, within about 12 days at an annealing temperature of 700°C. Annealing also occurs at 600°C, but it becomes insignificant for temperatures at or below 500°C. These predictions are in agreement with observation, though no dislocation density measurements have actually been found in the literature.

The set of Figs. 10 to 13 shows the predictions for the dislocation evolution in the ferritic phase of a ferritic steel such as 2-1/4 Cr-1 Mo. Comparison with the results for type 316 SS shows that thermal recovery plays a role in ferritic steels already at a temperature of 500°C. In fact, an irradiaton temperature of 500°C in ferritic materials corresponds roughly to 650°C in austenitic steels, and this difference is due to the difference in the self-diffusion energies for the two steels. At irradiation temperatures of 400°C and below, the saturation densities become again independent of temperature. The rate of recovery is in fact very similar to the rate in 20% CW 316 SS. However, for annealed materials, the dislocation density increases at a lower rate at 400°C or below in the ferritic structure than in the austenitic structure at 500°C or below. The reason is to be found in the lower dislocation bias in ferritic versus austenitic alloys.

5.7 Discussion

The model developed for the evolution of the network dislocation density reproduces remarkably well the experimental observations. This is significant for two major reasons. First, the materials parameters required are very fundamental and reasonably well known in the case of austenitic stainless steels. Therefore, with the exception of the mesh length parameter ℓ and the bias variance ζ, no other parameters require adjustments. The value chosen for ℓ, namely 400 nm, is also reasonably close to the mesh length of bowed-out dislocations observed in micrographs of irradiated steels.

The second important implication of the successful model is that the complex dislocation structure and its evolution can in fact be understood in terms of two simple processes: the Bardeen-Herring process[3] of climb in a material with supersaturation of point defects; and the climb-induced annihilation of dislocation dipoles.[2]

The fact that dislocation loops have not been explicitly considered in the present model constitutes both one of its strengths and its weaknesses. Large loops increase their line length very much like a bowed-out dislocation segment, independent of the presence or absence of a stacking fault. When the stacking fault energy is low, as is the case in type 316 SS,[7] the stacking fault does not contribute significantly to the line tension and to the vacancy concentration C_v^b in Eq. (24). Therefore, dislocation loops and bowed-out edge dislocations can indeed be treated as one at higher temperatures.

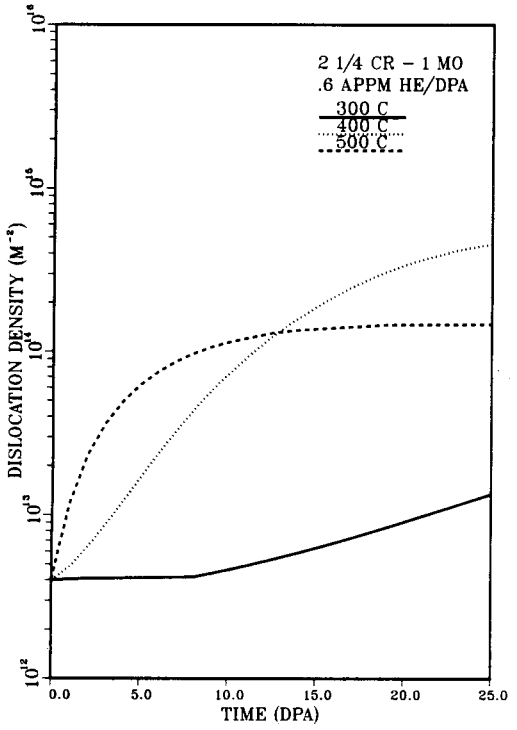

FIGURE 10. Dislocation Density Versus Dose in the Annealed Ferrite Phase of 2-1/4 Cr-1 Mo Steel Irradiated in a Breeder Neutron Spectrum.

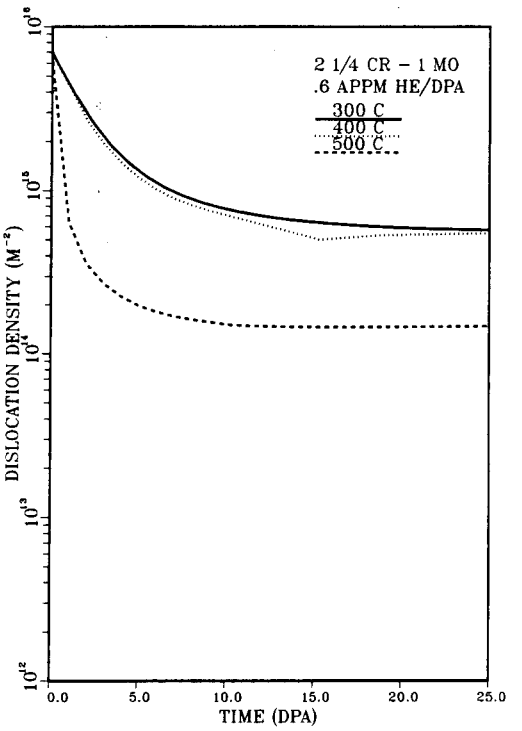

FIGURE 11. Same as Fig. 10 Except for a Heavily Dislocated Ferrite Phase.

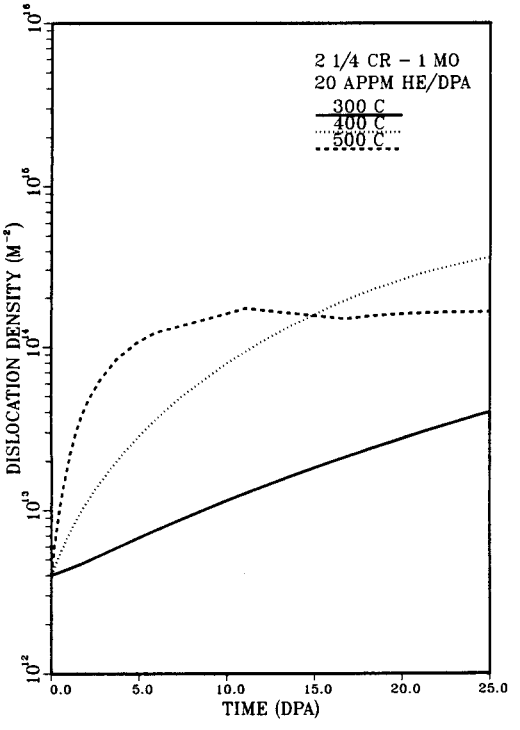

FIGURE 12. Dislocation Density Versus Dose in the Annealed Ferrite Phase of 2-1/4 Cr-1 Mo Steel Irradiated in a Fusion Neutron Spectrum.

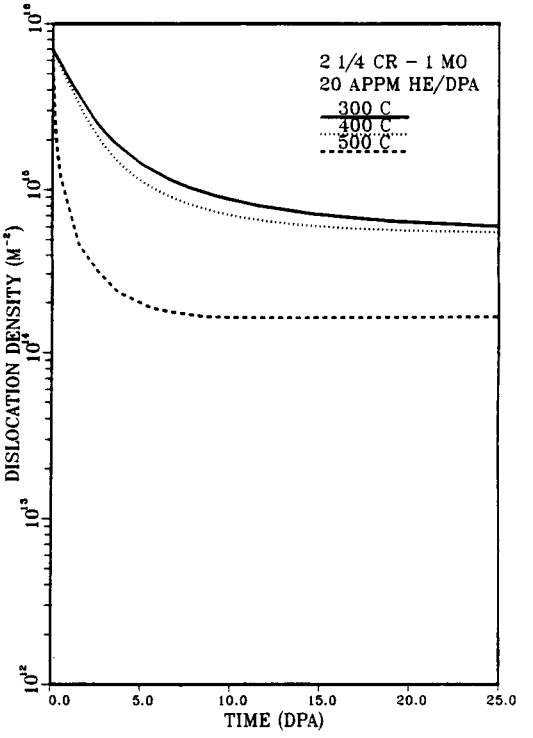

FIGURE 13. Same as Fig. 12 Except for a Heavily Dislocated Ferrite Phase.

However, when dislocation loops are small, it is no longer adequate to model them as edge dislocation segments. In this case, loops and network dislocations must be considered as different sinks, and their evolution will have to be described by different models. Based on experimental observation,[1] the loop density increases and their size decreases with decreasing irradiation temperature. It is therefore expected, that small dislocation loops are present in type 316 SS at an irradiation temperature of 300°C, and that these loops make a major contribution to the total dislocation density. Accordingly, the present model should not be applied to the entire dislocation structure in materials containing a high density of small dislocation loops.

6.0 References

1. F.A. Garner and W.G. Wolfer, ASTM STP 782 (1982) 1073.
2. F. Kroupa, Czech. J. Phys. B17 (1967) 220.
3. J.P. Hirth and J. Lothe, "Theory of Dislocations," McGraw-Hill, 1968, p. 565.
4. W.G. Wolfer, M. Ashkin and A. Boltax, ASTM STP (1975) 233.
5. J.J. Sniegowski and W.G. Wolfer, "Bias in Ferritic and Austenitic Alloys," DAFS Quarterly Progress Report DOE/ER-0046/13, Vol. 1, May 1983, p. 126.
6. B.B. Glasgow, A. Si-Ahmed, W.G. Wolfer and F.A. Garner, J. Nucl. Matls. 103 & 104 (1981) 981.
7. L.E. Murr, G.I. Wong and R.J. Horylev, Acta Met. 21 (1973) 595.

RELATIONS AMONG TENSILE TEST TEMPERATURE AND STRAIN RATE IN THE FRACTURE OF HELIUM-IRRADIATED TYPE 316 SS

R. D. Gerke and W. A. Jesser (University of Virginia)

1.0 Objective

The objective of this effort is to isolate the conditions under which temperature, strain rate and solute segregation become dominant in causing intergranular failure in irradiated austenitic stainless steel.

2.0 Summary

Helium irradiated microtensile specimens tensile tested under dual temperature test conditions failed intergranularly when a crack was initiated at 700°C but changed to transgranular failure when the temperature was lowered to 550°C. This suggests that helium and/or impurity atoms did not segregate at 700°C in such a manner as to permit intergranular failure at the lower temperature. Helium embrittlement seems to be strain rate and temperature dependent, and does not seem to be associated with bubbles on grain boundaries or grain boundary sliding. It seems that when the correct temperature and strain rate conditions are met, dislocations act to bring atomistic or submicroscopic clusters of helium to grain boundaries in sufficient numbers to produce the conditions for intergranular failure.

3.0 Program

Title: Simulating the CTR Environment in the HVEM
Principal Investigators: W. A. Jesser and R. A. Johnson
Affiliation: University of Virginia

4.0 Relevant DAFS Program Plan Task/Subtask

Subtask 11.C.13 Effects of Helium and Displacements on Crack Initiation and Propagation.

5.0 Accomplishments and Status

5.1 Introduction

The mechanism of helium embrittlement is an important area of investigation in the fusion community. Its effect on candidate first wall materials is of primary concern. There are many helium embrittlement theories currently being investigated today. Perhaps one of the most popular theories involves a helium bubble model. Helium embrittlement is thought to be caused by stress induced growth of helium filled cavities or bubbles on grain boundaries. Final fracture of the grain boundaries is thought to occur by the coalescence of these cavities [1] or by propagating a wedge crack through them [2]. Helium embrittlement is studied by direct injection of helium ions into a specimen and by neutron irradiation which produces (n,α) transmutational helium in specimens. A wide range of helium concentrations is possible, however, intergranular failure at high temperature can occur at helium concentrations as low as 0.1 appm (atomic parts per million) [3]. Helium seems to have a pronounced effect on high temperature fracture. At 700°C it has been observed that a significant amount of embrittling occurred in creep tested DIN 1.4970 stainless steel with as little as 5 appm helium [4]. At test temperatures below 700°C ($T < \sim 500$°C) type 316 stainless steel specimens containing large amounts of helium, irradiated with helium ions to an estimated 10,000 appm helium and higher, failed in a purely transgranular mode [5]. Many helium embrittlement theories treat the amount of helium filled cavities on the grain boundaries as a criterion for brittle failure. However, the presence of large amounts of helium does not seem to be sufficient by itself to cause embrittlement. Typical parameters that are investigated such as the grain boundary area fractional coverage by helium bubbles, α_B, [4,6,7] and pressure in grain boundary bubbles [4,6-8] may not be important in determining a mechanism for helium embrittlement. Grain boundary bubble spacing has been shown to be an important parameter when plotted against tensile test temperature [6]. There is a temperature dependent region for large bubble spacings (and diameters) and a temperature independent region for small (and non visible) bubbles and spacings which define the onset of intergranular failure. These results are plotted as a fracture map of cavity spacing versus tensile test temperature and produce a J-shaped boundary between a transgranular fracture region of the map and an intergranular region. This J-curve together with the lack

of a critical value of α_R being found seem to preclude any further consideration of a model of helium embrittlement based on a weakening of grain boundaries due to the presence of helium bubbles.

There is some experimental evidence of high temperature helium assisted solute segregation with neutron irradiated specimens. Highly embrittling phospherous and sulfur impurity atoms are suspected to accumulate at the intergranular fracture surface. Interaction with excess nickel and chromium is also known to occur with impurity segregation to grain boundaries. If this is to occur then the possibility exists for an embrittlement model of impurity segregation driven by the presence of helium. The presence of helium in specimens alters the fracture behavior at high temperatures and under appropriate microstructural conditions alters the failure mode at low temperatures (even room temperature) [6].

Another important variable which assists in the promotion of intergranular fracture is strain rate. At intermediate strain rates, tensile tests reveal fracture behavior as depicted by the 'J' curve. However, austenitic stainless steels containing ~20 appm helium tensile tested at slow strain rates and temperatures of ~700°C failed intergranularly while similar specimens tested at fast strain rates failed transgranularly [4,9]. Bubble dragging by moving dislocations have been invoked to explain these results. The presence of visible helium bubbles on grain boundaries existing due to thermal treatment or by plastic deformation does not seem to be sufficient cause for helium embrittlement. A unified helium embrittlement mechanism has not emerged due to discrepencies between experiment and theory. It does seem likely that the embrittlement is associated with helium increasing its presence along grain boundaries under the influence of applied stress. Temperature and strain rate have an effect in the temperature dependent region of the 'J' curve. Impurity atoms may also have an effect at high temperatures. It is therefore important to isolate conditions under which each contributing factor becomes dominant.

Austenitic stainless steel specimens were helium ion irradiated and tensile tested in-situ in a high voltage electron microscope (HVEM) at high temperatures. Intergranular fracture was investigated with particular reference to its dependence on strain rate and temperature. A possible mechanism relating fracture behavior in the temperature dependent and independent regions of the 'J' curve is suggested. Intergranular fracture was investigated with particular reference to its dependence on strain rate and temperature.

5.2 Experimental Results and Discussion

5.2.1 Experimental Procedure

As received AISI Type 316 stainless steel foil, 40μm thick, was punched into rectangular microtensile specimens 12.5 mm x 2.5 mm in size. Next the central portion of each specimen was electropolished to perforation in a 90% acetic acid-10% percholoric acid solution at room temperature. Specimens were then ion irradiated in an HVEM-ion accelerator facility [10]. Fluences of 9.4×10^{20} ions m^{-2}(flux = 3.9×10^{18} ions $m^{-2}s^{-1}$) were produced using 80 keV helium ions and irradiation temperatures were estimated to be ~300°C.

The effective depth of penetration of the helium ions in the type 316 stainless steel at this facility has been calculated by Horton [11] using the computer code E-DEP-1 of Manning and Mueller [12] which can calculate the displacements per atom (dpa) as a function of depth for a given incident species, energy and target material. Energy deposition as a function of depth and a projected range beneath the front surface for ion irradiations is calculated. Unlike the uniform displacement curve for neutrons, the displacement curve for ions exhibits a sharp maxima at a certain foil thickness and then rapidly tails off as the foil thickness continues to increase, due to the fact that 80 keV neutrons can produce displacement damage much farther than helium ions of the same energy. Thus at a fluence of 9.4×10^{20} ions m^{-2}(flux ~ 3.9×10^{18} ions $m^{-2}sec^{-1}$) the maximum number of displacements per atom is about 2 dpa at a 230 nm foil depth. Because the two foil surfaces act as efficient sinks for the oncoming ions, the helium deposition is assumed to be a gaussion distribution with a calculated projected helium range of 281.6 nm and a standard deviation of 77.9 nm for 80 keV helium [5]. It has been demonstrated that helium has an effect on the fracture mode at a much greater depth than the calculated penetration depth [11,13]. To increase the effect of the range of 80 keV helium ions in 316 stainless steel, irradiations were conducted on both sides of the foil microspecimens. This procedure insured that helium had an effect on a wider range of specimen thickness as the propagating crack, initiated at the electropolished perforation, left the electron transparent region and entered 'thicker' regions of the specimen. In addition, specimens were given a post-irradiation anneal in a vacuum (10^{-4}Pa or better) at 900°C to coarsen the microstructural features. Tensile testing in the HVEM was carried out in a hydraulically operated single tilt quantitative load-elongation tensile stage capable of heating the specimen to about 700°C [14]. Specimens were tensile tested to failure at temperatures between about 550°-700°C and at strain rates between ~10^{-4} sec $^{-1}$and ~1 sec^{-1}. During tensile testing HVEM observations were recorded on still micrographs in order to obtain the type of failure. Ductility was determined primarily by the nature of crack propagation through a specimen (in slow strain rate experiments). If most of the cracks propagated transgranularly then the specimen was said to fail in a ductile (T) mode. When grain boundary failure was observed (in the HVEM) the specimen was said to fail in a brittle intergranular (I) mode. Mixed mode failure (I + T) was also observed. Fracture surfaces observed in a SEM were also used to determine mode of failure in fast strain rate tensile tests (~1 sec^{-1}) where HVEM observations were not practical. In all experiments, where HVEM and SEM observations were available, both

techniques agreed with one another with respect to fracture mode.

5.2.2 Dual Temperature Tensile Testing

Specimens were tensile tested under two temperature regimes at a strain rate of ~10^{-4} sec^{-1}. The dual temperature tensile tests were initiated at 700°C. The specimen was strained until a crack had propagated some distance (usually~70 μm) corresponding to a foil thickness of ~30μm determined from the electropolished thickness profile [13] and then the straining was stopped. In every case the mode of failure was intergranular in the initial phase of the tensile test.

The thickness of the foil at this point in the tensile test is not so thick that the central portion of the foil (not penetrated by helium ions during irradiation) dominates the failure behavior of the specimen when tensile testing is resumed. Specimens tensile tested at high temperatures previously at this facility, irradiated on one side only, have exhibited brittle behavior at much greater thicknesses than studied here [11,13]. It is expected that helium ion irradiation conducted on both sides of the foils will eliminate the possibility that the non penetrated regions will dominate the failure behavior as discussed earlier. The straining was then resumed after the specimen temperature was lowered to 550°C. A temperature such as 550°C (or lower) was desired because ductile failure has been shown to occur at this temperature over a wide range of microstructures in irradiated austenitic stainless steels [6]. A mixed mode type of failure occurs between 550° and 700°C (i.e. ~550°C is the highest temperature for ductile type failure to occur). When the tensile test was resumed, the crack, which previously was propagating intergranularly always changed its propagation mode to a primarily ductile mode. Figure 1 is an HVEM micrograph montage showing

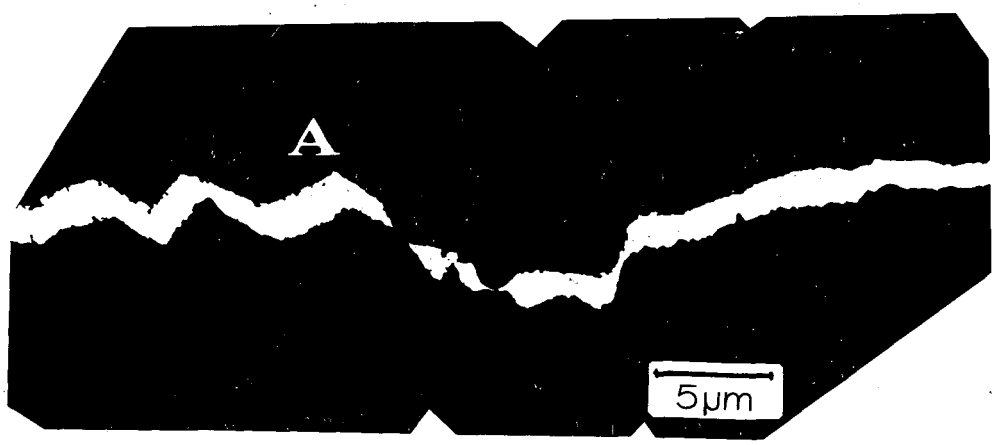

FIGURE 1. HVEM Micrograph Montage Showing a Change in Fracture Mode from Intergranular at 700°C to Transgranular at 550°C in a Dual Temperature Tensile Test. Intergranular Failure is Characterized by Sharp Changes in Crack Direction while Transgranular Failure is Shown as Smooth Crack Propagation. Point A Denote Where the Temperature Was Changed.

how the main microcrack, initiated in the electron transparent region, propagated in an intergranular mode at 700°C changed to a transgranular mode of failure when the temperature was lowered to 500°C. The failure mode tended to change almost immediately when the tensile test was resumed at the lower temperature. So, initiating brittle type fracture at a high temperature is not sufficient to permit a continuation of intergranular type fracture when the temperature is lowered (to an appropriate temperature known to exhibit transgranular failure).

5.2.3 The Effect of Strain Rate

To verify the effect of strain rate on the failure mode in microtensile specimens of austenitic stainless steels, tensile tests were conducted at two different strain rates on specimens at ~610°C where normally a mixed I & T failure mode is observed. Specimens tested at slow strain rates (~10^{-4} sec^{-1}) failed in a mixed mode while specimens tested at fast strain rates (~1 sec^{-1}) failed in a ductile (T) mode. This experiment verified similar results found by other researchers on bulk-like specimens which showed that strain rates close to the creep regime enhance the chance of brittle failure while fast strain rates caused ductile failure [4,9]. An effort to relate the effect of strain rate and tensile test temperature has been made with the suggestion of a possible mechanism to explain helium embrittlement.

5.2.4 Microstructural Aspects of Helium Embrittlement

Helium embrittlement at elevated temperatures can occur at helium concentrations of less than one appm [3] but its effect on ductility and % intergranular fracture saturates between 15 and 20 appm [4]. However,

large concentrations of helium (above 100 appm) is not a sufficient condition for intergranular failure at test temperatures below about 600°C [15,16]. Clearly, the presence of large amounts of helium is not sufficient by itself to cause embrittlement. The presence of large grain boundary bubbles has been suggested as the cause for high temperature embrittlement through grain boundary weakening [17]. The fraction of grain boundary area occupied by bubbles, α_R, has been proposed as a criterian for intergranular failure by Trinkaus and Ullmair [7]. They stated that the more fractional area occupied by bubbles, the weaker the grain boundary, and the more susceptible to intergranular failure. A critical value of $\alpha_R = 0.1$ was assigned for brittle failure. However, Bennetch and Jesser showed strong evidence that α_R is not a critical parameter for the onset of brittle fracture in neutron and helium ion irradiated austenitic stainless steel [6]. In certain cases, helium filled cavities have served to increase specimen ductility [16,18]. Therefore it can be assumed that only the presence of helium filled cavities, at any temperature, occupying area on grain boundaries of irradiated specimens is not sufficient to cause intergranular failure.

Helium embrittlement has been shown to be a thermally activated process in austenitic stainless steel [6]. A graph of edge to edge (grain boundary) bubble spacing, L, plotted versus tensile test temperature reveals a fracture 'map' indicating regions of transgranular and intergranular failure separated by a J-shaped boundary of mixed mode failure, as schematically shown in Figure 2. There are two distinctly different

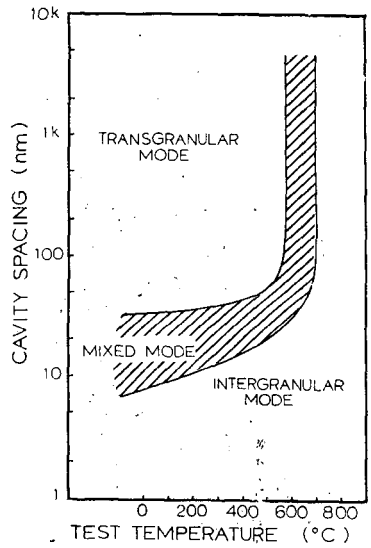

FIGURE 2. Schematic Plot of Cavity Spacing versus Tensile Test Temperature for Neutron and Helium Irradiated Austenitic Stainless Steel (After Bennetch et al [6]). Notice that Transgranular Failure is Separated from Intergranular Failure by a 'J' Shaped Region of Mixed Mode Failure.

boundaries of the L versus T graph, one temperature independent (< ~550°C) and one temperature dependent (> ~550°C). This result suggests that two processes of helium embrittlement occur in austenitic steels.

At temperatures below ~550°C, the parameters L, d(bubble diameter) and possibly helium bubble pressure seem to be significant [6]. A plot of d versus T closely parallels the 'J' shape of Figure 2 since d is probably not independent of L. There are critical values of $L <\sim 30$ nm and $d <\sim 4$ nm for which the onset of brittle fracture occurs. This would suggest a bubble hardening mechanism in this temperature range where a high density of small (possibly over pressurized) bubbles provide obstacles to dislocations moving through the grain interior. A high density of small dislocation loops can increase the yield stress by a factor inversely proportional to the loop spacing [19,20]. Also, a given density of small bubbles may increase the yield stress by a greater amount than an equal density of dislocation loops [21]. In addition, untrapped helium that diffuses to grain boundaries rather than escaping to the surface during irradiation may cause grain boundary bubbles to be more overpressurized than matrix bubbles, thus weakening the grain boundary relative to the hardened matrix. The possibility for brittle fracture may therefore exist below ~550°C. At temperatures below ~550°C cleavage cracks dominated the transgranular failure mode which suggested that extremely close packed small bubbles can embrittle solids by acting as effective dislocation obstacles [6]. In the temperature dependent region of the 'J' curve helium embrittlement was shown to be a function of only temperature for cavity spacings ranging over two orders of magnitude (~30 nm to > 3000 nm). Temperatures below 550°C resulted in transgranular failure, and mixed mode (I & T) failure occurred between 550°C and 700°C while an intergranular mode of failure occurred for all test temperatures above 700°C. It is an aim of this paper to relate the two regions of behavior, temperature independent and temperature dependent, where fracture behavior is governed primarily by small (sometimes non visible) bubbles and large bubbles, respectively. There are numerous examples of intergranular failure above and below 550°C occurring without visible helium bubbles (less than ~2 nmm) [4,9,22-24]. Sagües et al [4] observed that specimens implanted with helium and creep tested at 700°C failed intergranularly but did not show visible evidence of helium bubbles. This suggests that high temperature helium embrittlement may involve helium in solution acting as a mechanism causing intergranular failure, possibly existing in

small clusters or even atomistic helium. Other evidence that small clusters or atomistic helium contribute to helium embrittlement exist. Room temperature tensile tests of specimens containing He^3 fractured intergranularly [15] and specimens irradiated with He^4 ions fractured in a mixed mode at room temperature [23] and intergranularly at 500°C [24]. These results are consistent with the 'J' curve because they correspond to the bottom of the 'J', where critical values of cavity spacing, L, and bubble diameter, d, below 550°C are ~30 nm and ~4 nm, respectively. These values are thresholds below which the onset of brittle fracture occurs [6]. Since small clusters of atomistic helium migration is currently impossible to observe directly, means of indirect measuring must be used. Clausing and Bloom fractured neutron irradiated type 304 stainless steel specimens containing 28 appm helium with no visible bubbles (as shown by TEM) in an Auger spectroscopy system and found intergranular failure to occur [22]. Helium release was measured by a residual gas analyzer. They concluded that the helium segregated to the boundaries as a partial monolayer or in bubbles less than 2 nm in diameter (corresponding to a possible bubble spacing of ~10 nm and α_R ~0.045). It was also concluded that the helium may not be uniformly distributed but concentrated in regions of "bad fit." This result suggests that the helium concentration on the grain boundaries is higher than the matrix existing in small clusters rather than in large bubbles. In the temperature dependent region of the 'J' curve where intergranular failure occurs at high temperature and in the presence of large (visible) bubbles it may be possible that during the plastic deformation process trapped helium is released from the traps and either migrates or more likely is carried by dislocations to the grain boundary to reside there as dissolved helium or very small helium point defect clusters. This lattice helium, possibly distributed in regions of "bad fit" as suggested by Clausing and Bloom [22], then acts to reduce specimen ductility and promote intergranular failure. In order for these processes to occur, certain conditions must be present. Obviously high temperature and an applied stress must exist for intergranular failure to occur. The manner in which the stress is applied at high temperature may be important.

5.2.5 Contributions to Embrittlement Due to Stress and Strain

Applied stress to irradiated specimens is very important to the migration of helium into bubbles. Sagües observed that specimens creep tested at 800°C exhibited large bubbles (several hundred angstroms in diameter) on grain boundaries, precipitates and on grain boundary-precipitate interfaces while similar specimens not stressed showed very small helium bubbles [4]. Kramer et al observed that 2% strain in type 304 stainless steel was required to precipitate bubbles (10-20 nm in diameter) at 760°C at a concentration of 30 appm helium while in unstrained samples no bubbles were observed until after a four hour anneal at 815°C [3]. Both of these results are consistent with the possibility of dislocation assisted helium migration.

More important than simply a stress assisted helium embrittlement is the additional variable strain rate. Experiments involving strain rate as a variable at high temperatures have shown that slow strain rate tensile tests on irradiated austenitic stainless steel fracture intergranularly while a high strain rate test reveals transgranular failure [4,9]. Matsumoto et al showed the effect of strain rate on tensile properties, tensile strength, yield stress and elongation, in type 316 stainless steel irradiated up to 20 appm helium tested at 700°C [9]. In all cases the effect of irradiation was evident below strain rates of $4.2 \times 10^{-3} s^{-1}$, but no irradiation effect was discernible when the strain rate exceeded $4.2 \times 10^{-2} s^{-1}$. Also, the slower the strain rate the greater the effect of irradiation. Of more importance to this investigation, they showed by use of TEM that at slow strain rates ($\dot{\varepsilon} = 4.2 \times 10^{-4} s^{-1}$) intergranular failure was characterized by helium filled cavities (bubbles) located on grain boundaries and high strain rate tensile tests ($\dot{\varepsilon} = 4.2 \times 10^{-1} s^{-1}$) transgranular failure revealed bubbles strung along, but not on, grain boundaries. The bubbles in the later case were reported to be distinctly smaller both in size and number than in the case of slow straining despite the greater applied stress and strain. The proposed mechanism for intergranular failure was suggested to be associated with moving dislocations sweeping the bubbles toward the grain boundaries. These results agreed with Beeré who observed 100-200 Å bubbles dragged by dislocations in helium irradiated copper during recrystallization [25]. However, this does not explain how the two regions of behavior in the 'J' curve are related, because visible bubbles are not evident in the temperature independent region (bottom of 'J') and yet intergranular failure occurs. The foil microtensile specimens tested in this investigation under rapid and slow strain rates were tested at 610°C, a temperature where mixed mode (I + T) fracture behavior is shown to occur (Figure 2). The fact that the slow strain rate exhibited a mixed mode type of failure and changed to transgranular failure at fast strain rates supports previous work but also suggests that there is a temperature-strain rate relationship. At an intermediate temperature, between 550°C and 700°C for austenitic stainless steels as suggested by Figure 2, mixed mode failure is shown to occur for normal tensile test strain rates. It has been shown here that transgranular failure occurred under the same controlled conditions with only a change in strain rate. It is anticipated that an all intergranular failure is possible at this intermediate temperature if the applied strain rate is slow enough, perhaps in the creep regime ($\sim 10^{-6} s^{-1}$). Also, at a fixed strain rate it seems that if temperature is varied appropriately all three modes of failure could be observed. Figure 2 suggests this for specimens tensile tested under typical tensile test strain rates. The boundaries of the 'J' curve are suspected to shift their relative position with respect to temperature if drastically different strain rates were applied. For example, the 'J' may shift to lower temperatures for specimens pulled at creep strain rates. Conversely, when the applied strain rate is rapid the 'J' would be shifted to higher temperatures.

It seems from the above discussion that helium embrittlement is caused by more than just applying a high temperature. When helium is brought to the grain boundary by diffusion it appears that large bubbles form

and are not active in promoting intergranular failure. This is supported by evidence reported earlier in this section showing that large grain boundary bubbles can promote ductile failure. It seems that the rate of (plastic) deformation is very important in causing embrittlement. The observation made by other researchers that dislocations drag or sweep helium bubbles to grain boundaries and therefore cause intergranular failure, if the strain rate is slow enough for the bubbles to keep up with the dislocations, seems plausible at this time. However, it is not believed that bubbles are the cause but rather helium in small point defect clusters or atomistic helium as proposed by Clausing and Bloom [22]. It seems that if trapped helium atoms are released from their traps at an appropriate temperature and strain rate they can migrate to grain boundaries assisted by moving dislocations and reside there as lattice helium or submicroscopic clusters. The dissolved helium, possibly existing as a monolayer, can there participate in the intergranular process. It is not likely that de-cohesion is acting as the mechanism for the embrittlement because specimens tensile tested at this facility irradiated to over 10,000 appm helium (and fractured below 550°C) failed transgranularly [5]. In such high helium experiments, one might expect to exceed the critical concentration of lattice helium for intergranular failure. So it may be possible that moving dislocations at high temperature are necessary to set up a condition in the temperature dependent region of the 'J' curve (large helium bubbles) similar to the condition present in the temperature independent region (bottom of 'J') where non visible bubbles exist. Without dislocations the helium remains trapped and resides in bubbles which tend to be benign in the fracture process.

5.2.6 Effects of Segregation of Alloying and Impurity Elements

Alloying and undesirable impurity elements can segregate to solid-solid interfaces such as grain boundaries, phase boundaries and stacking faults. Many structural properties are effected due to changes in interface chemistry caused by the segregation. The major problems caused by grain boundary segregation of trace elements and impurities is their large effect on the loss of ductility and the fracture mode over various temperatures, usually high temperature service. Metalloid impurities such as S, Sn, Sb and As are known to reduce elevated temperature ductility and induce intergranular failure in nickel and nickel based alloys. In each case, these trace elements are usually associated with extensive grain boundary cavitation and cracking. A number of possible mechanisms have been proposed including trace element segregation to surfaces and grain boundaries to affect their 1) energies 2) diffusivities, and 3) vacancy source - sink behavior [26]. The sliding characteristics of the grain boundaries are likely to be influenced by trace impurity segregation to them. However, Gerke et al. have shown that grain boundary sliding is not a dominant process in the fracture of neutron and helium irradiated austenitic stainless steels [27]. Embrittled irradiated specimens which failed intergranularly at elevated tensile test temperatures failed primarily by Mode I cracking. Therefore solute, impurity and helium atoms are not considered to promote excessive grain boundary sliding as a major mechanism in helium embrittlement. It has been shown by White and Padgett that impurities may not be the only concern in the intergranular failure of unirradiated nickel at 600°C [26]. It was found that strain rate played an important role in whether the specimens failed intergranularly or transgranularly. Ductility in Ni-1% Sb specimens tensile tested at 600°C increased with increasing strain rate suggesting a temperature-strain rate relationship. There is some experimental evidence of high temperature helium assisted solute segregation to grain boundaries with EBR-II samples. Sklad et al. found an excess of P and S impurity atoms, in addition to a Ni excess and Cr depletion at the intergranular fracture surface of a PE-16 steel alloy tested at ~575°C containing ~8 appm helium [27]. In contrast, Horton found a large Cr excess (with respect to Ni and Fe) on the brittle part of the fracture surface of type 316 stainless steel, He ion irradiated > 20,000 appm and tested at 600°C [11]. The results of these cases hint at the possibility of a helium driven solute segregation and embrittlement. To see how feasible this idea is dual temperature tensile tests were conducted and showed that even though intergranular failure was initiated at 700°C, the conditions set up at the high temperature were not sufficient to cause the intergranular failure at a lower test temperature of 550°C. The two temperatures were chosen as the closest temperature range available representing two distinct failure modes (i.e. perturbing the system as little as possible).

5.3 Conclusions

It seems that it is not possible to set up conditions for intergranular failure at high temperatures (i.e. applied stress, appropriate temperature, strain rate and helium and impurity content) and continue the brittle failure in a temperature regime characteristic of ductile behavior. This suggests that the helium and/or impurity atoms did not segregate at 700°C in such a manner as to permit intergranular failure at the lower temperature. Even though this result suggests that segregation of helium and/or impurity atoms to the grain boundary is not a mechansim for helium embrittlement, nevertheless it has not been completely ruled out. Instead, we feel that there is dynamic condition set up between the strain rate (dislocation velocity) and temperature (helium mobility) which causes the fracture process to occur with the possible assistance of dislocations to actively promote segregation in the intergranular failure process. In other words, it seems plausible that when the correct temperature and strain rate conditions are met, the dislocations act to bring essentially atomistic or submicroscopic clusters of helium to the grain boundary in sufficient numbers to produce the conditions for intergranular failure. When these temperature and strain rate conditions are not met, the helium aggregate in bubbles or is not properly distributed at the grain boundary.

6.0 References

1. D. R. Harries, Journal of Nuclear Materials, 82, 1979, p. 2.

2. J. S. Waddington, Metal Science Journal, 1, 1967, p. 156.

3. D. Kramer, H.R. Brager, C.G. Rhodes, and A.G. Dard, Journal of Nuclear Materials, 25, 1968, p. 121.

4. A.A. Sagües, H. Schroeder, W. Kesternich, and H. Ullmaier, Journal of Nuclear Materials, 78, 1978, p. 289.

5. J.I. Bennetch, Microstructural Aspects of Helium Embrittlement in Stainless Steel, Doctoral Dissertation, University of Virginia, Charlottesville, Virginia, 1981.

6. J.I. Bennetch and W.A. Jesser, Journal of Nuclear Materials, 103 and 104, 1981, p. 809.

7. H. Trinkhaus and H. Ullmaier, Journal of Nuclear Materials, 85 and 86, 1979, p. 823.

8. D. Hull and D.E. Rimmer, Philosophical Magazine, 4, 1969, p. 673.

9. K. Matsumoto, T. Katooka, M. Terasawa, M. Shimada, S. Nakahigashi, H. Sakairi, and E. Yagi, Journal of Nuclear Materials, 67, 1977, p. 97.

10. W.A. Jesser, J.A. Horton, and L.L. Scribner, Radiation Effects, 29, 1976, p. 79.

11. J. A. Horton, HVEM Studies of Helium Embrittlement in Stainless Steel, Doctoral Dissertation, Univ. of Virginia, Charlottesville, VA, 1980.

12. I. Manning, G.P. Mueller, Comp. Phys. Comm., 7, 1974, 85.

13. T. Hanamura, The Effect of Neutron and He-Irradiation on the Crack Modes of Type 316 Stainless Steel, Doctoral Dissertation, University of Virginia, Charlottesville, Virginia, 1983.

14. R.D. Gerke and W. A. Jesser, Journal of Nuclear Materials, 117, 1983, p. 320.

15. D.E. Rawl, Jr., G.R. Caskey, Jr., and J. A. Donavan, Journal of Metals, 31, 1979, p. 124.

16. J.A. Horton, J.I. Bennetch, and W.A. Jesser, Journal of Nuclear Materials, 85 and 86, 1979, p. 829.

17. R.S. Barnes, Nature, 206, 1965, p. 1307.

18. I.O. Smith, B. Russell, Journal of Nuclear Materials, 37, 1970, p. 96.

19. A.W. Thompson, "Mechanical Behavior of Face-Centered Cubic Metals Containing Helium," Materials Science and Engineering, 21, 1975, p. 41.

20. P.J. Maziasz, "Precipitation Response of Austenitic Stainless Steel to Simulated Fusion Irradiation," The Metal Science of Stainless Steels, The Metallurgical Society of AIME, New York, 1979, p. 160.

21. E.E. Bloom, and Stiegler, Nuclear Technology, 17, 1972, p. 24.

22. R.E. Clausing and E.E. Bloom, Grain Boundaries in Engineering Materials, Claitor's Publishing Division 1975, 491.

23. J.I. Bennetch and W.W. Jesser, "Room Temperature Helium Embrittlement in 316 Type Stainless Steel," DAFS Quarterly Report DOE/ER-0046/3, Oct. 1980.

24. J.I. Bennetch and W.A. Jesser, "Microstructural Aspects of Helium Embrittlement," DAFS Quarterly Report DOE/ER-0046/4, Jan. 1981.

25. W. Beere´, Scripta Metallurgica, 9, No. 7, 1975, p. 999.

26. C.L. White and R.A. Padgett, "Trace Element Effects in Creep Cavitation," Metals and Ceramics Division Materials Science Program Annual Progress Report, ORNL-5672, June 1980, p. 96.

27. R.D. Gerke, T.Hanamura, and W.A. Jesser, Journal of Nuclear Materials, 1984, in press.

28. P.S. Sklad, R.E. Clausing, and E.E. Bloom, "Effects of Neutron Irradiation on Microstructure and Mechanical Properties of Nimonic PE 16," Radiation Effects on Microstructure and Properties of Metals STP 611 (American Society for Testing and Materials), 1976.

EFFECTIVE THERMOPHYSICAL AND ELASTIC PROPERTIES OF MATERIALS WITH VOIDS

W. G. Wolfer (University of Wisconsin) and F. A. Garner (Hanford Engineering Development Laboratory)

1.0 Objective

The object of this effort is to provide equations that describe the effect of void swelling on basic physical properties such as elastic properties and thermal and electrical conductivity.

2.0 Summary

The current theories describing the influence of void swelling on conductive and elastic properties have been reviewed and compared with the limited data available. Judgements have been made as to the most appropriate equations to describe the influence of voidage on thermal and electrical conductivity, and also the shear, bulk and Young's moduli and Poisson's ratio. These equations will be included in the Fusion Materials Handbook.

3.0 Program

Title: Irradiation Effects Analysis (AKJ)
Principle Investigator: D. G. Doran
Affiliation: Hanford Engineering Development Laboratory

4.0 Relevant DAFS Program Plan Task/Subtask

II.C.16 Composite Correlation Models and Experiments

5.0 Accomplishments and Status

5.1 Introduction

The extensive void swelling observed in austenitic stainless steels after high fluence irradiation leads to significant changes in basic properties, such as thermal conductivity and the elastic properties. These changes have not attracted much attention in contrast to other changes in mechanical properties related to plastic deformation and fracture. Whereas the latter properties are often strongly affected by low fluence irradiation, the former properties are changed only when the void volume fraction becomes large. This difference in behavior arises from the following considerations.

Plastic properties such as yield strength are determined by the interaction of dislocations with atomistic defects created by the radiation damage. In contrast, elastic properties are little influenced by the atomistic defects, and they are simply a property of the crystal structure. The effective elastic properties of a composite material are then functions of the elastic properties of each phase present in the composite. A similar argument can be made for the effective thermal and electrical conductivities at high temperatures. Here, the conductivity at high temperature of each phase present is nearly independent of the atomistic defect structure in each phase, since the conductivities are determined mainly by the vibrational properties of the lattice. However, it must be noted that this is no longer true for cryogenic temperatures. Here, both the thermal and the electrical conductivities are determined to a large extent by the concentration of atomic defects in each phase. For this case, the effective conductivities can no longer be expressed only in terms of the conductivities for each of the phases present. The results presented below are therefore valid only at elevated temperatures, i.e., at or above room temperature.

5.2 Thermal Conductivity

In order to obtain the effective thermal conductivity K* of a material containing a volume fraction $\Lambda = \Delta V/V$ of spherical voids we employ a model referred to as the composite sphere assemblage. Here, the material is thought of as being composed of spherical cells, each containing at its center a void. The individual cell radius, b, and its void radius, a, are selected such that

$$\left(\frac{a}{b}\right)^3 = \frac{\Delta V}{V} = \Lambda \tag{1}$$

To fill the space completely with cells requires that the spaces between the touching larger cells be filled with cells of even smaller radius.

We now select an arbitrary cell and consider it to be embedded in an effective medium whose thermal conductivity is denoted by K*. Sufficiently far from this generic cell the temperature distribution is assumed to be a linear function of $z = r\cos\theta$, where r is the radius from the origin of the generic cell. We wish now to evaluate the disturbance of this linear temperature distribution by the generic cell. Within the cell, the temperature is written as

$$T(r,\theta) = \frac{\Delta T}{\Delta Z} r\cos\theta + T_o(r,\theta) \tag{2}$$

and for the surrounding effective medium, we write,

$$T(r,\theta) = \frac{\Delta T}{\Delta Z} r\cos\theta + T^*(r,\theta) \tag{3}$$

The temperature disturbances T_o and T* are now obtained by solving the equation $\nabla^2 T = 0$ in each region.

On the void surface $\partial T/\partial r = 0$, so that

$$\left.\frac{\partial T^*}{\partial r}\right]_{r=a} = -\frac{\Delta T}{\Delta Z}\cos\theta \tag{4}$$

On the interface between the generic cell and the surrounding effective medium

$$T_o(b,\theta) = T^*(b,\theta) \tag{5}$$

and

$$K_o \frac{\Delta T}{\Delta Z}\cos\theta + K_o \left.\frac{\partial T_o}{\partial r}\right]_{r=b} = K^* \frac{\Delta T}{\Delta Z}\cos\theta + K^* \left.\frac{\partial T^*}{\partial r}\right]_{r=b} \tag{6}$$

where K_o is the conductivity of unvoided material. The solution for $T_o(r,\theta)$ in the cell is given by

$$T_o(r,\theta) = (A\cos\theta)\, r^{-1} + B\, r\cos\theta \tag{7}$$

whereas the temperature disturbance in the surrounding medium is given by

$$T^*(r,\theta) = (C\cos\theta)\, r^{-1} \tag{8}$$

Use of the boundary conditions (4) to (6) gives the following equations to determine the constants A, B, and C.

$$-2A/a^2 + B = -\frac{\Delta T}{\Delta Z} \tag{9}$$

$$A + b^3 B = C \tag{10}$$

$$-2K_o A/b^3 + K_o B + K_o \frac{\Delta T}{\Delta Z} = -2K^* C/b^3 + K^* \frac{\Delta T}{\Delta Z} \tag{11}$$

Solution of these equations gives

$$A\left[2 + \frac{K_o}{K^*} + \left(1 - \frac{K_o}{K^*}\right)\Lambda\right] = \frac{3}{2} a^2 \frac{\Delta T}{\Delta Z} \tag{12}$$

The flow of heat through the generic cell can be obtained from

$$q = \int_{-\pi/2}^{+\pi/2} K \left.\frac{\partial T}{\partial r}\right]_{r=b} \sin\theta \, d\theta$$

$$= \frac{1}{2} K_o \frac{\Delta T}{\Delta Z} + \frac{1}{2} K_o \left[-2A/b^3 + B\right] \tag{13}$$

If the region occupied by the generic cell had been modelled as part of the effective medium, then the heat flow through it would be

$$q = \frac{1}{2} K^* \frac{\Delta T}{\Delta Z} \tag{14}$$

Equating the two heat flows provides a relationship for the effective thermal conductivity K*. Using Eqs. (10) and (12) we obtain

$$\frac{K^*}{K_o} = \frac{(1-\Lambda)}{(1+\Lambda/2)} \tag{15}$$

This result, obtained earlier by Euken,[1] demonstrates the use of the so-called self-consistent procedure for obtaining effective properties of composite materials.

Numerous other results have appeared in the literature for evaluating the thermal conductivity of porous materials, and a quantitative comparison of these results has been made by Cheng and Vachon.[2] For our application the results of Loeb[3] and Russell[4] are most appropriate. Specializing their expression to spherical pores, one obtains for the Loeb expression

$$\frac{K^*}{K_o} = 1 - \Lambda^{2/3} \tag{16}$$

and for the Russell expression

$$\frac{K^*}{K_o} = \frac{1 - \Lambda^{2/3}}{1 + \Lambda - \Lambda^{2/3}} \tag{17}$$

Figure 1 shows a comparison of the three different results of Euken, Loeb, and Russell. Both Russell and Loeb arrive at their results for the effective thermal conductivity by treating material elements of different conductivity as conductors in series and in parallel. As a result their methods of derivation are not self-consistent in the sense of the derivation given above; namely, a pore in a medium of effective conductivity has no effect on the effective conductivity of the medium as a whole. We consider, therefore the expression of Eq. (15) as the better one to describe the conductivity by a medium with spherical voids. Unfortunately there are not data available on porous metals at high swelling levels with which to test the validity of this recommendation. These equations should be equally as valid for electrical conductivity.

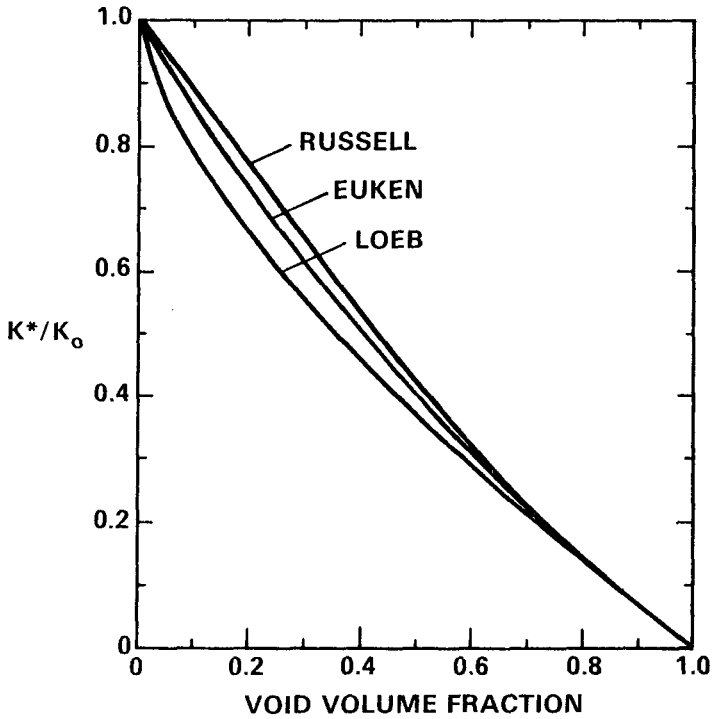

FIGURE 1. Predictions of Three Models Describing the Dependence of Thermal Conductivity K* for Voided Metals, Expressed as a Fraction of the Original Conductivity K_o of the Unvoided Metal.

5.2 Use of the Effective Thermal Conductivity in Practical Applications

Void swelling not only reduces the thermal conductivity of the structural materials used as reactor components but also changes their macroscopic dimensions. Therefore, in assessing the overall impact of void swelling on the thermal performance of a component both types of change must be considered. To illustrate this point, three examples are analyzed: (1) the temperature distribution through the cladding of a fuel element, (2) a plate subject to constant heat flux and, (3) the temperature distribution in a plate subject to nuclear heating.

5.2.1 Temperature Drop Across a Plate Subject to Constant Heat Load

If q represents the heat flux per unit area of a fuel element and h the plate thickness, then the temperature drop across the plate (or thin-walled cladding) is given by

$$K^* \Delta T = h\, q \tag{18}$$

At the beginning of the irradiation when the plate or cladding thickness was equal to h_o, the heat flux per unit area was q_o, and the temperature drop is given by

$$K_o \Delta T_o = h_o\, q_o \tag{19}$$

If A_o represents the initial area of the plate and A the present swelling-increased area, then

$$A\ q = A_o\ q_o \tag{20}$$

under the assumption that the fuel element maintains a constant power output. Since

$$\frac{A\ h}{A_o\ h_o} = \frac{V}{V_o} \tag{21}$$

and since void swelling is known to be isotropic,

$$A = A_o/(1 - \Delta)^{2/3} \tag{22}$$

and

$$h = h_o/(1 - \Delta)^{1/3} \tag{23}$$

Substituting these last two equations in Eq. (18) and the relationship (19) we find that the temperature drop across the cladding has changed according to the following relationship.

$$\frac{\Delta T_o}{\Delta T} = \frac{K^*}{K\ (1 - \Delta)^{1/3}} \tag{24}$$

5.2.2 Temperature Drop Across a Plate Subject to Constant Heat Flux

Consider now the case of a beam of energetic particles depositing energy on a plate subject to swelling. If the heat deposition is treated as a heat flux per unit area of surface then $q = q_o$ and

$$\frac{\Delta T_o}{\Delta T} = \frac{K^*}{K_o}\ (1 - \Delta)^{1/3} \tag{25}$$

5.2.3 Temperature Drop in a Plate Subject to Nuclear Heating

Consider a plate in which heat of the amount $\dot{Q}$ is generated per unit volume and per second. The temperature distribution is given by

$$T(x) = T_s + \frac{\dot{Q}}{4K^*}\ (h^2 - x^2) \tag{26}$$

where T_s is the surface temperature, h the plate thickness and x is the distance from the midplane.

Originally, the temperature distribution was

$$T_o(x) = T_s + \frac{\dot{Q}_o}{4K_o}\ (h_o^2 - x^2) \tag{27}$$

Since the nuclear heating per unit mass remains constant with swelling,

$$V \dot{Q} = V_o \dot{Q}_o$$

or

$$\dot{Q} = \dot{Q}_o (1 - \Lambda) \tag{28}$$

If we denote the temperature difference between the midplane and the surface by $\Delta T = T(o) - T_s$ we find that

$$\frac{\Delta T_o}{\Delta T} = \frac{K^*}{K_o (1 - \Lambda)^{1/3}} \tag{29}$$

This result is identical with that of Eq. (24) derived for the change in temperature across the cladding of a fuel element. This coincidence is most fortunate since it allows us to include both the heat flux and the nuclear heating in one simple formula for the temperature change of the cladding as a result of swelling.

Figure 2 gives the ratio $\Delta T_o/\Delta T$ according to Eq. (24) or (29) using the different expressions for the effective thermal conductivity given above. In constrast, Figure 3 shows the ratio $\Delta T_o/\Delta T$ for a constant heat flux according to Eq. (25). The difference in these two examples becomes even more evident when $\Delta T/\Delta T_o$ is plotted as a function of swelling, i.e., $\Delta V/V_o = \Lambda/(1 - \Lambda)$, rather than the void volume fraction. Figure 4 shows the ratio of $\Delta T/\Delta T_o$ according to Eq. (24) or (29), whereas Figure 5 gives the ratio according to Eq. (25). We see that the temperature difference across a plate subject to a constant heat flux doubles when swelling reaches 50%. However, for the cladding of a fuel element delivering constant power, the temperature increases only a factor of about 1.5 for 50% swelling.

5.3 Elastic Property Changes

The effective elastic moduli of composite materials depend not only on the elastic constants of the individual phases but also on their volume fractions and on their mutual arrangement. Because of this complexity, it is generally not possible to derive simple expressions for effective elastic constants. However, based on simplifying assumptions of the distribution of the various phases, and using elastic strain energy principles, Hashin and Shtrikman[5] have provided upper and lower bounds for the effective elastic moduli. Some of these bounds yield trivial results, however, when the elastic moduli of one phase are set equal to zero to describe a voided or porous material.

For the composite sphere assemblage discussed in the preceding section it is possible to obtain the following rigorous result for the effective bulk modulus K* as shown by Hashin:[6]

$$\kappa^*/\kappa = 1 - \frac{3 (1 - \nu) \Lambda}{2(1 - 2\nu) + (1 + \nu) \Lambda} \tag{30}$$

Here, κ and ν are the bulk modulus and the Poisson's ratio for a metal containing a void volume fraction of Λ. Figure 6 shows the predictions of Eq. (30) for $\nu = 0.3$. Since the composite sphere assemblage is an excellent representation of a voided material with a wide spectrum of void sizes, Eq. (30) is expected to give an accurate description of the reduction in bulk modulus with void swelling.

Unfortunately, an equally rigorous formula can not be given for the effective shear modulus. Instead, only upper and lower bounds have been found by Hashin[6] and Christensen.[7] The upper and lower bounds by Hashin[6] are given by

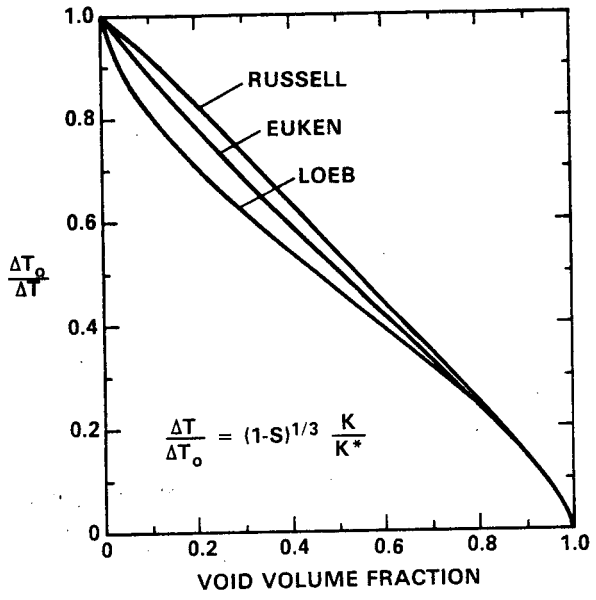

FIGURE 2. Ratio of Initial Temperature Drop to Final Temperature Drop Across the Cladding of a Fuel Element With Constant Power Production.

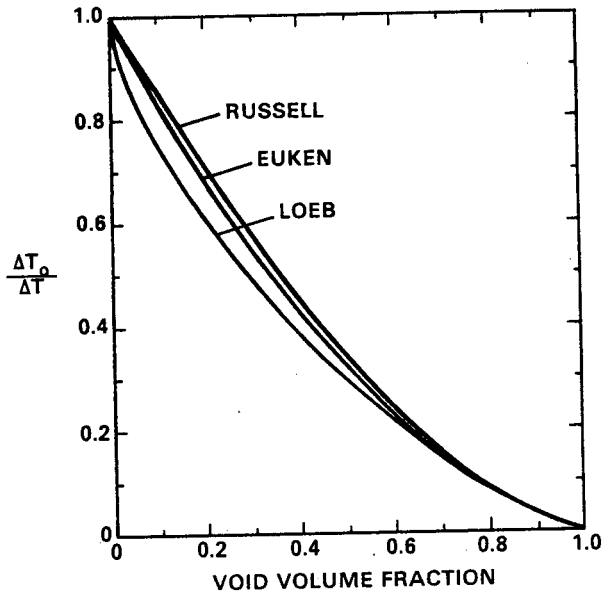

FIGURE 3. Ratio of the Temperature Difference Across a Plate Subject to Swelling When the Heat Flux per Unit Area Remains Constant.

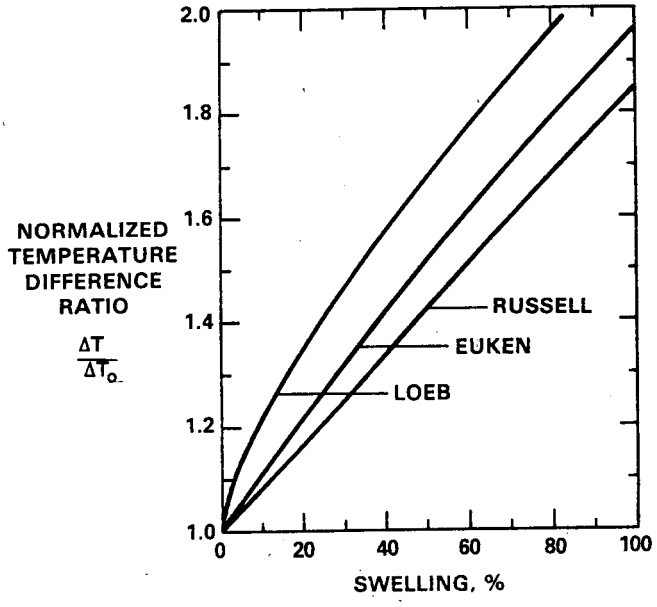

FIGURE 4. Normalized Temperature Difference Ratio Through Cladding Which Undergoes Void Swelling.

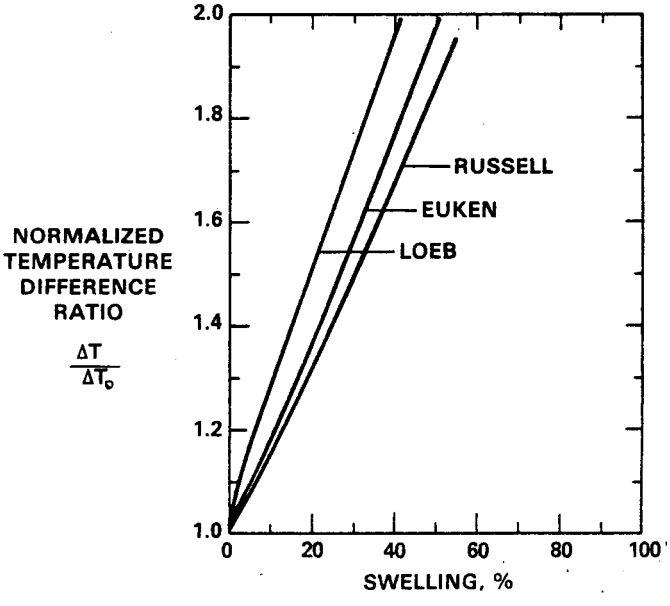

FIGURE 5. Normalized Temperature Difference Ratio Across a Plate Subject to a Constant Heat Flux.

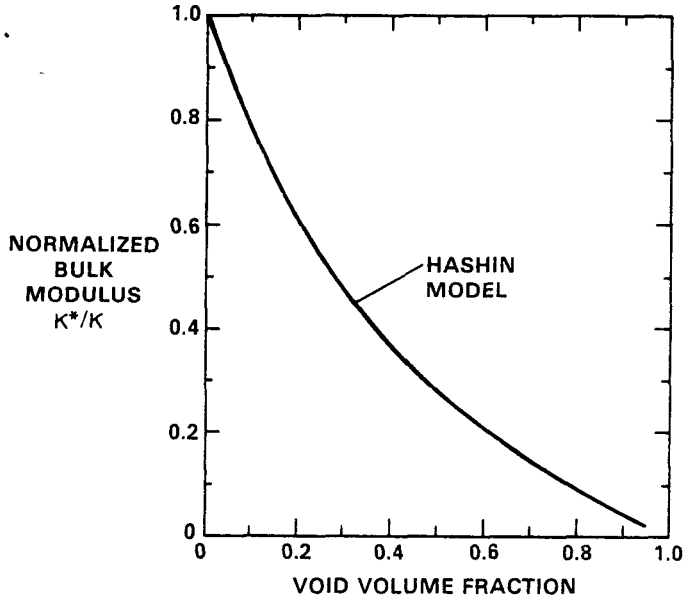

FIGURE 6. The Dependence of the Effective Bulk Modulus κ on Void Volume Fraction.

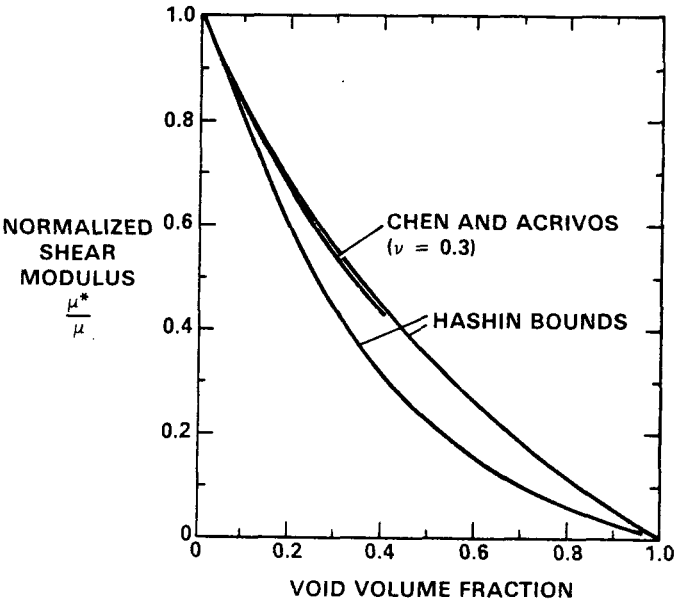

FIGURE 7. The Dependence of the Effective Shear Modulus μ on Void Volume Fraction, Expressed as Upper and Lower Bounds.

$$1 - \frac{15\,(1-\nu)\Lambda}{(7-5\nu)+2(4-5\nu)\Lambda} \leq \frac{\mu^*}{\mu} \leq 1 - \frac{15\,(1-\nu)\Lambda}{(7-5\nu)+F(\Lambda)\Lambda} \tag{31}$$

where

$$F(\Lambda) = 2\,(4-5\nu) - \frac{126}{(7+5\nu)}\,\frac{(1-\Lambda^{2/3})^2}{1-\Lambda^{7/3}} \tag{32}$$

and μ is the shear modulus of the matrix.

The upper bound reported by Christensen differs from the one given by Hashin. For $\Lambda \leq 0.2$, Christensen's upper bound is somewhat lower, but for $\Lambda > 0.2$, it exceeds the Hashin bound significantly.

A second method of obtaining effective elastic moduli employs a perturbation method in which the void volume fraction is considered to be small. Hence, this method provides valid results only for $S \ll 1$. Both Walpole[8] and Chen and Acrivos[9] have treated the case of spherical cavities in a solid, and their results can be written as

$$\frac{\mu^*}{\mu} = 1 - \frac{15\,(1-\nu)}{7-5\nu}\,\Lambda + \frac{30\,(1-\nu)\,(4-5\nu)}{(7-5\nu)^2}\,\Lambda^2\,H\,(\nu) \tag{33}$$

When the interaction between the stress field of adjacent voids is neglected, as did Walpole, the function $H(\nu) = 1$. However, as shown by Chen and Acrivos,[9] this interaction results in a reduction of the quadratic term in equation 33, with $H(\nu) \leq 0.75$, decreasing with increasing Poisson's ratio. For example, the numerical results show that $H(0.3) = 0.67$ and $H(0.4) = 0.60$.

Figure 7 shows how both the upper and lower bounds of the ratio μ^*/μ according to Hashin as well as the results of Chen and Acrivos for $\nu = 0.3$. When Λ exceeds 0.5, the expression of Eq. (33) predicts values above the upper bound of Hashin, and it becomes invalid. However, within the range $0 \leq \Lambda \leq 0.4$, the results of Chen and Acrivos closely resembly the upper bound of Hashin. We can therefore conclude that the the upper bound of Hashin provides an excellent expression for the effective shear modulus of a voided material.

The effective Young's modulus can now be obtained from the above results according to the equation

$$E^* = \frac{9\ \kappa^*\ \mu^*}{3\ \kappa^* + \mu^*} \tag{34}$$

and the Poisson's ratio is given by

$$\nu^* = \frac{3\kappa^* - 2\mu^*}{2(3\kappa^* + \mu^*)} \tag{35}$$

Figures 8 and 9 show the variation of E^*/E and ν^* with the void volume fraction. The lower bound for the shear modulus results in an increasing Poisson's ratio for large void volume fractions after an initial decline. In contrast both the exact results of Chen and Acrivos and the upper bound for μ^*/μ give a monotonic decline of Poisson's ratio with void volume fraction.

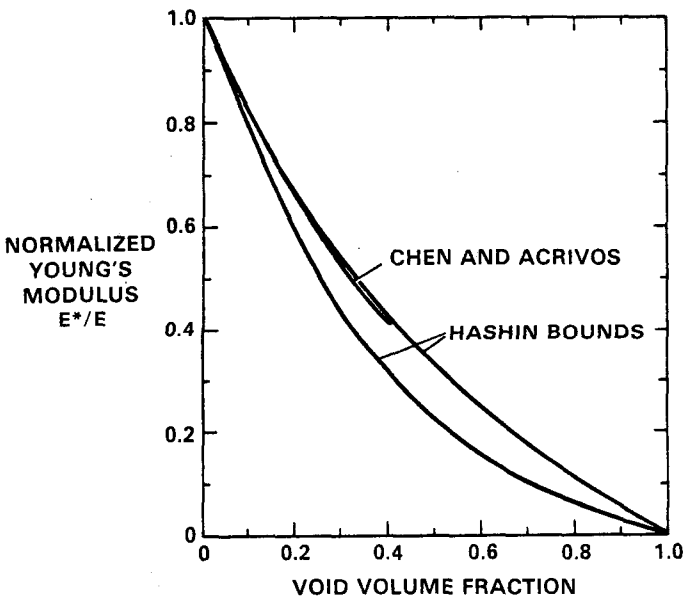

FIGURE 8. Dependence of the Effective Young's Modulus E* on Void Volume Fraction, Expressed as Upper and Lower Bounds.

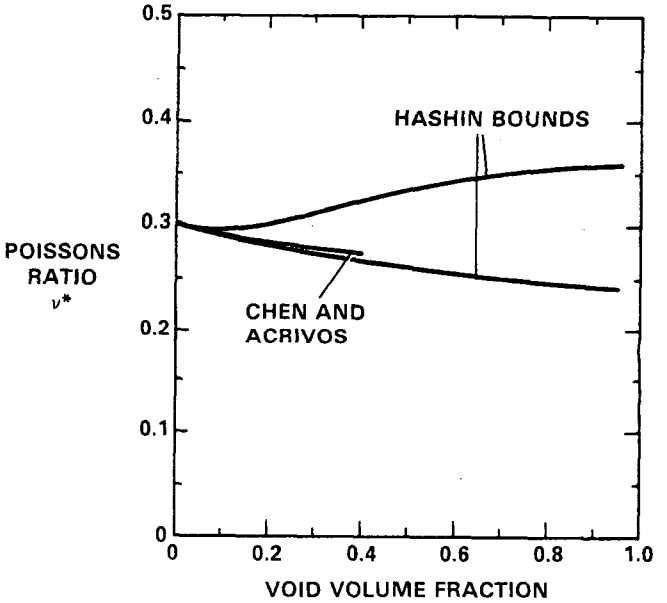

FIGURE 9. Dependence of the Effective Poisson's Ratio on Void Volume Fraction According to Several Models.

5.4 Comparison of Predictions With Data

Marlow and Appleby have measured Young's modulus of voided metals using a dynamic resonance technique on ring-shaped specimens cut from irradiated fuel cladding.[10-11] The swelling levels ranged from 1 to 10% in solution-annealed Types 316 and 347 stainless steel. They found that the modulus initially increased due to an increase in dislocation density and then declined at a rate of 1.6-2.7% for each precent of swelling.

Straalsund and Day[12] later used an ultrasonic technique to determine the elastic moduli of annealed type 304 stainless steel irradiated in EBR-II. The swelling levels ranged only up to 6.8% but the data were larger in number and more consistent than that of Marlow and Appleby. Assuming a linear decrease in moduli with swelling, Straalsund and Day determined that the shear, Young's and bulk moduli declined at rates of 2.3, 2.4 and 2.6% per percent swelling. Poissons ratio was found to decrease at a rate of 0.23% per percent swelling. Within the limits of the uncertainty they showed that the data were close to that predicted by the Christensen upper bound and therefore close to Hashin's upper bound. As shown in Figures 6-8, the asymptotes of the moduli at low void volume indeed have the same slope as that determined by Straalsund and Day. Their results for Poisson's ratio also closely match the results of Christensen or that arising from Hashin's upper bound.

As yet there are no data to test the validity of these models at higher void volume.

5.5 Use of the Effective Elastic Constants

The impact of the change in elastic properties as a result of swelling depends on the overall dimensional changes of a component and on the particular loading conditions. To demonstrate this, we consider three examples: a pressurized tube, a uniaxial creep experiment, and the thermal stresses developed in fuel cladding.

5.5.1 Hoop Stress in a Pressurized Tube

If D represents the diameter and h the thickness of a thin-walled tube pressurized by an internal gas of pressure p, then the hoop stress is given by

$$\sigma = p\ D/h \tag{36}$$

As a result of swelling both the diameter and the wall thickness change, but the ratio of the two remains constant, i.e., $D/h = D_0/h_0$, where D_0 and h_0 represent the original values. However, the gas volume increased from V_0 to $V = V_0 + \Delta V$, and hence, the pressure changed from its original value p_0 to

$$p = p_0\ V_0/V = p_0\ (1 - \Lambda) = p_0/(1 + S_0) \tag{37}$$

where $S_0 = \Delta V/V_0 = \Lambda(1 - \Lambda)^{-1}$ is the conventional measure of swelling. The hoop stress is then given by

$$\sigma = \sigma_0\ (1 - \Lambda) = \sigma_0/(1 + S_0) \tag{38}$$

and therefore decreases from its original value σ_0 as a result of swelling.

5.5.2 Uniaxial Tension

Suppose a uniaxial tension specimen is loaded with a dead weight P. The uniaxial stress is then $\sigma = P/A$. If the original cross-sectional area was A_0, the present stress is related to the original stress σ_0 by

$$\sigma = \sigma_0/(1 - \Lambda)^{2/3} \tag{39}$$

Hence, the uniaxial elastic strain is given by

$$\begin{aligned} \epsilon/\epsilon_0 &= E/[E^*(1 - \Lambda)^{2/3}] \\ &= E\ (1 + S_0)^{2/3}/E^* \end{aligned} \tag{40}$$

where ϵ_0 was the original elastic strain in the specimen. Figure 10 shows the ratio ϵ/ϵ_0 as a function of void swelling. It is seen that the elastic extension of the uniaxial specimen is doubled when the void swelling reaches 40%.

5.5.3 Thermal Stess in Fuel Element Cladding

The thermal stress in a thin-walled tube with a temperature difference ΔT_0 across the wall is given by

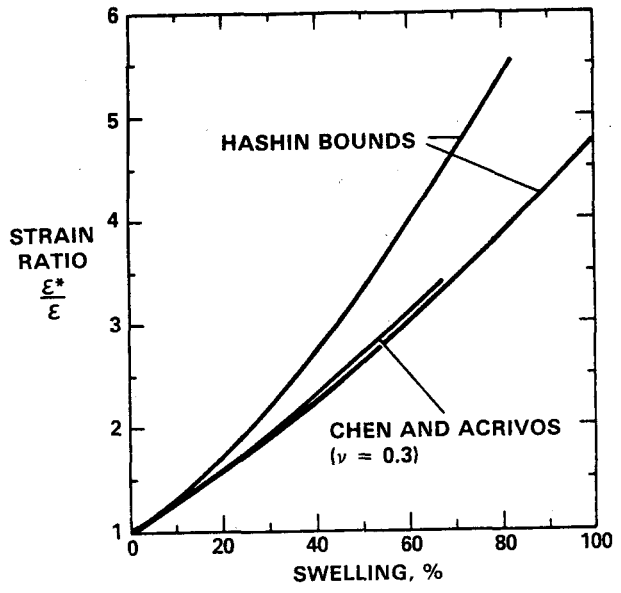

FIGURE 10. Strain Ratio for the Uniaxial Tension Case as Influenced by Swelling.

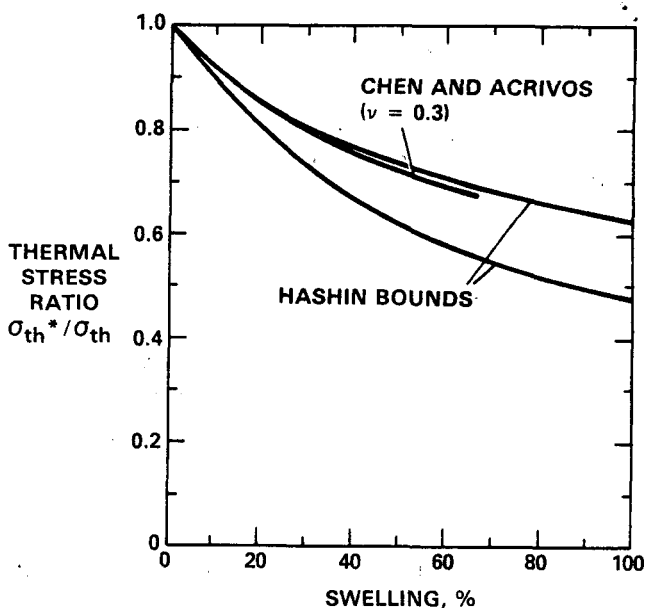

FIGURE 11. Thermal Stress Ratio for Thin-Walled Tubes as Influenced by Void Swelling.

$$\sigma_{th} = \pm \frac{E \alpha \Delta T_o}{2(1 - \nu)} \tag{41}$$

where the plus (minus) sign holds for the cold (hot) surface.

Swelling results in an increase of the temperature difference, a decrease in the Young's modulus, a slight change in Poisson's rato, but does not affect the coefficient of linear thermal expansion, α. Hence, the thermal stress change is given by

$$\frac{\sigma^*_{th}}{\sigma_{th}} = \frac{1 - \nu}{1 - \nu^*} \frac{E^*}{E} \frac{\Delta T}{\Delta T_o} \tag{42}$$

Using Eq. (24) and assuming the Euken expression of Eq. (15) for the effective thermal conductivity, we find

$$\frac{\sigma^*_{th}}{\sigma_{th}} = \frac{1 - \nu}{1 - \nu^*} \frac{E^*}{E} \frac{(1 + \Lambda/2)}{(1 - \Lambda)^{2/3}} \tag{43}$$

The thermal stress ratio for this case is shown in Figure 11 using the upper and lower bounds for the effective elastic moduli as well as the results of Chen and Acrivos. It is seen that in spite of the temperature increase across the cladding wall, the thermal stress decreases with void swelling because of the more dramatic decrease in Young's modulus.

6.0 References

1. A. Euken, Forsch. Geb. Ingenieurw., B3, Forschungsheft No. 353, 1932.
2. S. C. Chen and R. I. Vachon, J. Heat Mass Transfer 13, p. 537, 1970.
3. A. L. Loeb, J. Am. Cer. Soc. 37, p. 96, 1954.
4. H. W. Russell, J. Am. Cer. Soc. 18, p. 1, 1935.

5. Z. Hashin and S. Shtrikman, "A Variational Approach to the Theory of the Elastic Behavior of Multiphase Materials," J. Mech. Phys. of Solids 11, pp. 127-140, 1963.

6. Z. Hashin, "The Elastic Moduli of Heterogeneous Materials," J. Appl. Mech. 29E, p. 143, 1962.

7. R. M. Christensen, "Viscoelastic Properties of Heterogeneous Media," J. Mech. Phys. Solids 17, pp. 23-41, 1969.

8. L. J. Walpole, "The Elastic Behavior of a Suspension of Spherical Particles," Quart. J. Mech. and Appl. Math. 25, pp. 153-160, 1972.

9. Hsiao-Sheng Chen and A. Acrivos, Int. J. Solids Structures 14, p. 349, 1978.

10. General Electric Progress Report GEAP-10028-43, p. 10-6, 1972.

11. M. Marlowe and W. K. Appleby, Trans. Am. Nucl. Soc, 16, p. 95, 1973.

12. J. L. Straalsund and C. K. Day, Nucl. Tech. 20, p. 27, 1973.

CHAPTER 5

CORRELATION METHODOLOGY

CONSTITUTIVE DESIGN EQUATIONS FOR THERMAL CREEP DEFORMATION OF HT-9

R. J. Amodeo and N. M. Ghoniem (UCLA)

1.0 Objective

The purpose of this paper is to develop design equations for use in inelastic structural mechanics applications, for the most important thermal creep parameters for HT-9.

2.0 Summary

In this paper, we have developed useful design correlations for a number of commercial heats of HT-9. The design equations covered the following properties:

1) Rupture time as a function of applied stress and temperature, using a modification of the minimum comittment method.
2) Time to 5% strain as a function of stress and temperature.
3) Time to 1% strain as a function of stress and temperature.
4) Rupture strain as a function of stress and temperature.
5) Creep strain, as a function of time, temperature, and stress. This covers the primary, secondary and tertiary regimes of creep.

The HT-9 creep data in the range 500-600^{o}C was found to represent behavior typically described by dislocation creep. The phenomenological equation used to represent the data was based on an effective stress acting on dislocations. The friction stress was found to be only a function of temperature. This approach indicated that dislocation climb is controlled by vacancy absorption at dislocations.

3.0 Program

Title: Helium Effects on the Swelling of Steels
Principal Investigator: N. M. Ghoniem
Affiliation: University of California at Los Angeles

4.0 Relevant DAFS Program Plan Task/Subtask

Subtask Group C: Damage Microstructure Evolution and Mechanical Behavior

5.0 Accomplishments and Status

5.1 Introduction

HT-9 is a ferromagnetic iron-base alloy that has been optimized to operate at high temperatures. It contains a relatively high chromium content, on the order of 12%, with additions of other alloying elements to achieve its design goal. This alloy, developed by Sandvik Steel Company, has been proposed as a potential candidate alloy for fusion reactor applications[1]. The primary reasons for this choice can be summarized as:

1. Ferritic and Martensitic steels exhibit great resistance to void swelling under neutron bombardment.
2. The thermal stress resistance is greater than austenitic alloys allowing the use of thicker sections for first wall applications.
3. Limited evidence indicates that helium generation by neutron irradiation does not significantly degrade the mechanical properties[2].

In order to perform detailed structural analyses for fusion reactor blankets, designers must be provided with appropriate design equations. In this paper, we develop design equations for use in structural mechanics applications. Theoretically based creep equations may not be accurate enough to predict creep deformation. We will therefore present empirical equations that are accurate in a limited, yet important range. We will then present a phenomenological description of the creep rates to explain the measured experimental data.

5.2 Data Base

We consider here two classes of creep data: the creep rupture life of tested specimens as a function of operating temperature and stress, and elongation as a function of time. This information is provided by the Sandvik Steel Company for temperatures of 500^{o}C, 550^{o}C, and 600^{o}C, and stresses ranging from 12.5 -

50 ksi. These data are the result of up to 5 years testing time of nine melts of HT-9. It consists of times to 1% strain, 5% strain and rupture, and elongation to fracture for different stresses at each temperature. More details of the supplied creep test data are provided in reference (3).

5.3 Empirical Laws for Creep Deformation

5.3.1 Creep Rupture

Creep rupture data have been studied extensively, with the objective of extrapolating this data to design lives on the order of 30-40 years. In a review of available methods, Le May[4] considered five different functional forms for creep rupture data. There is, however, no universally acceptable "standard" method.

Minimum Commitment Method:

As a result, the Minimum Commitment Method, a general formulation[5], was developed in 1971 for NASA to avoid forcing data through a set pattern. The equation based on this method has the following form:

$$\ln t_r + A \cdot P(T) \ln t_r + P(T) = G \cdot \ln \sigma_r \qquad (1)$$

where t_r = rupture time, and σ_r = rupture stress.

Modified Commitment Method:

Ghoniem[1] has developed a general design equation which is a modified form of the Minimum Commitment Method. This equation has the following form:

$$\ln \sigma_r = K(T) - \frac{1}{m(T)} \ln t_r \qquad (2)$$

$$K(T) = \sum_{i=0}^{2} a_i T^i \qquad (3)$$

$$m(T) = \sum_{i=0}^{2} b_i / T^i \qquad (4)$$

T is in ^{o}K, t_r is in hrs., and σ_r is in ksi. The data for HT-9 were fit to the above relation using a least-squares method. The coefficients a_i and b_i are provided in Table (1)

Table (1)
Coefficients for Rupture Time vs. Stress

a_0= 138.4149302	b_0= -1531.358687
a_1= -0.3233496513	b_1= 2506695.289
a_2= 1.946588668E-4	b_2= -1017186681

5.3.2 Creep Design Equations

A plot of elongation versus time provides insight into the nature of material creep behavior. It is therefore important to preserve the overall shape of this curve for design purposes. The elongation versus time curve consists of the three following regions: (1) primary transient regime, (2) secondary linear regime, (3) tertiary regime extending to creep rupture.

Elongation for Three Creep Regimes:

It is found that over most of the temperature range, the 1% strain falls in the primary region or at the beginning of the secondary region. The 5% strain is on the borderline of the secondary-tertiary boundary, or well into the tertiary region. Extrapolating to $0.9*t_5$, where t_5 = time to 5% strain, provides a point in the secondary region. Coupled with the 1% strain point, this yields the following form for the primary-secondary region:

$$\varepsilon(T) = \{1 - \exp(bt^{\alpha})\} \cdot 100 \ \% \qquad (5)$$

The constants b and α are fit in the following manner: Let t_1 = time to 1% strain, and $\varepsilon_1 = 0.01$. Then

$$t' = 0.9 t_5 \qquad (6)$$

$$a = \ln 5 / t_5^2 \qquad (7)$$

$$\varepsilon_2 = 0.01 \exp(at'^2) \qquad (8)$$

$$\alpha = \ln\{\ln(1-\varepsilon_2)/\ln(1-\varepsilon_1)\}/\ln(t'/t_1) \qquad (9)$$

$$b = \ln(1-\varepsilon_1)/t_1^{\alpha} \qquad (10)$$

Here a, $\alpha > 0$ and $b < 0$. This fit is good for $0 < t < 0.9*t_5$.

In the region between $0.9*t_5$ and t_5, the fit is determined by equations (6-8), with the expression:

$$\varepsilon(t) = \exp(at'^2) \ \% \tag{11}$$

Finally, in the tertiary-rupture region, the fit is an exponential of the following form:

$$\varepsilon(t) = \exp(ct^{\gamma}) \ \% \tag{12}$$

$$\text{where} \quad \gamma = \ln(\ln\varepsilon_R/\ln\varepsilon_5)/\ln(t_r/t_5) \ ,$$

$$c = \ln(\varepsilon_R)/t_r^{\gamma}$$

and ε_R = elongation to fracture. This is good for $t_5 < t < t_r$. It is therefore found that the representations of creep strain can be described by the following equation:

$$\varepsilon = f\{t_1(t_r(\sigma,T),T),\ t_5(t_r(\sigma,T),T),\ t_r(\sigma,T),\ \varepsilon_R(t_r(\sigma,T),T)\}$$

Rupture Time Dependence:

It is necessary to fit these characterisitic points to a reliable parameter, such as the time to rupture discussed in section (3.1.2). Equation (2) can be re-written in the following form:

$$t_r = \exp\{m(T)\cdot K(T)\} / \sigma^{m(T)} \tag{13}$$

where σ is now the applied stress. The time to 1% strain, t_1, is found to be best fit to the rupture time by the following form:

$$\ln t_1 = J(T)\cdot \ln t_r + L(T) \tag{14}$$

$$J(T) = \sum_{i=0}^{2} J_i T^i \tag{15}$$

$$L(T) = \sum_{i=0}^{2} L_i T^i \tag{16}$$

and the coefficients L_i , and J_i are listed in Table (2).

Table (2)
Coefficients for t_1 vs. Rupture Time

J_0= -119.4828446	L_0= 1707.558058
J_1= 0.2860065163	L_1= -4.091847968
J_2= -1.687029056E-4	L_2= 2.435742087E-3

The time to 5% strain is fit to a polynomial function of both temperature and rupture time:

$$t_5 = \sum_{i=0}^{2} \sum_{j=0}^{2} a_{ij} T^j t_r^{\,i} \tag{17}$$

with coefficients a_{ij} found in Table (3)

Table (3)
Coefficients for t_5 vs. Rupture Time

a_{00} = 5.800300737E4	a_{12} = -4.906002324E-6
a_{01} = -142.9532355	a_{20} = 1.275428065E-3
a_{02} = 8.746716625E-2	a_{21} = -2.979495964E-6
a_{10} = -2.257160655	a_{22} = 1.74509467E-9
a_{11} = 7.669299551E-3	

Finally, the elongation to fracture ε_R is found to roughly fit the rupture time in the following functional form:

$$\ln\varepsilon_R = n(T)\cdot \ln t_r + p(T) \tag{18}$$

$$n(T) = \sum_{i=0}^{2} n_i T^i \tag{19}$$

$$p(T) = \sum_{i=0}^{2} p_i T^i \qquad (20)$$

The coefficients n_i, and p_i are in Table (4).

Table (4)
Coefficients for Elongation vs. Rupture Time

n_0 = 54.32308035	p_0 = -465.7071298
n_1 = -0.1286025719	p_1 = 1.110624330
n_2 = 7.581206028E-5	p_2 = -6.547203129E-4

Accuracy and Range of Applicability:

For the creep rupture curves, errors on a log scale for calculating the rupture time versus stress may translate into substantial errors (Figure (1)). Therefore, a given stress level can only provide a fair but reasonable estimate of the time to rupture, based on the nature of the data. This amounts to about 20%-30% error in rupture times for the given stress and temperatures. There is considerable error in the functional determination of times to 1% and 5% strain, as much as 50%, but the data spread is so wide for these two particular times as a function of stress that such a deviation can be expected. These characteristic times also depend on the accuracy of the determination of rupture time.

In spite of these differences, the primary and secondary regions were fit with reasonable accuracy to the data, as can be seen in Figure (2). The tertiary and rupture regions are generally underestimated. As seen in Figure (2), this can ammout to an error of about 20%-30%. In general it can be concluded, however, that the overall form of the creep strain curve is preserved with a certain degree of accuracy. The range of applicability is defined by the temperature limits 500°C - 600°C. The upper and lower limits of the stress in ksi versus temperature in °K are given by:

$$\sigma_u = -\frac{T}{5} + 202.63 \text{ ksi} \qquad (21)$$

$$\sigma_l = -\frac{T}{5} + 189.63 \text{ ksi} \qquad (22)$$

5.4 Phenomenological Model

The dependence of the steady state creep rate on applied stress and temperature can be analyzed using as Ashby-type deformation map[6]. In particular, it is found that for HT-9 the phenomenon of dislocation creep is characteristic of the data supplied by Sandvik Laboratories. Steady state dislocation creep involves the climb and glide of dislocations by means of stress-assisted vacancy movement, and is described by phenomenological expressions such as[7]

$$\dot{\epsilon} = A\sigma^n \exp(-Q_c/RT) \qquad (23)$$

where Q_c is the activation energy for self-diffusion. It is found that for most pure metals n is usually in the range of 4-6, but in dispersion hardened alloys, the value of n has been found to be significantly higher[8].

To explain this anomalous behavior, it has been suggested[7] that the creep takes place under the influence of an active or effective stress $\sigma - \sigma_o$, where σ is the applied stress and σ_o is the friction stress which the dislocation must overcome to move through the lattice. The dependence of creep rate on temperature and stress can be represented by the following form[4] due to the process of dislocation creep:

$$\dot{\epsilon} = (16\pi^3 D_v b c_j / G^2 KT)(\sigma-\sigma_o)^3 \qquad (24)$$

where $\dot{\epsilon}$ = steady-state creep rate, c_j = concentration of jogs, σ_o = Av/b, v = velocity of mobile dislocations, and A = temperature dependent time constant. For HT-9, it is found that the above expression can be written using least squares:

$$\dot{\epsilon} = \frac{B}{KT}(\sigma-\sigma_o)^3 \exp(-Q^*/KT) \qquad (25)$$

where B = 7.385 x 10^{-3}, Q* = 1.23eV, σ_o = aT + C, a = -0.2185, and C = 198.178. T is in °K, σ and σ_o, are in ksi.

The value of Q* is close to the migration energy of vacancies, 1.2 - 1.3 eV, which may suggest that the dislocation creep mechanism in HT-9 is controlled by vacancy movement. This phenomenological formulation is good for the temperature range of 500° - 600°C and stress levels limited by equations (21,22).

6.0 References

1. N.M. Ghoniem, and R.W. Conn, Assessment of Ferritic Steels for Steady-State Fusion Reactors, in: International Atomic Energy Agency Proc on Fusion Reactor Design and Technology, IAEA-TC-392/62: Vol II, p. 389, 1983.

2. R.L. Klueh, J.M. Vitek, and M.L. Grossbeck, Journal of Nuclear Materials 103 & 104, (1981) 887

3. R.J. Amodeo, and N.M. Ghoniem, Constitutive Design Equations for Creep Deformation of HT-9, UCLA Report PPG-743, September(1983)

4. I. LeMay, Principles of Mechanical Metallurgy,(Elsevier, New York, 1982)

5. S.S. Manson, and C.R. Ensign, NASA TM.X-52999 (1971)

6. M.F. Ashby, Acta. Met., 20, (1972) 887

7. J.D. Parker, and B. Wilshire, Metal Science 9, (1974) 248

8. B.A. Wilcox, and A.H. Claver, Trans. Met. Soc. AIME, 236 (1966) 570.

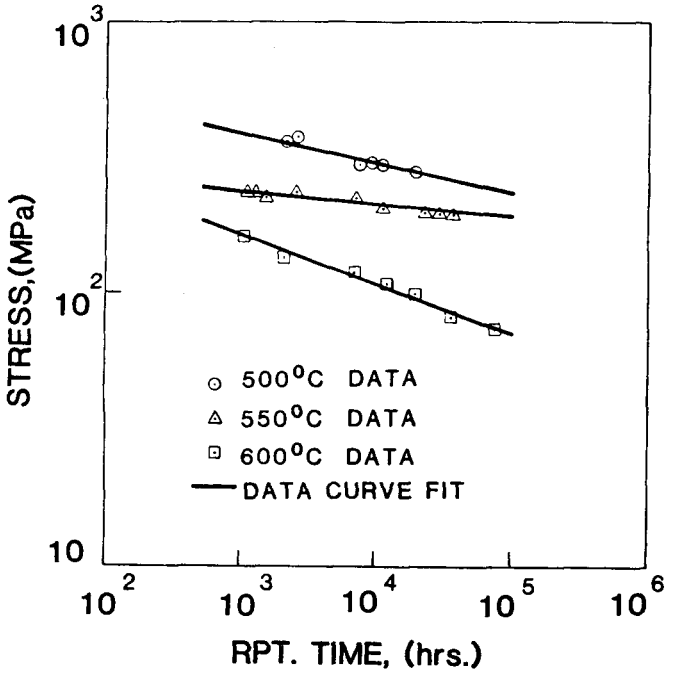

FIGURE 1. HT-9 Rupture Stress Versus Rupture Time.

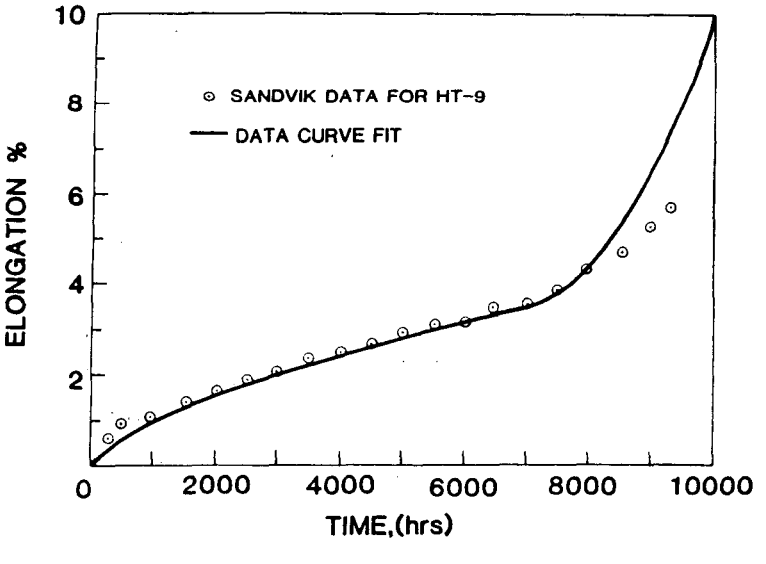

FIGURE 2. Elongation Versus Time for Test Temperature 600°C and Stress Level 15.2 ksi.

OWR/RTNS-II LOW EXPOSURE SPECTRAL EFFECTS EXPERIMENT

H. L. Heinisch and S. D. Atkin (Hanford Engineering Development Laboratory)

1.0 Objective

The object of this experiment is to determine the effect of the neutron spectrum on radiation-induced changes in mechanical properties for metals irradiated with fission and fusion neutrons.

2.0 Summary

Miniature flat tensile specimens of Fe, Cu, 316 stainless steel and A302B pressure vessel steel are to be irradiated to a range of fluences in RTNS-II and the Omega West Reactor at 90°C and 290°C. The first RTNS-II irradiation is now in progress, and preparations are being made for the first Omega West Reactor irradiation. Some specimens are also being irradiated at room temperature in RTNS-II. The flat tensile specimens lend themselves to a variety of measurements, many of which, including the tensile tests, can be done on the same specimen.

3.0 Program

Title: Irradiation Effects Analysis
Principal Investigator: D. G. Doran
Affiliation: Westinghouse Hanford Company

4.0 Relevant DAFS Program Plan Task/Subtask

Subtask II.B.3.2 Experimental Characterization of Primary Damage State; Studies of Metals
Subtask II.C.6.3 Effects of Damage Rate and Cascade Structure on Microstructure; Low-Energy/High-Energy Neutron Correlations
Subtask II.C.16.1 14-MeV Neutron Damage Correlation

5.0 Accomplishments and Status

5.1 Introduction

A major objective of the DAFS program is to develop correlations for the irradiation effects resulting from exposure of materials to different irradiation environments, in particular, fission-fusion correlations. The Rotating Target Neutron Source (RTNS-II) at Lawrence Livermore National Laboratory is currently the strongest source of D-T fusion neutrons, but it is extremely weak compared to neutron fluxes expected at the first wall of a fusion reactor. Nevertheless, RTNS-II provides the opportunity to study effects of high energy neutrons on the initial damage state in the low exposure experiments that are possible there.

In this experiment the effects of two very different neutron spectra on the changes in tensile properties and microstructure of metals irradiated to exposures < 0.1 displacements per atom (dpa) are being determined. Data from previous experiments comparing the effects on tensile properties of fusion neutrons and fission reactor neutrons in copper[1] and stainless steel[2] indicate the existence of spectral effects that cannot be accounted for simply on the basis of dpa[3]. The earlier fission (LPTR) and fusion (RTNS-I) irradiations were conducted at different temperatures (65°C and 25°C respectively), so their failure to correlate with dpa could represent, at least in part, a temperature effect. The earlier experiments attained very low fluences in RTNS-I (<0.001 dpa). One of the goals of our experiment is to corroborate the earlier measurements over a higher fluence range and with uniform irradiation temperatures.

For the present experiment irradiations will be performed at the RTNS-II and the Omega West Reactor (OWR) at Los Alamos National Laboratory. Flat miniature tensile specimens will be irradiated in both spectra at two temperatures, 90°C and 290°C. The maximum fluences will be at least 5 to 10 times higher than in earlier experiments. The first RTNS-II irradiation, to 0.006 dpa (2×10^{18} n/cm^2), is in progress, and an additional irradiation to 0.03 dpa at RTNS-II has been requested. A few specimens are also being irradiated at room temperature in RTNS-II to about 0.003 dpa (1×10^{18} n/cm^2). Table 1 gives a summary of the irradiation conditions and the materials to be tested.

TABLE 1

OWR/RTNS-II SPECTRAL EFFECTS EXPERIMENT

Material	Heat Treatment	Irradiations (RTNS-II Peak Fluences, OWR Total Neutrons)		
		Facility	Fluence (n/cm^2)	(dpa)	Temperatures
Cu, Marz Grade	450°C, 15 min, air cooled	RTNS-II	5×10^{17}	0.0015	*90°C, 290°C
Fe, Marz Grade	800°C, UHV, 2 hr, furnace cooled	RTNS-II	2×10^{18}	0.006	*90°C, 290°C
316 Stainless Steel	1000°C, 10 min, air cooled	RTNS-II	1×10^{19}	0.03	*90°C, 290°C
316 Stainless Steel, 20% Cold Worked		RTNS-II	8×10^{17}	0.003	25°C
A302B Pressure Vessel Steel		OWR	5×10^{18}	0.001	90°C, 290°C
		OWR	2×10^{19}	0.003	90°C, 290°C
		OWR	5×10^{19}	0.01	90°C, 290°C
		OWR	2×10^{20}	0.03	90°C, 290°C

* Both temperatures in a single irradiation with the DTVI furnace.

The materials being irradiated are annealed Marz grade Cu, annealed Marz grade Fe, solution annealed and 20% cold worked AISI 316 stainless steel, and A302B pressure vessel steel. Thus, at two temperatures one will be able to compare spectral effects with respect to austenitic versus ferritic steels, annealed versus cold worked conditions, fcc versus bcc crystal structures, and pure materials versus engineering materials. Also, the temperature sensitivity of the property changes is different for each material, so there will be a range of behaviors at the temperatures chosen.

The high multiplicity of specimens of each material throughout the dose range will insure good statistics for the tensile data, while allowing for examination by transmission electron microscopy (TEM) and performance of other mechanical tests. Sets of approximately 20 Fe and 20 stainless steel specimens with about the same dose in each spectrum will be available for annealing studies.

The miniature tensile specimens are flat with the typical "dog-bone" shape; see Figure 1. Because the specimens are flat, they can be used for more than tensile tests. The end tabs are suitable for shear punch tests and also for preparation as TEM specimens. Resistivity measurements and hardness tests can be done along the entire specimen. We are investigating the possibility of performing multiple tests, including the tensile test, on one specimen. The tensile testing apparatus is described in detail elsewhere.[4]

5.2 Test Materials

A prime concern in the materials selection was that the expected relative change in yield strength due to irradiation at low exposures would be large enough that the effects could be easily measured.

AISI 316 stainless steel is an engineering material with a large data base for irradiation effects. It is also the material used in the studies by Vandervoort, et al[2]. At low doses, changes in yield strength may be difficult to detect in 20% cold worked 316 stainless steel; however, in its solution annealed condition, radiation-induced changes in tensile properties should be easily discernable.

Copper has a large data base with respect to many properties. Mitchell et al[1] investigated radiation strengthening of copper under the same conditions as the Vandervoort experiment on SA 316 stainless

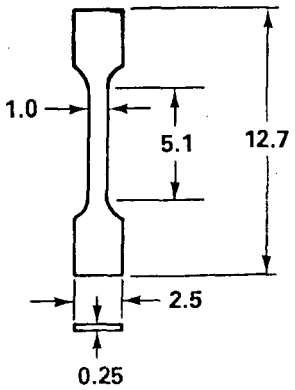

FIGURE 1. Miniature Tensile Specimen Dimensions in mm.

steel. As with stainless steel, the tensile data for copper did not correlate on the basis of dpa. The situation in copper is more likely to have been complicated by temperature effects, since defects in copper are much more mobile than those in stainless steel at the irradiation temperatures. Copper and copper alloys are also of interest to the fusion program as engineering materials.

Iron represents the ferritic materials. It was chosen instead of an alloy such as HT-9 because it does not have the high yield strength of the engineering ferritic alloys that would tend to make the increase in yield strength due to low doses of irradiation difficult to measure. The effects of irradiation temperature on the property changes of Fe are expected to be intermediate to those of Cu and 316 stainless steel. A302B pressure vessel steel is also included in this experiment, especially because much data exists for radiation effects at 290°C in this material.

5.3 Irradiation Temperatures

One of the aims of this experiment is to study possible temperature effects. We will be doing an experiment similar to those of Vandervoort et al and Mitchell et al, without the temperature differences they had between fission and fusion neutron irradiations. Also, we will investigate the effects of temperature by irradiating at the same two temperatures in both neutron spectra.

The choice of temperatures is limited to those that can be easily maintained in the available irradiation facilities. The lower temperature, 90°C, is essentially dictated by the OWR coolant temperature, the gamma heating rate, and the capabilities of the In-core Reactor Furnace, built at LLNL, which uses the reactor coolant as a furnace coolant. The higher irradiation temperature should be one at which defects become significantly more mobile, yet not so high that the residual damage is slight at these low fluences. Another consideration is that the test materials have different temperatures at which defect mobility becomes significant. With respect to vacancy mobility, 290°C can be considered a relatively high temperature for Cu, low for 316 stainless steel, and intermediate for Fe and A302B. A large data base exists for A302B pressure vessel steel at 290°C, which also makes this temperature desirable. The two temperatures, 90°C and 290°C, are easily within the operating range of the dual-temperature vacuum-insulated (DTVI) furnace used for the RTNS-II irradiations.

5.4 Neutron Fluences

In RTNS-II the neutron flux decreases rapidly with distance from the source. From front to back of the "prime volume," defined here as the first 6 mm of the specimen cavities of the DTVI furnace, the flux diminishes by about 75%. In both temperature zones of the furnace tensile specimens will be placed throughout the prime volume and at four other locations spanning a flux range of two orders of magnitude. Three irradiations have been requested at RTNS-II to peak fluences of 5×10^{17}, 2×10^{18}, and 1×10^{19} n/cm^2.

In the Omega West Reactor four irradiations are scheduled at each temperature to damage levels from 0.001 to 0.03 dpa. A fifth, long-term irradiation to 0.1 dpa is being considered, pending the outcome of the earlier parts of the experiment.

5.5 Damage Rate Effects and Helium Effects

The OWR was chosen for this experiment because it has a low damage rate, although it has a damage rate about six times higher than RTNS-II. Such differences in damage rates among fission reactors have been shown to have little effect on tensile properties of stainless steel. In the Vandervoort et al[2] experiments irradiations were done at two positions in LPTR, differing in damage rate by a factor of four, with no apparent rate effects on the yield strength of annealed 316 stainless steel. Also, their

data show only small differences from data on stainless steel irradiated in HFR[5] (Petten), which has nearly an order of magnitude higher displacement rate.

Rate effects on tensile properties for low exposures to 14 MeV neutrons can be investigated in RTNS-II. In the three irradiations planned, there will be overlap in the fluxes and fluences over at least two orders of magnitude.

The influence of He production is expected to be small. There is more than an order of magnitude difference in the He production for the two spectra, but even the greater amount of He generated in RTNS-II is quite small (0.3 appm at 0.03 dpa), and should produce no measurable effect in the tensile properties of any of the materials at the planned irradiation temperatures.

5.6 Status

The tensile specimens were punched from as-received sheet stock, with the exception of the A302B pressure vessel steel, which was punched from coupons sliced from a piece of plate. The Cu, Fe and some of the 316 SS specimens were annealed as described in Table 1. Identificaton codes were laser-engraved on the end tabs of the specimens.

The first RTNS-II irradiation was started April 19, 1983, using the DTVI furnace, Model I, but the furnace was destroyed by a malfunction of the RTNS-II target. A new DTVI furnace ,Model II, has been fabricated, installed, and tested. The first irradiation with the new furnace, to a goal fluence of 2×10^{18} n/cm^2, commenced February 24, 1984.

The prime volume of each temperature zone of the DTVI furnace is occupied by 88 tensile specimens. Another 92 tensile specimens are located throughout the remaining specimen volume in each zone. These tensile specimens are only one part of this joint HEDL/Japan elevated temperature irradiation at RTNS-II. Specimens for eleven Japanese experimenters occupy about 60 % of the total specimen volume. Other U.S. specimens are included for experiments on damage production in insulators, for cross section measurements for reduced activation studies, for TEM studies of copper alloys, and for flow property measurements on a series of Fe alloys.

As an adjunct to the experiment, eighteen tensile specimens of annealed copper and solution annealed 316 stainless steel are currently being irradiated at room temperature to a range of fluences up to almost 1×10^{18} n/cm^2 in a Japanese RTNS-II irradiation coordinated by Professor Katunori Abe of Tohoku University.

6.0 References

1. R. R. Vandervoort, E. L. Raymond and C. J. Echer, Rad. Effects, 45 (1980).

2. J. B. Mitchell, R. A. VanKonynenburg, C. J. Echer and D. M. Parkin, Radiation Effects and Tritium Technology for Fusion Reactors, J. S. Watson and F. W. Wiffen, eds, Gatlinburg, Tennessee, 11, 172 (1975).

3. H. L. Heinisch and R. L. Simons, DAFS Quarterly Progress Report, January-March, 1982, DOE/ER-0046/9, 147 (1982).

4. N. F. Panayotou, S. D. Atkin and R. J. Puigh, Proceedings of the ASTM Symposium on Use of Non-standard, Sub-sized Specimens for Irradiation Testing, Albuquerque, NM, September 23, 1983.

5. H. R. Higgy and F. H. Hammad, J. Nuc. Mat., 55, 177 (1975).

6. N. F. Panayotou, DAFS Quarterly Progress Report, July-September 1982, DOE/ER-0046/11, 10 (1982).

7.0 Future Work

The various parts of the experiment will continue as planned. OWR irradiations should begin by mid-summer of 1984, and a second, long-term RTNS-II irradiation should begin in the latter part of the year.

8.0 Acknowledgements

Many others have contributed to the planning of this experiment, most notably, R.L. Simons, D.G. Doran, N.F. Panayotou, and F.A. Garner.

IMAGE INTERACTION BETWEEN A PRISMATIC DISLOCATION LOOP AND A BUBBLE

W.G. Wolfer, W.J. Drugan, M.F. Wehner (University of Wisconsin), and H. Trinkaus (Oak Ridge National Lab.)

1.0 Objective

Helium bubble formation in metals at temperatures below about half of the melting point and under conditions of high He/dpa ratios has been found to be accompanied by loop punching. In analyzing this process of bubble growth the image interaction with the loop has not been considered because it was unknown. This image interaction has now been evaluated, and it gives rise to an activation barrier for loop punching by overpressurized bubbles.

2.0 Summary

The elastic interaction between a spherical cavity and a prismatic dislocation loop has been derived. In spite of the complexity of the elasticity solution, the image interaction can be written in a relatively simple form and be evaluated readily.

3.0 Program

Title: Effects of Radiation and High Heat Flux on the Performance of First Wall Components
Principal Investigator: W.G. Wolfer
Affiliation: University of Wisconsin-Madison

4.0 Relevant DAFS Program Task/Subtask

II.C.17: Microstructural Characterization
II.B.2.3, Subtask C: Correlation Methodology

5.0 Accomplishments and Status

5.1 Introduction

The formation of highly overpressurized helium bubbles formed during helium implantations in solid is now firmly established experimentally.[1-5] It is also evident that these bubbles may grow at temperatures below about half the melting point by athermal processes, involving the expulsion of either self-interstitial atoms or small prismatic loops.[6-9] The latter may also form by the acclomeration of self-interstitials trapped near the overpressurized bubble. These interstitials originate either from the bubble itself as more helium is trapped inside the bubble, or they are captured from the surrounding matrix where they have been produced by displacement damage.

The basic reason why the interstitials remain trapped near an overpressurized bubble is that a strong attractive image interaction exists. The repulsive interaction caused by the stress field due to the overpressure remains small when a self-interstitial atom or three-dimensional interstitial cluster has a nearly isotropic dipole tensor, i.e. when it can be modeled as a nearly spherical inclusion.[9,10]

If the interstitial cluster assumes however a nonspherical shape and in the extreme becomes a prismatic loop, then the repulsive pressure-induced interaction may overcome the attractive image interaction. The loop is then expelled into the surrounding matrix and the bubble volume expands by the loop volume.[9,10] Further accumulation of helium will repeat the process of interstitial emission, loop formation and expulsion. However, the loop punching process may also take place without the precursor stage of clustering of trapped self-interstitial atoms. In both cases, the energy considerations involving both the image and the pressure-induced interaction remain the same.

The image interaction is the more difficult one to evaluate, and except for the earlier work by Willis and Bullough,[11] it has not been attempted before. Their derivation of the image interaction force is based on an elegant use of the fact that the axial displacement component and the dilatation produced by a prismatic loop on the symmetry axis can be expressed by simple functions. Expansion of these functions in power series yields then the coefficients for another series which describes the displacement field of the loop in the spherical coordinate system of the cavity. The tractions produced by the loop on the cavity surface can then be obtained, and the image field is determined such that its tractions cancel those of the loop. Willis and Bullough obtained thereby the stress components of the image field from which the glide and climb force on the loop can be derived. However, their results for these forces were not expressed in a concise form. Furthermore, to obtain the image interaction energy from their results would require a very cumbersome integration.

If, on the other hand, a sufficiently compact expression can be derived for the image interaction energy, simple derivatives can generate both the glide and climb force on the loop as exerted by the cavity.

Our approach accomplishes this. It uses a Hankel transform representation for the stress field of the prismatic dislocation loop and two relationships which connect zero-order Bessel functions with spherical harmonics. This general method has been employed extensively by Japanese researchers[12-15] for elasticity problems involving spherical cavities.

In the following section the method of solution will be outlined briefly and the final result will be given. The detailed derivation will be published elsewhere.[16]

5.2 Solution of the Elasticity Problem

A prismatic dislocation loop of radius ℓ is situated at a distance D from the center of a pherical cavity of radius a, as illustrated in Fig. 1. For reasons of simplicity, we assume that the loop plane is perpendicular to the polar axis. As a result, the elastic field is axially symmetric and torsion-free, and it can therefore be derived from two harmonic functions Φ and Ψ according to the Boussinesq solution

$$\vec{u} = \vec{\nabla} (\Phi + z\Psi) - 4(1 - \nu)\, \hat{z}\Psi \,. \tag{1}$$

Here, $\vec{u}$ is the displacement field, ν the Poisson's ratio, and $\hat{z}$ is the unit vector along the z-axis.

The total displacement field can now be decomposed into three contributions

$$\vec{u} = \vec{u}^{\ell} + \vec{u}^{p} + \vec{u}^{I} \tag{2}$$

where $\vec{u}^{\ell}$ is the displacement field of the loop in the absence of the cavity, $\vec{u}^{p}$ is the displacement field produced by the overpressurized bubble in the absence of the loop, and $\vec{u}^{I}$ is finally the image field. The latter is independent of $\vec{u}^{p}$, but not of $\vec{u}^{\ell}$. For each displacement field one obtains the associated stress field, so that the total stress at any location is

$$\sigma_{ij} = \sigma^{\ell}_{ij} + \sigma^{p}_{ij} + \sigma^{I}_{ij} \,. \tag{3}$$

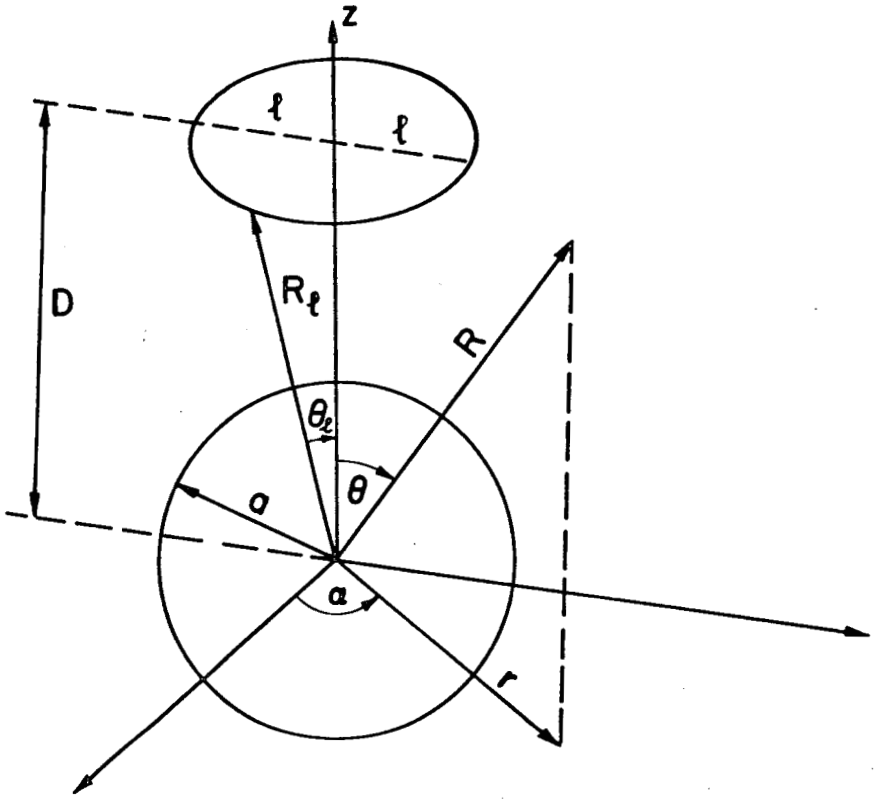

FIGURE 1. Prismatic Dislocation Loop Near a Spherical Cavity.

The image field is now determined by the condition that the tractions produced by σ^{ℓ}_{ij} and σ^{I}_{ij} have to vanish on the cavity surface. If $\vec{n}$ is the normal vector on the cavity surface, then

$$\sigma^{I}_{ij}\, n_j = -\sigma^{\ell}_{ij}\, n_j \,. \tag{4}$$

The pressure-induced field is determined by the condition

$$\sigma^{p}_{ij}\, n_j = -(p - 2\gamma/a) \tag{5}$$

on the cavity surface, where γ is the surface tension.

The first task is to determine the field of the loop. Using the approach of Kroupa[17] we construct it with the help of the two harmonic functions

$$\Phi^{\ell}(r,z) = \int_0^{\infty} d\lambda\, F(\lambda)\, e^{-\lambda|z-D|}\, J_0(\lambda r) \tag{6}$$

$$\Psi^{\ell}(r,z) = \int_0^{\infty} d\lambda\, \lambda G(\lambda) e^{-\lambda|z-D|}\, J_0(\lambda r) \tag{7}$$

expressed in terms of two unknown, zero-order Hankel transforms[18] $F(\lambda)$ and $G(\lambda)$. These are now determined by first deriving the axial displacement component $u^{\ell}_z(r,z)$ and the shear stress component $\sigma^{\ell}_{rz}(r,z)$, and then satisfying the boundary conditions

$$\sigma_{rz}^{\ell}(r,D) = 0 \tag{8}$$

and

$$\lim_{\eta \to 0} u_z^{\ell}(r,D\pm\eta) = \begin{cases} \pm b/2 & \text{for } 0 \leq r \leq \ell \\ 0 & \text{for } r > \ell \end{cases} \tag{9}$$

where b is the Burgers vector. This results in

$$F(\lambda) = -[\lambda D \pm (1 - 2\nu)]G(\lambda) \tag{10}$$

and

$$G(\lambda) = \mp \frac{b\ell}{4(1 - \nu)\lambda} J_1(\lambda\ell) \tag{11}$$

where J_1 is the Bessel function of first order.

The representation of the loop field in cylindrical coordinates is not suitable for evaluating its tractions on the spherical cavity surface. Hence, a representation in spherical coordinates is chosen next with the harmonic functions

$$\phi^{\ell} = \sum_{n=0}^{\infty} F_n R^n P_n(\cos\theta) \tag{12}$$

$$\Psi^{\ell} = \sum_{n=0}^{\infty} G_n R^n P_n(\cos\theta) \tag{13}$$

where P_n is the Legendre polynomial of degree n. Since these functions must be identical to the expressions (6) and (7), the coefficients F_n and G_n are related to the functions $F(\lambda)$ and $G(\lambda)$. This connection can be established with the help of the relationship[19]

$$e^{\lambda z} J_0(\lambda r) = \sum_{n=0}^{\infty} \frac{1}{n!} (\lambda R)^n P_n(\cos\theta) . \tag{14}$$

A length calculation shows that

$$G_n = -\frac{b}{4(1 - \nu)} R^{-n}(\cos\theta P_n - P_{n-1}) \tag{15}$$

and

$$F_n = (1 - 2\nu)\frac{1}{n} G_{n-1} - DG_n \qquad \text{for } n \geq 1 . \tag{16}$$

For $n = 0$, $F_0 = 0$, and $G_0 = b(1 - \cos\theta)/4(1 - \nu)$. The loop field is now determined both in cylindrical and in spherical coordinates for $R \leq a$.

The image field is next derived from the harmonic functions

$$\phi^I = \sum_{n=0}^{\infty} A_n R^{n-1} P_n(\cos\theta) \tag{17}$$

$$\Psi^I = \sum_{n=0}^{\infty} B_n R^{-n-1} P_n(\cos\theta) . \tag{18}$$

From them we derive the stress components $\sigma_{RR}^I(R,\theta)$ and $\sigma_{R\theta}^I(r,\theta)$ and determine the constants A_n and B_n from the boundary conditions (derived from Eqs. (4))

$$\sigma^I_{RR}(a,\theta) = -\sigma^\ell_{RR}(a,\theta) \tag{19}$$

$$\sigma^I_{R\theta}(a,\theta) = -\sigma^\ell_{R\theta}(a,\theta) \ . \tag{20}$$

The lengthy expressions for A_n and B_n will not be shown here.

For obtaining the image interaction E^I, the integral in the following equation must be evaluated.

$$E^I_o = -\pi b \int_o^\ell r \, dr \, \sigma^I_{zz}(r,D) \ . \tag{21}$$

Note that the image stress field must now be expressed in cylindrical coordinates. To accomplish this, we employ the formula

$$R^{-n-1}P_n(\cos\theta) = \frac{1}{n!} \int d\lambda \, e^{-\lambda z} \, J_o(\lambda r) \tag{22}$$

to write the harmonic functions (17) and (18) in terms of the cylindrical coordinates (r,z) which are related to the spherical coordinates (R,θ) by $z = R\cos\theta$ and $r = R\sin\theta$.

The very lengthy derivation will be omitted, but it eventually results in the concise expression

$$E^I_o = -\frac{2\mu V_\ell^2/V_o}{3(1-\nu)} \sum_{n=1}^{\infty} \Big\{ \frac{2[n^2 - n(1-2\nu) + 1 - \nu]}{n(n+1)(2n-1)(2n+1)} \tag{23}$$

$$+ \frac{[(2n+3)(n^2 - 2 + 2\nu) - n(n+1)(2n+1)a^2/R_\ell^2]^2}{2n^2(n+1)(2n+1)(2n+3)[(n+1)^2 + (n+1)(1-2\nu) + 1 - \nu]} \Big\} \Big(\frac{a}{R_\ell}\Big)^{2n+4} (P'_n)^2$$

where

$$P'_n = \frac{dP_n(\cos\theta_\ell)}{d(\cos\theta_\ell)} \tag{24}$$

and R_ℓ is the distance from the cavity center to the dislocation line. It is seen that the image interaction energy is proportional to the square of the loop volume $V_\ell = \pi b \ell^2$ and inversely proportional to the cavity volume $V_o = 4\pi a^3/3$. For large distances, the image interaction energy falls off as $(a/R)^6$.

5.3 Numerical Results

The numerical evaluation of the sum in Eq. (23) can readily be carried out by using the recursion relationship

$$P'_n = \frac{2n-1}{n-1} \cos\theta_\ell \, P'_{n-1} - \frac{n}{n-1} P'_{n-2} \tag{25}$$

for $n > 2$ and the starting values $P'_o = 0$ and $P'_1 = 1$. As R_ℓ approaches the cavity radius a, more and more terms are required to achive a sufficient accuracy. About 1500 terms need to be added when $R_\ell/a = 1.001$.

The numerical results for the image interaction energy are displayed in Fig. 2 for loop radii $\ell \leq 0.1$ a, and in Fig. 3 for loop radii in the range $0.1\ a \leq \ell \leq a$.

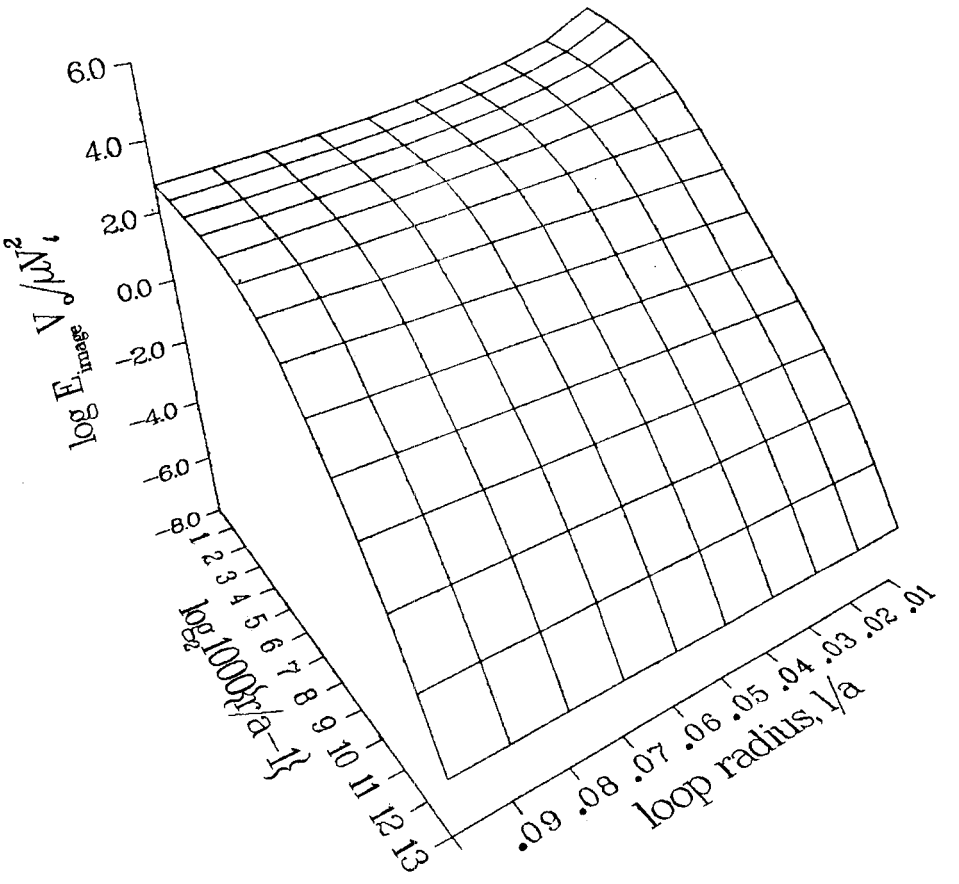

FIGURE 2. Image Interaction Energy of Prismatic Dislocation Loops with Radii $\ell \leq 0.1$ a, Where a is the Cavity Radius.

6.0 References

1. W. Jaeger, R. Manzke, H. Trinkaus, R. Zeller, J. Fink and G. Crecelius, Rad. Effects 78 (1983) 315.
2. R. Manzke, G. Crecelius, W. Jaeger, H. Trinkaus and R. Zeller, Rad. Effects 78 (1983) 327.
3. S.E. Donnelly, A.A. Lucas, J.P. Vigneron and J.C. Rife, Rad. Effects 78 (1983) 337.
4. A.A. Lucas, J.P. Vigneron, Ph. Lambin, S.E. Donnely and J.C. Rife, Rad. Effects 78 (1983) 349.
5. H-G. Haubold, Rad. Effects 78 (1983) 385.
6. J.H. Evans, A. van Veen, and L.M. Caspers, Rad. Effects 78 (1983) 105.
7. G.J. Thomas, Rad. Effects 78 (1983) 37.
8. H. van Swygenhoven and L.M. Stals, Rad. Effects 78 (1983) 157.
9. H. Trinkaus, Rad. Effects 78 (1983) 189.
10. H. Trinkaus and W.G. Wolfer, "Conditions for Dislocation Loop Punching by Helium Bubbles," Report UWFDM-554, Sept. 1983, Proc. 3rd Topical Meeting on Fusion Reactor Matls., Albuquerque, NM, to be published in J. Nucl. Matls.
11. J.R. Willis and R. Bullough, "The Interaction Between a Void and a Dislocation Loop," in Voids Formed by Irradiation of Reactor Matls., Proc. of BNES, Europ. Conf., Reading, March 1971, Ed. by S.F. Pugh, M.H. Loretto and D.I.R. Norris, p. 134.

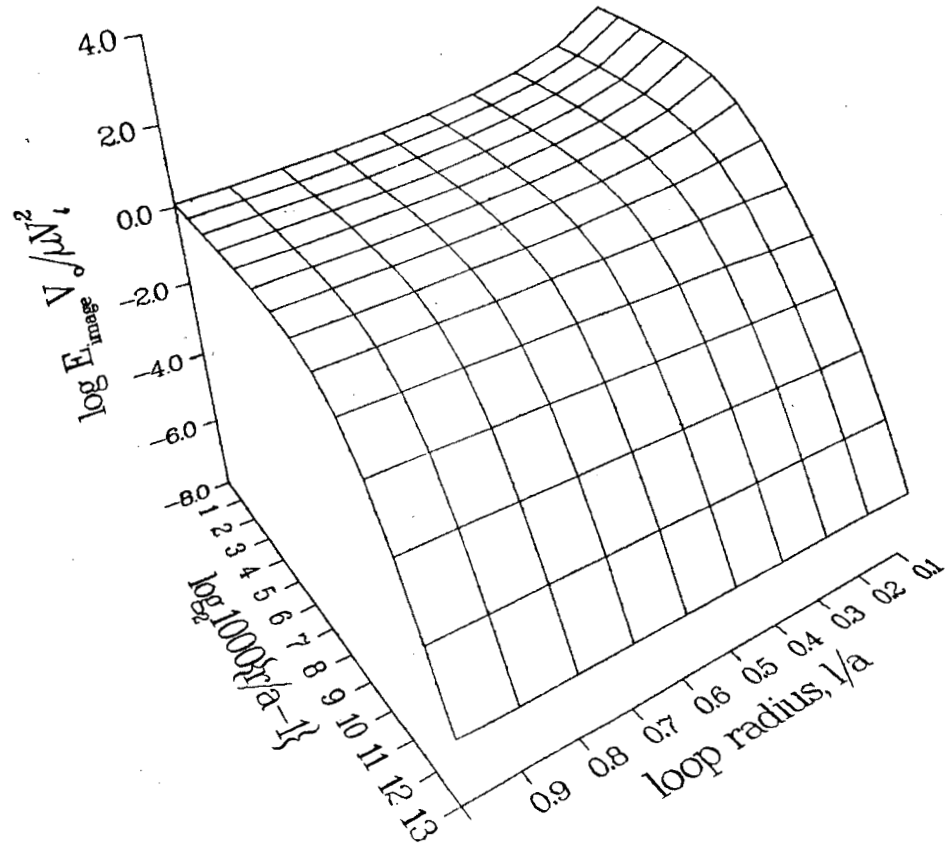

FIGURE 3. Image Interaction Energy of Prismatic Dislocation Loops with Radii in the Interval 0.1 a ≤ ℓ ≤ a.

12. E. Tsuchida and I. Nakahara, Bull. JSME 13 (1970) 499.

13. E. Tsuchida and I. Nakahara, Bull. JSME 15 (1972) 1.

14. H. Hirai and M. Satake, J. Appl. Mechanics 47 (1980) 806.

15. A. Atsumi and Y. Shindo, Int. J. Engng. Sci. 21 (1983) 269.

16. W.G. Wolfer and W.J. Drugan, to be published in J. Appl. Mechanics.

17. F. Kroupa, Czech. J. Phys. B10 (1960) 284.

18. I.N. Sneedon, Fourier Transforms, McGraw Hill, New York, 1951, p. 514.

19. P.M. Morse and H. Feshback, Methods of Theoretical Physics, Vol. 2, McGraw-Hill, New York, 1953, p. 1318.

7.0 Future Work

For a comprehensive assessment of the loop punching and loop expulsion mechanism two additional interaction energies are required: the pressure-induced interaction and the compressibility interaction. The former is caused by the stress-field of the overpressurized bubble, whereas the latter originates from the pressure change in the bubble as the loop changes its distance from the bubble. Their evaluation will be reported in future contributions.

STABILITY OF HELIUM-VACANCY CLUSTERS DURING IRRADIATION

Shahram Sharafat and Nasr M. Ghoniem (UCLA)

1.0 Objective

One of the major uncertainties in understanding cavity nucleation and growth is the degree of stability of Helium-Vacancy Clusters (HVCs) in an irradiation field. Such stability is a complex function of irradiation variables (damage rates, helium production rates, and fluence), as well as material parameters (sink density, temperature, and defect parameters). The goal of investigating the stability of HVCs is to understand and consequently to model cavity size distributions.

2.0 Summary

The present research first investigates helium-vacancy binding energies, which are then used in analyzing the stability of HVCs under irradiation. Using an equation of state (EOS) for helium that takes into account the high pressures caused by large He/V ratios in HVCs we have demonstrated the following:

1. A continuum approach has been used to solve for Vacancy and Helium Binding Energies for large clusters which match well with atomistic calculations for very small HVC.
2. Utilizing these binding Energies in a nodal-line formulation, critical HVC sizes have been determined as a function of He/dpa ratios.
3. Regimes of spontaneous and delayed nucleation have been identified as a function of temperature and He/dpa ratios for both reactor and accelerator conditions.
4. Consistent with experimental results, we always find delayed cavity nucleation for EBR-II irradiation conditions. In HFIR, a transition from spontaneous to delayed nucleation occurs at higher temperatures. This is also consistent with experimental findings.
5. In accelerator conditions, we find a shift in the demarkation line between spontaneous and delayed nucleation by about 50 to 100°C. This shift is due to increased dynamic cavity formation processes compared to thermal dissociation mechanisms.
6. The exact temperature separating spontaneous and delayed nucleation is sensitive to the re-solution parameter. This fact can be used in experiments designed to measure this parameter.

3.0 Program

Title: Stability of Helium-Vacancy Clusters During Irradiation
Principal Investigator: N. M. Ghoniem
Affiliation: University of California at Los Angeles

4.0 Relevant DAFS Program Plan Task/Subtask

Subtask Group C: Damage Microstructure Evolution and Mechanical Behavior

5.0 Accomplishments and Status

5.1 Introduction

Helium introduced by (n, α) reactions is thermodynamically insoluble and thus tends to precipitate into cavities. Whereas helium concentrations in steels typical of fast breeder reactors are in the range 1-10 atppm/year, expected concentrations in fusion reactor environments are about 2 orders of magnitude greater.

Since the displacement rates in these two types of reactors are comparable, the helium to displacement ratio (He/dpa) will be a crucial factor in simulating fusion environments. The He/dpa ratio has a profound influence on the stability of HVCs, as will be discussed later. The stability of a HVC dictates the critical size or He/V ratio which ensures growth. The critical size of HVCs affects the size distribution, which determines the nature of detrimental helium effects on material properties. Two levels of analyses have generally been used to study the degree of stability of HVCs. The first is an atomistic[1] approach in which HVCs are analyzed using appropriate interatomic potentials. Stable configurations and He/V ratios, as well as binding and migration energies are found. Disadvantages of this approach are: (1) the method is not applicable to large size clusters; (2) the effect of kinetic processes due to irradiation cannot be included. On the other hand, purely kinetic descriptions are used to derive simplified analytic expressions for the "critical cavity size" for cavity growth and nucleation[2-3]. This approach may ignore important detailed mechanisms.

The present study is aimed at identifying the mechanisms influencing the binding of the last vacancy and the last helium to a cluster. Binding energy calculations are based upon high-density equations of state for helium. Those equations are quite realistic since they are based on interatomic helium-helium potentials. A nodal-line stability analysis is then performed to define the stability boundaries in a two-dimensionsal vacancy-helium phase-space. Those are determined by solving for the equilibrium conditions coresponding to the emission of the last vacancy, and the last helium atom from a cluster.

5.2 Binding Energies

Atomistic calculations by Wilson et al.[1] have provided binding energies for small clusters. However, these calculations can not be extended to investigate larger size HVCs. To obtain reasonable results for large HVCs (He>20; V>2) we must resort to continuum approaches. This leads to the question of a valid equation of state (EOS) for helium that takes into account the high pressures caused by large He/V ratios in HVCs. Such a numerical equation has been formulated by Wolfer et al.[4] using an interatomic He-He potential.

The work done in compressing residing helium atoms when a vacancy is emitted from the cluster is calculated by:

$$W = -\int_{V_1}^{V_2} P \, dV \qquad (1)$$

Expressing the pressure in terms of virial coefficients:

$$\frac{PV}{kT} = z = 1 + \frac{B}{V} + \frac{C}{V^2} + \ldots \qquad (2)$$

and substituting (2) into (1) we obtain, using up to 3 virial coefficients, the following expression for the work:

$$W = -kT\{\ln\left(\frac{V_2}{V_1}\right) - B\left(\frac{1}{V_2} - \frac{1}{V_1}\right) - \frac{C}{2}\left(\frac{1}{V_2^2} - \frac{1}{V_1^2}\right)\} \qquad (3)$$

The virial constants, B and C, are obtained by fitting equation (2) to Wolfer's EOS over a limited pressure range. Knowing the work done in compressing helium atoms, we now estimate the binding energy (E_v^B) of the last vacancy by adding the energy gained due to the change in surface area (ΔE_S) and the vacancy formation energy (E_v^F) :

$$E_v^B = E_v^F + \Delta E_s + W \qquad (4)$$

The results of such calculations for Ni-parameters are shown in Fig.1.

Comparing our results to the atomistic calculations of Wilson and Baskes[1], satisfactory agreement has been found, down to small sizes of HVCs.

In evaluating the helium-binding energy, we use a straight line approximation for evaluating the change in energy content of the HVC; and equation (1) is approximated by:

$$W = -\frac{1}{2}\,[P_2 + P_1][V_2 + V_1] \qquad (5)$$

This approach has been chosen because we no longer have a thermodynamic system of constant mass when a helium atom is emitted. By reducing the helium content of the HVC by one atom, we effectively evaluate the energy gained in allowing n-1 Helium to atoms expand to a new low pressure.

The helium-binding energy is evaluated by adding the energy of the "Heat of Solution" of helium to the expansion work. Ingelsfield and Pendry[5] concluded that it takes at least 2.07 eV to keep a helium atom dissolved in a Molybdenum matrix. We have used $E_H^S = 3.5$ eV because no precise value is yet available.

5.3 Nodal Line Analysis

Nodal line analysis has been developed for stability studies of kinetic systems. Recently, Russell[6] used the same approach to analyze phase stability under irradiation. We follow here a similar method for the linear stability analysis of helium-vacancy clustering. An important aspect of our work is, that we use vacancy and helium binding energies instead of changes in free energy to describe various HVC growth and shrinkage processes under irradiation.

We begin by considering HVCs as characterized in a two-dimensional phase space. In such a phase-space, kinetic processes can be represented schematically. An HVC can grow by capturing a vacancy or helium atom ($R_{v,h}^c$) , or by emitting a self-interstitial atom (SIA) (R_i^e) . Also it may shrink by thermal emission of either vacancy or helium atom ($R_{v,h}^e$) , or by capture of SIAs (R_i^c) , or by a gas-replacement mechanism (R_i^{gr}) or due to PKA's (R_h^r) . The summation of these rates results in corresponding component velocities in phase space, given by:

$$\dot{v} = R_v^c - R_v^e - R_i^c \qquad [6]$$

$$\dot{h} = R_h^c - R_h^e - R_i^{gr} - R_h^r \qquad (7)$$

The rates in equations (6) and (7) are calculated by using quasi steady-state values for C_v, C_i, and C_{He}. In the present analysis we ignore SIA emission.

Ghoniem and Gurol[7] showed approximations for vacancy and SIA concentrations. With knowledge of an effective helium diffusion coefficient[8] as a function of C_V and C_i, we were able to estimate a quasi steady-state helium concentration.

By setting $\dot{v} = 0$ and $\dot{h} = 0$ and plotting the loci of points which satisfy this condition in the helium-vacancy phase-space, we find the helium and vacancy nodal lines. By investigating the trajectories in the vicinity of these nodal lines, regions of growth or shrinkage of HVCs in this phase-space can be determined, as shown in Fig. 3.

We find that:

* In region I, HVCs grow in vacancy but shrink in He-atom content.
* In region II, HVCs shrink in both number of vacancies and He-atoms.
* Region III lets HVCs grow in helium contents but they shrink by a net loss of vacancies
* Only in region IV do all HVCs experience growth in both number of vacancies and number of He-atoms.

Thus region IV can be termed the "region of stability" which will ensure growth of HVCs. The boundary of this growth region thus separates the stable from unstable HVCs. We can therefore view the HVCs residing on the boundaries of region IV as the "critical HVCs".

5.4 Discussions

5.4.1 Binding Energies

Of Particular interest is a comparison between our continuum binding energy calculations to atomistic calculations performed by Wilson et al.[1]. This determines the smallest HVC size to which our continuum approach may still be valid.

A series of 2-D plots comparing our results of binding energies to those of Wilson et al.[1] were produced, (see Fig. 4). Agreement between atomistic and continuum calculation increases as the size of the HVC increases. From these comparisons, it can be seen that our approach is applicable to HVCs containing as little as 2 or 3 vacancies.

5.4.2 Cavity Nucleation

We have found, using the nodal line analysis/clustering method, that there are two general nucleation modes. In the first one, helium precipitation in bubbles occures spontaneously (see Fig. 2). Very small nucleation barriers exist in this case, and nucleation proceeds homogeneously in the matrix. This occurs under irradiation conditions of high helium generation rates, low temperature, and low sink density. The high helium generation rates tip the competition for vacancies between SIAs and helium atoms in favor of helium atoms. This reduces vacancy anihilation rates and gas-replacement rates by SIAs, and the chance for fundamental HVCs surviving is enhanced.

The second mode of nucleation is that of delayed nucleation (see Fig. 3). Here, cavity formation proceeds with substantial nucleation barriers (such as regions I, II or III in Fig. 3), which must be overcome by subcritical HVC embryos, in order to reach stable configurations. This case is best achieved at high temperatures, high dislocation sink density and low helium generation rates. The combination of high temperature and high sink density renders short defect mean-life times. These coupled with low helium generation rates increased SIA's chances in competing against helium for vacancies. These effects (nucleation barriers) supress the production of stable HVC embryos. Therefore stable HVCs must be produced by some mechanism, such as a stochastic one, able to overcome the nucleation barriers.

5.4.3 Spontaneous and Delayed Nucleation Regimes

To simulate fusion irradiation environments with existing facilities, extensive use has been made of the HFIR, the EBR-II, and accelerators. These facilities differ mainly in their He/dpa ratios. In HFIR the He/dpa ratio is 57 while in EBR-II it is 10^{-6} dpa/sec of damage production.

The basic experimental findings[9] concerning cavities in the temperature range of 300 to 650°C are as follows: (1) in HFIR cavities appear to be bubbles rather than voids, (2) they are about 10 times smaller, and (3) they are 20 to 50 times more numerous in HFIR than voids are in EBR-II irradiated steels.

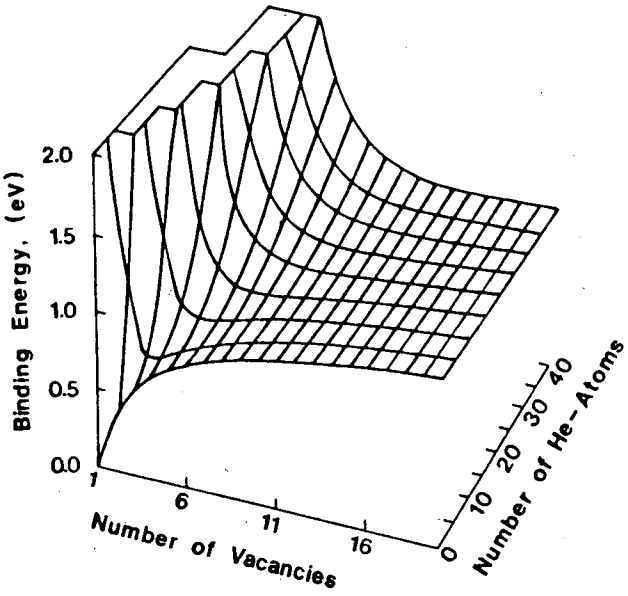

FIGURE 1. Vacancy Binding Energy to a HVC.

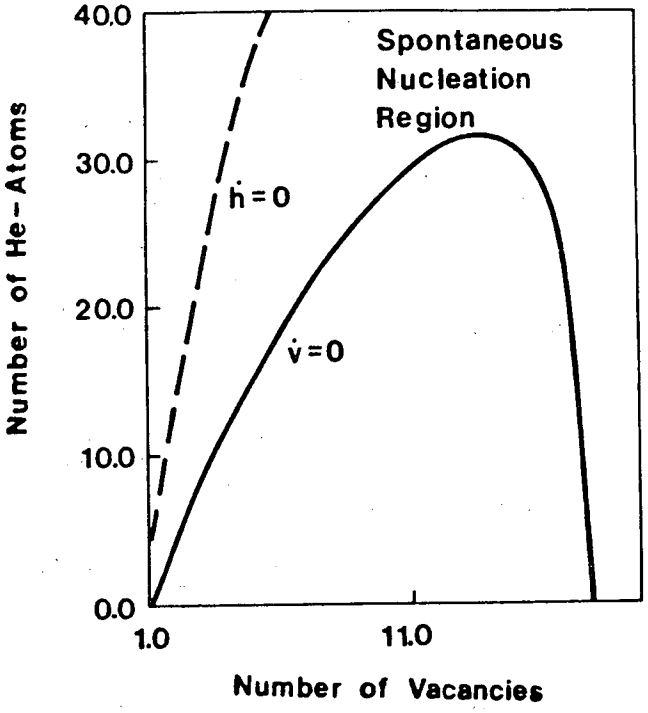

FIGURE 2. Stability Analysis for HVC Showing Spontaneous Nucleation ($T = 500^{o}C$, $\varrho = 10^{18}$ cm^{-2}).

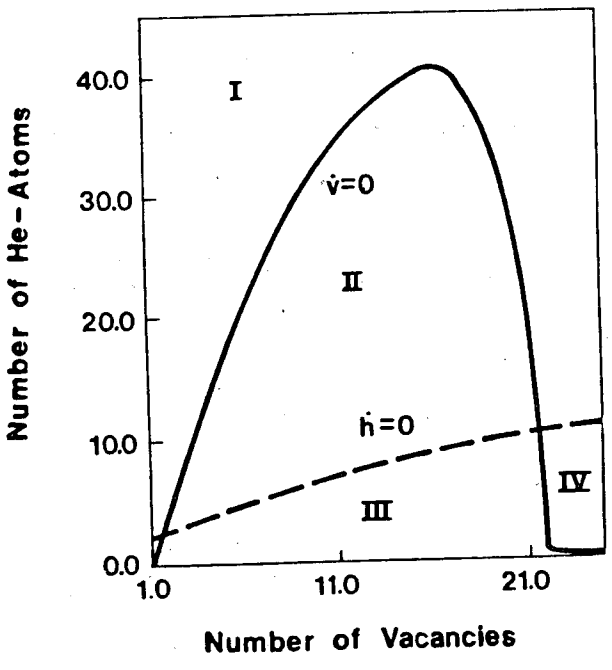

FIGURE 3. Stability Analysis for HVC Showing Delayed Nucleation ($T = 500^{o}C$, $\varrho = 10^{11}$ cm^{-2}).

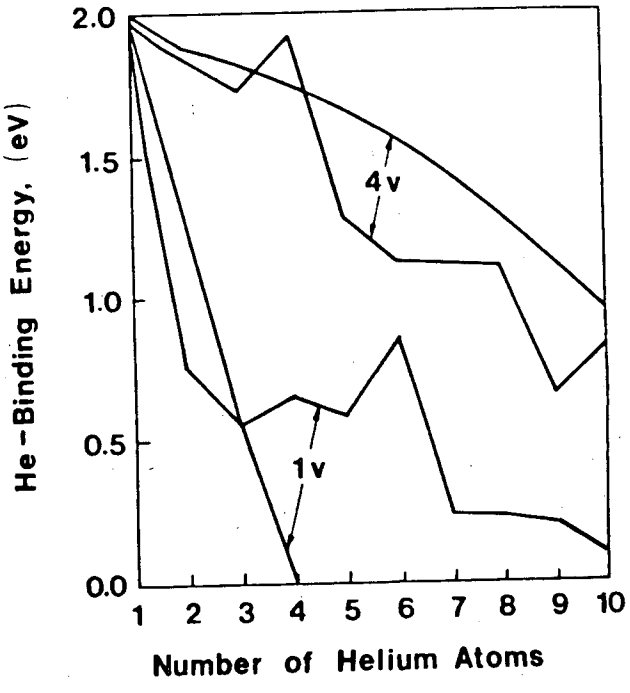

FIGURE 4. Comparison of Atomistic-to-Continuum Helium Binding Energies to a Single- and Four-Vacancy Cluster (contiuum-smooth curve).

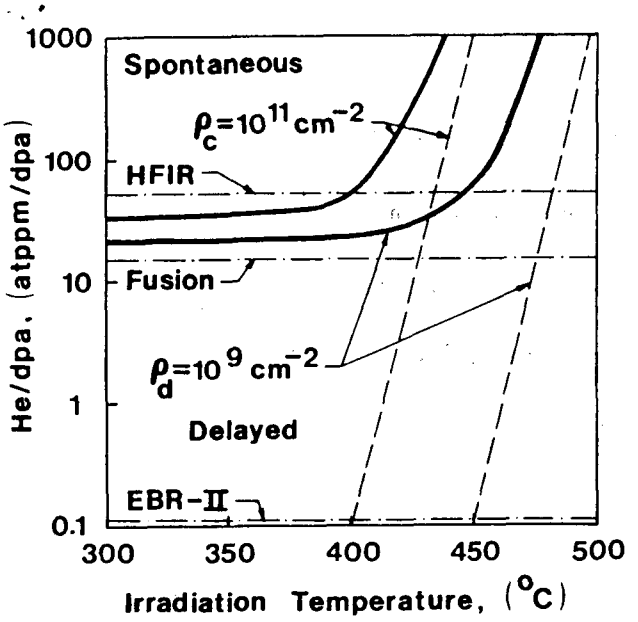

FIGURE 5. Nucleation Regime Analysis for Reactor Conditions Showing Spontaneous and Delayed Regions (dotted line is resolution parameter = 0).

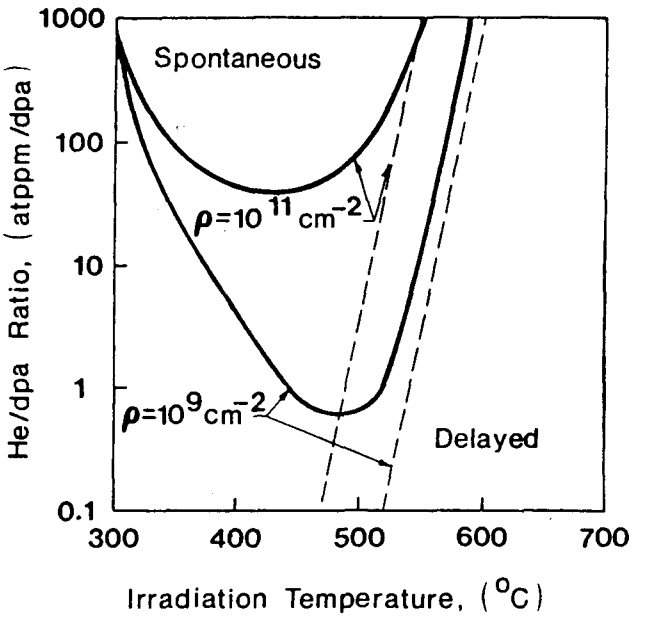

FIGURE 6. Nucleation Regime Analysis for Accelerator Conditions Showing Spontaneous and Delayed Regions (dotted line is resolution parameter = 0).

Scanning a temperature range between 300 and 650°C with other irradiation conditions (He/dpa ratio, dislocation sink density, and dpa) fixed, we were able to trace the loci of points which seperate regions of spontaneous from delayed nucleation as a function of temperature and He/dpa ratios (see Figures 5 and 6).

We find (Fig.5) for EBR-II irradiation that all cavity nucleations proceed as "delayed". Nodal line analysis for EBR-II conditions show strong nucleation barriers, such as shown by region II in Fig. 3. Nucleation of critical HVCs is delayed because any size HVC outside of region IV disossociates to subcritical clusters. When the He/dpa ratio is increased, the nucleation barrier, region II, (see Fig.3) is reduced until it vanishes completely. These conditions are met in HFIR experiments where small cavities with a high number density are found.

Decreasing the dislocation line density shifts the spontaneous nucleation region to higher temperatures and lower He/dpa ratios (see Figurs 5 and 6).

Investigating accelerator conditions (10^{-3} dpa/sec) similar spontaneous and delayed nucleation regimes can be identified (see Fig.6). The basic difference as compared to reactor conditions (10^{-6} dpa/sec) can be seen in the low temperature region. Here we see the reappearance of nucleation barrier after a minimum between 400 and 500°C. The growth of the nucleation barrier shifts the nucleation mode back into the delayed one. This can be explained by the high re-solution taking place in accelerator environments. As the temperature is increased from 300 to 400°C, the re-solution becomes less significant, because helium capture rates increase with increasing temperature. By further increasing the temperature beyond 500°C, the helium emission rates take over and the nucleation barriers become stronger.

This high temperature behavior of HVC number densities in accelerator environments has been established experimentally[10] as a function of temperature and He/dpa ratios.

The effect of HVC re-solution at lower temperatures (<400°C) can be investigated in the following manner: The dashed line in Figures 5 and 6 represents the same calculations but with the re-solution parameter set equal to zero. In a parametric study we can vary the re-solution parameter. Experiments at low temperatures could be performed and the best fit for our parametric study would then allow us to deduce a value for the re-solution parameter.

6.0 References

1. Wilson, W.D., Bisson, C.L., and Baskes, M.I., "Self Trapping of Helium in Metals", Phys. Rev.B, 24(1981)5616-5624.

2. Mansur, L.K., and Coghlan, W.A., "Mechanisms of Helium Interaction with Radiation Effects in Metals and Alloys," to be publ. in J. Nucl. Materials.

3. Hishinamu, A., and Mansur, L.K., "Critical Radius for Bias-Driven Swelling," to be publ.

4. Wolfer, W.G., "High-Density Equation of State for Helium and its Application to Bubbles in Solids", Effects of Radiation on Materials: Tenth Conference, ASTM STP 725. 1981, pp. 201-212.

5. Inglesfield, J.E., and Pendry, J.B. Phil. Mag., 34(1976)205-215.

6. Maydet, S.I., Russel, K.C., J. Nucl. Materials, 82(1979)271-285.

7. Ghoniem, N.M., Gurol H., Radiation Effects, 55(1981)209-222.

8. Ghoniem, N.M., Sharafat, S., Mansur, L.K., "The Theory of Helium Transport and Clustering in Materials Under Irradiation," J. Nucl. Materials 117(1983)96-105.

9. Masiasz, P.J., and Grossbeck, M.L., J. Nucl. Materials 103&104(1981)987-992.

10. Snykes, M., and Ruedl, E., J. Nucl. Materials, 103&104(1981)1075-1078.

FUNDAMENTAL ALLOY STUDIES

H. R. Brager and F. A. Garner (Hanford Engineering Development Laboratory)

1.0 Objective

The object of this effort is to provide an alloy series with which to investigate the fundamental nature of swelling and creep resistance in Fe-Cr-Ni and Fe-Cr-Mn alloys.

2.0 Summary

A series of four alloy groups have been produced to investigate the origin of swelling and creep resistance in the Fe-Ni-Cr austenitic system and also to explore the possible existence of a high swelling resistance in the corresponding Fe-Cr-Mn austenitic system. This extension is based on a correlation observed between swelling resistance and the analomous property regime commonly referred to as the Invar regime. Many of these alloys have recently been included in irradiation experiments conducted in EBR-II, HFIR and FFTF.

3.0 Program

Title: Irradiation Effects Analysis (AKJ)
Principal Investigator: D. G. Doran
Affiliation: Hanford Engineering Development Laboratory

4.0 Relevant DAFS Plan Task/Subtask

Task II.C.1 Effects of Material Parameters on Microstructure
Task II.C.16 Composite Correlation Models and Experiments

5.0 Accomplishments and Status

5.1 Introduction

The compositional dependence of swelling in Fe-Ni-Cr ternary alloys has been explored in a series of recent reports.[1-3] It was shown that the compositional dependence resides primarily in the transient regime of swelling and that the greatest resistance to swelling occurs in the compositional regime where the nickel content is between 35 and 45% and the chromium content is less than 15%. This regime is also characterized by anomalous property behavior where many physical properties such as thermal expansion, elastic moduli, lattice parameter and excess free energy exhibit a marked variation with composition. This anomalous behavior is best exemplified by the Invar phenomenon, wherein the thermal coefficient of expansion reaches a minimum near Fe-35Ni. At another composition, Fe-7.8Cr-35Ni, the thermoelastic coefficient indeed becomes zero over a significant temperature range. This composition is known as Elinvar and fortuitously corresponds almost exactly with the composition of one of the most swelling-resistant ternary alloys previously irradiated in the range 400-650°C. This alloy is designated as E37 and has the composition Fe-7.5Cr-35.5Ni.

Perhaps it is only coincidental that the Invar and particularly the Elinvar compositions correspond to the region where the duration of the transient regime of Fe-Ni-Cr austenitic alloys appears to be the longest. If one evaluates the current theories of void swelling, however, it appears that parameters such as lattice parameter and elastic moduli indeed are important determinants of swelling behavior, particularly when radiation-induced segregation occurs at void surfaces.[6] Accordingly, we suggest that a direct connection may exist between the anomalous behavior regime and maximum swelling resistance. Another factor also

appears to contribute to the compositional dependence of swelling and that is the sensitivity of elemental diffusivities on the nickel and chromium content of the alloy.[7,8]

In order to explore the potential of the Invar-swelling resistance correlation, four fundamental alloy series have been developed. Each of these is explored in the following sections.

5.2 Phase I: Fe-Ni-Cr Simple Ternary Alloys (DAFS-Funded)

The ion irradiation experiments of Johnston and coworkers did not explore the anomalous compositional regime in any great detail, as shown in Figure 1, but it is clear that a strong resistance to swelling resides in this region.[9] The Phase I alloy series is designed to explore the radiation-induced microstructural evolution of this compositional regime. It contains twenty-five alloys, five of which are original alloys of Johnston,[9] one of which is the swelling resistant E37 and twelve new heats. The compositions of these alloys are shown in Figure 2 and Table 1. With one exception all alloys were prepared in the annealed condition (1030°C for 30 minutes). The alloy E37 is also included in the 20% cold-worked condition to determine whether cold-working has any effect on the radiation-induced elemental segregation that occurs in this alloy.[3,4] In at least one Fe-Ni-Cr-Mo alloy there does not appear to be any effect of cold-work on void formation and this insensitivity has been attributed to the absence of solutes such as silicon and carbon.[10] Specimens of a well-characterized heat of AISI 316 (FFTF first-core heat 81592) in the solution-annealed condition were also included to serve as a reference point.

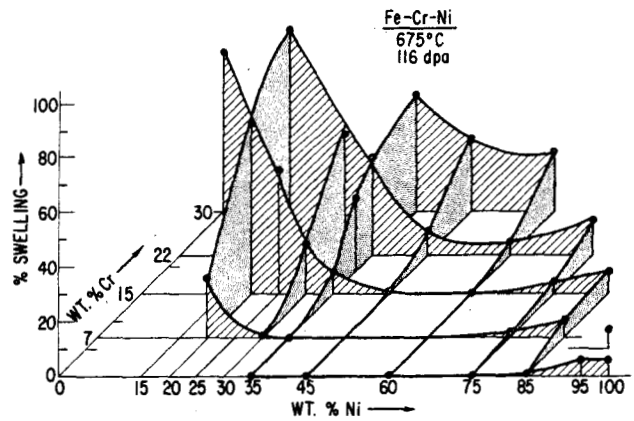

FIGURE 1. Compositional Dependence of Swelling in Fe-Ni-Cr Alloys as Observed by Johnston and Coworkers Using 5 MeV Ni^+ Ions.[9]

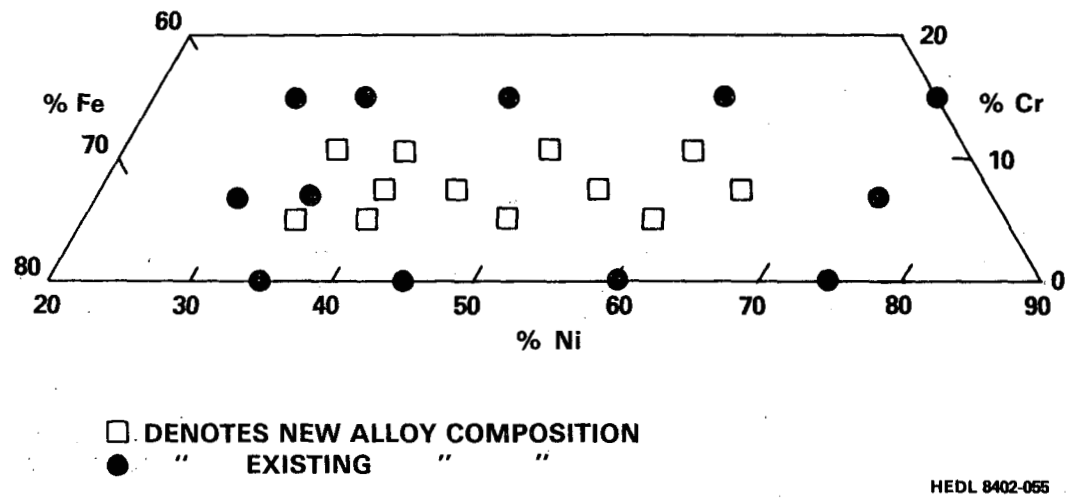

FIGURE 2. Composition of Phase-I Fe-Ni-Cr Ternary Alloys.

COMPOSITION OF Fe-Cr-Ni ALLOYS IN PHASE I

Alloy No.	New Alloys (wt%) Fe	Cr	Ni	Alloy No.	Existing Alloys (wt%) Fe	Cr	Ni
				G22*	63	7	30
R8*	60	5	35	E21	55	15	30
R7*	54	11	35	G5*	65	0	35
R6*	55	5	40	G6	58	7	35
R14*	52.5	7.5	40	G7*	50	15	35
R5*	49	11	40	G10*	55	0	45
R4*	47.5	7.5	45	G11*	40	15	45
R9*	45	5	50	G26	40	0	60
R3*	49	11	50	G13	25	15	60
R10*	37.5	7.5	55	G29	25	0	75
R11	35	5	60	G71	18	7	75
R12	29	11	60	G14	10	15	75
R13	27.5	7.5	65	E37*	57.5	7.5	35

*These alloys were included in the MOTA experiment discussed in Section 5.7.

5.3 Phase II: Minor Solute Additions to Fe-Ni-Cr Ternary Alloys (DAFS-Funded)

The annealed E37 ternary alloy exhibits a swelling resistance superior to solute-laden cold-worked alloys such as AISI 316. It is not anticipated that in the unmodified condition that E37 would serve as a structural alloy, however. Solute additions are known to provide a wide range of austenitic alloys with improved strength and enhanced resistance to swelling and creep.[5] Unfortunately, these same solutes often also participate in the development of radiation-induced phase instabilities. In order to assess the potential for extending the swelling resitance of a known low-swelling alloy (E37), fifteen fundamental alloys representing solute modifications of E37 were produced. To develop both strength and acceptable ductility, both solid-solution-strengthening and precipitate-strengthening were employed, the latter provided by MC carbides and/or γ' precipitates based on Al and Ti. The Al and Ti levels are significantly lower than that employed in the nickel base superalloys in an attempt to avoid the low ductility often observed in super-alloys after irradiation. Large silicon additions were avoided due to silicon's strong role in radiation-induced segregation and phase stability.[5]

All fifteen alloys were prepared in the 20% cold-worked condition to capitalize on the often-demonstrated benefit of cold-work in delaying the swelling of solute-modified alloys. Eight of these alloys were also prepared in various cold-worked and aged conditions and two were prepared in the annealed condition. The compositions of these alloys are shown in Table 2a.

5.4 Phase III: Manganese Substitutions for Nickel (Fe-Mn-Cr) (DAFS-Funded)

There are several reasons for exploring the possibility that successful fusion-relevant alloys might be developed by substituting manganese for nickel. Nickel is a strategically sensitive material in the U.S. Nickel also leads to higher residual activation than does manganese.[11] The reduction of activation levels to meet criteria for shallow land burial is a recently adopted objective of the alloy development program.

Even more importantly there exist manganese-based Invar-like alloys (Fe-30Mn and Fe-30Mn-10Cr) with the possible potential of a swelling resistance comparable to that of Fe-Ni-Cr Invar alloys.[12/13] A review of the available literature on Fe-Mn-Cr alloys reveals that the Invar region has not been adequately explored. Most commercial developmental efforts have concentrated on alloys having lower levels of manganese.

It was therefore decided to explore two compositional ranges. The first is Fe-30Mn(0-10)Cr range and the second is closer to the existing commercial range, Fe-15Mn(5-15)Cr, as shown in Table 3. Ten simple Fe-Cr-Mn ternaries were selected to bridge both regimes.

TABLE 2a

COMPOSITION OF SOLID-SOLUTION-STRENGTHENED ALLOYS USED IN PHASE II

	R15*	R16	R17	R18	R19	R20	R21	R22*	R23	R24	R25*	R26*	R27*	R28	R29
Fe	Bal	Bal	Bal	Bal	Bal	Bal	Bal	Bal	Bal	Bal	Bal	Bal	Bal	Bal	Bal
Ni	40.0	40.0	40.0	40.0	40.0	40.0	40.0	40.0	40.0	40.0	40.0	40.0	40.0	35.0	25.0
Cr	7.5	7.5	11.0	7.5	7.5	7.5	7.5	7.5	5.0	7.5	7.5	7.5	7.5	7.5	7.5
Mn	2.0	2.0	2.0	2.0	2.0	2.0	2.0	2.0	2.0	2.0	2.0	2.0	2.0	2.0	2.0
Mo	1.0	1.0	1.0	2.0	1.0	1.0	1.0	1.0	1.0	3.0	2.0	1.0	1.0	1.0	1.0
Si	0.1	0.1	0.1	0.1	0.1	0.1	0.1	0.1	0.1	0.1	0.1	0.0	0.1	0.1	0.1
C	0.02	0.02	0.02	0.02	0.0	0.05	0.02	0.02	0.02	0.02	0.0	0.02	0.08	0.02	0.02
Ti	0.01	0.1	0.1	0.1	0.1	0.2	0.1	0.1	0.1	0.1	0.1	0.1	0.2	0.1	0.1
Nb	0.1	0.1	0.1	0.1	0.1	0.1	0.1	0.1	0.1	0.1	0.4	0.1	0.4	0.1	0.1
P	0	0	0	0	0	0.0	0.03	0.03	0	0	0	0	0	0	0
B	0.0	0.005	0	0	0	0	0	0.005	0	0	0	0	0	0	0
W	0	0	0	0	0	0	0	0	0	0	1.0	0	0	0	0

TABLE 2b

COMPOSITION OF PRECIPITATION-STRENGTHENED ALLOYS USED IN PHASE II

	R90*	R91*	R92*	R93*	R94*	R95*	R96*	R97*	R98*	R99*
Fe	Bal	Bal	Bal	Bal	Bal	Bal	Bal	Bal	Bal	Bal
Ni	40.0	40.0	40.0	42.5	40.0	40.0	40.0	35.0	25.0	40.0
Cr	7.5	7.5	7.5	7.5	7.5	7.5	7.5	7.5	7.5	11.0
Mn	2.0	2.0	2.0	2.0	2.0	2.0	2.0	2.0	2.0	2.0
Mo	1.0	2.0	1.0	1.0	1.0	2.0	1.0	1.0	1.0	1.0
Si	0.1	0.1	0.1	0.1	0.1	0.5	0.1	0.1	0.1	0.1
C	0.08	0.08	0.08	0.02	0.02	0.08	0.02	0.08	0.08	0.04
Ti	0.2	0.2	0.4	0.82	0.41	0.2	0.2	0.4	0.4	0.2
Nb	0.4	0.4	0.1	0.1	0.1	0.4	0.1	0.1	0.1	0.1
P	0.04	0.04	0.04	0.04	0.04	0.04	0.08	0.04	0.04	0.04
B	0.005	0.005	0.005	0.005	0.005	0.005	0.005	0.005	0.005	0.005
W	0	1.0	0	0	0	1.0	0	0	0	0
Al	0	0	0.05	0.30	0.15	0	0	0	0	0

*These alloys were included in the MOTA experiment discussed in Section 5.7.

5.5 Phase IV: Minor Solute Additions to Fe-Mn-Cr Alloys (ADIP-Funded)

Fifteen solute-modified simple Fe-Cr-Mn alloys were developed to assess the impact of solutes on the basic ternary behavior. These are described in Table 4.

In addition, five representative commercial alloys were selected from the twenty or so major Fe-Mn-Cr alloys discussed in the literature. The selection criteria were the availability of the alloys, availability of performance data and selection of compositions which lie in the proximity of existing low activation guidelines. Table 5 lists the designations and compositions of these alloys.

Most of these alloys were prepared in the 20% cold-worked condition, but ten were also prepared in the cold-worked and aged condition, two in the annealed condition and four in the annealed and aged condition.

5.6 Stability of Manganese-Substituted Alloys

While much attention has been directed toward the stability during irradiation of the Fe-Cr-Ni system, there are only a few sets of charged particle irradiation data for alloys the Fe-Mn-Cr and Fe-Ni-Mn-Cr systems.[14-16] These data indicate that manganese-substituted alloys are not immune from swelling and that radiation-induced phase instabilities can occur.

Therefore the Phase III and Phase IV alloys will be used to address the following fundamental questions.

(a) Is the correlation between swelling resistance and Invar-like behavior retained in the Fe-Mn and Fe-Mn-Cr systems?

(b) In Fe-Cr-15Mn alloys, does manganese segregate during irradiation in a manner similar to that of nickel? If such segregation occurs will it lead to a loss of austenite stability and/or a loss of swelling resistance?

(c) Are there any unanticipated phenomena or weaknesses that develop in this alloy system during irradiation?

The concern over radiation-induced loss of stability is of course predicated on the condition that the alloy is sufficiently stable in the absence of irradiation. There are three approaches being used to assess the ex-reactor stability of these alloys. The first is to thermally age the alloys and such ageing studies are currently underway. This is particularly necessary for commercial and developmental solute-modified alloys.

For simple ternaries, one can employ the equilibrium phase diagrams in the relevant temperature range. Figure 3a shows such a diagram for the various manganese-substituted alloy subsets. While these diagrams are not strictly applicable for the solute-modified alloys, they offer a convenient way to demonstrate the compositional range of the various alloy subsets as shown in Figures 3b and 3c.

Equilibrium phase diagrams might not adequately represent the more harsh conditions experienced by the alloys during welding, however. The Schaeffler diagram can be used to make a rough assessment of the stability of these alloys during welding and it has the additional advantage of incorporating the influence on stability of the major solute elements.[17] As shown in Figure 4a, all but one of the commercial alloys lie well within the austenite phase regime.

Figure 4b shows, however, that on the Schaeffler diagram none of the simple Fe-Mn-Cr ternary Phase III alloys are expected to be fully austenitic after welding. Published information on wrought alloys in the composition range shows that these alloys can be fully austenitic, however.[18] The Schaeffler diagram of Figure 4c shows that the solute-modified Phase IV ternaries are expected to be fully austenitic after welding.

5.7 Irradiation Experiments in Progress

Portions of these four alloy series and one previously developed solute-modified Fe-Ni-Cr alloy series[19] have been included in various on-going irradiation experiments.

Fifteen of the alloys from the Phase I and Phase II studies (designated by asterisks in Tables 1 and 2) were included in the MOTA 1B experiment in FFTF, along with all of the Phase III and Phase IV alloys. This experiment is projected to operate at three temperatures (400, 500, and 600°C) and reach four fluence levels, the first being 15 dpa at the end of FY84. A total of 720 TEM disks involving the 30 manganese-substituted alloys is accompanied by 40 miniature tensile specimens for the two Fe-Mn-Cr alloys R77 and R87.

TABLE 3

COMPOSITION OF PHASE III Fe-Cr-Mn TERNARY ALLOYS (wt%)

	Fe	Cr	Mn		Fe	Cr	Mn
R66	80	5	15	R71	75	0	25
R67	70	15	15	R72	70	0	30
R68	80	0	20	R73	65	5	30
R69	70	10	20	R74	60	10	30
R70	65	15	20	R75	65	0	35

TABLE 4

COMPOSITION OF PHASE IV SOLUTE-MODIFIED Fe-Cr-Mn ALLOYS (wt%)

	Mn	Cr	C	N	V	P	B	Al	W	Ni	Si
X-75	30	2.0	0.10	0.15	-	-	-	-	-	0.5	0.4
R76	30	2.0	0.60	0.05	-	0.05	0.005	-	-	0.5	0.4
R77	30	2.0	0.40	0.15	1.0	0.05	0.005	-	1.0	0.5	0.4
R78	30	5.0	0.05	0.15	-	-	-	-	-	0.5	0.4
R79	30	10	0.05	0.10	-	-	-	-	-	0.5	0.4
R80	30	10	0.50	0.10	2.0	-	0.005	1.0	2.0	0.5	0.4
R81	20	15	0.05	0.10	-	-	-	-	-	0.5	0.4
R82	15	5	0.40	0.10	-	-	-	-	-	0.5	0.4
R83	15	5	0.60	0.05	-	0.05	0.005	-	-	0.5	1.0
R84	15	5	0.70	0.10	2.0	-	-	1.0	-	0.5	0.4
R85	15	15	0.05	0.15	-	-	-	-	-	0.5	0.4
R86	15	15	0.10	0.35	-	-	-	-	-	0.5	0.4
R87	15	15	0.10	0.10	-	0.05	0.005	-	-	0.5	1.0
R88	15	15	0.30	0.30	2.0	0.05	0.005	-	2.0	0.5	0.4
R89	15	15	0.50	0.10	2.0	-	-	1.0	2.0	0.5	0.4

TABLE 5

COMPOSITION OF COMMERCIAL Fe-Cr-Mn AUSTENITIC ALLOYS

Designation	Vendor	Composition (wt%)
NITRONIC ALLOY 32	ARMCO	18Cr-12Mn-1.5Ni-0.6Si-0.2Cu-0.2Mo-0.4N-0.1C-0.02P
18/18 PLUS	CARTECH	18Cr-18Mn-0.5Ni-0.6Si-1.0Cu-1.1Mo-0.4N-0.1C-0.02P
AMCR 0033	CREUSOT-MARREL	10Cr-18Mn-0.7Ni-0.6Si-0.06N-0.2C
NMF3	CREUSOT-MARREL	4Cr-19Mn-0.2Ni-0.7Si-0.09N-0.02P-0.6C
NONMAG 30	KOBE	2Cr-14Mn-2.0Ni-0.3Si-0.02N-0.02P-0.6C

COMMERCIAL Fe-Cr-Mn AUSTENITIC ALLOYS

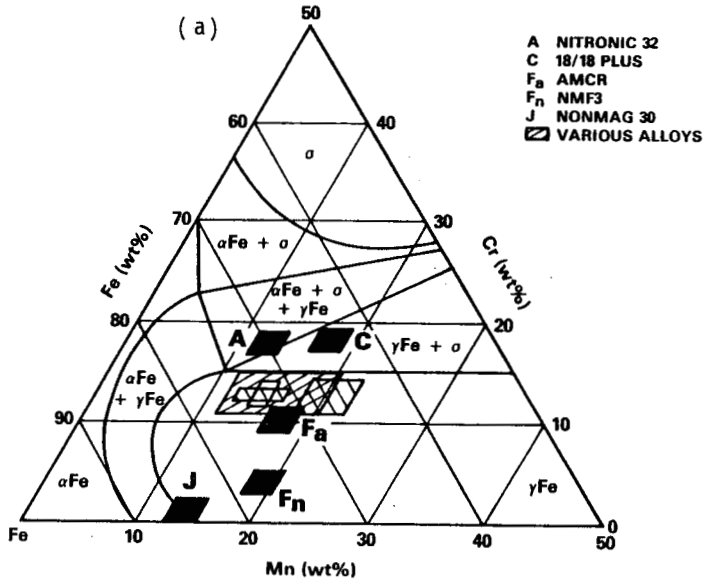

Fe-Cr-Mn SIMPLE TERNARIES

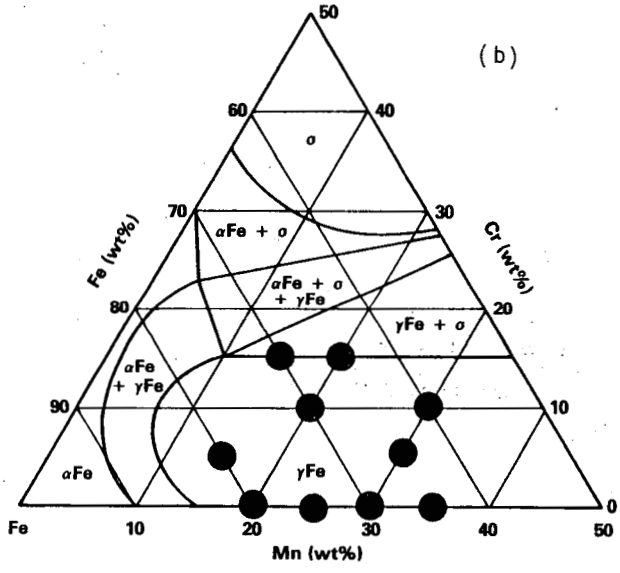

Fe-Cr-Mn DEVELOPMENTAL AUSTENITIC ALLOYS

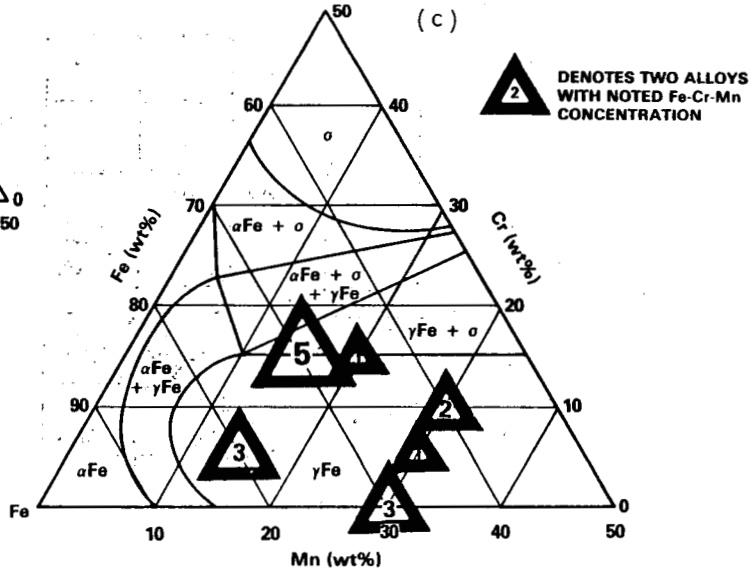

FIGURE 3. Equilibrium Phase Diagrams (650°C Isotherm) for Phase III and Phase IV Alloys.

COMMERCIAL Fe-Cr-Mn AUSTENITIC ALLOYS

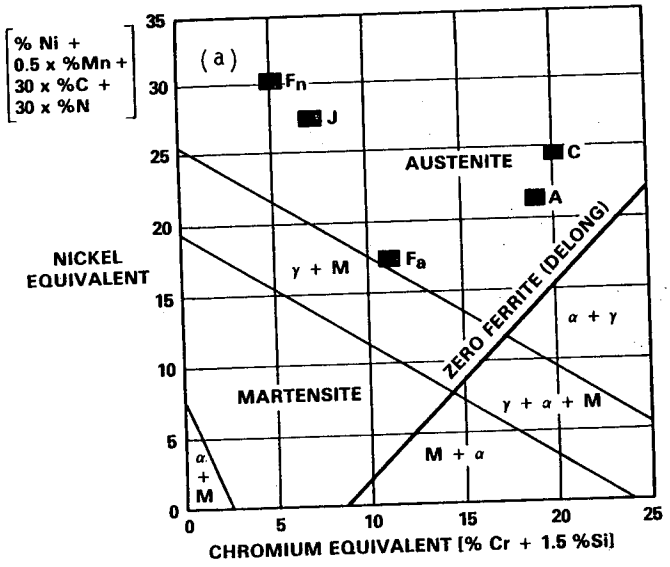

Fe-Cr-Mn SIMPLE TERNARIES

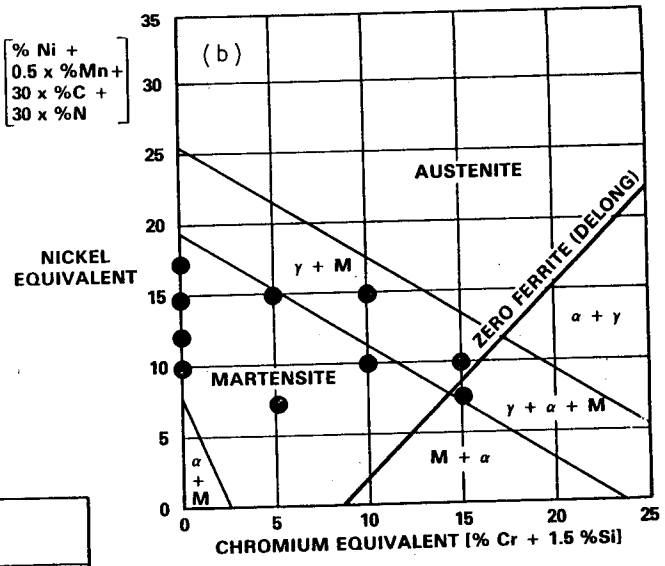

Fe-Cr-Mn DEVELOPMENTAL AUSTENITIC ALLOYS

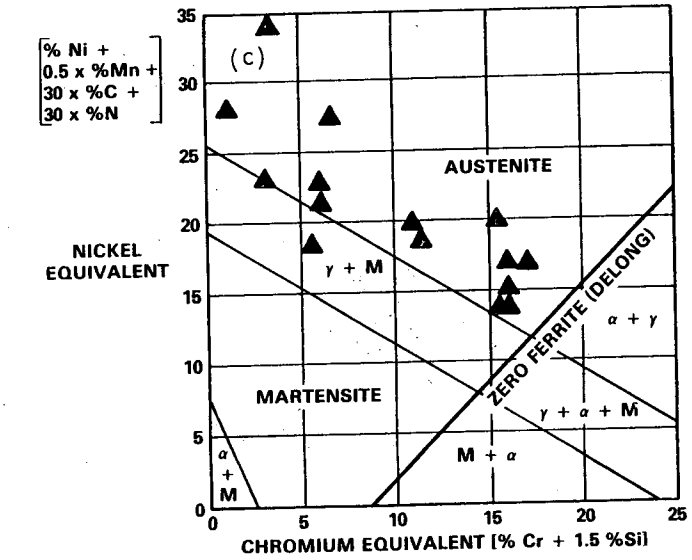

FIGURE 4. Schaeffler Diagrams for Phase III and Phase IV Alloys.

Subsets of the Phase I, Phase II alloys and Simple Solute Series[19] are also included in the HFIR-MFE RB1 and RB2 experiments at 55°C. Two exposures were planned in this experiment, 10 and 20 dpa. The former level has been reached and the specimens are now available for examination.

Larger subsets of the Phase I, Phase II and Simple Solute series have been included in the AA-XIV experiment in EBR-II (400, 500 and 600°C), which has been irradiated to ~15 dpa and is now being irradiated to ~30 dpa.

6.0 References

1. F. A. Garner, "Dependence of Swelling on Nickel and Chromium Content in Fe-Ni-Cr Ternary Alloys," DAFS Quarterly Progress Report, DOE/ER-0046/14, August 1983, p. 157.

2. H. R. Brager and F. A. Garner, "Swelling of High Nickel Fe-Ni-Cr Alloy in EBR-II," DAFS Quarterly Progress Report, DOE/ER-0046/14, August 1983, p. 152.

3. H. R. Brager and F. A. Garner, "Radiation-Induced Evolution of Fe-Ni-Cr Ternary Alloys," DAFS Quarterly Progress Report, DOE/ER-0046/12, February 1983, p. 170.

4. H. R. Brager and F. A. Garner, "Microsegregation Induced in Fe-35.5Ni-7.5Cr by Irradiation in EBR-II," DAFS Quarterly Progress Report, DOE/ER-0046/14, August 1983, p. 120.

5. F. A. Garner, "Recent Insights on the Swelling and Creep of Irradiated Austenitic Alloys," DAFS Quarterly Progress Report, DOE/ER-0046/16, February 1984, p. 58.

6. W. G. Wolfer, F. A. Garner and L. E. Thomas, "On Radiation-Induced Segregation and the Compositional Dependence of Swelling in Fe-Ni-Cr Alloys," ASTM STP 782, 1982, p. 1023.

7. F. A. Garner and W. G. Wolfer, "Factors That Determine the Swelling of Austenitic Stainless Steels," DAFS Quarterly Progress Report, DOE/ER-0046/15, November 1983, p. 89.

8. F. A. Garner, B. Esmailzadeh and A. Kumar, this report.

9. W. G. Johnston et al., "The Effect of Metallurgical Variables on Void Swelling," Radiation Damage in Metals, N. L. Peterson and S. D. Harkness, Eds., Am. Soc. of Metals, 1976, pp. 227-266.

10. H. R. Brager and F. A. Garner, "The Effect of Cold Work Level, Solute and Helium Content on the Swelling of "Pure" AISI 316 (Fe-17Cr-16.7Ni-2.5Mo)," ASTM STP 782, 1983, pp. 152-165.

11. F. M. Mann and W. E. Kennedy, Jr., "Activation of Components of a Fusion Alloy," DAFS Quarterly Progress Report, DOE/ER-0046/14, August 1983, p. 63.

12. O. G. Sokolov and A. I. Mel'ker "Invar Properties of Fe-Mn Alloys," Soviet Physics-Doklady 9, 1965, pp. 1019-1021.

13. O. A. Khomenko and I. F. Khil'Kevich "Effect of Chromium and Aluminum on the Physical and Mechanical Properties of Precipitation - Hardened Elinvars" Met. Term Okhra Met., 1982, p. 42.

14. D. J. Mazey, J. A. Hudson and J. M. Titchmarsh, J. Nucl. Mater. 107, 1982, pp. 2-19.

15. R. M. Boothby, D. R. Harries and T. M. Williams, J. Nucl. Mater. 115, 1983, pp. 16-24.

16. M. Snykers and E. Ruedl, J. Nucl. Mater. 103 & 104, 1981, pp. 1075-1078.

17. A. L. Schaeffler, Metal Properties 56, 1949, p. 680 B.

18. Y. Endoh, Y. Noda and M. Iizumi, "Lattice Dynamics and Invar Properties in FCC FeMn Alloys," J. Phys. Soc. Japan 50, 1981, pp. 469-475.

19. H. R. Brager and F. A. Garner, "Expanded Matrix of Fe-Ni-Cr Solute Alloys for HEDL Experiments," DAFS Quarterly Progress Report, DOE/ER-0046/4, February 1981, p. 178.

7.0 Future Work

Examination of selected irradiated Fe-Ni-Cr ternary alloys will proceed to determine whether compositional differences affect dislocation evolution. The first set of ageing studies on the Fe-Mn-Cr specimens aged for 1000 hours will be removed from the furnace and examined for phase stability.

8.0 Publications

None.

SWELLING BEHAVIOR OF TITANIUM-MODIFIED AISI 316 ALLOYS

F. A. Garner (Hanford Engineering Development Laboratory)

1.0 Objective

The object of this effort is to use breeder reactor data to forecast the potential swelling behavior in fusion reactors of titanium-modified AISI 316 alloys such as PCA.

2.0 Summary

It appears that titanium additions to stainless steels covering a wide compositional range around the specifications of AISI 316 result only in an increased delay period before neutron-induced void swelling proceeds. Once swelling is initiated the post-transient behavior of both annealed and cold-worked steels is quite consistent with that of AISI 316, approaching a relatively temperature-independent swelling rate of ~1%/dpa.

3.0 Program

Title: Irradiation Effects Analysis (AKJ)
Principal Investigator: D. G. Doran
Affiliation: Hanford Engineering Development Laboratory

4.0 Relevant DAFS Program Plan Task/Subtask

Subtask II.C.1 Effects of Material Parameters on Microstructure

5.0 Accomplishments and Status

5.1 Introduction

In several earlier reports it was shown that a wide range of Fe-Ni-Cr ternary alloys irradiated in EBR-II eventually swell at a rate of 5% per 10^{22} n/cm^2 (E > 0.1 MeV) or 1%/dpa.[1-3] This rate is attained over a wide range (400 - 650°C) of breeder-relevant temperatures. It has also been shown that AISI 316 and 304 eventually swell at this same rate.[4-6] The current swelling correlation for AISI 316 employs a strongly temperature-dependent steady-state rate that is always less than 5% per 10^{22} n/cm^2.[7] More recent analyses have shown that this steel swells at a rate approaching 5% per 10^{22} n/cm^2 over a wide range of temperature and that the observed temperature dependence of swelling resides primarily in the duration of the transient regime.[4-6,8]

The question is often raised whether the modification of austenitic steels by solute additions can forestall the inevitability of reaching the same swelling rate exhibited by the ternary alloys and various 300 series stainless steels. Although it is known from numerous studies that titanium additions tend to suppress swelling of austenitic alloys, it has not been shown whether the benefit of adding titanium and other elements is retained at high fluence or merely represents a temporary respite from the onset of swelling. In a recent design study on the Starfire Tokamak fusion plant it was stated that the assumed swelling of the titanium-modified alloy designated PCA (Prime Candidate Alloy for the fusion Path A alloy series) was one-tenth that of AISI 316.[9] This optimistic assumption implies that solute additions, particularly of titanium, suppress the steady-state swelling rate rather than just extend the incubation period.

The most directly relevant data would appear to be that derived primarily from irradiations of PCA and 316+Ti in the high He/dpa environment of HFIR,[10-11] but these are judged by this author to be insufficient to address whether the inherent swelling rate of austenitics (~1%/dpa) can be modified by titanium and other elements. If one ignores the possibly synergistic effects of helium and solutes, however, there are relevant data from the U.S breeder reactor program that can be used to address this question. It has earlier been shown from comparative irradiations of AISI 316 (DO-Heat) in HFIR and EBR-II that the difference in helium level does not affect the swelling behavior substantially.[12-13]

Two sets of EBR-II data will be considered in this report. The first data set will be used to establish the relative behavior of Ti-modified 316 with unmodified 316, and the influence of cold-work on this relationship. Using the insight gained from this analysis a second data set will be analyzed for the effect of more extensive compositional variations. The composition of the alloys mentioned above and that

of the first data set are presented in Table 1. The compositions corresponding to the second data set are presented on the figures contained in a later section.

TABLE 1

COMPOSITIONS OF SOME 316-TYPE ALLOYS CURRENTLY UNDER STUDY IN U.S. BREEDER AND FUSION PROGRAMS

	Weight Percent						
	Ni	Cr	Mo	Si	Mn	Ti	C
316 (N-lot)	13.5	16.5	2.5	0.5	1.6	--	0.05
*316 (DO-Heat)	13	18	2.6	0.8	1.9	0.05	0.05
*316 + Ti	12	17	2.5	0.4	0.5	0.23	0.06
*PCA	16	14	2.3	0.4	1.8	0.24	0.05
LS-1	13	16	1.8	0.9	1.0	0.10	0.05

*These alloys are being studied primarily in the U.S. Fusion Program.

5.2 Swelling of LS-1

The alloy LS-1 was developed at Oak Ridge National Laboratory and is one of the earliest titanium-modified alloys irradiated in the U.S. Breeder Program. Consequently this alloy has one of the highest levels of reactor exposure.

Figure 1a shows a comparison of the swelling behavior of 20% cold-worked LS-1 at seven temperatures with the temperature-independent behavior of 20% cold-worked N-lot AISI 316. Both were irradiated in capsule B-121 of the RS-1 experiment.* N-lot contains very little titanium and does not exhibit the temperature sensitivity of incubation observed in many heats of AISI 316. It is therefore used as a standard "template" curve with which to compare the development of swelling in other alloys. Note that for swelling levels >5% the LS-1 curves tend to parallel the N-lot curve. The transient behavior of LS-1 appears to be quite sensitive to temperature however.

Figure 1b shows that the annealed condition of LS-1 at 510°C also is swelling at a rate comparable to that of N-lot. Note also that the dotted lines drawn in Figure 1b indicate that the N-lot steel at comparable voidage levels swells at the same rate as that determined for LS-1 at 510°C. An alternate approach to describing this data is shown in Figure 2 and ignores the curvature between data points as well as the curvature that occurs beyond the last datum. This approach leads to an underestimate of the eventual swelling rate and the erroneous conclusion not only that LS-1 swells at a lower steady-state rate than AISI 316 but also that it exhibits a strong temperature sensitivity of swelling rate.

Figures 3a and 3b show that annealed LS-1 at other temperatures also approaches a steady-state swelling rate comparable to that of the N-lot steel. It therefore appears that the compositional differences between LS-1 and AISI 316 only affect the incubation or transient regime of swelling. The steady-state swelling rate of Ti-modified alloys also appears to be relatively insensitive to irradiation temperature over a very broad temperature range.

5.3 Swelling of a Variety of Titanium-Modified Alloys

The reactor exposures attained for the other titanium-modified alloys listed in Table 1 are insufficient to determine whether the steady-state swelling rate is suppressed by titanium additions or whether the incubation period is merely extended. It should be noted that the other titanium-modified alloys in Table 1 also possess compositional differences in elements other than titanium.

One experiment has been performed from which the general effect of titanium can be assessed in synergism with that of other compositional changes typical of the alloys in Table 1. The MV-III experiment involved the irradiation in EBR-II of a large number of compositionally-modified 316-base alloys. Density change data are available at 540°C for these alloys at exposure levels of about 6 and 10 x 10^{22} n/cm^2.[10-11] In general the effect of titanium is to reduce swelling of annealed steels at 540°C, while titanium's influence on the swelling of cold-worked steels is not as obvious, except in Zr-modified steels (see Figures 4 through 7).

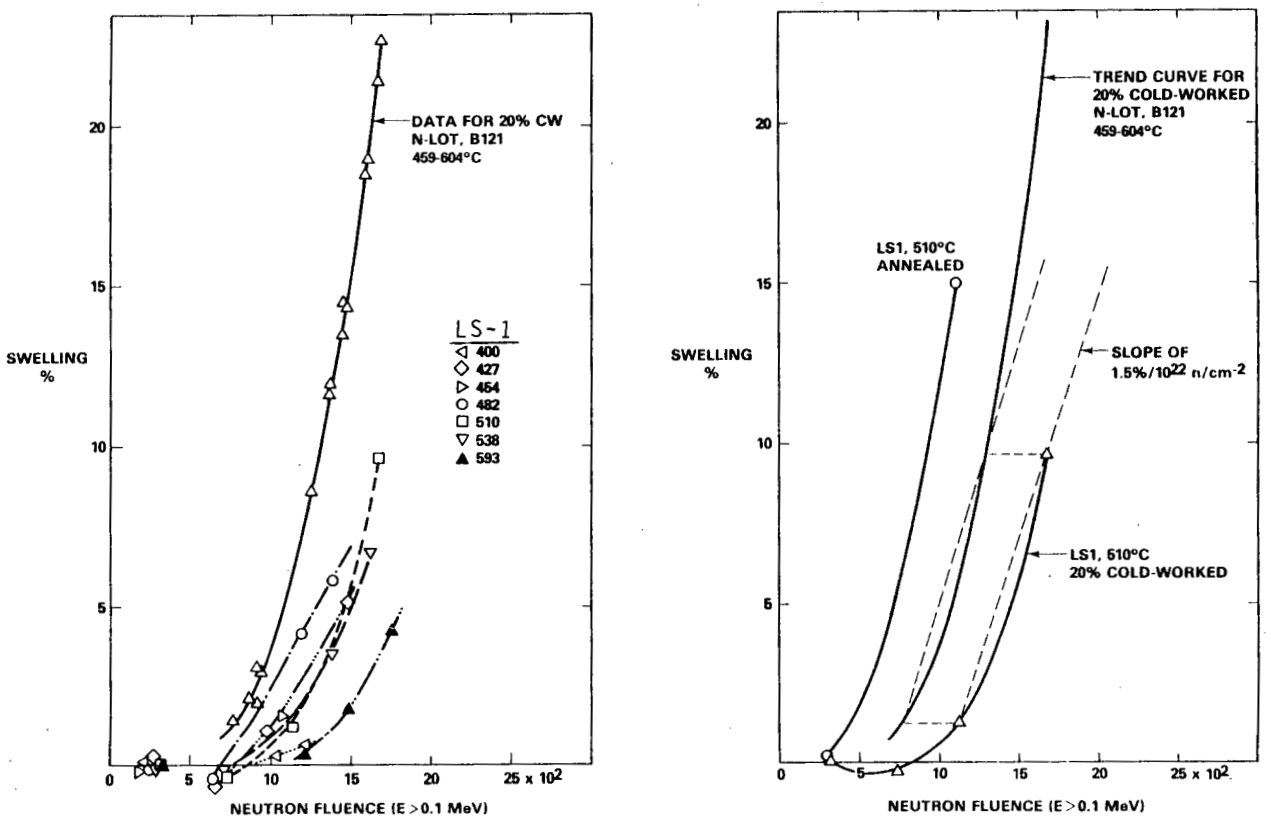

FIGURE 1. (a) Comparison of the Swelling Behavior of N-Lot AISI 316 and LS-1 at Various Temperatures. Both alloys are in the 20% cold-worked condition and were irradiated together.
(b) Comparison of Annealed and Cold-Worked LS-1 Swelling Behavior at 510°C. Note that linear extrapolation of LS-1 data gives the same result as would be obtained for N-lot at comparable swelling levels.

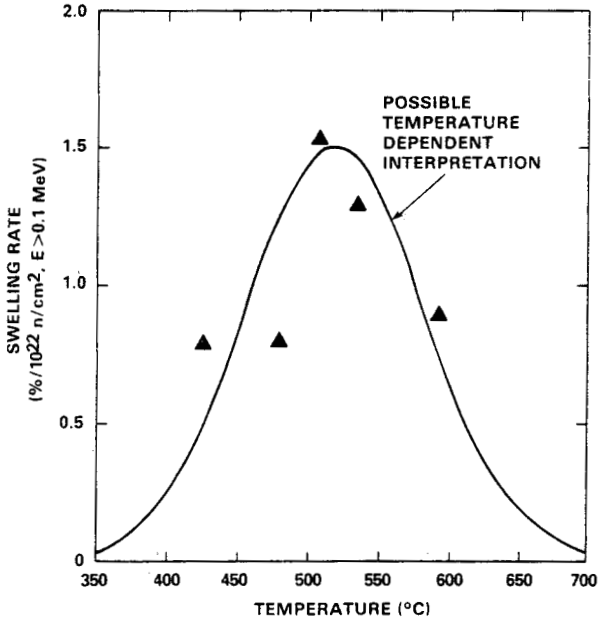

FIGURE 2. "Linear" Swelling Rates Determined for 20% Cold-Worked LS-1 in EBR-II. As shown in Figure 1b, these swelling rates were determined by drawing a straight line between the data at the two highest fluences and ignoring any curvature between or beyond these data. Therefore the derived linear rates are clearly underestimates of the eventual swelling rate.

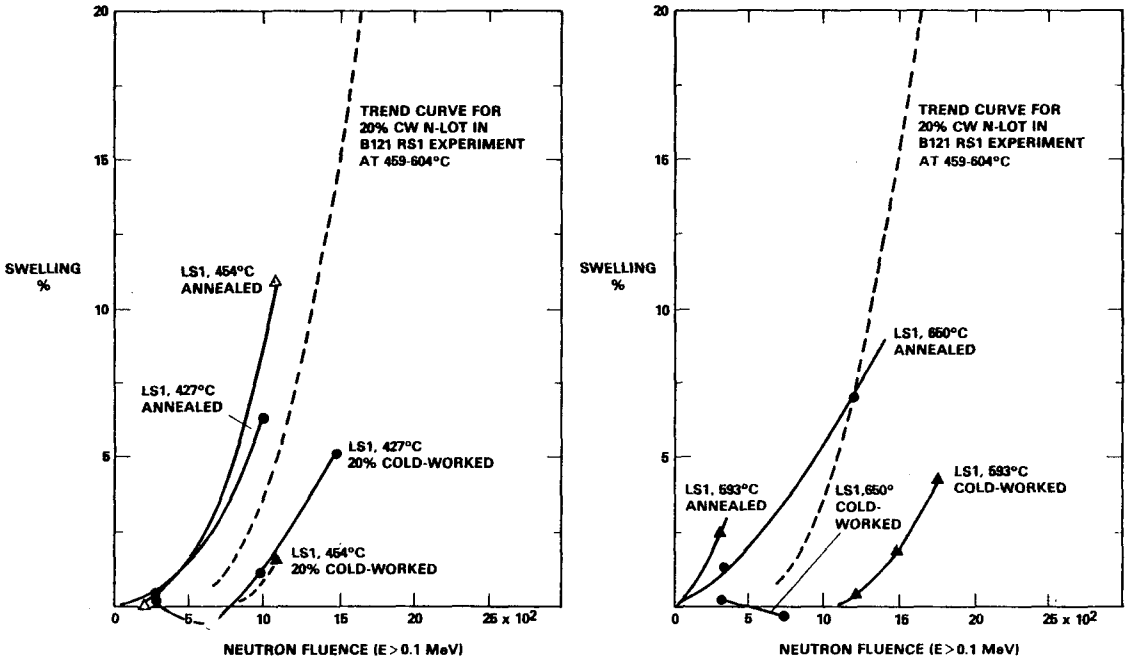

FIGURE 3. Comparison of Swelling Behavior of Annealed and Cold-Worked LS-1 at Temperatures of 427, 454, 593 and 650°C.

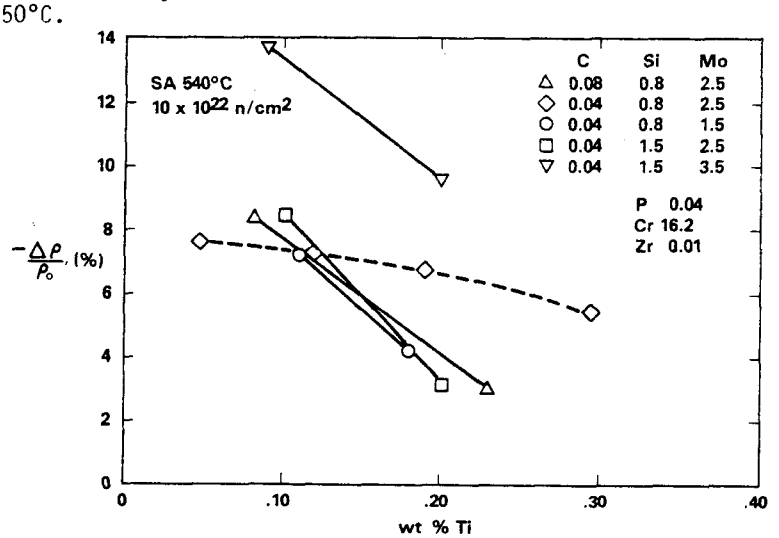

FIGURE 4. Swelling at 10 x 10^{22} n/cm² (E > 0.1 MeV) of Annealed Modified 316 Alloys at 540°C vs Titanium Level for Various Levels of C, Si and Mo.

In order to determine whether the influence of titanium extends beyond the transient regime it is necessary to select only those data subsets wherein the swelling attained at the higher influence is well out of the transient regime. This restricts the choice of data to the annealed condition only and excludes the cold-worked data field. As earlier shown for LS-1, however, the effect of cold-work is only to extend the transient regime and not to affect the steady-state behavior. All annealed alloy data subsets considered to be relevant to determination of the swelling behavior vs titanium contant are shown in Figures 8 and 9.

Note that with few exceptions the addition of titanium results only in a shift of the swelling curve to higher fluence. The resulting swelling rates for solution annealed alloys are comparable to the behavior of the 20% CW N-lot heat of AISI 316, however. If the data are replotted to show the influence of other solutes, a similar conclusion can be drawn, namely that solute additions affect primarily the duration of the transient regime. In some cases the transient regime can be shortened rather than extended.

5.4 Conclusions

It appears that titanium additions to stainless steels covering a wide compositional range about that of AISI 316 result only in an increased delay period before neutron-induced void swelling proceeds. All

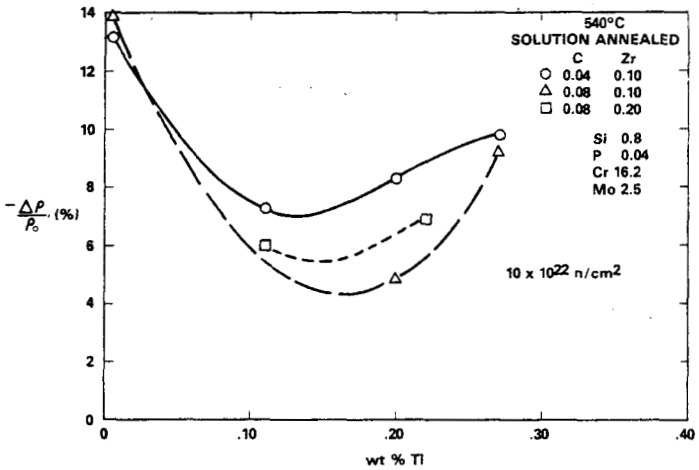

FIGURE 5. Swelling at 10 x 10^{22} n/cm² (E > 0.1 MeV) of Annealed Modified 316 Alloys vs Titanium Level for Zr-Modified Alloys.

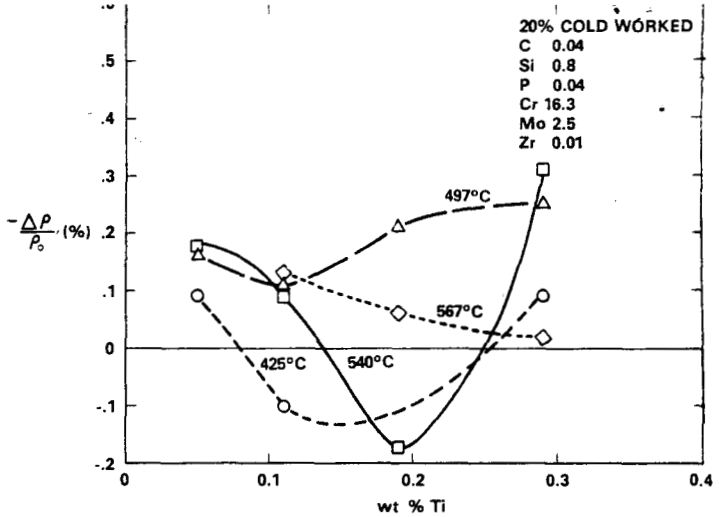

FIGURE 6. Swelling at 10 x 10^{22} n/cm² (E > 0.1 MeV) of Cold-Worked Alloys vs Titanium Level at Various Temperatures.

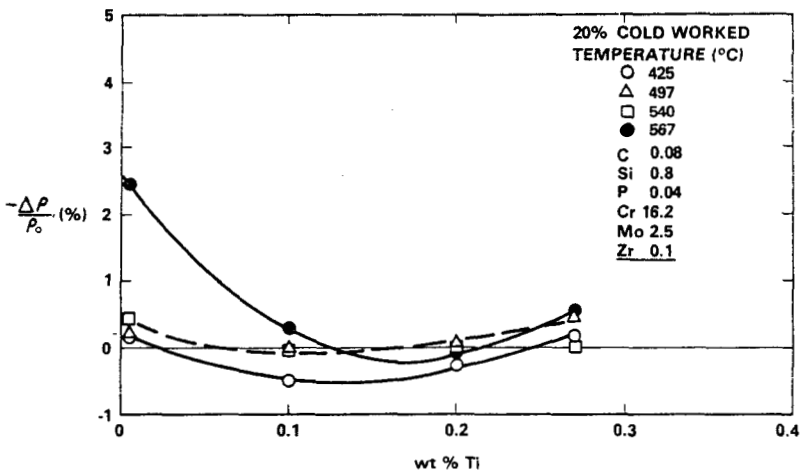

FIGURE 7. Influence of Titanium on the Swelling at 10 x 10^{22} n/cm² (E > 1.0 MeV) of Zirconium-Modified Cold-Worked Alloys with High Carbon at Various Temperatures.

austenitic alloys regardless of their composition appear to be subject to the inevitability of a steady-state swelling rate approaching 1%/dpa or 5% per 10^{22} n cm^{-2} (E > 0.1 MeV). This eventual swelling rate appears to be independent of irradiation temperature over most of the breeder-relevant range.

6.0 References

1. F. A. Garner, "The Dependence of Swelling on Nickel and Chromium Content in Fe-Ni-Cr Ternary Alloys," DAFS Quarterly Progress Report, DOE/ER-0046/14, p. 133, August 1983.

2. W. J. S. Yang and F. A. Garner, "Relationship Between Phase Development and Swelling of AISI 316 During Temperature Changes," Effects of Radiation on Materials, Eleventh Conference, ASTM STP 782, pp. 186-206, 1982.

3. F. A. Garner and H. R. Brager, "Swelling of Fe-Cr-Ni Alloys at High Exposure," DAFS Quarterly Progress Report, DOE/ER-0046/16, p. 38, February 1984.

4. F. A. Garner, "Recent Insights on the Swelling and Creep of Irradiated Austenitic Alloys," DAFS Quarterly Progress Report, DOE/ER-0046/16, p. 49, February 1984.

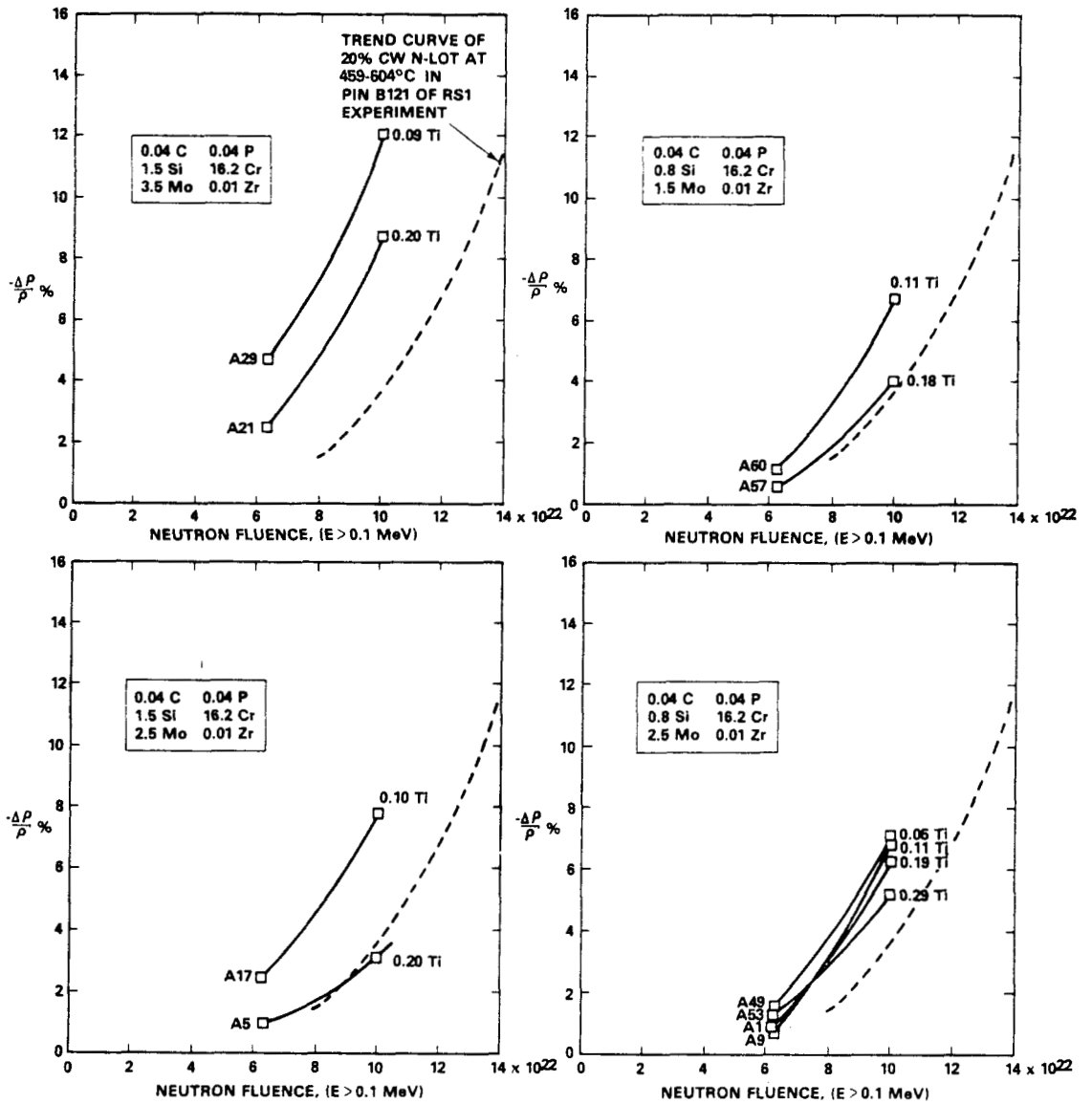

FIGURE 8. Influence of Titanium on Swelling of Various Compositionally-Modified 316-Type Alloys in the Annealed Condition at 540°C. Alloy designations and compositions are shown for each alloy series. Note that percent density change $\Delta\rho/\rho_0$ rather than swelling is plotted in these curves.

5. F. A. Garner and W. G. Wolfer, "Recent Theoretical and Experimental Insights on the Swelling of Austenitic Alloys," Proceedings BNES Symposium on Dimensional Stability and Mechanical Behavior of Irradiated Metals and Alloys, Brighton, England, Vol. II, p. 21, April 11-14, 1983, .

6. F. A. Garner and D. L. Porter, "A Reassessment of the Swelling Behavior of AISI 304 Stainless Steel," Ibid, p. 41.

7. J. F. Bates and M. K. Korenko, "Empirical Development of Irradiation Induced Swelling Design Equations," Nuclear Technology, 48, p. 303, May 1980.

8. F. A. Garner, "The Influence of Reactor Spectra and Irradiation Temperature on the Swelling of AISI 316 Stainless Steel," DAFS Quarterly Progress Report, DOE/ER-0046/12, pp. 178-193, February 1983.

9. "Starfire - A Commercial Tokamak Fusion Power Plant Study," ANL/FPP-80-1, Volume 1, (see page 10-41).

10. P. J. Maziasz and E. E. Bloom, "Comparison of Titanium-Modified and Standard Type 316 Stainless Steel Irradiated in HFIR: Swelling and Microstructure," ADIP Quarterly Progress Report, DOE/ET-0058/1, p. 40, August 1978.

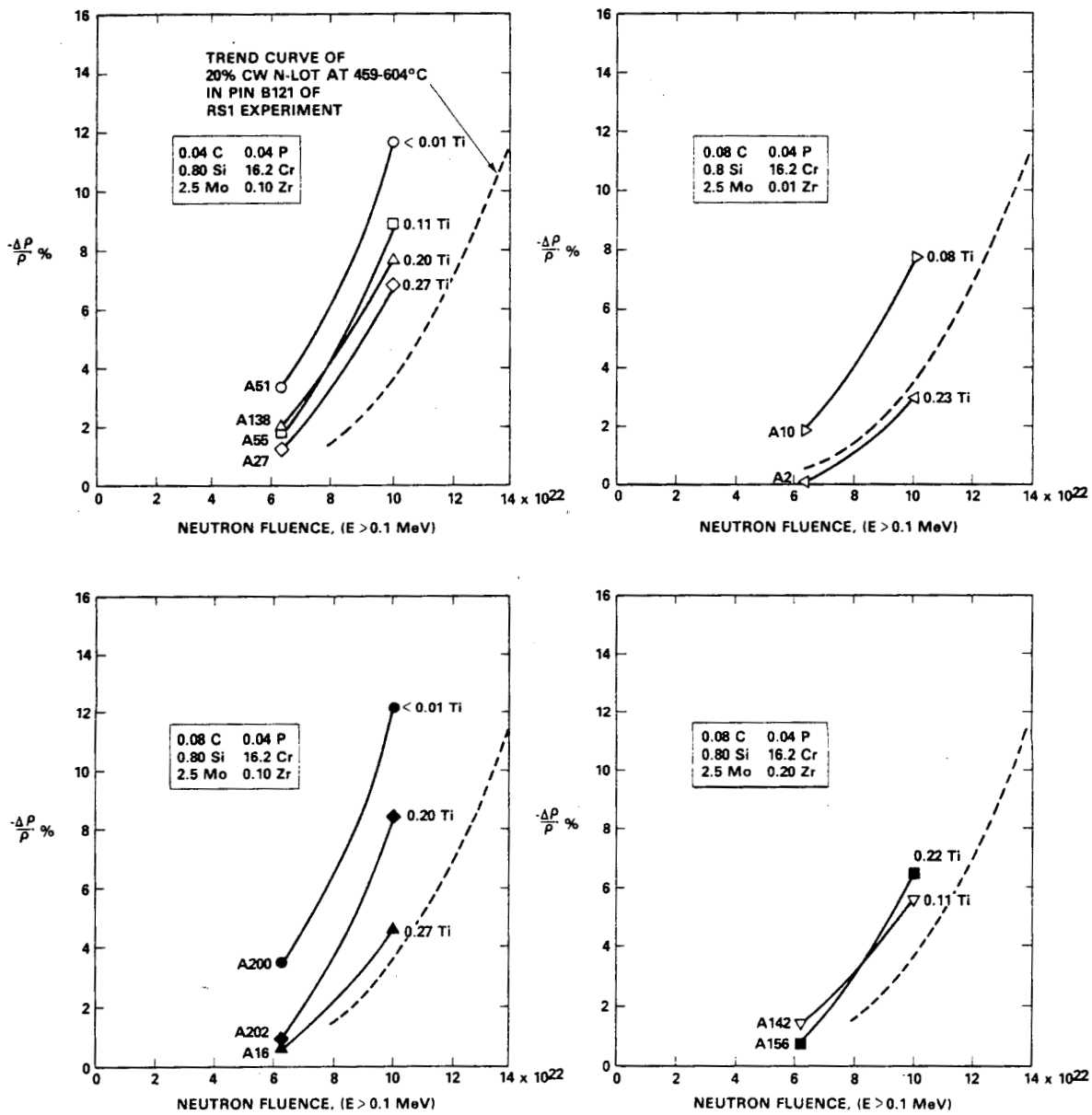

FIGURE 9. Additional Data on the Influence of Titanium on Swelling of Various Compositionally-Modified 316-Type Alloys in the Annealed Condition at 540°C.

11. P. J. Maziasz and D. N. Braski, "Swelling and Microstructural Development in Path A PCA and Type 316 Stainless Steel Irradiated in HFIR to about 22 dpa," ADIP Semiannual Progress Report, DOE/ER-0045/9, p. 44, September 30, 1982.

12. H. R. Brager and F. A. Garner, "Microstructural and Microchemical Comparisons of AISI 316 Irradiated in HFIR and EBR-II," J. Nucl. Mater. 117, p. 159, 1983.

13. H. R. Brager and F. A. Garner, "The Microchemical Evolution and Swelling of AISI 316 Irradiated in HFIR and EBR-II," in ref. 5, Vol. II, p. 1.

7.0 Future Work

Analysis of the compositional and environmental sensitivity of swelling and creep will continue.

8.0 Publications

None.

CHAPTER 6

FUNDAMENTAL STUDIES OF SPECIAL PURPOSE MATERIALS

MECHANICAL PROPERTIES AND MICROSTRUCTURES OF HIGH-STRENGTH COPPER ALLOYS FOLLOWING THERMAL ANNEALING

S.J. Zinkle, D.H. Plantz, R.A. Dodd and G.L. Kulcinski (University of Wisconsin-Madison)

1.0 Objectives

To investigate the microstructures of two high-strength, high-electrical conductivity alloys following an annealing schedule similar to that experienced during an ion irradiation. This will allow microstructural comparisons to be made between irradiated and annealed specimens.

2.0 Summary

Vickers microhardness measurements have been made on specimens of as-received AMZIRC and AMAX-MZC copper alloys as a function of annealing time and temperature. In addition, electrical resistivity measurements have been performed on both alloys as a function of annealing temperature following a 1 hour anneal. The results indicate that both alloys have an unirradiated recrystallization temperature of about 475°C.

3.0 Program

Title: Radiation Effects to Reactor Materials
Principal Investigators: G.L. Kulcinski and R.A. Dodd
Affiliation: University of Wisconsin-Madison

4.0 Relevant DAFS Program Plan Task/Subtask

Subtask II.C.1.1: Phase Stability Mechanics
Subtask II.C.1.2: Modeling and Analysis of Effects of Materials Parameters on Microstructure

5.0 Accomplishments and Status

5.1 Introduction

High-strength, high-conductivity copper alloys have recently been considered for various applications in proposed fusion reactors.[1] Two candidate high-strength, high-conductivity copper alloys have been selected for an investigation of their thermal and irradiated microstructure. AMZIRC and AMAX-MZC are heat-treatable copper alloys which have unirradiated yield strengths of 400-500 MPa and electrical conductivities which may have values as high as 80-90% IACS (International Annealed Copper Standard).[2] A previous investigation[3] found that the correlated yield strengths of as-received AMZIRC and AMAX-MZC samples were in good agreement with the manufacturer's specifications, but the measured electrical conductivities were substantially (~ 35%) lower than expected.

Recent results obtained from ion-irradiated AMZIRC and AMAX-MZC samples indicate that radiation-enhanced recovery occurs in both of these alloys.[4] Both AMZIRC and AMAX-MZC rely heavily on thermomechanical treatment for their strength. It is therefore important to understand the detailed microstructural processes which occur upon annealing of these alloys in order to assess the significance of the observed changes due to radiation damage.

TABLE 1

NOMINAL COMPOSITION OF AMZIRC AND AMAX-MZC
(from Ref. 2)

Alloy	Zr %	Cr %	Mg %	Cu
AMZIRC	0.13-0.20	-	-	balance
AMAX-MZC	0.15	0.80	0.04	balance

5.2 Experimental Procedure

The nominal alloy composition of AMZIRC and AMAX-MZC is listed in Table 1. The alloy heat treatment consisted of a solution anneal, followed by 90% cold-rolling and then aging for 30 minutes at 375°C for the AMZIRC alloy and 400°C for the MZC alloy. All measurements were made on 250 μm thick foils.

As-received specimens from both copper alloys were mechanically polished using 0.3 μm alumina powder prior to their thermal annealing treatment. Individual specimens were annealed for times ranging from 0.25-10 hours in a high vacuum furnance and cooled using a combination of furnace and air cooling. The specimen temperature decreased by at least 100°C within 1 minute following the anneal. Temperature control was maintained to within ±5°C. The annealing temperatures investigated ranged from 300-600°C in 50°C increments. Different specimens of each alloy were used for each annealing condition. The pressure in the vacuum chamber ranged from 1×10^{-6} to 1×10^{-9} Torr during the anneal. All specimens were electropolished upon removal from the furnace in order to remove the oxide layer present from the anneal.

Vickers microhardness measurements were made on as-received and annealed specimens of both alloys at an indenter load of 200 g using a vibration-islolated Buehler Micromet® microhardness tester. A minimum of nine different indentations in three widely separated areas were measured for each specimen at the different annealing conditions. Electrical resistivity measurements were performed on the as-received and annealed alloy specimens using standard 4 point probe techniques. The preparation method for the resistivity specimens has been previously described.[3] One to two resistivity "wires" were measured for each thermal annealing condition.

Selected specimens from the thermal anneal study were examined in a JEOL TEMSCAN-200CX electron microscope. Transmission electron microscope (TEM) specimens were jet-electropolished using a solution of 33% HNO_3/67% CH_3OH cooled to -20°C at an applied potential of 15-20 V.

5.3 Results

The Vickers microhardness results obtained from AMZIRC and AMAX-MZC following a 1 hour anneal at temperatures from 350-600°C is shown in Fig. 1. Both AMZIRC and AMAX-MZC exhibit signs of dislocation recovery for annealing temperatures above 350°C. The recrystallization temperature of both alloys is about 475°C. This value may be compared to the recrystallization temperature of copper, which is ~ 150°C. The strength of both AMZIRC and AMAX-MZC decreases dramatically for annealing temperatures above 400°C. Upon recrystallization, their microhardness numbers approach values typically found for annealed copper.

Figure 2 shows the Vickers microhardness of as-received AMZIRC as a function of annealing time and temperature. It can be seen that an increase in the annealing time from 0.25 hr to 10 hr results in a decrease in the recrystallization temperature from 525°C to 450°C. The Vickers microhardness number (VHN) after recrystallization is about 50 HV. The VHN for solution annealed AMZIRC (shown by the arrow in Fig. 1) has also been found[4] to be 50 HV. This indicates that no precipitation hardening mechanism exists in AMZIRC specimens which have been recrystallized.

The Vickers microhardness of as-received AMAX-MZC is shown in Fig. 3 as a function of annealing time and temperature. The annealing behavior of AMAX-MZC is seen to be similar to that of AMZIRC -- as the annealing

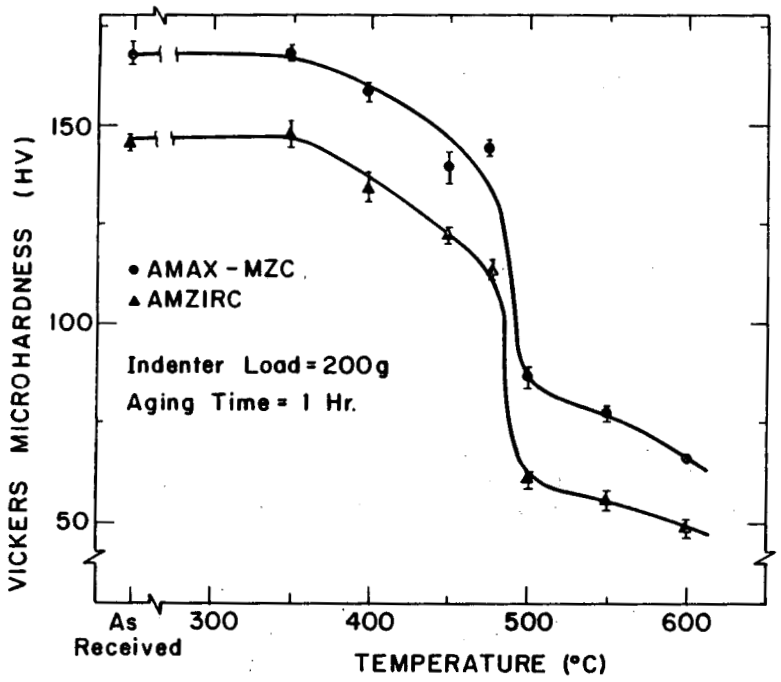

FIGURE 1. Vickers Microhardness of As-Received AMZIRC and AMAX-MZC as a Function of Temperature Following a 1-hour Anneal.

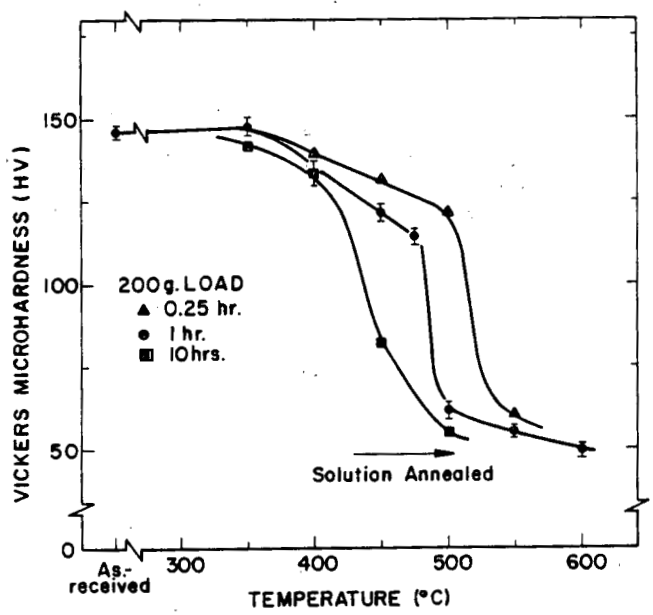

FIGURE 2. Vickers Microhardness of As-Received AMZIRC as a Function of Annealing Time and Temperature.

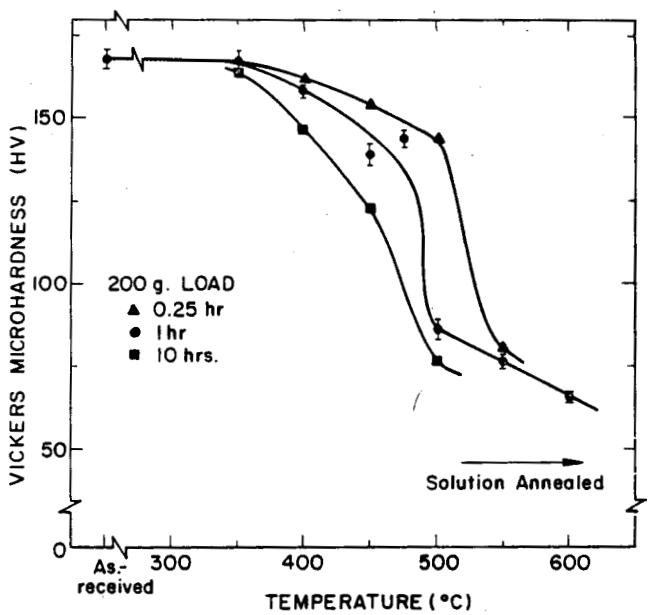

FIGURE 3. Vickers Microhardness of As-Received AMAX-MZC as a Function of Annealing Time Temperature.

time increases from 0.25 hr to 10 hr the recrystallization temperature shifts from 525°C to 450°C. However, the microhardness numbers of the recrystallized MZC specimens are substantially higher than that of solution-annealed MZC[4] (see arrow on Fig. 3). It therefore appears that a precipitation hardening mechanism is still operating in AMAX-MZC upon recrystallization.

The electrical resistivity of both AMZIRC and AMAX-MZC was observed to decrease following a 1 hour anneal for temperatures between 350-550°C. Table 2 lists the preliminary values for the alloy electrical conductivities in units of % IACS. The % IACS conductivities were calculated by assuming that pure copper has a

TABLE 2

ELECTRICAL CONDUCTIVITY OF AS-RECEIVED AMZIRC AND AMAX-MZC

AS A FUNCTION OF TEMPERATURE FOLLOWING A 1 HOUR ANNEAL

	Electrical Conductivity (% IACS) Following Anneal At Temperature							
Alloy	As-received	300°C	350°C	400°C	450°C	475°C	500°C	550°C
AMZIRC	75%	80%	84%	88%	92%	94%	97%	97%
AMAX-MZC	58%	56%	73%	78%	86%	84%	94%	88%

resistivity of[5] 16.73 nΩ-m at 20°C with a temperature coefficient of 0.068 nΩ-m /°C. The estimated error in the conductivity measurements is less than 5%. The results in Table 2 show that both AMZIRC and AMAX-MZC exhibit high electrical conductivities (greater than 90% IACS) when they have recrystallized. The AMZIRC alloy has a higher electrical conductivity than AMAX-MZC for all annealing conditions which were investigated.

The microstructures of AMZIRC and AMAX-MZC in the as-received condition and following a 1 hour anneal at 450°C and 500°C is shown in Fig. 4. In the as-received state, the dominant microstructural feature for both alloys is the high dislocation density. The dislocation density has become greatly reduced at 450°C, and subgrain boundaries are becoming well-defined. The subgrain diameters range from 0.1 - 1 μm. After annealing for 1 hour at 500°C, both alloys have completely recrystallized and have average grain sizes greater than 10 μm.

5.4 Discussion

The general form of the microhardness annealing curve for both alloys is in good agreement with published results in the literature.[2,6-8] The exact value of the recrystallization temperature for AMZIRC and AMAX-MZC appears to depend strongly on the alloy's prior thermomechanical history. Various researchers have observed recrystallization temperatures which are significantly lower[9] and higher[6,10] than the value of 475°C which was found in the present investigation. The large decrease in microhardness which occurs as the alloys are annealed at temperatures of 400-500°C indicates that the strength of both alloys is largely due to cold-working.

It appears that the as-received AMZIRC and AMAX-MZC copper alloys may have been given an insufficient aging treatment by the manufacturer. Table 2 shows that the electrical conductivities of both alloys are substantially lower than the expected conductivities of 80-90% IACS. A close inspection of Fig. 1 and Table 2 reveals that aging of the as-received alloys for an additional hour at 400°C greatly increased the electrical conductivity while causing only a small decrease in the microhardness. This additional anneal treatment leads to mechanical properties which are more suitable for fusion reactor applications.

Some confusion exists in the literature concerning whether Cu-Zr alloys (such as AMZIRC) are precipitation-hardenable. Some researchers have concluded that Cu-Zr is precipitation-hardenable,[6] while others concluded that there is only slight or no observable precipitation hardening.[8,10,11,12] In general, it appears that aging can cause a small increase in the strength of Cu-Zr, but the alloy strength is derived mainly from cold-working.[13] Therefore, Cu-Zr should not be classified as precipitation-hardenable.

A comparison of the annealing behavior of AMZIRC vs. AMAX-MZC (Fig. 1) shows that the MZC alloy has the higher microhardness value both before and after recrystallization occurs. The larger strength of MZC compared to AMZIRC is believed to be due to precipitation-hardening. A supplemental annealing study has given direct evidence that this is indeed true.[4] AMZIRC and AMAX-MZC specimens were solution annealed in vacuum, and then following a water quench one-half of the specimens were aged at 470°C for 1 hour. The microhardness numbers of the solution annealed (SA) and the SA plus aged AMZIRC specimens were found to be identical, indicating no precipitation hardening for these conditions. Conversely, the MZC aged specimens were found to be significantly harder than the SA specimens. Figure 5 shows the TEM microstructures of both aged alloys. The matrix of the AMZIRC specimen is fairly clean, with only isolated precipitates visible. The AMAX-MZC specimen has a high density of coherent precipitates, which contribute significantly to this alloy's strength.

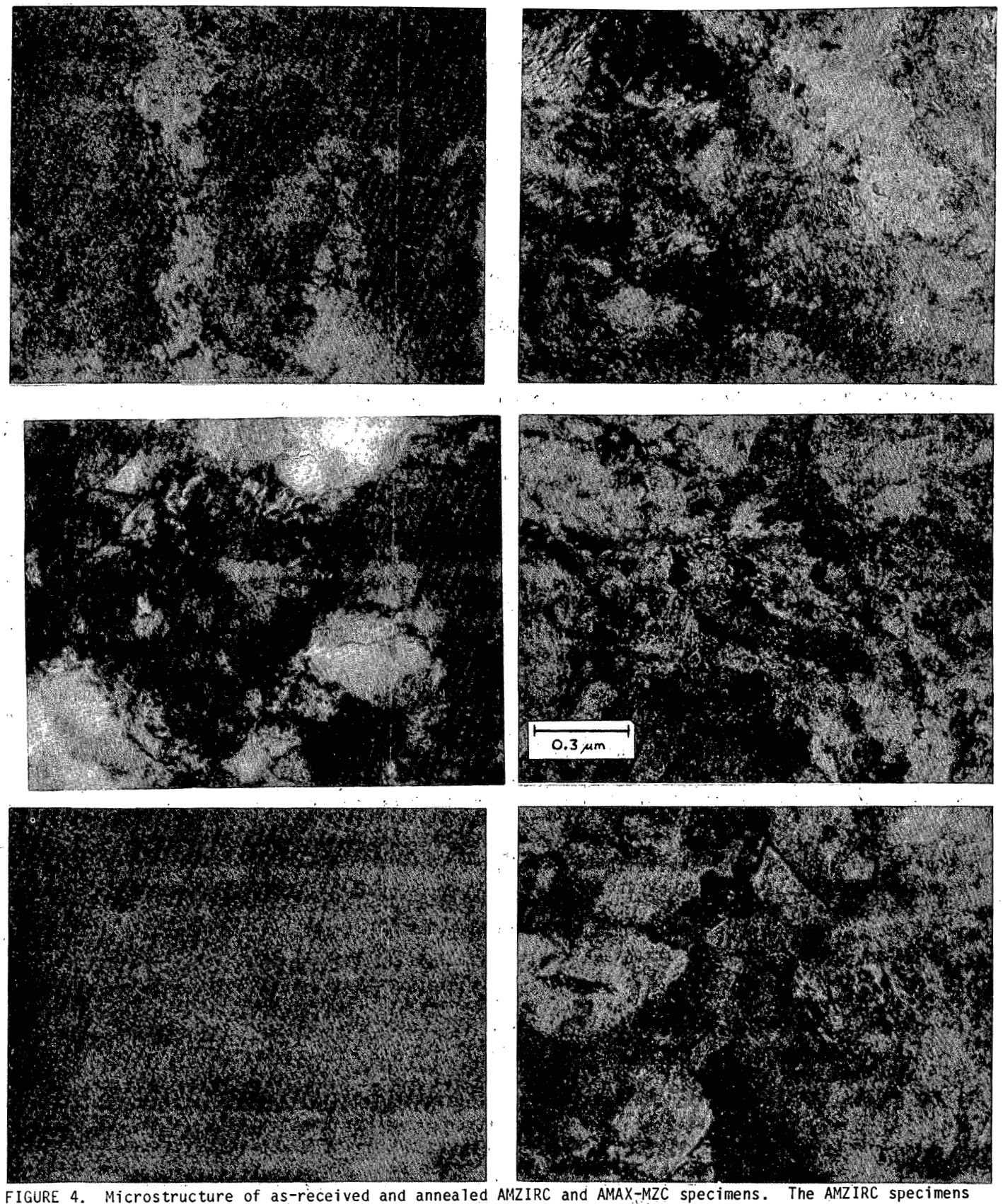

FIGURE 4. Microstructure of as-received and annealed AMZIRC and AMAX-MZC specimens. The AMZIRC specimens are in the left column and the MZC specimens are in the right column. The top micrographs are from the as-received alloys, the middle micrographs are from as-received specimens which have been annealed for 1 hour at 450°C, and the bottom micrographs are as-received specimens which have been annealed for 1 hour at 500°C.

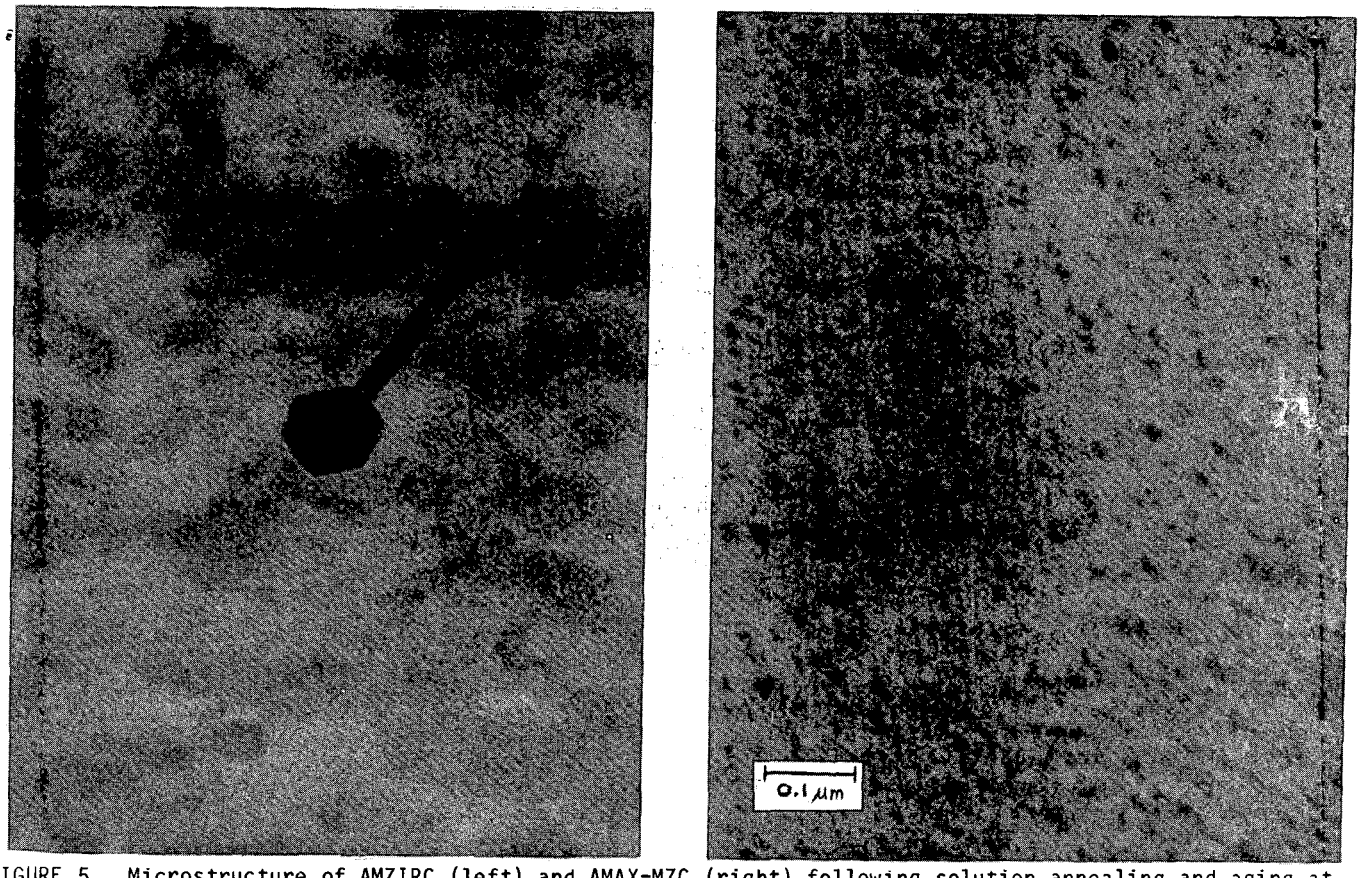

FIGURE 5. Microstructure of AMZIRC (left) and AMAX-MZC (right) following solution annealing and aging at 470°C for 1 hour.

From an engineering point of view, both the AMZIRC and the AMAX-MZC alloys are unsuitable for use as high-strength materials when they are exposed to an environment which causes recrystallization to occur. In a non-irradiation environment, this refers to ambient temperatures greater than or equal to about 400°C. In the presence of irradiation and/or large stress fields, the recrystallization temperatures of both of these alloys may be lowered by a significant amount. Irradiated specimens of AMAX-MZC exhibit signs of dislocation recovery and grain recrystallization at temperatures as low as 300°C.[4] This behavior may severely restrict the applicability of these type of copper alloys to fusion reactors.

5.5 Conclusions

[1] Both as-received AMZIRC and AMAX-MZC show a recrystallization temperature of about 475°C for a 1 hour anneal, in good agreement with results from the manufacturer. The microhardness values of both alloys decrease by more than 50% betwen the as-received and recrystallized condition, which indicates that a large portion of their strength is due to cold-working. This lack of intrinsic high-temperature strength may make these alloys unsuitable for fusion reactor applications.

[2] The discrepancy between the (low) measured as-received electrical conductivity of AMXIRC and AMAX-MZC and (high) expected conductivity is likely due to insufficient aging by the manufacturer.

[3] The electrical conductivities of both alloys may exceed 90% IACS under appropriate annealing conditions. AMZIRC has the higher electrical conductivity for all annealing conditions which were investigated, while AMAX-MZC has the larger microhardness values.

[4] AMAX-MZC shows signs of precipitation-hardening, while AMZIRC does not for the conditions investigated in the present study.

6.0 Acknowledgements

This work performed under appointment to a Magnetic Fusion Energy Technology Fellowship and with funds supplied by the Department of Energy.

7.0 References

1. F.W. Wiffen, T.C. Reuther and R.E. Gold, "Copper and Copper Alloys for Fusion Reactor Applications: Summary Report of a DOE-OFE Workshop", Third Topical Meeting on Fusion Reactor Materials, Albuquerque, NM (Sept. 1983). Workshop proceedings to be published by Oak Ridge National Laboratory.

2. Interim Publications on AMZIRC and AMAX-MZC Copper Alloys, AMAX Copper, Inc., New York, NY (1982).

3. S.J. Zinkle, S.N. Farrens, G.L. Kulcinski and R.A. Dodd, DAFS Quarterly Progress Report DOE/ER-0046/15 (Nov. 1983) p. 127.

4. S.J. Zinkle, R.A. Dodd and G.L. Kulcinski, "Comparison of Thermal and Irradiated Behavior of High-Strength, High-Conductivity Copper Alloys", to be presented at the 12th International Symposium on the Effects of Radiation on Materials, Williamsburg, VA (June 1984). Proceedings to be published by ASTM.

5. CRC Handbook of Chemistry and Physics, R.C. Weast (Ed), 59th edition (1979).

6. T. Maruta, J. Japan Copper and Brass Res. Assn. 2 (No. 1) (1963) 89-96.

7. W.R. Opie, Y.T. Hsu and R.J. Smith in "Copper and Its Alloys," Institute of Metals Monograph No. 34 (1970), Institute of Metals, London, 264.

8. T. Nagai et al., Trans. Japan Inst. Metals 14 (1973) 462-469.

9. C. Logan et al., J. Nucl. Mater. 103 & 104 (1981) 1551-1556.

10. H. Suzuki, M. Kanno and I. Kawakatsu, J. Japan Inst. Metals (NKG) 33 (1969) 628-633.

11. M.J. Saarivirta, Metal Ind. 103 (1963) 685-688.

12. B.I. Bozic, D.V. Mihailovic and M.L. Kostic, Glas Hem Drus, Beograd 35 No. 7-8 (1970) 405-414.

13. Source Book on Copper and Copper Alloys, American Society for Metals (1979), Metals Park, Ohio, pp. 156, 163, 166.

8.0 Future Work

Additional resistivity specimens for each of the various annealing conditions will be analyzed in order to give a more complete and accurate picture of the fundamental processes which are occurring in these alloys during annealing. Microhardness and resistivity measurements will be reported on specimens which have been annealed for 100 hours. Residual resistivity ratio measurements will be made on selected specimens and the results will be compared to theoretical resistivity predictions.

9.0 Publications

None

COMPARISON OF THERMAL AND IRRADIATED BEHAVIOR OF HIGH-STRENGTH, HIGH-CONDUCTIVITY COPPER ALLOYS

S.J. Zinkle, R.A. Dodd and G.L. Kulcinski (University of Wisconsin-Madison)

1.0 Objectives

To investigate the irradiated response of high-strength, high-electrical conductivity copper alloys as a function of heavy ion damage level. The microstructural evolution of candidate high-strength copper alloys under irradiation are studied in order to determine what events may limit the useful lifetime of the material in a fusion reactor.

2.0 Summary

The microstructures of two candidate high-strength, high-electrical conductivity copper alloys (AMZIRC and AMAX-MZC) have been studied after heavy ion irradiation and after thermal annealing. An investigation of the behavior of these alloys following thermal treatment has revealed that much of their strength is due to cold-working (high dislocation density). Microhardness measurements revealed that the MZC and AMZIRC copper alloys have a recrystallization temperature of about 475°C. Both alloys have been irradiated with 14-MeV Cu ions in the temperature range of 400-550°C (0.5-0.6 T_m). Samples were irradiated to maximum fluences of 3 x 10^{20} ions/m^2, which corresponds to a calculated peak displacement damage of 15 dpa based on a damage efficiency of K = 0.3. The irradiated foils have been examined in cross-section in an electron microscope. No void formation was observed in either alloy for this temperature range. Irradiation was found to enhance dislocation recovery and grain recrystallization processes in both alloys at the lower temperatures. The observed results imply that the MZC and AMZIRC copper alloys may undergo a serious degradation in their mechanical properties when exposed to irradiation at temperatures around 400°C.

3.0 Program

Title: Radiation Effects to Reactor Materials
Principal Investigators: G.L. Kulcinski and R.A. Dodd
Affiliation: University of Wisconsin-Madison

4.0 Relevant DAFS Program Plan Task/Subtask

Subtask II.B.3.2 Experimental Characterization of Primary Damage State; Studies of Metals
Subtask II.C.1.2 Modeling and Analysis of Effects of Material Parameters on Microstructure
Subtask II.C.6.3 Effects of Damage Rate and Cascade Structure on Microstructure; Low-Energy/High-Energy Neutron Correlations

5.0 Accomplishments and Status

5.1 Introduction

There has recently been a renewed interest in the irradiated properties of copper alloys as a result of design studies which call for incorporation of high-strength, high-conductivity materials in fusion reactors. A recent workshop sponsored by the Department of Energy serves to highlight the relative importance of copper alloys for fusion reactor applications.[1] Requirements of high axial magnetic fields have led to a hybrid magnet design where a normal-conducting coil is inserted inside of a shielded superconducting coil. High-strength copper alloys have also been considered for use as high magnetic field insert coils in both

tandem mirror and tokamak fusion reactors.[2] High strength copper alloys are also being considered for use as unshielded magnet coils and as the first wall in compact fusion devices.[3,4] Other proposed areas of use for copper alloys in high irradiation zones include diverters, limiters and rf antennas.

The properties of irradiated pure copper have been investigated in great detail, and a large data base has been established (see, e.g. Ref. 5 for a review). However, there is relatively little information available on the response of copper alloys to irradiation. Several copper alloys which are commercially available have unirradiated mechanical and electrical properties which are suitable for the above-mentioned fusion reactor applications, and extensive alloy development work is continuing. Unfortunately, there is no known irradiation data available at the present time for these high-strength, high-conductivity alloys. There is therefore an urgent need for irradiation data at conditions which will be typical of the environment experienced by these alloys in the reactor. The temperature range of interest varies from 25°C to greater than 450°C. Expected lifetime damage levels for these alloys range from less than 1 dpa to greater than 100 dpa.[1]

Two candidate high-strength, high-conductivity copper alloys have been selected for an investigation of the microstructural alterations which occur during heavy ion irradiation. AMZIRC and AMAX-MZC are heat-treatable copper alloys which have unirradiated yield strengths of 400-500 MPa and electrical conductivities which may approach the range of 80-90% IACS (International Annealed Copper Standard).[6] An additional advantage of these copper alloys is that they have a relatively high recrystallization temperature of about 450°C. They are therefore potentially suitable for use at temperatures up to 400°C. Table 1 lists the composition of these alloys, along with some typical physical properties quoted by the manufacturer.

This study investigates the microstructural evolution of the AMZIRC and MZC copper alloys following Cu ion irradiation to moderate damage levels at temperatures near the upper range of interest for fusion reactor applications. The damage microstructure is compared to the microstructure observed following thermal annealing in order to estimate the magnitude of the change in physical properties due to irradiation.

5.2 Experimental Procedure

Samples of the AMZIRC and AMAX-MZC copper alloys were obtained from AMAX Copper, Inc. in the form of 250 μm thick foils. Specifications given to the manufacturer for the alloy heat treatment called for obtaining the highest electrical conductivity achievable which was consistent with a yield strength of 415 MPa (60 ksi). The alloy preparation consisted of a solution heat treatment at 900°C for 1 hr, followed by 90% cold-rolling and then aging for 30 minutes at 375°C for the AMZIRC alloy and 400°C for the MZC alloy. Tensile tests performed by the manufacturer on these two lots of materials indicated that both alloys had yield strengths in excess of 480 MPa (70 ksi). No electrical conductivity tests were made by the manufacturer.

Electrical resistivity measurements were performed on the as-received alloys using standard techniques.[7] Measurements were made at room temperature (23°C) and 4.2 K. The gage length over which the voltage drop was measured was about 5 cm and the current density was maintained at about 200 A/cm^2. Four specimens from each alloy were measured. Readings were taken with the current going both ways through the specimen and the results averaged in order to cancel the effect of thermal emfs.

As-received specimens from both copper alloys were mechanically polished using 0.3 μm alumina powder prior to their thermal annealing treatment. Specimens were annealed for 1 hour in a high vacuum furnace and cooled using a combination of furnace and air cooling. The specimen temperature decreased by 100°C within 1 minute following the anneal. Temperature control was maintained to within ± 5°C. The pressure in the vacuum chamber ranged from 1×10^{-6} to 1×10^{-8} Torr during the anneal. All specimens were electropolished immediately prior to making microhardness measurements in order to remove the oxide layer present from the anneal.

Vickers microhardness measurements were obtained from as-received and annealed specimens of each alloy at an indenter load of 200 g. A minimum of nine different indentations in three widely separated areas were measured for each alloy at the different annealing conditions. The measurements were obtained using a Buehler Micromet® microhardness tester and an antivibration test stand. Details of the specimen preparation and measurement procedure have been previously described.[8]

TABLE 1

COMPOSITION AND OPTIMUM PHYSICAL PROPERTIES OF AMZIRC AND MZC
(from Ref. 6)

Alloy	Zr (%)	Cr (%)	Mg (%)	Electrical Conductivity @ 20°C	Yield Strength (0.2% Offset)
AMZIRC	0.13-0.20	-	-	93% IACS	410 MPa
MZC	0.15	0.80	0.04	90% IACS	517 MPa

Specimens of the as-received AMZIRC and AMAX-MZC alloys were mechanically polished and then electropolished at an applied potential of 5 V in a solution of 33% HNO_3/67% CH_3OH cooled to -40°C prior to their irradiation. Irradiations were performed on the as-received alloys at the Heavy Ion Irradiation Facility of the University of Wisconsin tandem Van de Graaf accelerator[9] with 14-MeV Cu^{3+} ions. The incident ion flux was approximately 5 x 10^{16} ions/m^2-s for all of the irradiations. The resultant irradiation time for the high fluence samples was $\lesssim$ 2 hours.

The depth-dependent damage energy ($S_D(x)$) for 14-MeV Cu ions incident on copper was calculated using the BRICE code.[10] This damage energy was then converted into displacements per atom (dpa) using the modified Kinchin-Pease model:[11]

$$N_d(x)\ (\text{dpa/sec}) = (\phi/N)\ \frac{K\ S_D(x)}{2\ E_d} \qquad (1)$$

where ϕ is the incident particle flux, N is the atomic density of the target, E_d is the spatial-averaged displacement energy and K is the displacement efficiency. A value of E_d = 29 eV has been used in the dpa calculations.[12] The displacement efficiency (K) has generally been assumed to be equal to 0.8, independent of energy. Recent work indicates that K varies strongly with energy (see Ref. 13 for a review). At high energies, K becomes roughly constant with a value of 0.3 for copper. Therefore, we have used K = 0.3 for all of our dpa calculations in this paper. Figure 1 shows the calculated damage and injected ion distributions for 14-MeV copper ions incident on copper.

Following the irradiation, the samples were electroplated with copper and cut into foils suitable for cross-sectional analysis using techniques developed by Knoll et al.[14] Transmission electron microscope (TEM) specimens were jet-electropolished using a solution of 33% HNO_3/67% CH_3OH cooled to -20°C at an applied voltage of 15-20 V. Specimens were examined in a JEOL TEMSCAN-200CX electron microscope equipped with a Tracor-Northern TN2000 energy dispersive x-ray spectroscopy (EDS) system.

5.3 Results

5.3.1 Investigation of As-Received and Thermal-Annealed Specimens

The microstructure of the as-received AMZIRC and AMAX-MZC copper alloys is shown in Fig. 2. The dominant feature evident from these micrographs is the very high dislocation density present in the matrix. A relatively low density (~ $10^{18}/m^3$) of medium-sized precipitates (diameter $\lesssim$ 0.5 μm) were found to exist in both alloys. Examples of these precipitates are highlighted in Fig. 2. The MZC precipitates have been identified as pure chromium by using a combination of EDS and microdiffraction techniques. The exact composition of the AMZIRC precipitates is currently uncertain. Qualitative EDS analysis indicates that these precipitates are zirconium-rich. In addition, a very low density ($\lesssim$ $10^{17}/m^3$) of precipitates ranging in size from 1 μm to 10 μm were also observed in the AMZIRC alloy. Microdiffraction and EDS analysis has shown that these large precipitates are pure zirconium.

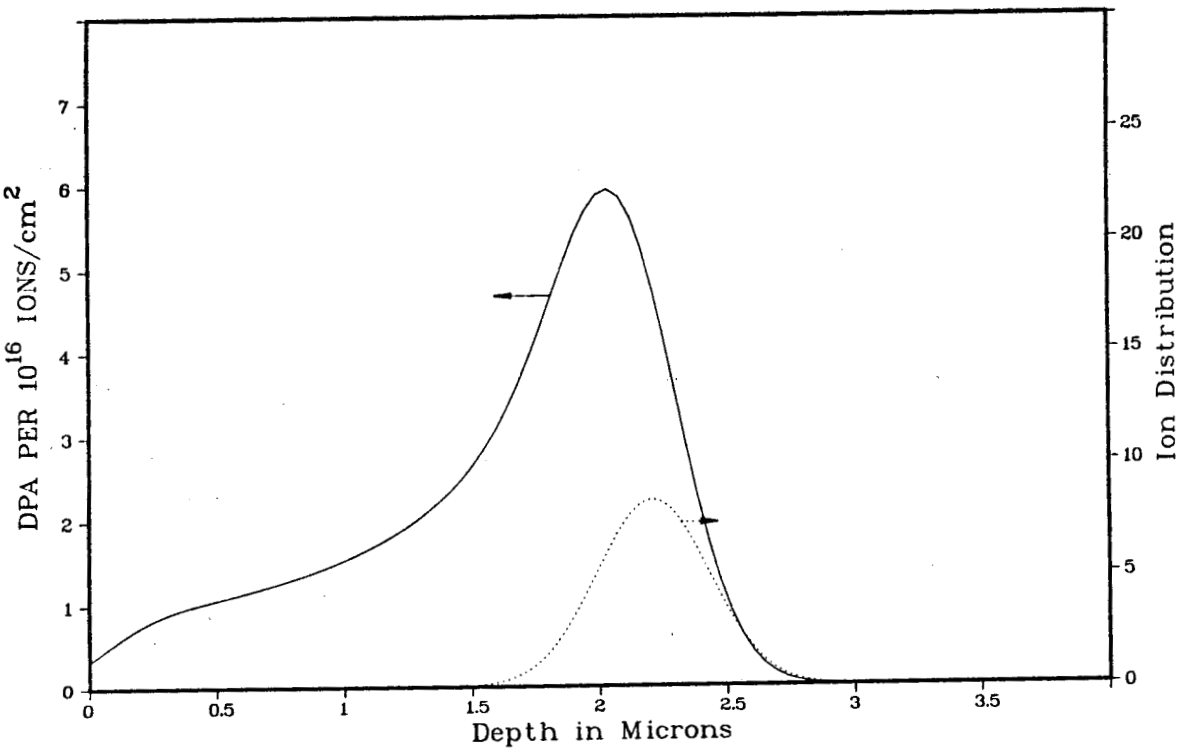

FIGURE 1. Calculated ion displacement damage and implanted ion distribution for 14-MeV Cu incident on a copper target using the BRICE code.[10] DPA calculation assumes a displacement efficiency of K = 0.3, as opposed to the "standard" value of 0.8 (see text).

The resistivity and Vickers microhardness (VHN) results obtained from the as-received alloys are shown in Table 2. The AMZIRC alloy has the higher conductivity and residual resistivity ratio (RRR), while the MZC alloy exhibits a larger microhardness number. The microhardness measurements were obtained using a 100 g load. A comparison between Table 1 and Table 2 reveals that both measured values of the alloy electrical conductivity are significantly lower (by ~ 35%) than the manufacturer's quoted optimum values.

Using appropriate hardness-yield strength correlations found in the literature, it is possible to estimate the yield strength of the two alloys:[15]

$$\sigma_y = (VHN/3)(0.1)^n \qquad (2)$$

where n is the strain hardening coefficient. Typical values for copper are n = 0.1 and n = 0.45 for cold-worked and annealed conditions, respectively.[16] Using n = 0.1, the results of this correlation may be

TABLE 2

MEASURED RESISTIVITY AND VICKERS MICROHARDNESS VALUES FOR AS-RECEIVED AMZIRC AND AMAX-MZC

Alloy	Resistivity (nΩ-m) 296 K	Resistivity (nΩ-m) 4.2 K	RRR = ρ 296 K/ρ 4.2 K	Conductivity (23°C)	Microhardness (HV_{100})
AMZIRC	23.2 ± 1.6	3.9 ± 0.3	6.0	73% IACS	144 ± 5
MZC	29.5 ± 1.6	13.5 ± 0.8	2.2	58% IACS	174 ± 7

TRANSMISSION ELECTRON MICROGRAPHS OF AS-RECEIVED COPPER ALLOYS

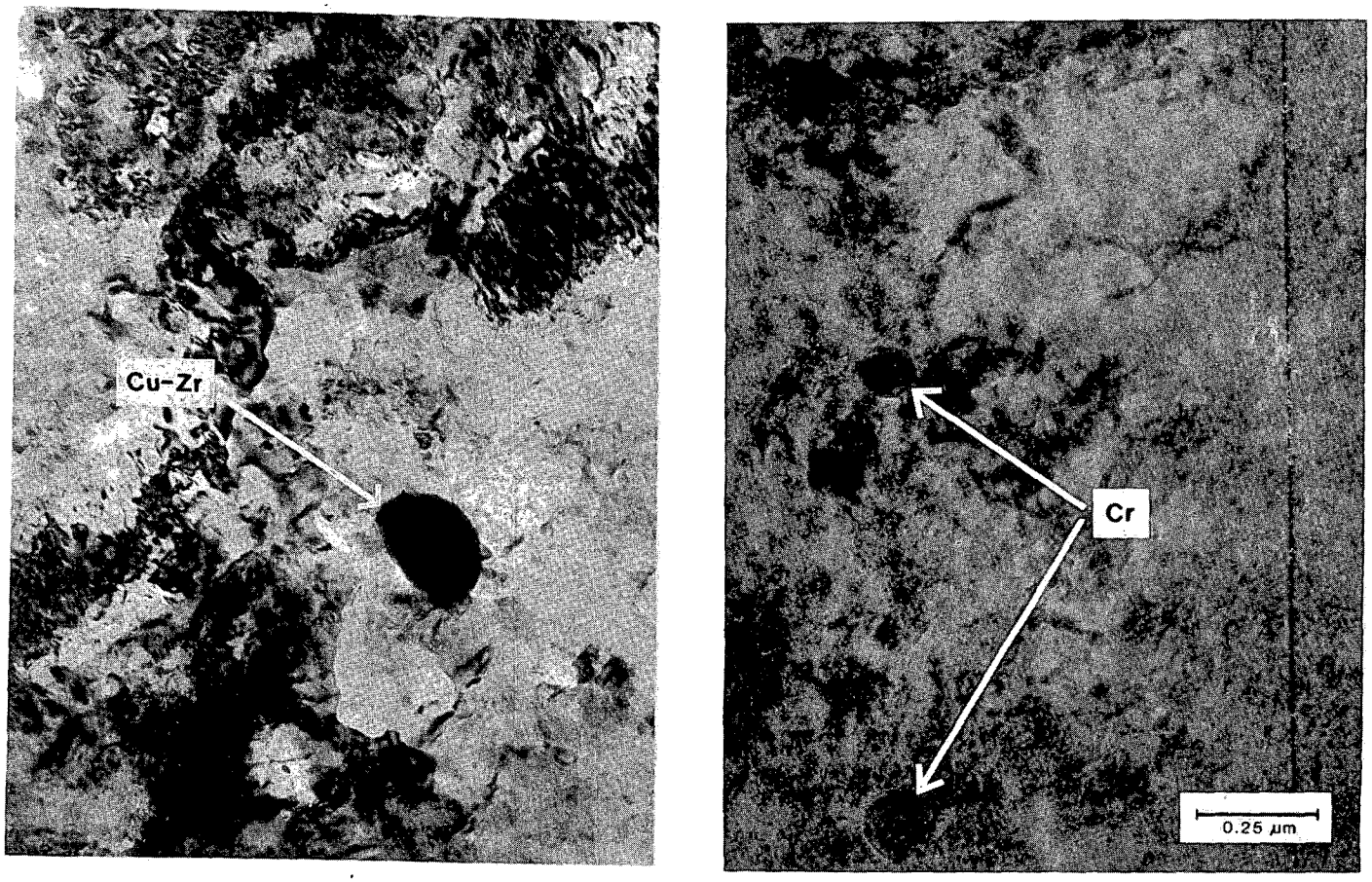

FIGURE 2. TEM micrographs showing the as-received microstructure of AMZIRC and AMAX-MZC at a magnification of 50,000.

plotted along with the observed electrical conductivity to give a "figure of merit" for high-strength, high conductivity materials. The results are shown in Fig. 3. For purposes of comparison, the quoted materials parameters of a high-strength, high-conductivity copper alloy being developed by INESCO, Inc.[3] are shown in this figure along with the properties of annealed and lightly cold-worked copper. The estimated yield strengths of AMZIRC and AMAX-MZC are both in good agreement with the manufacturer's specifications, but the electrical conductivities are substantially lower than expected.

The microhardness results obtained from the two alloys following a 1 hour anneal at various temperatures are shown in Fig. 4. Both AMZIRC and AMAX-MZC exhibit a recrystallization temperature of about 475°C. Upon recrystallization, their microhardness numbers approach values typically found for annealed copper.

5.3.2 Ion Irradiation Results

AMZIRC and AMAX-MZC samples were irradiated with 14-MeV Cu ions at temperatures betewen 400°C and 550°C (0.5 - 0.6 Tm) up to calculated peak damage levels of 15 dpa (K = 0.3). No void formation was observed in these alloys for these conditions. As reported elsewhere,[17] a 14-MeV Cu irradiation of AMZIRC to 15 dpa at 300°C resulted in the formation of a very low density of large voids (diameter $\lesssim$ 0.5 μm).

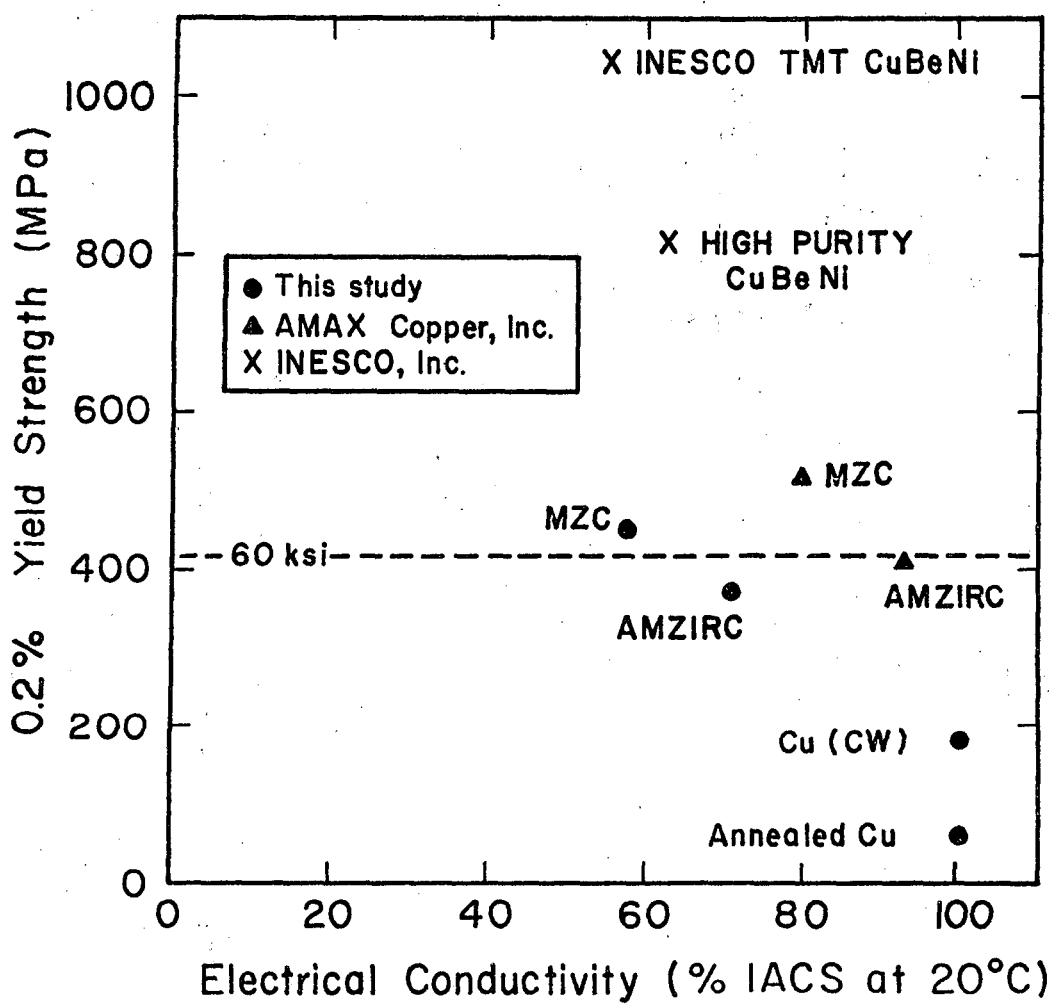

FIGURE 3. Measured electrical conductivity and correlated yield strength of as-received AMZIRC and AMAX-MZC as compared to other high-strength copper alloys and the manufacturers specifications. AMAX copper data is from Ref. 6. INESCO data is from Ref. 3.

The major effect of irradiation of AMZIRC and MZC in this temperature regime was to greatly accelerate re covery and recrystallization processes. Figure 5 shows the effect of irradiation on AMZIRC to a peak damage level of 15 dpa (K = 0.3) as a function of temperature. These cross-sectional micrographs allow both the damage region and the control region of the foil to be simultaneously examined. At 400°C there is evidence of dislocation recovery and subgrain nucleation in the damage region, while the control region microstructure shows no signs of recovery. Both the control and damage regions have completely recrystallized following irradiation at 500°C and 550°. Small Cu-Zr precipitates are visible in the recrystallized regions. No significant difference was observed in the precipitate size or density between the damage and control regions.

The effect of irradiation temperature on the damage microstructure of AMAX-MZC is shown in the cross-section micrographs of Fig. 6. At 400°C, Cu ion irradiation to a peak damage level of 15 dpa (K = 0.3) causes recrystallization to occur while the control microstructure remains essentially unchanged. Irradiation at 500°C results in a fine-grained (grain diameter ~ 0.5 μm) microstructure in the damage region, while the control region has completely recrystallized and has grains which have grown to a size $\lesssim$ 10 μm. Once again, small precipitates are visible in the fully recrystallized regions. No differences in the precipitate size or density of the damage region vs. the control region was discernible.

The AMAX-MZC alloy exhibited a more dramatic radiation-enhanced recrystallization behavior than AMZIRC for

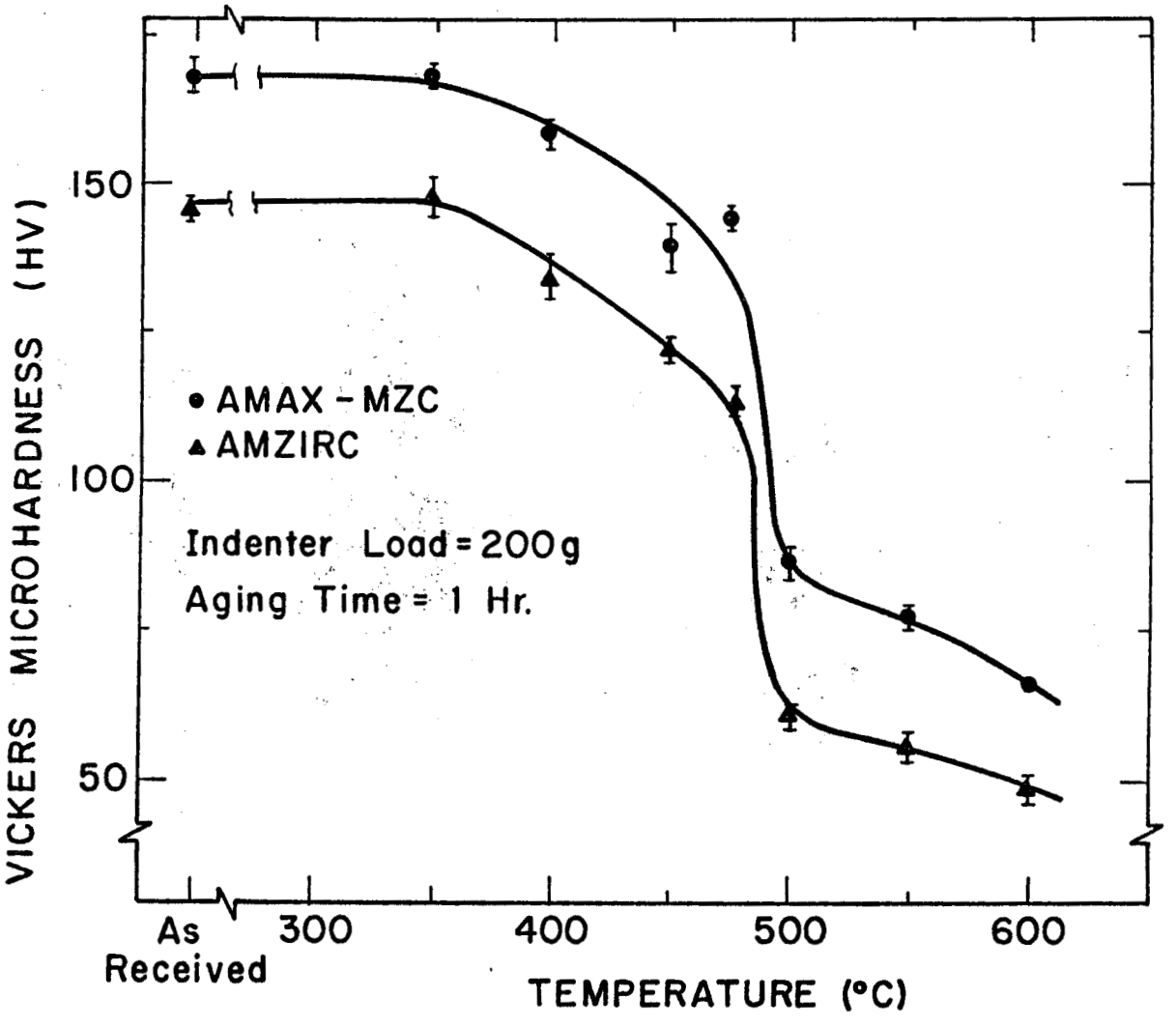

FIGURE 4. Vickers microhardness number of as-received AMZIRC and AMAX-MZC as a function of annealing temperature following a 1 hour anneal.

the same irradiation conditions. This result is conclusively demonstrated in Fig. 7, where cross-section microstructures of AMZIRC and MZC are compared following a 400°C, intermediate-fluence (peak damage level = 4.5 dpa, K = 0.3) irradiation. Subgrain formation is well established in the MZC damage region, while recrystallization is just beginning in the AMZIRC damage region.

In order to investigate the minimum irradiation temperature and damage level required to initiate recrystallization in AMAX-MZC, a low-fluence, low-temperature ion irradiation was performed. Figure 8 compares the cross-section microstructure in MZC following a 300°C, 1.5 peak dpa (K = 0.3) irradiation with the microstructure observed after a 400°C, 4.5 peak dpa (K = 0.3) irradiation. It is seen that some recrystallization has occurred in this alloy even at these relatively modest irradiation conditions.

5.4 Discussion

5.4.1 As-Received and Thermal Anneal Effects

As can be seen from Fig. 3, the correlated yield strength of the as-received AMZIRC and AMAX-MZC copper

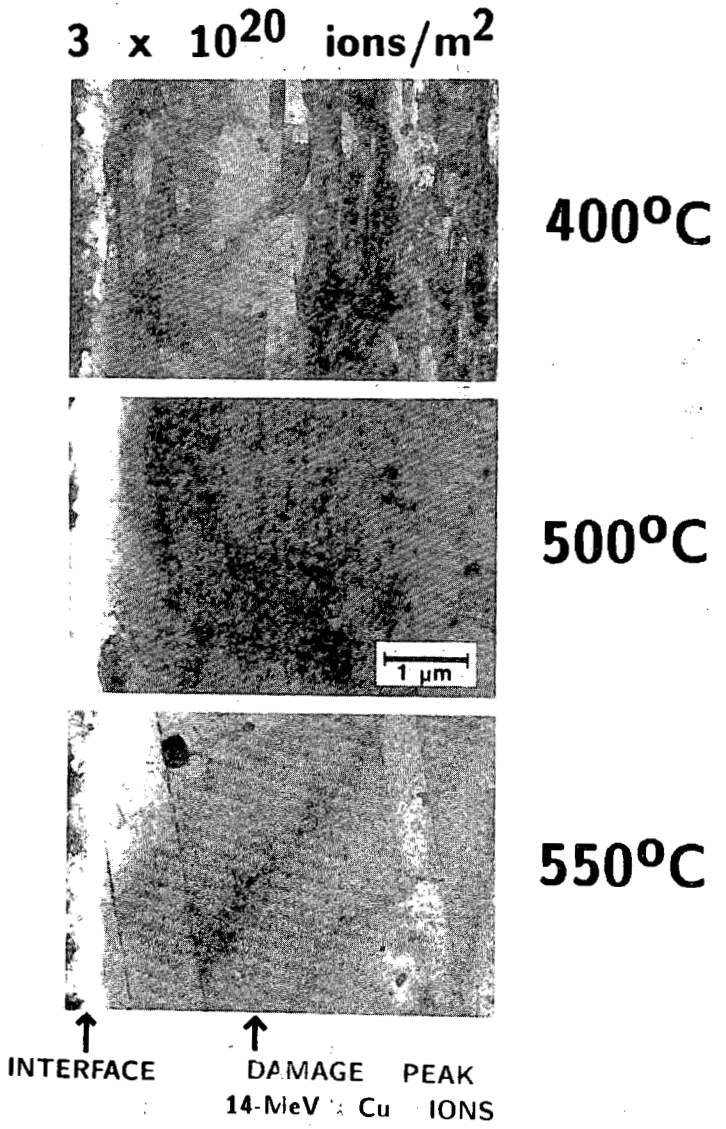

FIGURE 5. Depth dependent microstructure of ion-irradiated AMZIRC as a function of irradiation temperature following irradiation to a calculated peak damage level of 15 dpa (K = 0.3). The top through bottom figures correspond to irradiations at 400, 500 and 550°C, respectively.

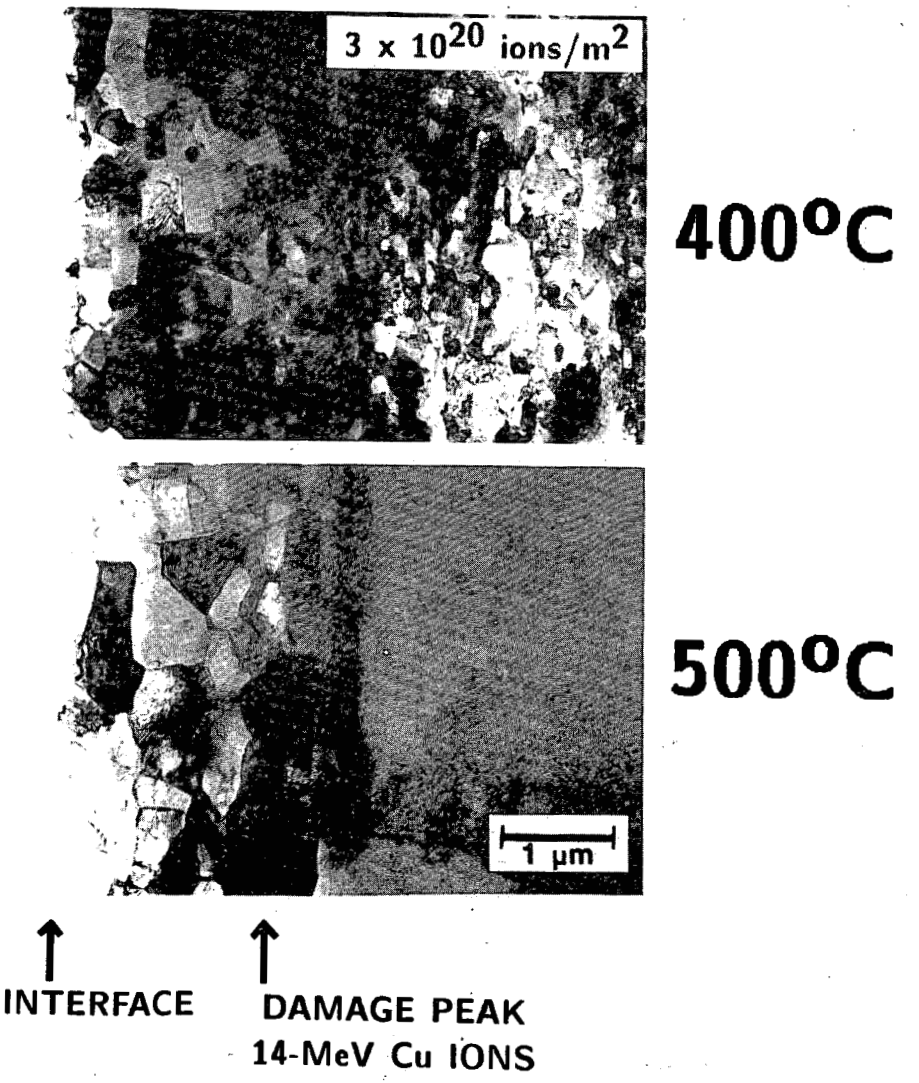

FIGURE 6. Depth dependent microstructure of ion-irradiated AMAX-MZC as a function of irradiation temperature following irradiation to a calculated peak damage level of 15 dpa (K = 0.3). Top figure: 400°C. Bottom figure: 500°C.

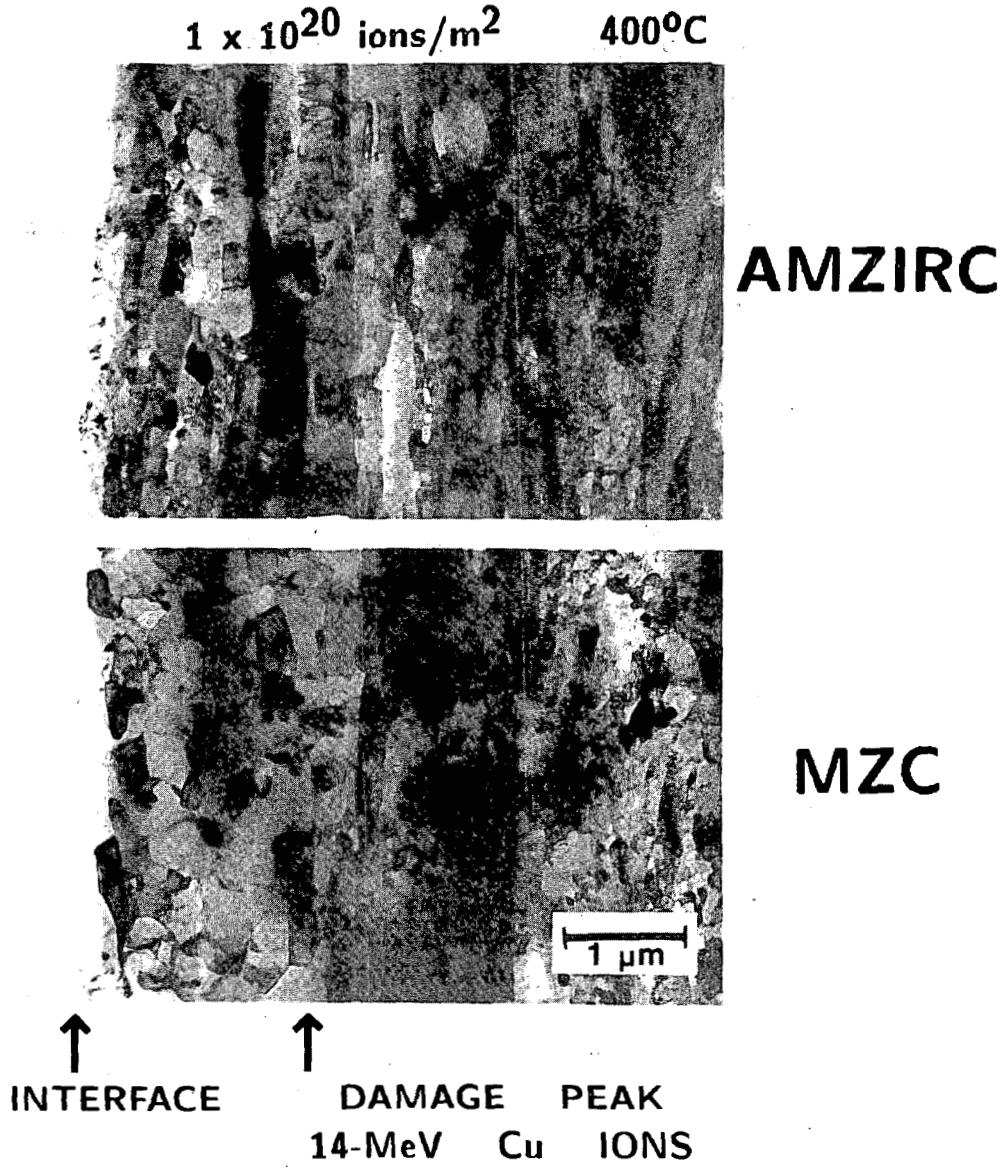

FIGURE 7. Comparison of the depth-dependent microstructures of ion-irradiated AMZIRC and AMAX-MZC following irradiation at 400°C to a calculated peak damage level of 4.5 dpa (K = 0.3). Top figure: AMZIRC. Bottom figure: AMAX-MZC.

alloys as inferred from microhardness measurements is in good agreement with the manufacturer's specifications. On the other hand, the measured electrical conductivities of both alloys were substantially below the manufacturer's quoted optimum values (by ~ 35%). This discrepancy is likely due to the presence of impurities in these commercial alloys. Several silicon-rich impurity precipitates have been observed from EDS measurements on these alloys during the course of this investigation. Some of the degradation in the electrical conductivity value may also be due to the presence of excess amounts of Cr and Zr solute in these alloys. The intermediate-sized Cr and Cu-Zr precipitates pictured in Fig. 2 are an indication that this is indeed the case, since these precipitates are too large to have been formed during the aging treatment alone. This means that Cr and Zr concentrations in excess of the solute solubility limit at the solution annealing temperature must be present in the AMAX-MZC and AMZIRC alloys, respectively.

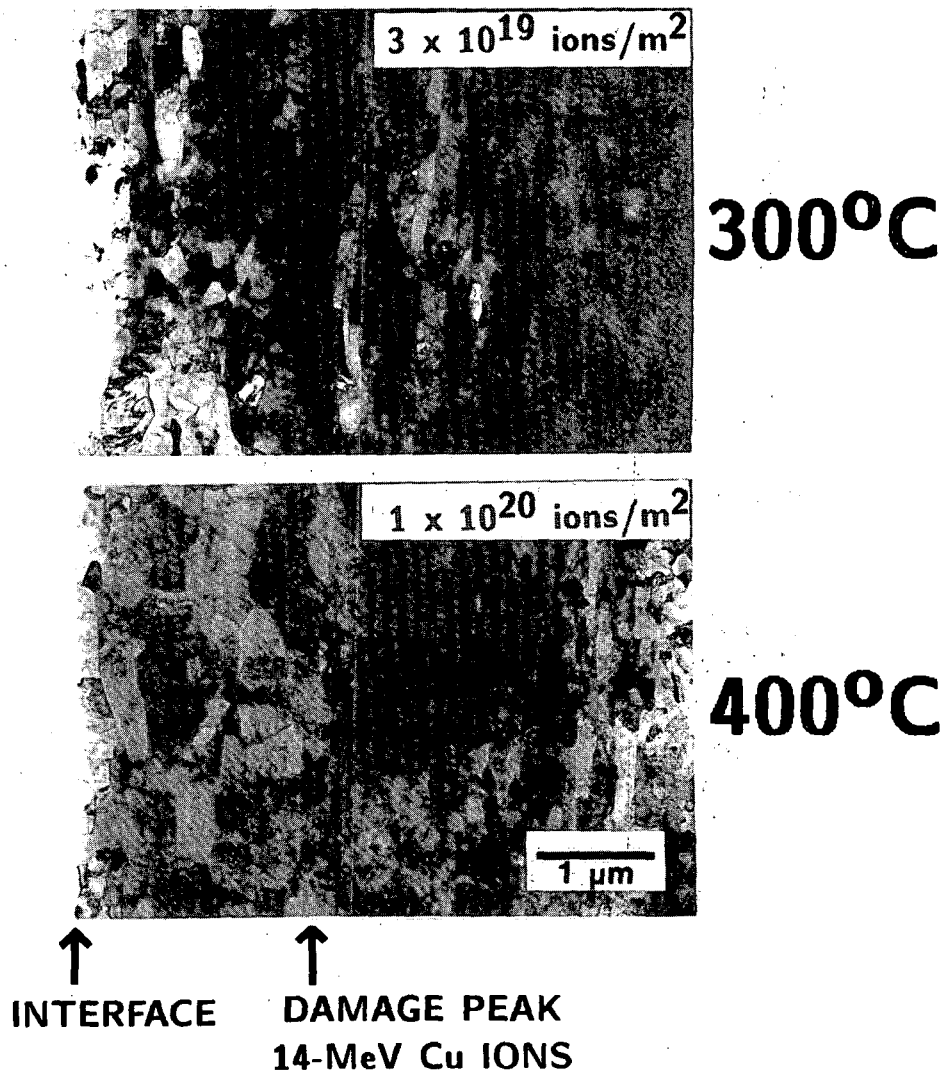

FIGURE 8. Evolution of the depth-dependent recrystallization region in ion-irradiated AMAX-MZC. The top figure corresponds to a 300°C, 1.5 peak dpa (K = 0.3) irradiation and the bottom figure corresponds to a 400°C, 4.5 peak dpa (K = 0.3) irradiation.

The thermal annealing study (Fig. 4) indicates that a substantial portion of the strength of these alloys is due to their cold-worked structure. In order to quantify the relative strength of these alloys due to precipitation hardening versus cold-working, a supplemental annealing study was performed. Several AMZIRC and AMAX-MZC specimens were encapsulated in evacuated quartz tubes and annealed at 950°C for 100 hours. Following a water quench, one-half of the specimens were resealed in quartz tubes and aged at 470°C for 1 hour. The results of microhardness measurements made on the solution annealed and solution annealed plus aged alloys are shown in Table 3. It can be seen from this table that the AMZIRC alloy has no observable response to precipitation hardening for these conditions. The MZC alloy shows a significant strength increase due to this precipitation-hardening treatment. This observation is in agreement with other thermal aging studies reported for these alloys.[18-20] Both aged alloys show microhardness numbers which are substantially below their as-received values. It can therefore be concluded that a large portion of the strength of both of these alloys is due to their cold-worked structure.

The recrystallization temperature for both AMZIRC and AMAX-MZC has been found to be about 475°C, in agreement with other literature results.[6,21] Upon recrystallization, the microhardness numbers for both alloys

TABLE 3

VICKERS MICROHARDNESS OF SOLUTION-TREATED COPPER ALLOYS
(200 g load)

	Microhardness (HV_{200})		
Alloy	As-Received	Solution Annealed (SA)	SA + Aged at 470°C
AMZIRC	146 ± 1	50 ± 2	48 ± 2
AMAX-MZC	168 ± 2	46 ± 5	84 + 4

are similar to the value for pure copper. Both AMZIRC and AMAX-MZC are therefore unsuitable for use as a high strength alloy when conditions are present which might cause recrystallization to occur.

5.4.2 Ion Irradiation Effects

A review of the published irradiation data on copper shows that void formation occurs readily for neutron irradiation temperatures between 220 and 550°C (0.35-0.60 Tm).[5] The present irradiations did not result in detectable void formation in either the AMZIRC or the AMAX-MZC alloy for temperatures between 400 and 550°C. A limited number of large voids were observed in a companion ion irradiation of AMZIRC at 300°C,[17] which indicates that the peak void swelling temperature for ion irradiation of these alloys is below 300°C. The cause of this large apparent shift in the void swelling temperature regime is speculated to be due to gas effects. Void nucleation calculations for copper irradiated in the absence of gas nucleating agents indicate that void formation is not expected for temperatures $\gtrsim$ 300°C.[17] Experimental studies on ion-irradiated copper by Glowinski[22] and Knoll[23] have found that de-gassed copper does not form voids for temperatures between 400-500°C. Both AMZIRC and AMAX-MZC are manufactured under carefully controlled (oxygen-free) environments using OFHC copper, so they do not initially contain any gas. It appears that more basic work regarding the effect of gas on void nucleation in copper is needed.

The main effect of ion irradiation on the microstructure of AMZIRC and AMAX-MZC at temperatures between 300 and 550°C was to greatly accelerate dislocation recovery and grain recrystallization processes. There are relatively few published reports which have examined the phenomenon of radiation-enhanced recrystallization. The major reported effect of radiation-enhanced recrystallization is to cause a reduction of the void density in the nucleated grains compared to unrecovered regions of the crystal.[24,25] Perhaps a more important effect to consider in the present case is the dramatic loss of strength in the AMZIRC and MZC alloys upon recrystallization. Since much of the strength of these alloys is due to their cold-worked structure, the irradiation results observed in Figs. 5-8 imply that AMZIRC and MZC will suffer a substantial degradation of strength during irradiation at temperatures $\lesssim$ 400°C. This argument will be quantified to a certain extent later in this paper.

A comparison of the irradiated microstructures of AMZIRC and AMAX-MZC for temperatures of 400-500°C reveals differences in their behavior (Figs. 4-6). The MZC alloy appears to be much more sensitive to irradiation with regard to grain recrystallization -- subgrain formation is observed to occur even at relatively modest irradiation conditions (Fig. 8) of 300°C and a peak damage level of 1.5 dpa (K = 0.3). Polygonization of the subgrains is observed in MZC following irradiation at 400°C to a peak damage level as low as 4.5 dpa (K = 0.3). In contrast, irradiation of AMZIRC at 400°C to a peak damage level of 15 dpa does not result in polygonization of the subgrains in the irradiated region. For higher irradiation temperatures (500°C), the AMZIRC alloy has completely recrystallized and there is no discernible difference between the irradiated and nonirradiated regions (Fig. 4). The MZC alloy has essentially retained the small polygonized subgrain structure in the damage region following a 500°C irradiation, while the nonirradiated region of the crystal has completely recrystallized. Microdiffraction analysis of the MZC damage region has revealed the presence of low-angle (~ 5°) sub-boundaries which separate the subgrains along with some high angle boundaries. It appears that some type of solute segregation/precipitation mechanism may be causing the pinning of the subgrain boundaries of MZC in the damage region. This mechanism apparently does not operate in the AMZIRC alloy.

There was no readily evident effect of irradiation on precipitate size or density for either AMZIRC or MZC due to inhomogeneities in the alloy precipitate distributions. In some specimens a lower density of precipitates was observed in the damage region compared to the control region, while the opposite effect was observed in different specimens exposed to similar irradiation conditions. One tenative observation is that there were generally fewer small precipitates in the damage region compared to the control region. Further study is required to confirm this finding.

Examination of Fig. 8 indicates that radiation-enhanced recrystallization may start to occur in AMZIRC and MZC irradiation conditions as moderate as 300°C, 1.5 peak dpa (K = 0.3). Since recrystallization is indicative of a large loss in strength, this implies that large engineering safety factors will be required when considering these type of alloys for high-strength reactor applications. Unfortunately, the strength of the ion-irradiated damage region cannot be directly measured due to its limited size. This is not due to technological difficulties -- several investigators have successfully developed microhardness indentation techniques which are capable of sampling regions as small as a few hundred nanometers in depth.[26,27] Instead, the problem is that it is presently impossible to directly correlate low-load microhardness results to bulk behavior due to the influence of the surface.[8]

An alternative approach which may be used to quantify the loss of strength of the AMZIRC and MZC alloys in the damage region is to directly compare the irradiated microstructure to the microstructure obtained from thermal annealed specimens. Such a comparison is made in Fig. 9. The top two micrographs correspond to the microstructure observed in AMZIRC and AMAX-MZC after annealing for 1 hour at 475°C (i.e, the onset of recrystallization). The two inset figures show the microhardness values which were obtained for this annealing condition (Fig. 4). The bottom two micrographs show the typical damage microstructure which is observed in AMZIRC and MZC after irradiation at conditions as indicated. The similarity in the annealed and irradiated microstructures for the two alloys is taken as an indication of equivalent strength. Two related effects are immediately evident: First, irradiation causes an effective shift of the recrystallization temperature to lower values. The magnitude of this shift is on the order of 100°C for AMZIRC irradiated to a peak damage level of 15 dpa (K = 0.3) and about 200°C for MZC irradiated to a peak damage level of 1.5 (this comparison once again shows the stronger influence of irradiation on the MZC alloy as compared to the AMZIRC alloy). One of the previously mentioned advantages of these copper alloys is that they offer an unirradiated recrystallization temperature which is substantially above that of pure copper. The above discussion indicates that this advantage will be lost to a large extent upon irradiation, and the recrystallization temperature may approach a value comparable to pure copper.

The second effect (which is caused by the above-mentioned shift in the recrystallization temperature) is that both alloys lose a significant portion of their strength when irradiated at temperatures of 300-400°C. Comparison with the thermal annealed microhardness numbers (VHN) indicates that the irradiated AMZIRC microhardness number has dropped to 80% of its original value, (new VHN = 115 HV) while the irradiated MZC microhardness number has fallen to 75% of its original value (new VHN = 130 HV). The corresponding decrease in yield strength will be even greater than the microhardness change. This is because the work-hardening exponent (n) will also change (increase compared to the cold-worked case) as the alloys undergo recovery and recrystallization (see discussion of Eq. 2). A simple estimation of the yield strength of the irradiated regions in AMZIRC and AMAX-MZC may then be made by assuming the work-hardening exponent n has a value similar to that for annealed copper (n = 0.45). This gives lower limits for the yield strength of the irradiated alloys of $\sigma_y \sim 130$ MPa and $\sigma_y \sim 150$ MPa, respectively for AMZIRC and MZC. This may be compared with their estimated unirradiated yield strengths of 375 and 450 MPa, respectively. The inferred dramatic loss of strength upon irradiation may make these alloys unacceptable for their proposed use in fusion reactors.

Still another factor to consider is that the present investigation dealt with radiation-enhanced recrystallization effects in the absence of any external stresses. High-strength copper alloys are being proposed for use in fusion reactors in places where they will be exposed to fairly large stress levels while they are being irradiated. Since it is well known that applied stress can accelerate the recrystallization process,[28] it appears obvious that the combined effects of stress and irradiation can lead to deleterious strength changes in any alloy which relies on thermomechanical treatment for a large portion of its non-irradiated strength.

In summary, it appears that an unacceptable loss in strength may occur in AMZIRC and AMAX-MZC (or any alloy which relies extensively on thermomechanical treatment for its strength) during irradiation. However, more data is needed at lower irradiation temperatures in order to confirm the trends which have been observed at the higher irradiation temperatures.

MICROSTRUCTURAL COMPARISON OF RADIATION DAMAGE vs. THERMAL ANNEALING EFFECTS

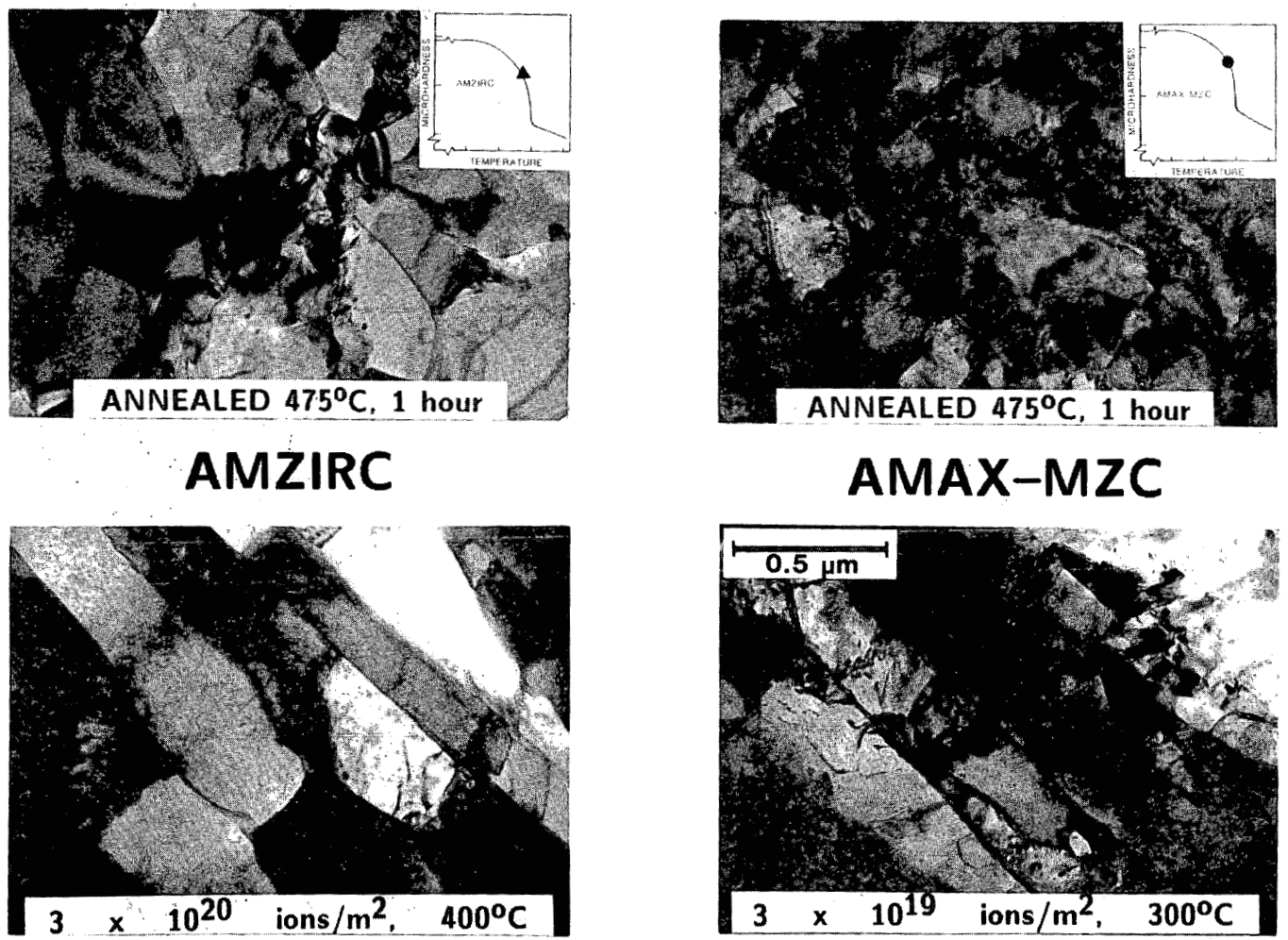

FIGURE 9. Microstructural comparison of thermal annealing vs. radiation damage effects in AMZIRC and AMAX-MZC. The AMZIRC specimen was irradiated at 400°C to a calculated peak damage level of 15 dpa (K = 0.3). The MZC specimen was irradiated at 300°C to a calculated peak damage level of 1.5 dpa (K = 0.3).

TABLE 4

CURRENT OR PROPOSED APPLICATIONS OF HIGH-STRENGTH COPPER ALLOYS IN THE FUSION ENERGY COMMUNITY

Device	Use	Peak Temperature	Max. Damage Level*	Design Yield Stress
RTNS-II[21]	14-MeV Neutron Source Targets	200-400°C	~ 0.01 dpa	345 MPa
RIGGATRON[3]	First Wall	$\gtrsim$ 250°C	40 dpa	> 1000 MPa
	Torroidal Coils	150°C	40 dpa	760 MPa
	OH Coils	130°C	<< 1 dpa	410 MPa
CRFPR[29]	First Wall	300-350°C	~ 65 dpa/FPY	70-80 MPa
MARS[2]	Insert Magnet	150°C	~ 20 dpa/FPY	360 MPa
STARFIRE[30]	Limiter	200°C	~ 15 dpa/FPY	330 MPa
TFCX[31]	Magnet	150°C	$\lesssim 10^{-2}$ dpa	?

*assuming damage efficiency K = 0.3

5.4.3 Application of Results to Current and Proposed Fusion Devices

Table 4 lists the various fusion applications for which high strength copper alloys are being considered. For devices where dpa values were not available, the damage level was calculated from the neutron wall loading by assuming that 1 MW/m^2 = 3 dpa/FPY (K = 0.3), where FPY stands for full power year of operation. It can be seen that several devices approach or exceed the irradiation conditions investigated in this paper. In particular, the extreme demands of the RIGGATRON[3] may require a very advanced high-strength, high conductivity alloy yet to be developed. The insert magnets for MARS[2] and the limiters for STARFIRE[30] are two other applications which may require further alloy development before a satisfactory material is found. The AMZIRC alloy is currently being used in RTNS-II as the 50-cm diameter rotating neutron source target.[21] Damage levels are probably too low to be of concern in this device.

5.5 Conclusions

The main effect of ion irradiation of AMZIRC and AMAX-MZC in the temperature region of 300-550°C is to cause an acceleration of the recovery and recrystallization processes. Since a significant amount of the strength of these alloys is due to their cold-worked structure, large safety margins must be used when considering these type of alloys for fusion reactor applications, at least for the above temperature range.

The effect of applied stress in conjunction with irradiation was not investigated in this study. However, since this type of environment will be present in reactor applications, basic work needs to be done to determine what additional enhancement at recrystallization kinetics, if any, will occur.

Inconclusive results were obtained on the effect of ion irradiation on precipitate evolution due to inhomogeneities present in the AMZIRC and AMAX-MZC alloys.

5.6 Acknowledgements

The authors gratefully acknowledge the assistance of D.H. Plantz during the course of this investigation. This work was performed under appointment to the Magnetic Fusion Energy Technology Fellowship Program and with funds supplied by the Office of Fusion Energy, Department of Energy.

6.0 References

1. F.W. Wiffen, T.C. Reuther and R.E. Gold, "Copper and Copper Alloys for Fusion Reactor Applications: Summary Report of a DOE-OFE Workshop," Third Topical Meeting on Fusion Reactor Materials, Albuquerque, NM (Sept. 1983); to be published in J. Nucl. Mat.

2. L.J. Perkins, "Materials Considerations for Highly Irradiated Normal-Conducting Magnets in Fusion Reactor Applications," Third Topical Meeting on Fusion Reactor Materials, Albuquerque, NM (Sept. 1983); to be published in J. Nucl. Mat.

3. S.N. Rosenwasser et al., "Materials and Design Aspects of the RIGGATORN Tokamak," Third Topical Meeting on Fusion Reactor Materials, Albuquerque, NM (Sept. 1983); to be published in J. Nucl. Mat.

4. R.L. Hagenson, "First Wall, Limiters, and Magnet Coils in Compact Concepts," in Ref. 1.

5. R.W. Knoll, "A Literature Review of Radiation Damage Data for Copper," University of Wisconsin Fusion Engineering Program Report UWFDM-384 (Oct. 1980).

6. Interim Publications on AMZIRC and AMAX-MZC Copper Alloys, AMAX Copper, Inc., New York, NY (1982).

7. S.J. Zinkle, S.N. Farrens, G.L. Kulcinski and R.A. Dodd, "Irradiated Behavior of High-Strength Copper Alloys," DAFS Quarterly Progress Report DOE/ER-0046/15 (July-Oct. 1983) p. 127.

8. S.J. Zinkle and G.L. Kulcinski, "Low-Load Microhardness Changes in 14-MeV Neutron Irradiated Copper Alloys," Symposium on the Use of Non-Standard Subsized Specimens for Irradiated Testing, Albuquerque, NM (Sept. 1983); to be published by ASTM.

9. H.V. Smith and R.G. Lott, Nucl. Instr. Methods 143 (1977) 125-132.

10. D.K. Brice, "Ion Implantation Range and Energy Deposition Codes COREL, RASE4 and DAMG2," Sandia National Laboratory Report SAND 75-0622 (July 1977), Albuquerque, NM.

11. I.M. Torrens and M.T. Robinson in "Radiation Induced Voids in Metals," J.W. Corbett and L.C. Ianniello (Eds.) U.S. Atomic Energy Commission Technical Information Center CONF-710601 (1972), p. 739.

12. R.R. Coltman, Jr., C.E. Klabunde and J.M. Williams, J. Nucl. Mat. 99 (1981) 284-293.

13. J.H. Kinney, M.W. Guinan and Z.A. Munir, "Defect Production Efficiencies in Thermal Neutron Irradiated Copper and Molybdenum," Third Topical Meeting on Fusion Reactor Materials, Albuquerque, NM (Sept. 1983); to be published in J. Nucl. Mat.

14. R.W. Knoll, P.W. Wilkes and G.L. Kulcinski in "Phase Stability During Irradiation," J.R. Holland, L.K. Mansur and D.I. Potter (Eds.) (1980) pp. 123-137.

15. J.R. Cahoon, W.H. Broughton and A.R. Kutzak, Met. Trans. 2 (1971) 1979.

16. D. Tabor, J. Inst. Metals 79 (1951) 1.

17. B. Badger, Jr. et al., "Experimental Investigation of the Effect of Injected Interstitials on Void Formation," these proceedings.

18. M.J. Saarivirta, Metal Ind. 103 (1963) 685-688.

19. H. Suzuki, M. Kanno and I. Kawakatsu, J. Japan Inst. Metals (NKG) 33 (1969) 628-633.

20. T. Nagai et al., Trans. Japan Inst. Metals 14 (1973) 462-469.

21. C. Logan et al., J. Nucl. Mat. 103 & 104 (1981) 1551-1556.

22. L.D. Glowinski and C. Fiche, J. Nucl. Mat. 61 (1976) 22-28.

23. R.W. Knoll, "Effects of Heavy Ion Irradiation on the Phase Stability of Several Copper-Base Alloys," Ph.D. Thesis, Nuclear Engineering Department, University of Wisconsin-Madison (UWFDM-436).

24. G. Das and T.E. Mitchell, Scripta Metall. 8 (1974) 1135.

25. W.V. Vaidya and K. Ehrlich, J. Nucl. Mat. 113 (1983) 149; also see references therein.

26. J.B. Pethica and W.C. Oliver in "Materials Formation by Ion Implantation," S.T. Picraux and W.J. Choyke (Eds.), Elsevier Science Publ. Co. (1982) p. 373.

27. K. Abe et al., J. Nucl. Mat. 104 (1981) 1169.

28. R.W.K. Honeycome and R.W. Pethen, J. Less Common Metals 28 (1972) 201-212.

29. F.W. Clinard, Jr., "Copper Alloy Irradiation Studies in Support of CRFPR First Wall," in Ref. 1.

30. "STARFIRE - A Commercial Tokamak Fusion Power Plant Study," (Sept. 1980) Argonne National Laboratory.

31. D. Cohn, personal communication (March 1984).

IRRADIATION OF COPPER ALLOYS IN FFTF

H. R. Brager and F. A. Garner (Hanford Engineering Development Laboratory)

1.0 Objective

The object of this effort is to provide data on the response of a high-conductivity, high-strength series of copper alloys to high fluence neutron irradiation and thereby predict their behavior in anticipated fusion environments.

2.0 Summary

Nine copper-base alloys in thirteen material conditions have been inserted into the MOTA-1B experiment for irradiation in FFTF at ~450°C. The alloy Ni-1.9Be is also included in this experiment, which includes both TEM disks and miniature tensile specimens.

3.0 Program

Title: Irradiation Effects Analysis (AKJ)
Principal Investigator: D. G. Doran
Affiliation: Hanford Engineering Development Laboratory

4.0 Relevant DAFS Program Plan Task/Subtask

II.C.1 Effect of Material Parameters on Microstructure

5.0 Accomplishments and Status

5.1 Introduction

The use of high-conductivity high-strength copper-base alloys is anticipated for use in operation of fusion devices, particularly in the magnets and high heat-flux components.

There is very little data available on the response of such alloys to high levels of neutron exposure, however. The temperature range of anticipated use is $\leq$500°C, with the major applications below 300°C.

An opportunity recently arose to include a series of copper-base alloys in the MOTA-1B experiment currently being irradiated in the Fast Flux Test Facility (FFTF). The lowest temperature available in this experiment is ~450°C due to the use of helium rather than sodium as a thermal conduction medium. The experiment is targeted to reach four exposure levels: 15, 45, 105 and 150 dpa.

As shown in Table 1, there are nine copper alloys, some of which are in more than one starting material condition. Table 1 also shows that a high-conductivity high-strength Ni-1.9Be alloy and AISI 316 were included, the latter to provide a reference state for the experiment. There are three sets of specimens presently being irradiated, one for each fluence level, and a fourth set to be inserted at a later time. Each set contains 14 miniature tensile specimens and 30 TEM disk specimens. The former serve also as electrical conductivity specimens. The latter will be used for both microscopy and material properties testing.

TABLE 1

CONTENTS OF COPPER-MOTA-1B EXPERIMENT

ALLOYS SUPPLIED BY INESCO

Material	Composition	Condition
Cu Ag	Cu - 0.1 Ag	CW
Cu Ag P	Cu - 0.5 Ag - .06 P - .08 Mg	CWA
Al-25	Cu - 0.25 Al_2O_3	CW, SA
MZC	Cu - 0.9Cr - 0.1Zr - 0.05 Mg	CWA
Cu Be Ni	Cu - 1.8Ni - 0.3 Be	CWA, SA&T
Cu Be	Cu - 2.0 Be	CWA, SA&T
Ni Be	Ni - 1.9 Be	CWA

ALLOYS SUPPLIED BY HEDL

Cu - 5% Ni	These alloys used in	CW
Cu - 5% Al	previous RTNS-II studies	CW
Cu (99.999%)		CW, SA
AISI 316		CW

SA = Solution-annealed
CW = Cold-worked
CWA = Cold-worked and aged
T = Tempered

6.0 References

None

7.0 Future Work

Experiments to irradiate copper-base alloys at lower temperatures are being investigated.

8.0 Publications

None

COMPARISON OF NEUTRON- AND GAMMA-IRRADIATION DAMAGE IN ORGANIC INSULATORS

D. S. Tucker and F. W. Clinard Jr (Los Alamos National Laboratory)

1.0 Objective

This study is being carried out to determine the effects of neutron irradiation at 4.2 K on epoxy and polyimide insulators, and to compare these effects with those from gamma-irradiations at the same temperatures and in the same materials.

2.0 Summary

One polyimide- and two epoxy-based materials have been neutron-irradiated to total doses of 2.6 and 4.1 $\times 10^{21}$ n/m^2, $E_n > 0.1$ MeV at 4.2 K in IPNS-II. The environmental and thermal conditions during and after irradiations were similar to those employed in previous studies of gamma-irradiation effects at ORNL to facilitate comparison of the irradiation effects. In the present study, we have determined the flexural mechanical properties parallel to the fabric wrap direction at 75 K. These studies have disclosed selected differences when compared to results for gamma irradiations.

3.0 Program

Title: Radiation Damage Analysis and Computer Simulation (Radiation Effects in Organic Insulators)
Principal Investigator: D. S. Tucker
Affiliation: Los Alamos National Laboratory

4.0 Relevant DAFS Program Plan

TASK II.B.4: Damage Production Insulators
SUBTASK II.B.4.3: Experimental Validation/Calibration of Theory

5.0 Accomplishments and Status

5.1 Introduction

In a previous report on this study,[1] the requirements for organic insulation in magnetic confinement fusion reactors and the need for neutron radiation damage studies were presented. A subsequent report on this study[2] described irradiations of five organic materials in the IPNS-I to 1.5 $\times 10^{21}$ n/m^2 and discussed electrical and mechanical test data associated with the irradiations. Electrical property measurements were made only on G-10CR and showed at most only small changes. In comparing results of the flexure and compression tests, the most consistent findings were a decrease in strength and corresponding decrease in failure strain for the G-10CR, increase in modulus for G-11CR, decrease in failure, strain of NP-530, and combined reduction of ultimate stress and strain of glass-filled Epon 828 measured in compression. All of these changes were small and, by themselves, represent no limitation to their use in a magnet environment.

This report presents results of mechanical flexure tests on three materials irradiated to higher doses in the IPNS-II. These results are compared to results for gamma-irradiation studies at ORNL.

5.2 Irradiation Experiment at IPNS-II

Samples for irradiation were G-10CR, G-11CR, and Norplex NP-530.* These materials are described in a previous report. This irradiation was carried out in two parts.

Samples from a previous irradiation (IPNS-I), along with fresh samples, were irradiated in the fall of 1982 and again in March, 1983, using the following procedure. Samples were weighed, measured, photographed, and then stacked in an aluminum foil pouch inside a coppery cylinder. Nickel dosimetry wires were attached axially around the edge of the pouch at 90° intervals with an additional wire approximately in the center. The copper cylinder was then electron-beam welded to a cap with a copper tube extending outward and sent to IPNS for irradiation.

---

*G-10CR - National Electrical Manufacturers Association (NEMA). A heat-activated amine-catalyzed bisphenol solid-type epoxy resin laminate reinforced with continuous filament E-glass fabric, silane-finished designated for cryogenic use; Spaulding Fibre Company.
G-11CR - Same as G-10CR, except that an automatic amine-hardener bisphenol liquid-type epoxy resin was used in its fabrication.
NP-530 - Polyimide resin matrix, analogue of G-10CR; Norplex Division, VOP, Inc.

At IPNS, a 10-foot length of stainless steel tube was mated to the copper tube extending from the experimental assembly. Swagelok fittings were used throughout. The assembly was helium leak-tested and evacuated with a diffusion pump.

After insertion in the IPNS target area, the system was cooled to liquid helium temperature. Helium gas was introduced into the assembly, allowed to condense at one atmosphere, and then valved off. After irradiation the helium was pumped from the system, which was then valved off and warmed to room temperature. Midway during the irradiation time, the assembly was rotated 180° about the vertical axis to ensure uniform irradiation in the sample volume.

After the irradiation was completed, the copper subassembly containing the samples was removed and returned to Los Alamos. Samples were removed, reweighed, photographed, and stored in a desiccator.

Dosimetry from the nickel wires was analyzed by Larry Greenwood, ANL. Results indicated fairly uniform doses of 1.3×10^{21} n/m^2, E > 0.1 MeV for each irradiation. The gamma dose is not accurately known but is estimated to be 15% of that from neutrons. An exposure history of the samples is shown in Table I. After removal from the irradiation capsule, samples were again weighed and measured. All of the samples were found to have changed color.

TABLE I. Exposure history of test samples

	Neutron Fluence (n/m^2, E > 0.1 MeV)			
	NS-1	IPNS-2A	IPNS-2B	Cumulative
IPNS-I + IPNS-II	1.5×10^{21}	1.3×10^{21}	1.3×10^{21}	4.1×10^{21}
IPNS-II Only		1.3×10^{21}	1.3×10^{21}	2.6×10^{21}

5.3 Results

Mechanical flexure tests were carried out at 75 K using a three-point bend test fixture actuated by the cryogenic compression tests apparatus described previously.[1] Deflections were measured by means of an LDVT, which detected relative movement of the platens of the compression fixture. Length between out spans was 2.54 cm, and pin diameter was 6.4 mm. Samples were 3.2 x 1.6 mm in cross section and were tested with the major stress parallel to the warp direction. Deflection rate was 1.3 mm/min. This test procedure follows the requirements of ASTMD 790-80.

Test results were analyzed to determine modulus of rupture (MOR), flexual modulus (E), and failure strain (E_f). MOR was calculated using the simple beam formula, which is valid for maximum fiber strains of 5% or less. These parameters as a function of neutron fluence are plotted in Figs. 1 through 3.

MOR results, Fig. 1, show that only G-10CR exhibited a significant loss in strength (67%) and a flux net of 4.1×10^{21} n/m^2. G-11CR showed only a small reduction in strength (12%), while NP-530 showed a slight increase in flexual strength at this fluence.

The failure strain, defined as the nominal strain is shown in Fig. 2. The G-10CR samples show a decrease from an original value of 4.4% to approximately 1.85% at a fluence of 4.1×10^{21} n/m^2. Although the G-11CR control samples have a lower E_f than the G-10CR samples, the decrease after irradiations is much less with a value of 3.8% at a fluence of 1.5×10^{21} n/m^2. After showing an initial decrease to 3% at a fluence of 1.5×10^{21} n/m^2, E_f values for the NP-530 samples remained constant.

Flexure modulus (Fig. 3) for all three materials remains relatively constant for all irradiation values. After an initial rise at a fluence of 1.5×10^{21} n/m^2, E for G-11CR decreases to the initial value (control sample) and remains constant. Only G-10CR shows a steady decrease in E, while NP-530 actually exhibits an increase in E for fluences greater than 1.5×10^{21} n/m^2.

5.3.1 Discussion of Results

Of the three candidate materials, G-10CR showed the most reduction in strength with G-11CR exhibiting only a slight decrease and NP-530 actually displaying a slight increase at fluences greater than 2.6×10^{21} n/m^2. This behavior can possibly be attributed to two factors. First, neutron irradiation dose is strongly sensitive to hydrogen content since approximately one-half of the maximum energy can be transferred to hydrogen during elastic collision producing energetic recoil nuclei. The ionizing dose decreases in going from G-10CR to G-11CR to NP-530 as a result of the same trend in hydrogen content, which reflects in the strength results. The second factor, thought to be of greater importance, takes into account the nature of the chemical and molecular structure of both the resin materials and curing agents. Both G-10CR and G-11CR

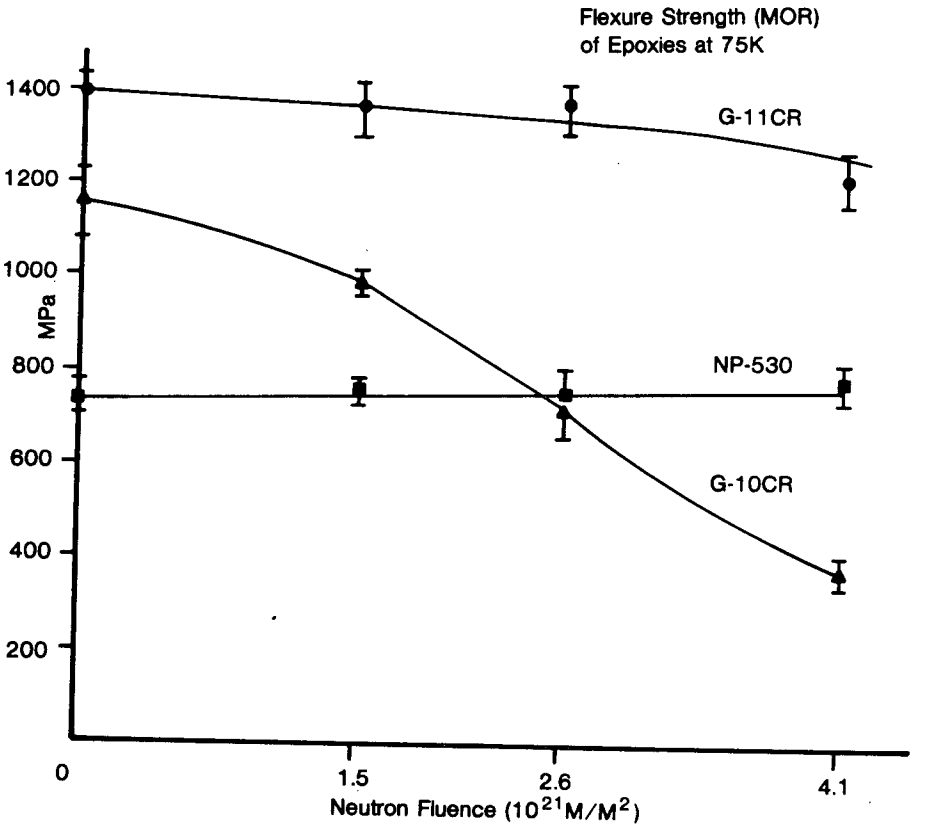

FIGURE 1. Flexure Strength vs. Neutron Fluence of G-10CR, G-11CR, and NP-530 at 75 K.

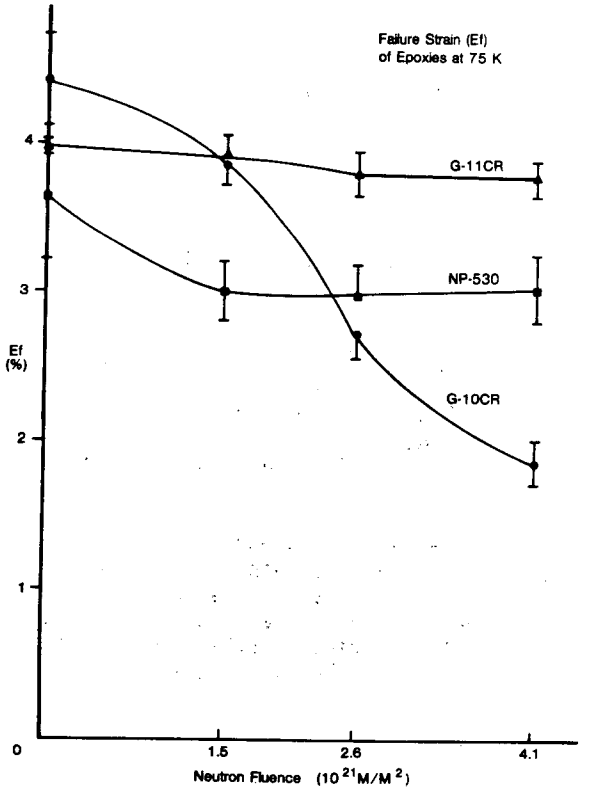

FIGURE 2. Failure Strain vs. Neutron Fluence for G-10CR, G-11CR, and NP-530 at 75 K.

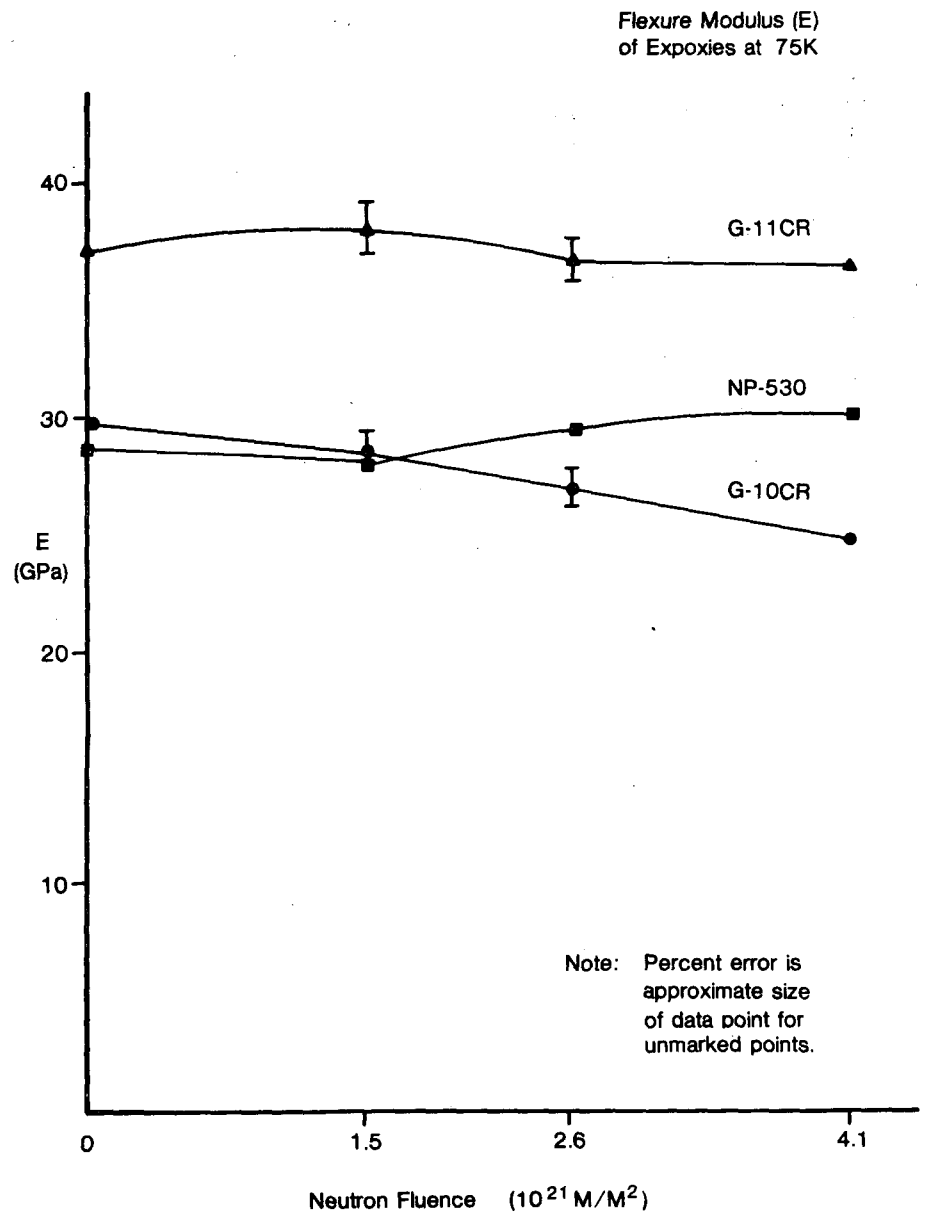

FIGURE 3. Flexure Modulus of G-10CR, G-11CR, and NP-530 at 75 K.

are identical, except that G-11CR utilizes an aromatic cure, while G-10CR incorporates an aliphatic curing agent. It has been established that the resonant ring structure of an aromatic is more resistant to radiation (γ, e^-) than the straight chain aliphatic structure, due to the ability of the nonlocalized elferrons in the aromatic ring to absorb and dissipate energy more readily than a single bond, characteristic of the aliphatic structure. The bond strength of the aromatic structure is also greater than that of the aliphatic structure, which enhances radiation resistance.

NP-530 is a polyimide, which is a nitrogen-carrying, condensed aromatic ring system. The aromatic ring is an electron-withdrawing group, which makes possible resonance between nitrogen and the ring. This, in turn, increases the radiation resistance of the structure by increasing the structure's resonant energy. This structure also contains sidechains with double bonds present, which again increases the resonant energy and provides easier paths for energy to pass into the rings and be evenly distributed around the ring. The matrix structures of both G-10CR and G-11CR are bisphenol-A epoxy resins. While this structure contains aromatic rings, the resonance energy is not as high as that for the polyimide structure. Also, polyimides contain meta-directing groups, which are more stable than the ortho- and para-directing groups found in the bisphenol-A structure. These effects could explain the enhanced radiation resistance of NP-530, especially compared to G-10CR.

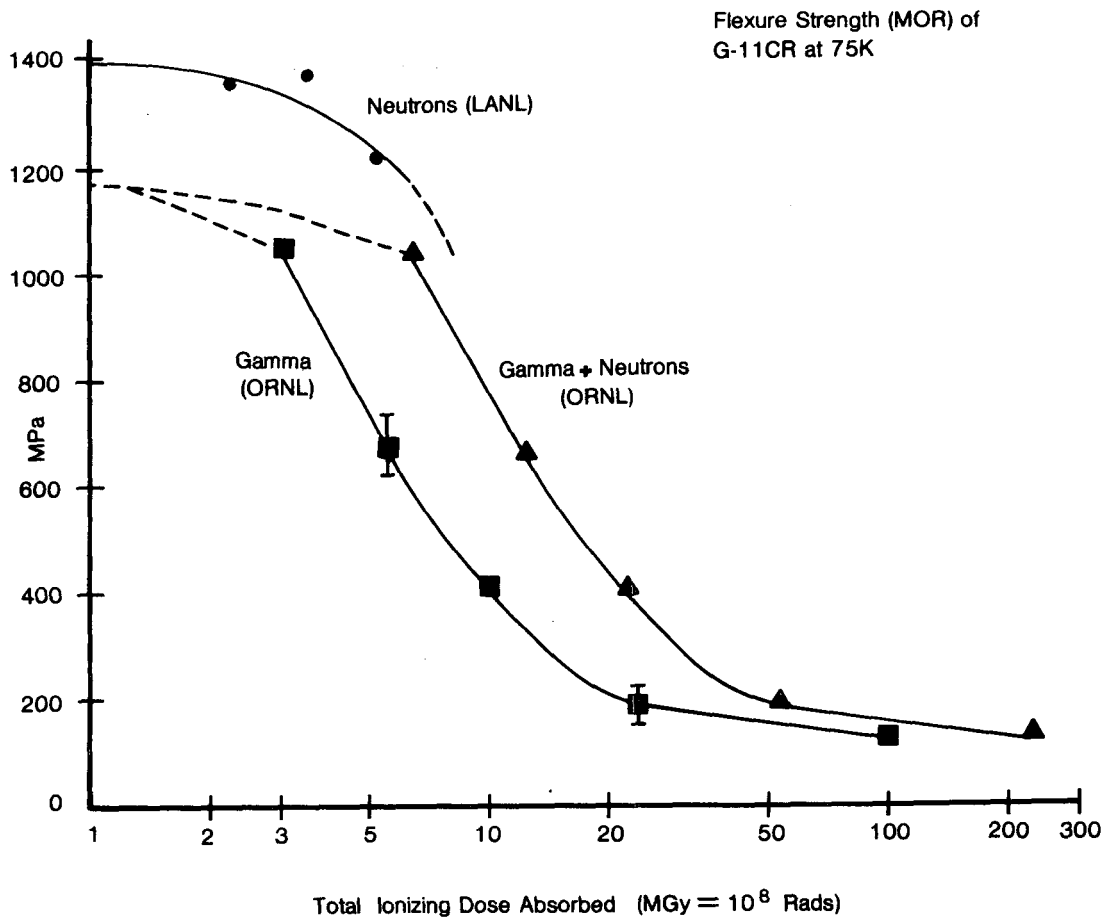

FIGURE 4. Comparison (gamma, neutrons) of Flexure Strength vs. Total Ionizing Dose Absorbed for G-11CR.

5.4 Comparison with Gamma-Irradiation

A comparison of fast neutron data (this work) with gamma-irradiation data[3] for flexure strength of G-11CR is shown in Fig. 4. As can be seen, there is a fairly large discrepancy between the strength curves for fast neutron irradiation and gamma irradiation. The fiber reinforcement in G-11CR is made from E-glass, which contains approximately 3% boron. The isotope ^{10}B has a large cross section for thermal neutrons resulting in the reaction $^{10}B(n,\alpha)^{7}Li$. If this reaction is taken into account, a corrected curve can be generated (gamma and thermal neutrons), which more closely agrees with the fast neutron data. Such a correction is not necessary when boron-free S-glass is used as the fiber reinforcement (Fig. 5). A comparison of fast neutron VS gamma-induced degradation in damage-resistant materials, such as NP-530, must await the results of higher dose tests now in progress.

6.0 References

1. G. F. Hurley, J. D. Fowler, Jr., and D. M. Parkin, "Neutron-Irradiation Plan for Calibration of Gamma and Neutron Damage Effects in Organic Insulators", in Damage and Fundamental Studies Quarterly Progress Reports for October - December, 1981.

2. G. F. Hurley, J. D. Fowler, Jr., R. Liepins, B. Jorgenson, and J. Hammond, "Comparison of Neutron and Gamma Irradiation Damage in Organic Insulators", in Damage Analysis and Fundamental Studies Quarterly Progress Report, in press.

3. R. R. Coltman, Jr., and C. E. Klabunde, "The Strength of G-10CR and G-11CR Epoxies After Irradiation at 5 K by Gamma Rays", in Journal of Nuclear Materials, 113, pp. 268-72, 1983.

7.0 Future Work

Work continues on this project in four areas: continuation of experimental measurements on samples from the third IPNS irradiation, correlation of these results with literature results for gamma irradiations, preparation of model compounds for comparative determination of structural changes in neutron and gamma

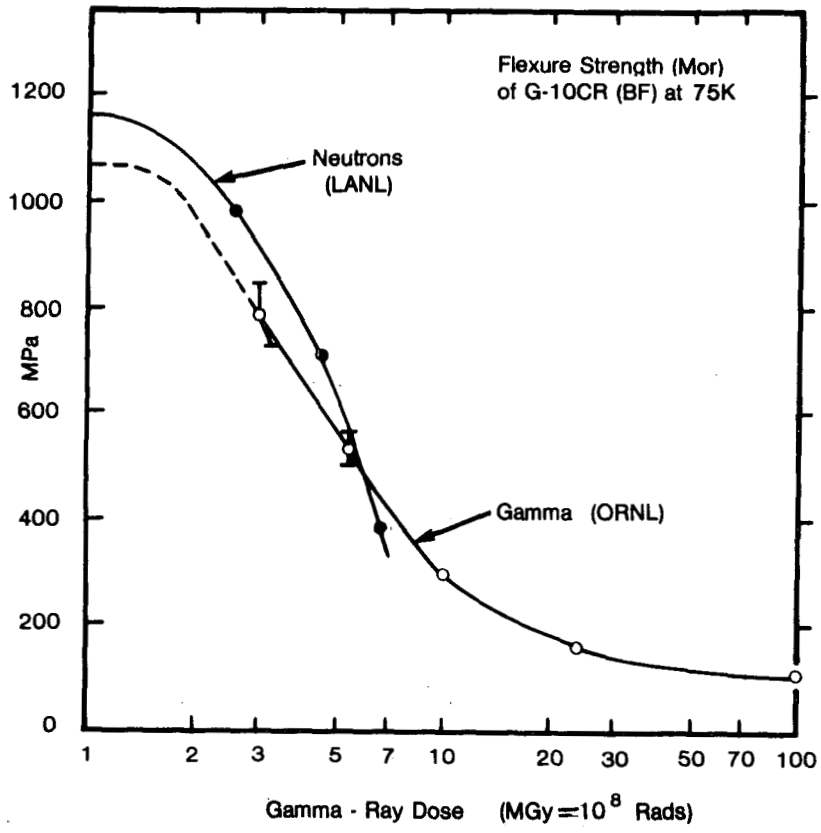

FIGURE 5. Comparison (gamma, neutrons) of Flexure Strength vs. Gamma-Ray Dose for G-10CR(BF) at 75 K.

irradiations, and preparation of further irradiation experiments for IPNS-II and RTNS-II. We will seek higher doses in IPNS-II and begin irradiations of model compounds in the RTNS-II in late summer, 1984.

Acknowledgements

The authors would like to acknowledge Mark Kirk, ANL, in carrying out the irradiation in IPNS and of Larry Greenwood, ANL, who is performing the dosimetry. The G-10CR and G-11CR were supplied by the Spaulding Fibre Company, Tonawanda, New York, and the NP-530 by Norplex Division, VOP, Inc., La Crosse, Wisconsin.

EXTERNAL DISTRIBUTION

UC-20 (106)

UC-20c (69)

DOE-HQ/Office of Breeder
Technology Projects
NE-53
Washington, DC 20545

PB Hemmig, Asst Director,
Reactor Physics Tech

DOE-HQ/Office of Fusion Energy (3)
Washington, DC 20545

JF Clark, ER-70
JF Decker, ER-54, G-256
S. Parket, ER-62, GTN

Argonne National Laboratory (5)
9700 South Cass Avenue
Argonne, IL 60439

LR Greenwood BA Loomis
A. Taylor H. Wiedersich
RE Nygren

Battelle
Pacific Northwest Laboratory (3)
P.O. Box 999
Richland, WA 99352

JL Brimhall
DA Dingee
TD Chikalla

Brookhaven National Laboratory
Associated Universities
Upton, Long Island, NY 11973

Chairman, Nuclear Energy Dept

Columbia University
Plasma Physics Laboratory
New York, NY 10027

RA Gross

Commission for the European Communities
200, Rue de la Loi
B-1049 Brussels, Belgium

J. Darvas

Energieonderzoek Centrum Nederland (2)
Netherlands Energy Research Foundation
Westinghouse 3
Postfach 1
NL-1755 ZG Petten, The Netherlands

B. vanderSchaaf
W. vanWitzenburg, Materials Dept

EURATOM
Joint Research Center Ispra
Materials Science Division
I-21020 Ispra, Varese, Italy

P. Schiller

General Atomic Company (2)
P.O. Box 81608
San Diego, CA 92138

GR Hopkins
JR Gilleland

Hahn-Meitner Institüt für Kernforschung
Glienickerstrasse 100
D-1000 Berlin,
Federal Republic of Germany

H. Wollenberger

Hokkaido University (2)
Metals Research Institute
Kita-hu, Sapporo, 060 Japan

Mihio Kiritani, Precision Eng
Taeo Takeyama

EXTERNAL DISTRIBUTION (Cont'd)

INESCO
11011 Torreyana Rd
San Diego, CA 92121

RD Stevenson

Japan Atomic Energy Research Institute (2)
Physical Metallurgy Laboratory
Tokai Research Establishment
Tokai-mura, Naka-gun, Ibaraki-ken, Japan

Shuichi Iwata, Physics
Kensuke Shiraishi, Nucl Fuel Research

Kernforschungsanlage Jülich GmbH
Postfach 1913
D-517 Jülich,
Federal Republic of Germany

H. Ullmaier

Kernforschungszentrum Karlsruhe
Institüt für Reaktorbauelemente
Postfach 3640
D-7500 Karlsruhe 1,
Federal Republic of Germany

K. Ehrlich

Kyushu University
Research Institute for Appl Mechanics
6-10-1 Hakozaki, Higashi-ku,
Fukuoka, 812 Japan

Kazunori Kitajima

Lawrence
Livermore National Laboratory (4)
P.O. Box 808
Livermore, CA 94550

WL Barmore
DW Dorn
MW Guinan, L-396
CM Logan

Lawrence
Livermore National Laboratory
P.O. Box 5511
Livermore, CA 94550

EC Dalder, L-643

Los Alamos National Laboratory (3)
P.O. Box 1663
Los Alamos, NM 87544

DJ Dudziak
CR Emigh
J. Fowler, E-546

Massachusetts Institute of Technology (4
77 Massachusetts Avenue
Cambridge, MA 02139

I-W Chen, 13-5118
NJ Grant, 8-305
L. Lidsky
JB van der Sande, 13-5025

Massachusetts Institute of Technology
Nuclear Reactor Laboratory
138 Albany St
Cambridge, MA 02139

OK Harling, NW12-204

McDonnell-Douglas Astronautics Co.
P.O. Box 516
St. Louis, MO 63166

D. Kummer

Mound Laboratory
P.O. Box 32
Miamisburg, OH 45342

Manager, Tech Appl & Dev

National Bureau of Standards
Gaithersburg, MD 20760

JA Grundl

EXTERNAL DISTRIBUTION (Cont'd)

National Research Council
Montreal Road
Ottawa, Canada

EV Kornelson

National Research Institute for Metals
Nuclear Materials Division
1-2-1 Sengen, Sakura-mura,
Niihari-gun, Ibaraki, 305 Japan

Naoki Kishimoto

Naval Research Laboratory (3)
Washington, DC 20375

I. Manning, Code 6672
JA Sprague, Code 6395
LE Steele, Code 6390

North Carolina State University
Department of Nuclear Engineering
Raleigh, NC 26707

JR Beeler Jr

Oak Ridge National Laboratory (12)
P.O. Box X
Oak Ridge, TN 37830

Director	M. Roberts
K. Farrell	J. Sheffield
ML Grossbeck	JO Stiegler
PJ Maziasz	C. Weisbin
LK Mansur	FW Wiffen
NH Packan,	Bldg 9204-1
FG Perey,	Bldg 9201-2

Osaka University (2)
2-1, Yamada-oka, Suita,
Osaka, Japan 565

Kenji Sumita, Dept of Nuclear Eng
Toichi Okada, Institute of
Scientific & Industrial Research

Princeton University (4)
Plasma Physics Laboratory
Forrestal Campus
P.O. Box 451
Princeton, NJ 08544

H. Conrads	R. Little
H. Furth	K. Wakefield

Risø National Laboratory
Postfach 49
DK-4000 Roskilde, Denmark

B.N. Singh

Rockwell International
8900 DeSoto Ave
Canoga Park, CA 91304

DW Kneff

Sandia National Laboratories (2)
P.O. Box 5800
Albuquerque, NM 87185

FL Vook, Org 5100

Sandia National Laboratories (2)
Livermore, CA 94550

W. Garrison, Div 8314
WD Wilson

Science Applications Inc
1200 Prospect
LaJolla, CA 92037

Dr. H. Gurol

Science University of Tokyo
Engineering Dept
Kagurazaka, Shinjuku-ku,
Tokyo, 162 Japan

RR Hasiguti

EXTERNAL DISTRIBUTION (Cont'd)

Studiecentrum voor Kernenergie
Centre d'Etude de l'Énergie Nucléaire
Boeretang 200
B-2400 Mol, Belgium

J. Nihoul

Swiss Federal Institute
for Reactor Research
CH-5303 Wuerenlingen, Switzerland

WV Green

Tokyo Institute of Technology
12-1, 2-Chome, O-Okayama
Meguro-ku, Tokyo, Japan

Kensutaka Kawamura

United Kingdom Atomic Energy Authority (2)
Atomic Energy Research Establishment
Oxfordshire, OX 11 ORA, UK

R. Bullough, Theoretical Physics Div

United Kingdom Atomic Energy Authority
Culham Laboratory
Applied Physics and Technology Div
Abingdon, Oxfordshire OX14 3OB, UK

GJ Butterworth

University of California (2)
Los Angeles, CA 90024

RW Conn
NM Ghoniem

University of Michigan
Nuclear Engineering
Ann Arbor, MI 48109

T. Kammash

University of Missouri
Mechanical & Aerospace Eng
1006 Engineering Bldg
Columbia, MO 65211

M. Jolles

University of Missouri
Dept of Nuclear Engineering
Rolla, MO 65401

A. Kumar

University of Tokyo (3)
7-3-1 Hongo
Bunkyo-ku, Tokyo 113, Japan

Naohira Igata, Met & Mater Science
Shiori Ishino, Nuclear Eng
Taijiro Uchida

University of Virginia
Dept of Materials Science
Charlottesville, VA 22901

WA Jesser

University of Wisconsin
1500 W. Johnson Drive
Madison, WI 53706

WG Wolfer

Westinghouse
Advanced Energy Systems Division
Fuels Materials Technology
P.O. Box 158
Madison, PA 15663

A. Boltax, Manager

Westinghouse
Research and Development Center (2)
1310 Beulah Road
Pittsburgh, PA 15235

JA Spitznagel
S. Wood

INTERNAL DISTRIBUTION

DOE-RL/AMCW (2)
FMIT Facility Project Office
FED/642-F

GM Chenevert, Proj Mgr

DOE-RL/AME
Breeder Technology Division
Technology Development &
Engineering Branches
FED/210

KR Absher, Chief

HEDL (29)

SD Atkin	W/A-58	EK Opperman	W/A-58
HR Brager	W/A-58	NF Panayotou	W/A-65
LL Carter	W/B-47	RW Powell	W/A-58
DG Doran	W/A-57	RJ Puigh	W/A-58
EA Evans	W/C-23	FH Ruddy	W/C-39
FA Garner	W/A-58	FA Schmittroth	W/A-4
DS Gelles	W/A-58	WF Sheely	W/C-62
R. Gold	W/C-39	RL Simons	W/A-57
JW Hagan	W/M-81	JL Straalsund	W/A-61
HL Heinisch	W/A-58	HH Yoshikawa	W/C-44
DL Johnson	W/A-4	Central Files (3)	W/C-110
GD Johnson	W/A-65	Publ Services	W/C-115
FM Mann	W/A-4	Microfilm Services	W/C-123
WN McElroy	W/C-39		